INVESTIGATION OF A NEW MODEL OF DIPOLAR-COUPLED NUCLEAR SPIN RELAXATION AND APPLICATIONS OF DYNAMIC NUCLEAR POLARIZATION

by

Eric G. Sorte

A dissertation submitted to the faculty of
The University of Utah
in partial fulfillment of the requirements for the degree of

Doctor of Philosophy

in

Physics

Department of Physics and Astronomy

The University of Utah

August 2011

The University of Utah Graduate School

STATEMENT OF DISSERTATION APPROVAL

The dissertation of **Eric G. Sorte**

has been approved by the following supervisory committee members:

Brian Saam	, Chair	**5/27/2011** Date Approved
David Kieda	, Member	**5/27/2011** Date Approved
Eugene Mishchenko	, Member	**5/27/2011** Date Approved
Christoph Boehme	, Member	**5/27/2011** Date Approved
Dennis Parker	, Member	**5/27/2011** Date Approved

and by **David Kieda**, Chair of the Department of **Physics and Astronomy**

and by Charles A. Wight, Dean of The Graduate School.

ABSTRACT

This work presents the results of various investigations using various techniques of hyperpolarizing the nuclei of atoms. Hyperpolarization implies magnetic order in excess of the thermal order obtained naturally as described by Curie's law.

The main portion of this work presents the results of a detailed experimental exploration of predictions arising from a new model of transverse nuclear spin relaxation in quantum systems, based on possible manifestations of microscopic chaos in quantum systems. Experiments have been carried out on a number of hyperpolarized xenon samples, each differing in its relative percentage of xenon isotopes in order to vary the homonuclear and heteronuclear dipole couplings in the spin system. The experiments were performed under a variety of conditions in an attempt to observe the behaviors predicted by the model. Additionally, much more extensive measurements were made on a number of samples of solid CaF_2 in both single crystal and powder forms. These samples, although thermally polarized, were observed with superior signal to noise ratios than even the hyperpolarized xenon solids, allowing for more precise measurements for comparison to the theory. This work thus contains the first experimental evidence for the majority of the model's predictions.

Additionally, this work contains the first precise measurements of the frequency-shift enhancement parameters for ^{129}Xe and krypton in the presence of spin-polarized Rb. The determination of these important numbers will be useful to many groups who utilize spin-exchange optical pumping in their labs. This work built on the prior knowledge of a precise number for the frequency-shift enhancement parameter of ^{3}He in Rb vapor.

Finally, I detail work using NMR to detect nuclear-spin polarization enhancement in silicon phosphorus by a novel, photo-induced hyperpolarization technique developed by the Boehme research group at the University of Utah. Significant nuclear polarization enhancements were observed by the Boehme group due to electron-photon interactions in semiconductor soilds; these enhancements were observed by their effects on the ambient electrons and measured with electron spin resonance techniques. The work described here details experiments to observe the enhanced nuclear polarization by directly measuring the intensity increase in an NMR measurement.

I will conclude this dissertation with a brief appendix giving a summary of one additional project involving the use of high pressure fluorinated gas NMR to measure the internal topology and characteristics of energy-rich oil shales.

"When it's over, I want to say: all my life
I was a bride married to amazement.
I was the bridegroom, taking the world into my arms.
When it is over, I don't want to wonder
if I have made of my life something particular, and real.
I don't want to find myself sighing and frightened,
or full of argument.
I don't want to end up simply having visited this world."
–Mary Oliver

CONTENTS

LIST OF FIGURES

LIST OF TABLES

ACKNOWLEDGMENTS

One of my earliest memories happened when I was a child in grade-school. I was riding in the back seat of our family car on my way to school with my mother at the wheel. I no longer recall how the conversation began, but we were discussing math. My mother made a comment that has stayed with me since that day, because I thought about it again and again over the ensuing weeks and years. I remember I had just informed my mother that, "I had already *learned* math," and I recall really believing that at the ripe old age of six or seven that I had learned what there was to know of the subject. I remember my mother giving me a look in the rear-view mirror, and informing me, "You don't know it, but there are all kinds of things in math that you've never even heard of." Confident she was wrong, I challenged her to name one thing in math that I didn't know. She asked me if I knew about imaginary numbers.

I knew about no such thing. I actually remember thinking she was making it up. When I found out she wasn't, it for some reason upset me. Imaginary? Why should there exist imaginary numbers? What did that even mean? Lacking Google (as one did when I was a child), it wasn't until high school that a math teacher was able to explain imaginary numbers to me. I must say that even now I'm not terribly comfortable with the idea, but as the popular quote says, "In mathematics you don't understand things. You just get used to them."[1] I sometimes recall that memory as one example of the academic challenges inspired by my mother and father, who actively encouraged exploration, and who placed a high emphasis in our home on education and learning. Without them, I would certainly not be writing this dissertation.

In the ensuing years, indeed as far back as I can remember, I always wanted to study things. It rarely mattered what the subject. There was simply a pleasure in learning things, for feeling that rush of understanding. I graduated high school knowing a little about a great deal, but not much about anything in particular. My undergraduate years were similarly unfocused, and I ended up in classes all over the academic map. I finally graduated with a

[1] Attributed to mathematician John von Neumann.

B.A. in Finance after taking at least as many classes outside my major as inside it. After agonizing exhaustively about it for the next five years, I finally decided to try to focus and get a deep understanding of one of the topics of interest to me — physics. I studied to catch up with where I needed to be with the math and science, and was eventually accepted to graduate school in physics.

It was with this somewhat haphazard resumè that I first walked into the office of Dr. Brian Saam in the summer of 2007, at the end of my first year of graduate school, asking for him to believe that I could, despite my past, concentrate on one area of study for longer than 20 minutes. I will be always grateful that Dr. Saam decided to take a risk, and see if he could take a kid with a degree in business, a lack of focus, and little background in science and see if he could teach him prudence, patience, analysis, and careful methodical thinking - that is, to be a scientist. The degree to which he succeeded is not clear, but I offer my most sincere thanks to the man who took me under his academic wing, and by example, taught me what it is to be a scientist. I could not have asked for a better mentor; apart from the first-rate scientific training, Dr. Saam also offered me his friendship, his confidence, and his trust.

Having been accepted into the group, I was put in the care and keeping of Gernot Laicher, who put me on the path to understanding NMR. With his encyclopedic understanding of spin physics, he taught me and showed me the experimental ropes of an NMR lab. Having the privilege of working closely with Dr. Laicher for over a year more than made up for my lack of undergraduate laboratory training. I will always be indebted to Dr. Laicher for the patience, kindness, and knowledge he shared with me.

Apart from these, I have been helped along the way of my graduate studies by many other people. Geoff Schrank, Zayd Ma and Mark Limes, my fellow graduate students with whom I shared the Saam labs, were always available for discussions and to help with understanding an idea, as well as for performing experiments with me often late into the night. Monica Allen was my irreplaceable study partner for endless tests and homework assignments over the years, and was a consistent friend when I needed one the most; she also saved me time and time again with her mathematical prowess when I was hopelessly outmatched by some seemingly intractable problem.

The other students and faculty here at the University with whom I collaborated or worked have also contributed enormously to my education. Tho Nyugen and Will Baker, with whom I always seemed to be running experiments well after hours, I am particularly

glad to know and call friends. Ben Anger, Kim Butler, Candice Murray, Laurel Hales, Haleigh Van Eerden, Tom Van Hook, Oliver Jeong, and Alison Schoeck all contributed to the lab in important ways and put up with me working beside them. I also enjoyed the friendship and tutelage of many great professors, including Jordan Gerton, Christoph Boheme, John Belz, David Kieda, and Eugene Mishchenko. Kathy Blair, JoLene Snyder, Harold Simposon, Wayne Wingert, Heidi Frank, Brad Hawks, Jackie Hadley, and Katherine Skollingsberg did everything in their power to make sure I had all the support and access to equipment, research papers, supplies, and anything else that I needed. Joe Atkin, Dan Bischoff, and Travis Bowers were and are a continual force for good in my life. I also want to thank Heidi Grieser and Kathy Sorte for proofreading, editing, and generally improving this manuscript - if there are shortcomings, it was much worse before they improved it.

CHAPTER 1

INTRODUCTION TO NUCLEAR MAGNETIC RESONANCE AND HYPERPOLARIZATION

Perhaps typically, my graduate school training has consisted of work on a wide variety of seemingly disparate projects for which it is hard to identify a common theme apart from the manipulation of nuclear spin magnetization. Though a few of the projects in which I participated did not bear results that we deemed publishable, I will here briefly detail the work and the results achieved on those abortive projects (as well as on those that yielded several publications) for the sake of archival completeness.

In this chapter, I will introduce the subject of nuclear magnetic resonance. After explaining the motivation behind the effort to enhance nuclear polarization, I will explain the techniques used in this work to enhance the nuclear polarization in solid samples. I will then conclude with a brief explanation of nuclear relaxation and an overview of some of the terminology used in this thesis.

1.1 Nuclear Magnetic Resonance

Speak a new language
so that the world
will be a new world.
–Rumi

1.1.1 Background

Throughout the vast majority of human history, natural scientists have been limited in their explorations of nature to what could be observed by the human eye, using only visible light as a probe. Under optimal conditions, the naked eye can resolve spatial separations of around 100 microns, thereby putting a lower spatial bound on the phenomena that we are used to experiencing in nature. Furthermore, the interior structures of matter remained in

large part inaccessible for most of this period. It was only with the discovery of X-rays by Roentgen in 1895, and their application to investigating the inner structure of matter on scales smaller than ever before, were the limitations of the unaided eye at last spectacularly overcome.

It was not many years later that we began to gradually understand that the laws that dictate the world of our common experience, what scientists would term the classical world, were in no way sufficient to describe what happens below the resolution limit of the naked eye, *i.e.*, in the microscopic world. This discovery made the first 30 years of the twentieth century unprecedented in terms of the production of revolutionary theories and experiments that attempted to grasp these "quantum" behaviors. Little by little, a veritable roll call of the best minds of the last 200 years pried us from our firm grasp on classical mechanics, and lead us gradually into the light of the new, richer, and fuller theory of quantum mechanics: Max Planck's experiments led to Planck's radiation law; Albert Einstein and Peter Debye developed their theories of specific heats; Neils Bohr developed an atomic model; Louis de Broglie constructed theories of matter waves; Arthur Compton and his graduate student performed the first X-ray scattering experiments; James Franck and Gustav Hertz provided the first experiments in support of the Bohr atom; Otto Stern and Walther Gerlach famously (and elegantly) demonstrated the quantization properties of quantum mechanics; Werner Heisenberg quantified the fermionic properties of some quantum particles; Erwin Schrödinger, in a brilliant year, published four papers wherein, among other important contributions, he derived the Schrödinger equation and solved the quantum harmonic oscillator problem; Paul Dirac furthered knowledge of quantum mechanics and quantum electrodynamics; and the list goes on. With the mountain of experimental evidence incontrovertible, and the new theories gradually ever more confirmed by exhaustive experiments, new and noninvasive probes into the atomic structure of matter were necessary to understand the properties and laws of this strange microscopic world.

Magnetic resonance rose in the late 1940s as a way to gain information about processes at the atomic level. The enormous pace of the development of the science of magnetic resonance has yielded an amazing variety of applications and methods across numerous fields of study. One of the most spectacular is its ability to "see" inside of solids — notably even living beings —and obtain information (and even pictures) of their interiors without disruption of biological or other important processes. The ability to see inside an object, coupled with submicrometer resolution, makes magnetic resonance an ideal tool for probing

the quantum world.

To perform a nuclear magnetic resonance signal, a sample is obtained that is comprised of atoms that have an intrinsic magnetic moment associated with the nucleus. This magnetic moment does not arise from a circulation of charge density, but it acts in much the same way as a moment derived from that mechanism would act. In particular, the magnetic moments associated with the nuclei in the sample will tend to align with an external magnetic field. The degree to which the moments do align with the magnetic field is termed the *polarization* of the sample, and for low polarizations varies it linearly with the field and inversely with the temperature of the sample. As will be explained below, the magnetic moments may be nutated away from their equilibrium alignment along the external field by means of a radiofrequency pulse oscillating at the appropriate frequency determined by the nucleus and the magnetic field. Once nutated away from the direction of the magnetic field, the net magnetic moment of the sample (comprised of the sum of the individual atomic moments) will continue to precess around the external field. If the sample is surrounded by a coil of wire, the precessing magnetization of the sample will induce an oscillating voltage in the coil. This oscillating voltage can be read by a voltmeter, and the signal recorded. This signal is termed a free induction signal. For reasons that will be explained in Sec. 1.3, the free induction signal will eventually diminish or decay away, and so the signal is colloquially known as a free induction decay signal, or FID. Not surprisingly, the shape, duration, frequency components, and intensity of the FID can tell us much about the atoms that are contributing to the signal. If several radiofrequency pulses are applied to the sample in specific combinations, the resulting signal is often termed an "echo" of one of various sorts. Through various combinations of different radiofrequency pulses, an astonishing amount of information can be gained from the resulting FID and echo signals. Chapter 2 will focus on a panoply of radiofrequency pulse combinations to investigate the samples used in those experiments by means of the shapes of the FIDs and echoes generated by their precessing nuclei. In that chapter and the rest of this work, the terms "lineshape," FID, echo lineshape, and similar terms are frequently used denote the shape of the signals obtained in the NMR experiments. It is to be recalled that what is being measured in all cases is simply the precession of the manipulated nuclei around the external magnetic field.

1.1.2 Motivation - Why We Hyperpolarize Nuclei

Hyperpolarized nuclei are nuclei in which the volume-averaged nuclear spin polarization has been augmented relative to the polarization expected in thermal equilibrium as predicted by Curie's law. There are many ways of achieving nuclear hyperpolarization; the field of dynamic nuclear polarization focuses on exploring and optimizing such techniques. In this work, spin-exchange optical pumping of noble-gases was used as the hyperpolarization technique of choice for many experiments, but we also employed other novel techniques to achieve high nuclear polarizations in some experiments.

As will be described later, nuclear magnetic moments are extremely weak. For example, a ^{129}Xe nucleus has a magnetic moment that is over 2300 times smaller than that of an isolated electron ($\gamma_{electron} = -1.76 \times 10^{11}\ rad\ s^{-1}\ T^{-1}$, $\gamma_{^{129}Xe} = 73.99 \times\ 10^{6}\ rad\ s^{-1}\ T^{-1}$), making NMR signals far weaker than their electron resonance counterparts. As a result, equilibrium thermal nuclear polarizations achievable even with magnetic fields of many Tesla are small, usually on the order of 10^{-6}. That is, only one or a few particles in a million are contributing to the detectable NMR signal. Nonetheless, nuclear magnetic resonance can still provide relatively large and easily detectable signals in many solids and liquids due to the high particle density in such samples, which may be as high as 10^{23} atoms in a few milliliters.

In the gas phase, however, the situation is more difficult. The density of an ideal gas at standard temperature and pressure (STP) is 2.69×10^{19} atoms/cc, three orders of magnitude less than typical liquid densities. In equilibrium, the thermal polarization of low density gas-phase samples results in signals that are much more difficult and time consuming to acquire. Hyperpolarization techniques use various methods to overcome this density limitation by enhancing the polarization of the gas, thereby increasing the number of particles contributing to the signal. Depending on the technique, polarization enhancements of 100,000 times can be routinely accomplished. Such enhancements can result in nuclear polarizations of 80% or higher, more than make up for the low density, and yield signals comparable to or larger than those of thermally polarized solid samples.

1.2 Hyperpolarization Techniques

Researchers have developed many ingenious and varied techniques of hyperpolarizing nuclei in solid- liquid-, and gas-phase atoms. The methods vary widely: dynamic nuclear polarization using off-resonance radiation has been studied in great detail [2, 3]; complicated

pulse trains and adiabatic fast passage effects have been used to increase nuclear polarization [4, 5]; electrical manipulation, due to free carrier injection, has been successfully implemented [6]; optical excitation with polarized light has proven effective under some conditions [7, 8]; and the list goes on at some length. Extensive reviews on the subject of hyperpolarization and dynamic nuclear polarization have been published; the reader may wish to consult them for more detailed descriptions and more complete listings than are appropriate here (see for example Refs. [9, 10, 11] among many others). For this work, we used spin exchange optical pumping and a variation on the Overhauser effect to enhance the nuclear polarization of our samples. Below, we'll discuss both technique in more detail.

1.2.1 Spin Exchange Optical Pumping

Spin exchange optical pumping (SEOP) is carried out in a two-step process. In the first step, angular momentum is transferred from circularly polarized photons to the valence electron of an alkali-metal atom in vapor via depolarization optical pumping. Transitions are induced in a low density vapor by means of high-frequency irradiation. In the second (spin exchange) step, the alkali-metal atom interacts with a noble-gas nucleus through the hyperfine interaction, and transfers angular momentum from the alkali-metal atom to the noble-gas. During and between each of these exchanges, the alkali-metal and noble-gas atoms experience interactions which tend to drive their respective polarizations back to thermal equilibrium through various relaxation processes. The following is a simple overview of SEOP; for a complete theoretical treatment the reader is directed to the excellent reviews by Thad Walker [12] or Stephan Appelt [13].

1.2.1.1 Depopulation Optical Pumping

Depopulation optical pumping is the process through which the spin angular momentum of a photon is transferred to the orbital angular momentum of the valence electron in an alkali-metal atom. In our experiments requiring hyperpolarization by SEOP, we used rubidium metal; other alkali-metals have also been employed with success in other experiments (see for example [14]). The rubidium atom consists of a spherically symmetric arrangement of core electrons and one optically-active electron in the valence shell with orbital angular momentum L=0,1,2,3, etc. In the absence of a magnetic field, the alkali-metal atom is subject to a Hamiltonian approximately given by

$$\mathcal{H} = \mathcal{H}_0 + \mathcal{H}_{LS} + \mathcal{H}_{HF}, \tag{1.1}$$

where the three terms are

$$\mathcal{H}_0 = \frac{\mathbf{p}^2}{2m_e} + V_c(r) \tag{1.2}$$

$$\mathcal{H}_{LS} = \frac{1}{2m_e^2 c^2 r}\frac{dV_c(r)}{dr}\mathbf{L}\cdot\mathbf{S} \tag{1.3}$$

$$\mathcal{H}_{HF} = a\frac{8\pi}{3}\delta(r)\mathbf{I}\cdot\mathbf{S}. \tag{1.4}$$

In Eqs. (1.1) – (1.4), $\mathcal{H}_0$ is the kinetic energy term of the Hamiltonian, $\mathbf{p}$ is the momentum operator, m_e is the mass of the electron, $V_c(r)$ is the distance dependent (Coulombic) potential, $\mathcal{H}_{LS}$ is the spin-orbit coupling term, c is the speed of light, $\mathcal{H}_{HF}$ is the hyperfine interaction terms, and a is a measure of the strength of the hyperfine coupling. The operators **L, I, S** have their usual meanings representing the angular momentum operators of orbital, nuclear spin, and electronic spin angular momentum, respectively.

The energy level diagram for ^{87}Rb resulting from Eq. (1.1) is shown in Fig. 1.1a. The ground state has orbital angular momentum L=0, resulting in a total angular momentum quantum number J=1/2. The S-state and P-state degeneracy is lifted by the fact that the higher L-states, having a larger spatial extent, are more susceptible to repulsion from the valence electron cloud. This is a reflection of the fact that the electrostatic potential $V_c(r)$ in $\mathcal{H}_0$ of Eq. (1.2) is no longer purely Coulombic. The first excited state (L=1) is split by the spin-orbit coupling $\mathcal{H}_{LS}$ into two levels, the $^2P_{1/2}$ and $^2P_{3/2}$ (not shown in Fig. 1.1). Both the ground state and the first excited state are themselves further split by the hyperfine coupling $\mathcal{H}_{HF}$ into the F=1 and F=2 levels. We have used the common spectroscopic notation $^{2S+1}L_J$ which is valid for the low energy levels of the rubidium atom. The transition from the $^2S_{1/2}$ to $^2P_{1/2}$ is called the D_1 splitting, and is the transition of primary concern for SEOP discussed in this dissertation. The wavelength of this transition in vacuum is 794.98 nm. For ^{87}Rb, which has nuclear spin I = 3/2, the D_1 transition frequency of 3.8×10^{14} Hz is many orders of magnitude larger than the hyperfine splitting. At magnetic fields which are low compared to the hyperfine field [Eq.(1.4)], the spin angular momentum of the nucleus mixes with the total angular momentum of the valence electron

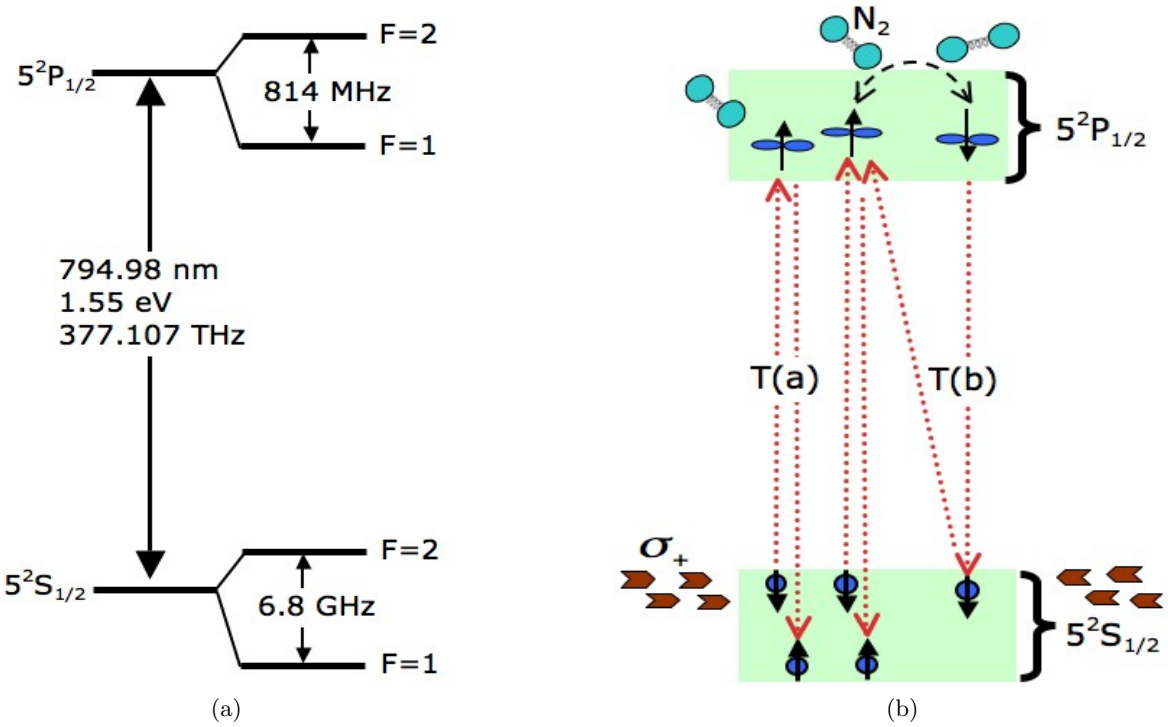

Figure 1.1: **Energy diagram of a rubidium valence electron** (a) Energy diagram of a rubidium valence electron in a vacuum at zero magnetic field. Presence of a magnetic field causes the F states to split due to Zeeman coupling. (b) Interaction of rubidium electrons with left-circularly polarized light (shown as red arrowheads). Electron radial probability distributions are represented as blue distributions, with total azimuthal spin quantum number m_J represented as an arrow ($m_J = +\hbar/2 = \uparrow, m_J = -\hbar/2 = \downarrow$). Nitrogen molecules involved in quenching collisions are represented as balls on a spring in gray. Dotted red lines show transitions. Note there are no transitions *out* of the $5^2S_{1/2}$, $m_J = +\hbar/2$ state. Energy levels are shown broadened by ambient gas pressure — in our typical experiment these absorption lines are broadened to 50 GHz or more.

to form so-called **F** states, where the operator **F**=**I**+**J** with **J** being the usual combination of electronic angular momenta **J**= **L**+ **S**. In magnetic fields, an additional Zeeman splitting of each F level is obtained into 2F+1 sublevels. In a magnetic field of 2 T, the transition frequency between neighboring F sublevels is on the order of the hyperfine splitting .

For optical pumping, photons with energy equal to the D_1 transition are introduced to excite electrons from the $^2S_{1/2}$ to $^2P_{1/2}$ levels. In our SEOP experiments, we use a 30 Watt diode array laser, externally narrowed with a Littrow Cavity [15], to produce a 150 GHz full-width-at-half-maximum (FWHM) laser profile. Our samples are at such high gas pressures that the pressure broadening of the Rb energy absorption lines (about 20

GHz/atm) leaves the hyperfine transitions completely unresolved. Hence, all the hyperfine levels are pumped equally. This leads to consideration of another picture of the rubidium energy levels, shown in Fig. 1.1b. Here, the energy levels are shown broadened by the ambient gas pressure, and the azimuthal spin quantum number (m_J) is explicitly represented as an arrow ($m_J = +\hbar/2 = \uparrow, m_J = -\hbar/2 = \downarrow$).

Figure 1.1b contains the main physics of SEOP. The incident photons may be prepared in a left-circularly polarized ($\sigma+$) state relative to the direction of the external magnetic field; the photons then carry $+1\hbar$ of angular momentum. Because the photon carries the appropriate energy of 1.55 eV, equal to the splitting between the $^2S_{1/2}$ and $^2P_{1/2}$ states, the electron absorbing this photon is excited. Since the $^2S_{1/2}$ to $^2P_{1/2}$ is an electric dipole transition, it is only possible if the $\Delta \mathrm{m}_F = \pm 1$ selection rule is satisfied. To conserve angular momentum, only an electron with $m_J = -\hbar/2$ can absorb the photon with $+\hbar$ spin angular momentum, as is the case in this example. It follows that electrons with $m_J = +\hbar/2$ will not be affected by the light. Neglecting relaxation, once an electron reaches this state, it will remain there — further interactions with light are forbidden for that atom. Thus, again neglecting relaxation, all the electrons will eventually populate this state. As shown in Fig. 1.1b, the electron is pumped from the $^2S_{1/2}$, $m_J = -\hbar/2$ to the $^2P_{1/2}$ $m_J = +\hbar/2$ energy level upon absorption of the photon. If allowed to remain in this state for times of around 30 ns, the rubidium electron will radiatively de-excite back to the ground state, emitting an unpolarized photon in the process. Such a situation is undesirable for two reasons. First, the relaxing electron will return to the $^2S_{1/2}$, $m_J = \pm\hbar/2$ states with probabilities to populate each of 1/3 and 2/3 respectively, as given by the Clebsch-Gordan coefficients governing the coupling of angular momentum. Since there is a 2/3 probability that the electron will return to the optically active $m_J = -\hbar/2$ state, we would need more photons than are optimal to move each electron to the $m_J = +\hbar/2$, as desired. Second, an unpolarized photon may be absorbed by a rubidium atom in the $m_J = +\hbar/2$, causing a "leak" in our optically pumped state, a process called radiation trapping. The introduction of a small partial pressure of N_2 gas (0.1 amagat or more) provides a remedy for both problems [16]. If enough nitrogen molecules are available such that it is relatively likely that one will collide with an excited rubidium electron before it de-excites radiatively, the collision can cause the electron to de-excite *nonradiatively* in a process called quenching. This process transfers energy and angular momentum away from the electron into the rotational and vibrational modes of the N_2 molecule. No unpolarized photon is emitted in

the process, and as an added benefit, the transition probabilities are modified such that the probabilities to decay to the $m_J = \pm\hbar/2$ states are now $1/2 : 1/2$. In this situation, fewer photons are needed to move an electron to the optically inactive state. Each spin-$\hbar$ photon then deposits $\hbar/2$ units of angular momentum to the alkali-metal vapor on average, with the rest being lost to vibrational and translational motion.

Although we have discussed pumping the alkali-metal atoms into the low-energy state ($m_J = +\hbar/2$), the situation can be easily reversed so that the atoms are pumped into the high-energy state ($m_J = -\hbar/2$). This is accomplished by irradiating the sample with σ_- light as opposed to σ_+. It becomes clear that the only states that can absorb the incident photons are those that are in the low-energy state, while the optically inactive state becomes the high energy state. σ_+ light can be easily transformed into σ_- light by simply flipping the quarter-wave plate in the optical train by 180° about the vertical axis (or 90° about the horizontal axis defined by the optical path). This point will become relevant in Ch. 3 when we attempt to make comparisons of nuclear resonance signals in the presence of rubidium atoms polarized in the two different states.

1.2.1.2 Spin Exchange

In the spin-exchange step of SEOP, a polarized Rb atom can collide with a noble-gas atom, causing a transfer of the spin angular momentum in the Rb electron to the noble-gas nucleus. The transfer of angular momentum can occur while the atoms are bound together in a van der Waals molecule, (which may survive for a nanosecond or more at low pressures) or in a simple binary collision (with lifetimes on order of a picosecond). For the experimental conditions involved in this work, the spin-exchange due to molecules is insignificant for two reasons: at the multiatmosphere pressures with which most of the experiments were performed, the collisionally-limited lifetimes of the molecules are so short that effects from these molecules become indistinguishable from binary collisions, and contributions from molecules are more than suppressed at the multitesla fields used in our experiments [17, 18].

Spin-exchange proceeds as follows: the rubidium vapor absorbs photons at a rate given by [12]

$$\langle \delta\Gamma \rangle = [1 - 2\langle S_z \rangle] R_p, \tag{1.5}$$

where $\langle S_z \rangle$ is the ensemble average polarization of the alkali-metal electrons, and R_p is the

mean pumping rate, which can be calculated from the frequency-dependent alkali-metal scattering cross-section $\sigma_0(\nu)$ and the intensity profile $I(\nu)$ of the light as

$$R_p = \int_0^\infty \frac{I(\nu)\sigma_0(\nu)}{h\nu}\, d\nu. \tag{1.6}$$

With R_p we can easily calculate the rate of change of the rubidium electron spin polarization $\langle S_z \rangle$ as

$$\frac{d\langle S_z \rangle}{dt} = \frac{1}{2}[1 - 2\langle S_z \rangle]R_p - \Gamma_a \langle S_z \rangle, \tag{1.7}$$

where we recognize the pumping rate R_p from Eq. (1.5), and Γ_a is the rate angular momentum is lost through the various relaxation processes available to the alkali-metal. The most dominant of these relaxation processes are often collisions with other alkali atoms, noble-gas atoms, and the cell walls.

In steady state then, the alkali-metal polarization depends on these two rates in as

$$P_a = \frac{R_p}{R_p + \Gamma_a}. \tag{1.8}$$

The alkali atom electron then undegoes a collision with a noble-gas atom, and some fraction of rubidium atom's angular momentum is transfered to the noble-gas nucleus through an interatomic hyperfine interaction with a term in the Hamiltonian similar to the intraatomic Eq. (1.4)

$$\mathcal{H}_{\mathcal{SE}} = -2\gamma_{Xe}\mu_B\mu_K \frac{8\pi}{3}\delta(r)\mathbf{K}\cdot\mathbf{S} \tag{1.9}$$

where $\mathbf{K}$ is the ^{129}Xe nuclear spin, γ_{Xe} is the gyromagnetic ratio of the ^{129}Xe nucleus, μ_K is its magnetic moment, and μ_B is the usual Bohr magneton. The interaction (1.9)transfers polarization from the alkali-metal electron to the noble-gas nucleus, and this process proceeds with a spin-exchange rate Γ_{SE}. The contribution to the spin-exchange rate Γ_{SE}

from binary collisions is $\approx 2 \times 10^{-17}$ cm^3/sec for xenon-rubidium mixtures, which leads to typical polarization times of minutes for the xenon gas. The noble-gas atom may also undergo relaxation processes characterized by the rate T_1^{-1}. The differential equation which governs the dynamics of the noble-gas spin polarization $\langle K_z \rangle$ is therefore

$$\frac{d\langle K_z \rangle}{dt} = \Gamma_{SE}[\langle S_z \rangle - \langle K_z \rangle] - \frac{1}{T_1}\langle K_z \rangle. \tag{1.10}$$

Eq. (1.10) shows that high nuclear polarizations $\langle K_z \rangle$ in the noble-gas require the spin-exchange rate Γ_{SE} to be larger than the noble-gas nuclear relaxation rate given by T_1^{-1}, so that in steady state, the noble-gas polarization P_K will be given by

$$P_K = P_a \, \frac{\Gamma_{SE}}{\Gamma_{SE} + 1/T1}(1 - \exp^{-(\Gamma_{SE}+1/T_1)t}). \tag{1.11}$$

The above basics of SEOP are sufficient to understand the work carried out in this dissertation. I have chosen not to expound on the intricacies of spin-exchange or specific relaxation mechanisms involved in the physics of SEOP for the sake of a semblance of brevity. However, it is with some reluctance that I omit these discussions as they elucidate rather beautiful and quite satisfying physics; the reader is encouraged to the plentiful reviews and discussions in the literature for the details (see [12] and references therein as a start, or a simpler treatment in [19]). For now, we continue with the second hyperpolarization technique used in these experiments.

1.2.2 Overhauser Effect

In 1953 Albert Overhauser published a theoretical observation that enhanced nuclear polarization should occur due to hyperfine relaxation processes when the electron-spin resonance is saturated [20]. This effect predicted a factor of 10^3 increase in nuclear polarization, and was originally predicted to take place only in metals. In Ch. 4 we shall illustrate how an analog to this mechanism in doped semiconductors is invoked to explain nuclear hyperpolarization in that system. In this section, we review the basic result Overhauser derived following the descriptions laid out in other manuscripts (*e.g.*, [21, 22]).

We consider a system of two coupled spins, such as an electron and nucleus. For simplicity in demonstration, we consider both to be spin-1/2. This is, for example, the

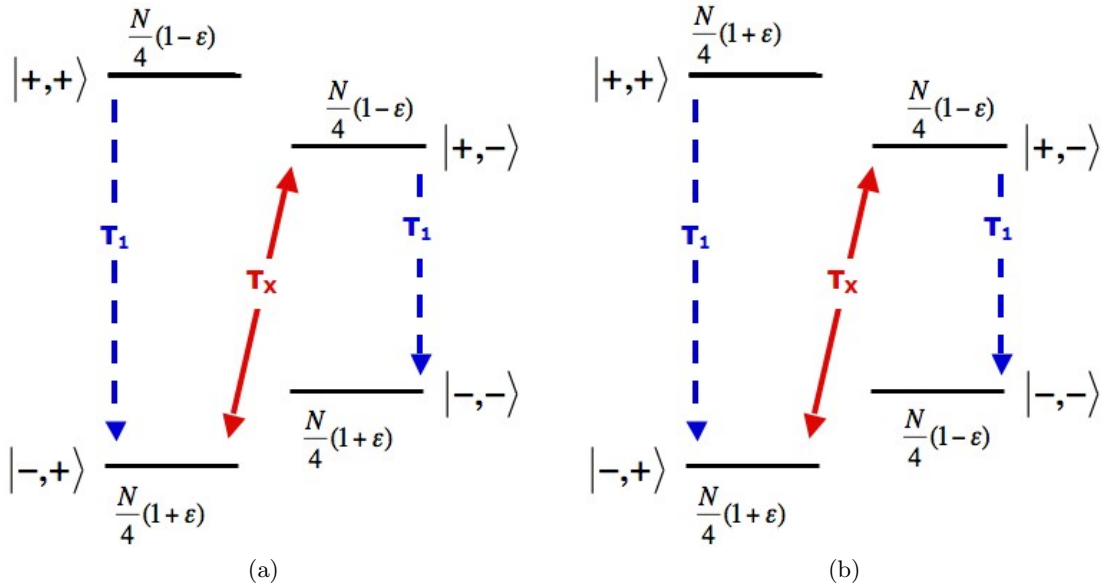

Figure 1.2: **Schematic description of the Overhauser effect.** The four-level system of two coupled spins **S** and **I** shown in a magnetic field, with states labeled with spin projections as $\mid m_S, m_I\rangle$. Arrows show relaxation processes, while the occupation of each energy level is listed. (a) The two-spin system in thermodynamic equilibrium with Boltzmann distribution of population. (b) The two-level system under microwave saturation of both electronic (vertical) transitions.

case of the silicon phosphorus system studied in Ch. 4. In such a system, the application of an external magnetic field will split the otherwise degenerate product state energy levels characterized by the state ket $\mid m_S, m_I\rangle$ into four levels, as shown in Fig. 1.2. The notation $\mid m_S, m_I\rangle$ is meant to signify the azimuthal spin projection along the quantization axis for the electron and nucleus, respectively. In this figure, the vertical direction signifies energy, *i.e.*, lower lines are at lower energy levels, though the schematic is not to scale.

The arrows in Fig. 1.2 show the allowed spin-lattice relaxation processes, divided into two categories. The processes that connect the vertical states with time constant T_1 are electron spin-lattice relaxation processes, which could include spin-orbit coupling modulated by lattice phonons, capture/emission processes, or any other allowed spin-lattice relaxation process. The process connecting diagonal states with time constant T_X is a phonon-mediated hyperfine interaction, which couples the electron and nuclear spins via the dipolar interaction

$$\mathcal{H}_{\mathcal{HF}} = a\frac{8\pi}{3}\delta(r)\mathbf{I}_a \cdot \mathbf{S}. \qquad \text{(Same as Eq. (1.4))}$$

In the thermal equilibrium state, shown in Fig. 1.2a, the energy levels are populated according to the electron Boltzmann factors signified by $\varepsilon \approx \mu_e B/kT$, which is the first-order correction to the populations from unity in a magnetic field at temperature T. This diagram, with the levels populated as shown, neglects the nuclear moment μ_n compared to the electron moment μ_e — it is typically 10^3 times smaller. Also neglected for simplicity is the hyperfine coupling Eq. (1.4) with respect to the electronic Zeeman interaction. The levels are thus populated with the lower energy states acquiring a slightly higher population by a factor ε, and the higher energy levels acquiring a slightly lower population by the same factor.

Now, we apply to the sample an alternating microwave field at the frequency of the electronic transition. This pulse is of sufficient intensity to saturate the electron transition, *i.e.* to equalize the populations between the $|\ +,+\rangle$ and $|\ -,+\rangle$ states and between the $|\ +,-\rangle$ and $|\ -,-\rangle$ states. Crucially, however, during this saturation time, the T_X process continues unabated, and will maintain the thermal equilibrium condition between the *diagonal* states $|\ -,+\rangle$ and $|\ +,-\rangle$. The resulting population distribution is shown in Fig. 1.2b. Notice that the Boltzmann distribution is satisfied between the diagonal states, while the vertical states show the appropriate saturated equivalent populations.

If one attempts to measure the nuclear polarization of the sample in thermal equilibrium, the appropriate calculation would yield a polarization of a few times 10^{-5} or less for typical temperatures and magnetic fields. The nuclear polarization P_n can be calculated as

$$P_n = \frac{N_+ - N_-}{N_+ + N_-}, \tag{1.12}$$

where N_+/N_- are the occupations of the lower/higher energy states, respectively. Using the occupation numbers in Fig. 1.2a, we calculate $P = 0$ for the nuclear polarization, which is a result of neglecting the nuclear moment in our simple picture. As mentioned above, the actual nuclear polarization will be perhaps 10 parts in a million, which is a good approximation of 0, and justifies our initial assumption.

If the nuclear polarization of the sample is measured using the occupation numbers from Fig. 1.2b during the microwave saturation we find

$$N_\pm = \frac{N}{4}(1 \pm \varepsilon) + \frac{N}{4}(1 \pm \varepsilon) \tag{1.13}$$

so that Eq.(1.12) becomes

$$\begin{aligned} P_n &= \frac{\frac{N}{2}(1+\varepsilon) - \frac{N}{2}(1-\varepsilon)}{\frac{N}{2}(1+\varepsilon) + \frac{N}{2}(1-\varepsilon)} \\ &= \varepsilon = \frac{\mu_e B}{kT}. \end{aligned} \tag{1.14}$$

In other words, the *nuclear* polarization has now acquired a magnitude equal to that expected from the *electronic* moment, which is 10^3 times larger as stated above. This is the general statement of the Overhauser effect.

1.3 Relaxation in Solids

We conclude this brief review of the hyperpolarization techniques relevant to this work with a brief review of the basic features of relaxation in spin systems; thorough treatments can be found in any of the canonical NMR texts (*e.g.*, [22, 23, 24]). By "relaxation" we mean the return of a perturbed system to thermodynamic equilibrium. In NMR, we may distinguish between two important relaxation processes after a system has been perturbed. The first type of relaxation, termed longitudinal relaxation, describes the relaxation to $\mathbf{M}_0 = \frac{\chi_0}{\mu_0}\mathbf{B}_0$, and is characterized by the spins occupying energy levels according to a Boltzmann distribution. The second, transverse relaxation, describes a very different process in which the decay to zero of magnetization transverse to $\mathbf{B}_0$ is characterized by a quasi-equilibrium state where the population of every transverse spin state is equally likely.

When introduced into a magnetic field, a nucleus with nonzero spin will experience a split in its otherwise degenerate Zeeman energy levels. For a xenon nucleus in a 2 T field, this energy splitting is $\gamma\hbar B_0 = 2 \times 10^{-27}$J ($1 \times 10^{-8}$ eV), which is about 6 orders of magnitude smaller than the thermal energy available to the sample at room temperature ($k_B T = 4 \times 10^{-21}$J or 30 meV). Nonetheless, this energy difference is finite and leads to a slight preference for the nuclear spins to orient along the direction of the external field — a state referred to as thermal polarization. When perturbed from this equilibrium situation, the nuclei will then relax back toward the thermal polarization state at a rate referred to as the longitudinal relaxation rate, spin-lattice relaxation rate, or T_1^{-1}. It should be

emphasized that this relaxation involves an exchange of magnetic energy density $-\mathbf{M}\cdot\mathbf{B}$ with the lattice.[1]

Transverse relaxation, in contrast, does not involve energy exchange with the lattice. This process can most easily be thought of as destructive interference caused by spins moving at different rates in the NMR experiment. This process is also known by the somewhat sophistical term "spin-spin relaxation."[2] In describing this decay mechanism, we consider a classical magnetization vector made of individual isochromats distributed throughout the NMR sample. In a magnetic field, each isochromat will precess around the external field. This can be seen by solving the most basic equation of motion for spins in a field [23]

$$\frac{d\mathbf{M}}{dt} = \gamma\mathbf{M}\times\mathbf{B}. \tag{1.15}$$

If the z-component of every isochromat, and therefore the entire magnetization vector, is quickly rotated into a direction transverse to the field, then, according to Eq. (1.15), $\mathbf{M}$ will continue to precess once again about the external field forever with no change. In practice, however, we observe that the transverse magnetization does not precess about the external field forever. Instead, we observe that the magnetization perpendicular to the field decays away. This can be understood by considering that the local magnetic field each spin in the sample sees is slightly different (and may even fluctuate with time). This causes the isochromats that constitute $\mathbf{M}$ to dephase and lose coherence.[3] Eventually, the dephasing will reach a point where there are as many spins pointing in a given direction as there are spins pointing in the direction directly opposite. At this stage the transverse magnetization has decayed to zero.

---

[1] By lattice, we refer to nomenclature first used in the early days of NMR when investigators were mainly studying solids – exchange of energy in longitudinal relaxation processes then occurred principally between the spins and the crystal lattice. The term has now come to refer to any other degree of freedom in the system, since total energy must be conserved in liquid- and gas- as well as solid-NMR.

[2] The term spin-spin relaxation seems to imply that interactions between the spins are necessary to induce the decay. Though such interactions are often present, all that is needed for transverse relaxation to occur is a simple distribution of local fields in a sample – a condition that will always be met in a real experiment even in the absence of interactions between spins.

[3] Note, however, that transverse decay times of tens or hundreds of milliseconds are not uncommon, which means that the nuclei may stay in phase precessing together for many *millions* of cycles before losing coherence – a rather astonishing fact.

Neither longitudinal nor transverse relaxation appears in Eq. (1.15). To rectify this, Felix Bloch [25] added terms to Eq. (1.15) phenomenologically in 1946 to obtain a macroscopic set of equations that now bear his name: the Bloch equations. They are

$$\begin{aligned} \frac{d\mathbf{M}_x}{dt} &= \gamma|\mathbf{M}\times\mathbf{B}|_x - \frac{M_x}{T_2} \\ \frac{d\mathbf{M}_y}{dt} &= \gamma|\mathbf{M}\times\mathbf{B}|_y - \frac{M_y}{T_2} \\ \frac{d\mathbf{M}_z}{dt} &= \gamma|\mathbf{M}\times\mathbf{B}|_z + \frac{M_0 - M_z}{T_1}. \end{aligned} \tag{1.16}$$

These equations predict strictly exponential decay, and are therefore clearly not valid for solids or whenever the relaxation is not observed to have exponential character. Physically, the Bloch equations pertain predominately to the regime where the spin-spin interaction terms are weak; such is not the case in the solids treated in these experiments. Nonetheless, the use of the Bloch equations has become so pervasive that the relaxation rates T_1^{-1} and T_2^{-1} are still used in cases of non-exponential decay to give rough ideas of the timescales of relaxation in the experiments. It is in this sense that these rates are used in the work here described.

One source of the distribution in local fields which causes the transverse relaxation is inhomogeneity in the applied external field. This type of inhomogeneity is usually undesirable and can be corrected with shimming procedures and/or clever pulse sequences. Of more interest is the second source of local field distributions: the nuclei themselves. Even though the distances between nuclei is vast compared with their size, some nuclei are able to influence each other by way of their intrinsic magnetic moments. Examples of such interactions include short- and long-range dipole interactions, J-couplings, quadrupole couplings, etc. Local electrons may also influence transverse spin relaxation via mechanisms such as spin-orbit coupling or hyperfine interactions. From simple wave mechanics, we may estimate the timescale T_2 for these interactions as the inverse of the frequency distribution

$$T_2 = \frac{1}{\gamma b}, \tag{1.17}$$

where the magnitude of the dipolar field at a distance r from a magnetic moment μ is

$$b \approx \frac{\mu_0}{4\pi}\frac{\mu}{r^3}. \tag{1.18}$$

Using the solid xenon interatomic separation of 4.4 $\mathring{A}$ and $\gamma_{Xe} = 2\pi \times 11.77$ MHz/T, we get an estimate for T_2 of a few milliseconds for ^{129}Xe; the appropriate values of 2 $\mathring{A}$ and $\gamma_F = 2\pi \times 40.06$ MHz/T yields 25 μs for ^{19}F. We will see in Sec. 2.4 that both estimates are surprisingly accurate.

1.4 Summary of Dissertation

As stated in the introduction, the experiments carried out and reported in this dissertation include a range of concepts and ideas with application from the practical (alternative energy) to the fundamental (microscopic chaos, frequency shift enhancement factors). Controlled manipulations of nuclear spins is the common background on which all the experiments are staged. A brief overview of the coming chapters will help guide the reader to the sections of interest.

Chapter 2 details my work on possible manifestations of microscopic chaos in the transverse relaxation of nuclei in the solid state. Initial experiments, performed by Morgan *et al.*[26], showed confirmation of some aspects of a new theory of nuclear spin dynamics in ^{129}Xe in 2008. At the time, the theory made an unexpected prediction about the behavior of the transverse decay of strongly coupled dipolar quantum systems under certain circumstances, which the work in Ref. [26] verified experimentally in a solid xenon lattice. This chapter describes the theory in some detail, and then goes on to describe our work in exploring new predicted behaviors of the theory in a wide parameter space of systems, nuceli, and conditions.

Chapter 3 explains our work in determining a much sought-after parameter for spin-polarized xenon, $(\kappa_0)_{\mathrm{XeRb}}$. In addition to its essential role in spin-exchange, the isotropic hyperfine interaction between the rubidium electron and noble-gas nucleus also has another effect. As we will show in Ch. 3, this interaction produces a shift of the magnetic resonance frequency of both the alkali-metal and the noble-gas atoms [27, 28]. This frequency shift is characterized by the parameter $(\kappa_0)_{\mathrm{XeRb}}$, which is the shift seen in the xenon nuclear spin resonance frequency due to the Fermi-contact interaction it experiences in the presence of a proximate alkali-metal atom. Barton *et al.* measured κ_0 for Rb-He in 1994 [29]; the

measurement for Rb-Xe remained much more elusive and is a contribution we have made to the literature [28].

In Ch. 4 we discuss the work we did in collaboration with the Boehme research group using NMR to detect the nuclear enhancement from a novel photo-induced hyperpolarization technique they had recently developed. In this work we attempted to use NMR to directly measure an effect observed indirectly by the Boehme group in 2008; they used electron manipulations to measure the degree of nuclear hyperpolarization obtained using a modified Overhauser process in phosphorous doped silicon. These experiments were performed at in an 8 T field at temperatures below 4.2 K using a variety of light sources to induce the hyperpolarization.

The chapters above constitute my main contributions to the literature, though not necessarily the bulk of the time I spent as a graduate student. During my tenure at the University of Utah, I have been involved with several other interesting projects, some of which yielded no publishable results and some of which are nascent and ongoing. Rather than exclude these projects entirely from this dissertation, I include a few of the more interesting projects as brief appendices.

Appendix A will detail work using NMR to probe the internal topography of various oil shales. The goal with this work was to discover whether the internal structure of the shale was porous enough to permit the percolation of gases or liquids, the characterization of which is important for discrimination amongst various possible *in situ* oil extraction techniques. We used xenon gas and fluorinated gases at high pressures to determine under what conditions gas could be made to penetrate the rock. Though most of the results from this work remain unpublished, I detail in this section some of our discoveries of previously unknown properties of these energy-rich rocks. Research into the viability of various oil extraction methods based on the particular properties of the oil shale still continues.

Finally, Appendix B presents a chart of liquid helium vapor pressures vs. temperatures, which is useful for determining temperature when working below liquid helium temperatures. I include it in the hopes that it may save someone else the time of compiling their own such chart in the future.

CHAPTER 2

TRANSVERSE NUCLEAR RELAXATION DYNAMICS - MICROSCOPIC CHAOS

In solid-state NMR, transverse spin-spin relaxation is one of the important sources of microscopic information. Unfortunately, despite the ubiquitous applications of the methods and results of solid-state NMR, the accuracy of first-principle calculations of many spin-spin relaxation related quantities continues to be limited [25, 30, 31, 1, 22, 32]. While many theories have been proposed to describe NMR spin-spin relaxation under various manipulations, as will be described in Sec. 2.1, none has succeeded in providing a controllable method for predicting measurements from a knowledge of the microscopic Hamiltonian of the many-spin system. The properties of the spin-spin relaxation at times long compared to the characteristic spin-spin correlation time T_2 (the "long-time" regime) are of particular interest in this respect because they are the most difficult to predict.

Recently, various authors have looked into the connections between many-body quantum dynamics and classical chaotic behavior [33, 34]. In his thesis work in 2000 [35], Dr. Boris Fine laid out the first sketches of a model that was intended to provide a deeper insight into the long-time behavior of the transverse nuclear relaxation decays that researchers have been struggling to quantify since the first nuclear induction signals were reported in 1946. Below, I will outline the basics of the model and the contributions we have made to its development. Since then, Fine and others have attempted to refine the theory and provide experimental evidence in support of its predictions. During my tenure as a graduate student, several new predictions were developed as further progress on the model was made. These were put to the test for the first time in this work.[1]

In this chapter, I will first summarize some of the past work that has gone into the problem of theoretically predicting the lineshapes in solid-state NMR to give the reader a

[1]Some of the data presented in this dissertation have already been published [36, 37]; such material is copyright 2011 by the American Physical Society and is reproduced here by permission of the American Physical Society.

flavor for the scope and variety of methods employed to treat the problem. Section 2.2.3 will then outline the new chaos-based model and highlight the ensuing predictions that motivated many of the experiments I performed. Section 2.3 will contain the experimental details of the data to follow, including a description of the convection cells used for SEOP of the noble-gas nuclei. Finally, I will detail the experiments, present the data, and elaborate on the contributions and influence that my work has had on the continued development of the theory.

2.1 Historical Experimental and Theoretical Models

In 1946, Purcell, Bloembergen, and Pound made the first continuous wave measurements on a [110] single crystal of CaF_2 in an attempt to study the linewidth and signal intensity as a function of crystal orientation [38]. That same year, the first theoretical attempt to quantify the results of nuclear magnetic resonance lineshapes was made by Felix Bloch. He formulated the Bloch equations as described above [Eq. (1.16)] which provided a phenomenological model for nuclear spin relaxation [25]. These equations predict exponential relaxation; it was therefore immediately clear that they could only be rigorously applied to liquid and gas relaxation. Nonetheless, as mentioned, the extensive use of the parameters of the Bloch equations motivates the colloquial use of the term "T_2" to describe spin-spin relaxation times even in the solid-state, where the decay is often not a single exponential function.

Two years later, in 1948, Van Vleck introduced his seminal work wherein he derived the absorbtion lineshape $F(t)$ in terms of a moment expansion [30]

$$F(t) = \sum_{n=0}^{\infty} (-1)^n M_{2n} \frac{t^{2n}}{(2n)!}. \tag{2.1}$$

Equation (2.1) gives an exact expression for the lineshape in terms of the moments M_{2n}; however, many terms are required to fit an experimental FID for arbitrarily long times. Second and fourth moments were calculated in Van Vleck's work, which gave good agreement with the early-time behavior of the measured line shapes; however, it was realized by Van Vleck himself that a complete description of the lineshape by this method was computationally "prohibitively difficult."[2]

[2]For example, see Eq. 2.8.

Later in 1948, Pake and Purcell used a new crystal, also in the [110] direction, to measure the second and fourth moments for comparison with the Van Vleck calculations for all three crystal directions [39]. After Bruce made significant improvements to the experiments and thereby produced more accurate results, the agreement between Van Vleck's calculated moments and the measurements was good [40]. Also in 1948, Bloembergen, Purcell, and Pound made the first estimates of relaxation parameters in nuclear magnetic resonance experiments [41].

The next step was taken in 1953, when Anderson and Weiss studied systems where there exists a definite separation of the timescales of the local magnetic field fluctuations and the evolution of the spin itself [42]. In such systems, they derived a model that indicated an expected exponential decay of the local correlation functions. This is the case of motional narrowing in liquid NMR, and is analogous to the classical damped harmonic oscillator. However, for the harder problem of spins trapped in a solid lattice where the local field fluctuations and the spin itself evolve on the same timescale, the model appeared to have no validity.

The next major step was made by Lowe and Norberg [31]. In 1957, they used the same crystal used by Pake and Bruce to make the first pulsed NMR experiments on CaF_2 crystals. Making careful measurements at liquid nitrogen temperatures, they were able to observe the decay of the ^{19}F FID over two orders of magnitude for all three crystal orientations. In that paper they also made the important step of deriving the equivalence between the Fourier transform of the spectral density function and the FID. As a confirmation of this derivation, they performed the Fourier transform of Bruce's data and showed that it matched the FIDs obtained in their experiments. The paper concludes with the first proposed approximation scheme for the calculation of the FID

$$F(t) = \mu(0) \cos \omega t \left(\Pi'_j \cos B_{jk} t / 2\hbar \right) V(t) \tag{2.2}$$

where $V(t)$, after several simplifying assumptions, is reduced to

$$V(t) = 1 - \frac{1}{6}\left[\left\{\sum_l \frac{B_{jl}t}{2\hbar}\tan\left(\frac{B_{jl}t}{2\hbar}\right)\right\}^2 - \sum_l\left\{\frac{B_{jl}t}{2\hbar}\tan\left(\frac{B_{jl}t}{2\hbar}\right)\right\}^2\right] \tag{2.3}$$
$$+\frac{2}{9}\left[\left(\sum_l\left(\frac{B_{jl}t}{2\hbar}\right)^2\right)\left\{\sum_l \frac{B_{jl}t}{2\hbar}\tan\left(\frac{B_{jl}t}{2\hbar}\right)\right\} - \sum_l\left(\frac{B_{jl}t}{2\hbar}\right)^3\tan\left(\frac{B_{jl}t}{2\hbar}\right)\right]$$
$$-\frac{1}{12}\left[\left(\sum_l\left(\frac{B_{jl}t}{2\hbar}\right)^2\right)^2 - \sum_l\left(\frac{B_{jl}t}{2\hbar}\right)^4\right],$$

where $B_{jl} = 3[(\gamma\hbar)^2/2r_{jl}^3](1-3\gamma_{jl}^2)$ is the angle dependent coefficient of the Ising part of the dipolar coupling. While the fit of this function to the data was good in the early part of the decay, the calculation is obviously somewhat complex and the agreement did not extend to the long-time portion of the decay.[3]

Bruce tackled the calculation of the fourth moment of the cubic lattice in 1957, using a 26 nearest neighbor lattice sum [40]. That same year found Glebashev attempting to calculate the sixth moment analytically, but the results were later found to be inaccurate [43].

While the fit of Lowe and Norberg was impressive for a significant portion of the CaF_2 relaxation lineshape, Abragam was not convinced, and in his 1961 comprehensive NMR textbook [22] criticized fitting procedures using the moment expansions of the lineshape. Abragam's view was that such a procedure "...is obviously not unique..." and that "...the real argument in its favor is its agreement with experiment." He went on to argue that *any* even function with the appropriately chosen derivatives has the same claim to validity, and that simplicity ought to be the criteria for the choice of function. To illustrate, Abragam made the observation that the function

$$F(t) = \exp\left(-\frac{a^2t^2}{2}\right)\frac{\sin(bt)}{bt} \tag{2.4}$$

makes a somewhat better fit to the data than did previous attempts, including the function of Lowe and Norberg, provided one chooses the values of a and b correctly.

A new approach to the problem was introduced by Tjon in 1965 [44], and later refined by Parker and Lado. Tjon found that the relaxation of the spin correlation function, which he denoted $\Phi_0(t)$, could be described by the equation

[3] Actually, the fit of Lowe and Norberg eventually diverges after several times T_2.

$$\frac{d\Phi_0(t)}{dt} = \int_0^t d\tau\ \alpha(\tau)\Phi_0(t-\tau) \tag{2.5}$$

where $\alpha(\tau)$ was called the memory function. According to Eq. (2.5), $\Phi_0(t)$ depends on $\Phi_0(t-\tau)$, that is, there is some correlation or "memory" in the system from earlier times $(t-\tau)$ affecting the evolution of the function at time t. This memory is controlled by the function $\alpha(\tau)$ — hence the name memory function.

The careful measurements of Lowe and Norberg in 1957 had become the gold standard measurements; most theorists attempting to explain dipolar-coupled lineshapes dedicated their time to explaining the lineshapes of CaF_2. It was soon realized that better measurements were needed for the investigations to proceed. In 1966, Barnaal and Lowe were able to obtain improved signal-to-noise in ^{19}F measurements at 10 MHz and 47 K on a new crystal of CaF_2 believed to be more accurately oriented [45]. Furthermore, papers that were published after the measurements of Lowe and Norberg elucidated methods for correcting NMR signals for effects due to the finite width of the excitation pulse and finite bandwidth of the receiver and pickup coil — and these corrections were applied to their data. They were rewarded with improved agreement between the measured second and fourth moments with the calculations.

The year 1966 also saw the application of a different technique to the problem of NMR relaxation that had no reference to moment anaylsis. In that year, Mansfield employed a retarded Green's function method, similar to that employed two years earlier by Tomita and Tanaka [46], to calculate lineshapes in ferromagnetic substances. Mansfield improved on the method by introducing a coupled set of differential equations, which he solved by using a frequency dependent decoupling approximation [47]. This method turned out to be equivalent to the memory function method, and his fit was not better than that of Lowe and Norberg, although his fit did have the virtue of converging at long times.

Yet another method was attempted the next year by Evans and Powles [48]. This was basically another way to use perturbation theory to try to approximate the decay. Of course, their treatment suffered from the same problem as the other perturbative attempts; there is not, strictly speaking, a small parameter in the truncated Hamiltonian that justifies a perturbative approach that allows retention of only the first several terms of an expansion. As a result, their fit was also not better than that of Lowe and Norberg.

Borckmans and Walgraef brought yet another method of calculation to bear on the problem in 1968 [49]. They pointed out that no perturbative approximation scheme to date had fit the CaF_2 data beyond the third zero-crossing, and no quantum statistical mechanics methods had been any more successful (and those, moreover, suffered from semiphenomenological assumptions that had to be made to solve the equations). They also criticized the previous attempts for not providing a description of the long-time behavior of the functions. Borckmans and Walgraef proposed the use of a memory-function-like integro-differential equation with the memory function assumed to have a Gaussian shape. From a Laplace transform of their memory function equation, they determined that the long-time behavior of the CaF_2 FID should converge to an exponentially damped sinusoidal curve. Naturally, the long-time behavior of the FID is governed by the long-time behavior of the chosen memory function. As was shown in Ch. 8 of Ref. [50] and in Ref. [35], however, this treatment simply shifts the difficult problem of calculating the long-time behavior of the FID to the even more difficult problem of guessing the correct long-time behavior of the memory function.

Based on this observation, a 1970 paper by Parker [51] showed that Abragam's equation Eq. (2.4) was actually the first term of an exact expansion of the lineshape $F(t)$ in terms of the moments

$$F(t) = e^{-\alpha^2 t^2} \sum_{n=0}^{\infty} a_{2n} j_{2n}(\beta t), \tag{2.6}$$

where j_{2n} are the spherical Bessel functions, and the coefficients a_n are constants depending on the moments and scaling factors α and β. Using Eq. (2.6) as a memory function with the values of the first four known even moments ($M_2 - M_8$) to adjust the parameters, they obtained good agreement for their fit with the data using a generalization of Taylor's expansion theorum known as a Neumann expansion. While the good agreement of their result is not terribly surprising considering the inputs to the model, it was an important contribution of this work to realize that the memory function decays faster than the relaxation function, and not on the same timescale. Since that is the case, relatively modest improvements to the memory function could be expected to lead to much better relaxation functions.

Yet another approach to the problem was introduced by Powles and Carazza in 1970 [52]. They attempt in this work an entropic method whereby they minimize a quantity they call

the "information," which they defined as

$$I = \sum p(\omega_i) \ln p(\omega_i), \tag{2.7}$$

where $p(\omega_i)$ is related to the discretized spectral density function. Adjusting $p(\omega)$ with the values of the second and fourth moments and taking the continuum limit and gives a reasonable approximation to the data. While the method outlined in their paper offers a systematic method for lineshape calculation, it does suffer from some serious defects, not least of which that the function $p(\omega)$ does not have an analytic Fourier transform. The agreement of their method with experiment is reasonable, but not better than other schemes.

Around this time, computers became available and computational techniques were developed for evaluating the higher-order moments. Canters and Johnson [53] took up Bruce's fourth moment calculation again in 1972 and were able to make a more accurate evaluation of the lattice sums than Bruce was able to do. In 1973, Jensen and Hansen achieved a symbolic evaluation of the noncommuting commuators and traces to arrive at an analytical expression for the moments up to M_8. Using numerical methods newly possible on computers, they evaluated the lattice sums and were able to evaluate M_8 numerically. The analytical expression derived by Jensen and Hansen [54] is

$$\begin{aligned}
M_8 \;=\; & \frac{\gamma^{16}\hbar^8}{32805}\Big\{[I(I+1)]^4\Big[18385S_2^4 + \frac{5101107}{896}S_8 - 32520S_2^2 + \frac{20015923}{896}S_6S_2 - \frac{2240717}{448}S_5S_3 \\
& + \frac{772447}{256}B_{jk}^6R_{jk}(11) - \frac{147573}{64}B_{jk}^5R_{jk}(21) + \frac{2804121}{1792}B_{jk}^4R_{jk}(31) \\
& + \frac{43779481}{1792}B_{jk}^4R_{jk}(22) - \frac{292981}{128}B_{jk}^3R_{jk}(32) + 1360B_{jk}R_{jk}(41)R_{jk}(11) \\
& + 3344B_{jk}R_{jk}(31)R_{jk}(21) + 632B_{jk}R_{jk}(22)R_{jk}(21) - 1720B_{jk}R_{jk}(21)R_{jk}^2(11) \\
& + 1640B_{jk}^2R_{jk}^3(11) - 30480B_{jk}^2R_{jk}(31)R_{jk}(11) - 3648B_{jk}^2R_{jk}(22)R_{jk}(11) \\
& + 6500B_{jk}^2R_{jk}(21)^2 - 1140\left(\sum_k B_{jk}^2R_{jk}(11)\right)^2 + 4928B_{jk}^3R_{jk}(21)R_{jk}(11) \\
& - 6780B_{jk}^4R_{jk}^2(11) - 6780B_{jk}^4R_{jk}(11)^2 + 3690R_{jk}(22)R_{jk}(11)^2 + \\
& + 2512R_{jk}(42)R_{jk}(11) - 1720R_{jk}(21)^2R_{jk}(11) - 2744R_{jk}(31)^2 + 1640R_{jk}(31)R_{jk}(22) \\
& - 2744R_{jk}(31)^2 + 1640R_{jk}(31)R_{jk}(22) - 2498R_{jk}(22)^2 + 6370S_2^2B_{jk}^2R_{jk}(11) \\
& - 8220S_2B_{jk}^4R_{jk}(11) - 1792S_2B_{jk}^3R_{jk}(21) - 20550S_2B_{jk}^2R_{jk}(22) + 1076S_3B_{jk}^3R_{jk}(11)
\end{aligned}$$

$$
\begin{aligned}
&-664S_3B_{jk}^2R_{jk}(21) - 1822S_4B_{jk}^2R_{jk}(11) + 24300S_2B_{jk}^2R_{jk}^2(11) \\
&-3320S_2B_{jk}R_{jk}(21)R_{jk}(11) - 2870S_2B_{jk}R_{jk}^2(21) - 920B_{jk}^2B_{jl}B_{kl}R_{jk}(11)R_{jl}(11) \\
&+12960B_{jk}^2B_{jl}B_{kl}R_{jl}(11)R_{kl}(11) - 4480B_{jk}B_{jl}B_{kl}R_{jk}(21)R_{jl}(11) \\
&-1820B_{jk}^2B_{kl}^2R_{jk}(11)R_{jl}(11) + 180B_{jk}^2B_{jl}R_{kl}(21)R_{jl}(11) \\
&-2000B_{jk}B_{kl}R_{jk}(21)R_{jl}(21) - 50B_{jk}^2R_{jl}(22)R_{kl}(11) \\
&-240B_{jk}B_{jl}\left(\sum_m B_{jm}B_{km}B_{lm}\right)^2 + 944Q(221) + 4224Q(311) - 8468Q(212) \\
&-2000S_2Q(111) - 420B_{jk}R_{jk}(11)B_{jl}B_{jm}B_{kl}B_{km}B_{lm} \\
&-720B_{jk}R_{jl}(21)B_{jm}B_{kl}B_{km}B_{lm} - 1000B_{jk}^2B_{jl}B_{jm}B_{kl}R_{km}(11)B_{lm} \\
&-580B_{jk}B_{jl}B_{jm}^2B_{kl}R_{kl}B_{km}B_{lm}\Big] + \frac{[I(I+1)]^3}{2}\Bigg(\frac{5866291}{448}S_4^2 - \frac{13063987}{896}S_8 - 39390S_4S_2^2 \\
&+6972S_3^2S_2 + \frac{17172019}{448}S_6S_2 - \frac{10521907}{896}S_5S_3 + \frac{358809}{896}B_{jk}^6R_{jk}(11) \\
&-\frac{2012851}{224}B_{jk}^5R_{jk}(21) - \frac{2990131}{448}B_{jk}^4R_{jk}(31) + \frac{47674521}{896}B_{jk}^4R_{jk}(22) \\
&-\frac{5875507}{448}B_{jk}^3R_{jk}(32) + 3360B_{jk}R_{jk}(41)R_{jk}(11) + 8940B_{jk}R_{jk}(32)R_{jk}(11) \\
&+4044B_{jk}R_{jk}(31)R_{jk}(21) + 1782B_{jk}R_{jk}(22)R_{jk}(21) - 44760B_{jk}^2R_{jk}(31)R_{jk}(11) \\
&+192B_{jk}^2R_{jk}(22)R_{jk}(11) + 8160B_{jk}^2R_{jk}^2(21) + 10728B_{jk}^3R_{jk}(21)R_{jk}(11) \\
&-10728B_{jk}^3R_{jk}(21)R_{jk}(11) - 7845B_{jk}^4R_{jk}^2(11) + 3732R_{jk}(42)R_{jk}(11) \\
&-6324R_{jk}^2(31) + 3210R_{jk}(31)R_{jk}(22) - 1818R_{jk}^2(22) + 3630S_2B_{jk}^4R_{jk}(11) \\
&+9528S_2B_{jk}^3R_{jk}(21) - 23715S_2B_{jk}^2R_{jk}(22) + 1416S_3B_{jk}^3R_{jk}(11) \\
&+2946S - 3B_{jk}^2R_{jk}(21) - 1182S_4B_{jk}^2R_{jk}(11) + 2724Q(221) + 4704Q(311) \\
&-11073A(212)\Bigg) + \frac{[I(I+1)]^2}{1792}[4906137S_4^2 - 5706547S_8 + 9260697S_6S_2 \\
&-3880396S_5S_3 - 1657497B_{jk}^6R_{jk}(11) - 3612211B_{jk}^5R_{jk}(21) - 5680281B_{jk}^4R_{jk}(31) \\
&+16790630B_{jk}^4R_{jk}(22) - 5289753B_{jk}^3R_{jk}(32)] - I(I+1)\frac{297043}{448}S_8\Bigg\}, \qquad (2.8)
\end{aligned}
$$

where we have (mercifully) used the shorthand quantities

$$
\begin{aligned}
B_{jk} &= \frac{3}{2}\frac{1-3\cos^2\theta_{jk}}{r_{jk}^3} \\
S_m &= \frac{1}{N}\sum_{j,k}\left[\frac{3}{2}\frac{1-3\cos^2\theta_{jk}}{r_{jk}^3}\right]^m (j \neq k)
\end{aligned}
$$

$$
\begin{aligned}
R_{jk}(pq) &= \sum_{l} \left[\frac{3}{2}\frac{1-3\cos^2\theta_{jl}}{r_{jl}^3}\right]^p \left[\frac{3}{2}\frac{1-3\cos^2\theta_{lk}}{r_{lk}^3}\right]^q \quad (j \neq k) \\
Q(pqr) &= \frac{1}{N}\sum_{j,k,l,m} \left[\frac{3}{2}\frac{1-3\cos^2\theta_{jk}}{r_{jk}^3}\right]^p \left[\frac{3}{2}\frac{1-3\cos^2\theta_{jl}}{r_{jl}^3}\right]^q \left[\frac{3}{2}\frac{1-3\cos^2\theta_{jm}}{r_{jm}^3}\right] \\
&\qquad \times \left[\frac{3}{2}\frac{1-3\cos^2\theta_{kl}}{r_{kl}^3}\right] \left[\frac{3}{2}\frac{1-3\cos^2\theta_{km}}{r_{km}^3}\right] \left[\frac{3}{2}\frac{1-3\cos^2\theta_{lm}}{r_{lm}^3}\right]^r
\end{aligned}
$$

in order to represent the expression in a somewhat compact form. We show Eq. (2.8) to demonstrate the complexity that rapidly arises in the evaluation of the higher-order moments. Clearly, for a lattice of any appreciable size, the evaluation of (2.8) will quickly become infeasible, let alone evaluation of higher-order moments. For comparison, the second moment M_2 in this notation is simply

$$M_2 = \frac{1}{3} I(I+1)\gamma^4\hbar^2 S_2.$$

Jensen and Hansen state that the numerical evaluation of M_8 took 1200 times the computing time compared to M_6 [54], which in itself is a daunting expression.

This year also saw further refinements of past works. Parker and Lado [55] published a refinement of Tjon's 1965 memory function approach with new restrictions. A talk by Lowe, Vollmers, and Punkinen [56] was given in Amsterdam in 1973 (with the work being later published in 1978 [57]), wherein the authors developed a technique called zero-time resolution. Using this technique, they were able to overcome the finite recovery time of NMR receivers and measure the value of the FID at arbitrarily short times. As the authors mention, it is the observation of the early-time behavior that most readily allows for calculation of the moments.

Building on all the previous knowledge, a major paper was published in 1974 by Engelsberg and Lowe [1]. They used the zero-time resolution method to measure the early-time decay of the FID to a fraction of microsecond at 77K, and then conventional pulsed techniques at 4.2 K to measure the long-time portion of the FID. Joining the data together, they observed the decay of the ^{19}F FID over four orders of magnitude, and were able to extract the numerical values of the first 14 even moments for comparison to theory. The agreement was excellent. They provided an empirical fit for their data using an infinite product, but offered no theoretical justification for its use. However, the quality of the

experimental results was excellent, and this work became the new standard for CaF_2 FID measurements.

The problem of calculating the free induction decay lineshape in dipolar coupled systems still evaded a solution. In 1975, another attempt was made by Englesberg and Chao [58] using yet another method, that of continued fraction approximations as a means to decouple the equations of motion of the Green's functions. While the method did make use of the known moments, it was very sensitive to the exact values of those moments. Still, adjusting the parameters of the equation appropriately did lead to good agreement with the data. Furthermore, they were able to apply their results to the problem of motionally narrowed lines in paramagnetic fluoride compounds, and achieve good agreement in that case as well. However, their agreement is criticized as somewhat coincidental in Ref. [35] based on the fact that the functional form of the calculated FID they obtain is independent of the specific form of the spin-spin interactions, and would therefore give the same answer no matter what the interaction.

The following year, Becker, Plefka, and Sauermann [59] presented an integral equation deduced from an equation-of-motion method using the physical picture of a spin moving in a static average field driven by a time-dependent component. They compared their resulting function to one direction of the magnetic field with respect to the CaF_2 crystal, and the agreement was also good. However, the other orientations were not presented, and there was no attempt to apply the results to other materials or systems.

Another physical model was considered in 1976 by Lundin and Provotorov [60]. Using Abragam's Eq. (2.4), they attempted to attribute the exponential to the mean field generated by spin's outside a nearest-neighbor "shell," and the sinc function to the interactions with nearest-neighbors. This work was revised and expanded upon several times throughout the following decades by Lundin and collaborators (see for example [61, 62]). The idea of a cell of interaction ultimately did not prove very useful for actual lineshape calculations.

The remaining work on the subject has consisted mainly of refinements and more sophisticated extensions of the above methods. Notable in this regard is the 1985 work of Fedders and Carlsson [63] on the information theory, or maximum entropy, method and the 1995 work of Jensen [64] on continued fractions.

In conclusion, it is clear that, despite a large variety of formalisms adopted to treat the problem, no complete solution to the problem of relaxation in a dipole-coupled spin system has been found. While the approximation schemes detailed above often give good

agreement between functional forms and the data in certain regimes, no one theory has provided a description of the relaxation for all timescales, nor provided a first-principles derivation of the relaxation functions.

2.2 The Chaos-Based Model

A new approach to the theoretical prediction of solid-state NMR lineshapes was postulated by Boris Fine in 2000 in his dissertation work [35]. His model was based on the notion that microscopic chaos plays a role in the long-time behavior of nuclear transverse magnetization decays. While chaos has been known to the scientific world since early in the 20th century, it was only in the mid-1970s with the advent of the personal computer that chaos became generally known – and even then most applications were to classical dynamical systems. It is only recently that chaos has begun to be associated with the quantum world, and therefore its possible role in the spin-spin interactions of relaxing nuclei bears some discussion.

2.2.1 Chaos Defined

Chaos theory is often explained colloquially as a study of dynamical systems that have a high degree of sensitivity to the initial conditions of their evolutions. This is a necessary, though not sufficient, condition of a chaotic system. Additionally, a chaotic system will experience topological mixing, meaning that any given region of points in phase space at the beginning of an evolution will eventually spread over all of the available phase space. Both conditions are necessary to define a chaotic system; it is the second that we shall focus on in the discussion to follow.

More precisely, we can define chaos as an exponential divergence of the trajectories of a Hamiltonian system characterized by the maximal Lyapunov exponent.[4] Formally, we can write that for a small initial separation $\delta\mathbf{X}$, two phase-space trajectories can at most diverge exponentially as

$$|\delta\mathbf{X}| \approx e^{\lambda_{max}t}|\delta\mathbf{X}|, \tag{2.9}$$

where λ_{max} is the maximum Lyapunov exponent. Since the initial separation is arbitrary, and the divergence rate can depend on that initial condition, there is a whole spectrum of

[4]Named for famous Russian mathematical physicist Aleksandr Lyapunov.

Lyapunov exponents. The largest of these is the maximal Lyapunov exponent, and systems characterized by a *positive* maximal Lyapunov exponent are chaotic [65]. The dynamical instability characterized by Eq. (2.9) is at the origin of a hyperbolic phase space picture in which the phase space is covered by stable and unstable regions of the initial probability density.

Another way to state the condition of chaos in a Hamiltonian system is that such systems are not integrable. Integrable models have as many integrals of motion (*e.g.*, energy, linear momentum, angular momentum, etc.) as there are degrees of freedom in the system. Lifting of integrability leads to chaotic motion [66]. There are several examples of very simple systems in which integrability can be lifted [67, 68, 69]; a common cause is interactions between atoms. Introducing interactions between atoms is known to make the dynamics of an atomic system comprised of as few as two atoms already chaotic [70].

It is at first counterintuitive that the assumption of chaos would be at all helpful in the goal of a controllable prediction of atomic behavior. After all, Eq. (2.9) implies that long-time predictions are always limited to statistical terms after the Lyapunov time t_{Ly} which is proportional to the inverse maximum Lyapunov exponent $t_{Ly} \propto \lambda_{max}^{-1}$. After this time, the error between the predicted and actual phase space trajectories of a chaotic system becomes larger than the required final precision, and prediction is no longer possible. Nonetheless, we will see the redemption of the idea of dynamical instabilities in that they define intrinsic timescales of a system's dynamics, which will justify certain assumptions necessary in the model.

2.2.2 Microscopic Chaos in a Quantum System

Chaotic behavior is observed and well understood in many classical systems. The state of a classical system is often described by a set of continuous dynamic variables (*e.g.*, position and momentum) which define points in the phase space whose trajectories can be observed. While nonchaotic motion is associated with smooth periodic trajectories of these points in phase space, chaotic motion is identified by more complex nonperiodic trajectories that, again, display an exponential dependence on the initial configuration of the system. In particular, hyperbolic chaotic systems manifest the property that any continuous set of points initially occupying a small part of phase space will eventually become distributed over the whole phase space in a particular way — expanding in some (unstable) directions and contracting in other (stable) directions.

Conventional formulations of quantum mechanics, however, do not allow for a similar

definition of chaotic behavior in quantum systems, or indeed in any system where dynamical variables are discreet. It is possible (at least in principle) in a discreet system to prepare an arbitrary pure state such that the density matrix ρ is indempotent, *i.e.* $\rho^2 = \rho$. The ability to prepare a pure state obviates the sensitivity to small errors in initial conditions — in principle such errors can be made to vanish in a discreet system. Furthermore, even if small errors were present in the preparation of the initial state, the error would not grow exponentially since quantum mechanics is a unitary theory, that is, the inner product of two states is an invariant quantity, and therefore two states with a given separation in the Hilbert space will retain that separation without deviation throughout the evolution [71]. Finally, the uncertainty principle also forbids simultaneous knowledge of conjugate variables such as position and momentum, making the whole idea of a coarse-grained phase space with cell size smaller than $\hbar$ nonsensical.

Nonetheless, it is still possible to represent a quantum state in phase space provided one chooses to represent the state of the system in the form of a delocalized probability distribution whose dynamics are governed by the Schrödinger equation [72, 73]. The present theory uses this representation to postulate a quantum phase space of dynamics analogous to classical hyperbolic chaotic systems, and from this postulate, derives several predictions that lend themselves to experimental verification. These experiments explore an aspect of chaotic manifestations in quantum systems distinct from, but complementary to, the usual focus on energy level statistics and random matrix theory [74, 75].

2.2.3 Outline of the Model

Here I will outline the basic tenets of the model developed by Boris Fine as laid out in Refs. [35, 33, 76, 37] and which inspired much of this work. Underlying the model is the following conjecture, which I quote directly from Ref. [33]:

> *Conjecture*: We consider a many-body system relaxing to equilibrium in the linear response regime and conjecture that in this process, after the memory of the initial probability distribution is lost, a kind of randomness subsequently propagates to very short space- and timescales. This randomness is such that, considering the nonequilibrium behavior of the *ensemble averaged* quantities, it is appropriate to invoke a Brownian-like Markovian[5] description, which is consistent with the long-time

[5]Markovian system: a system that does not retain a memory of its initial state, *i.e.* the present state of the system is independent of its past state.

> Markovian assumptions, but, at the same time, is based on a very fine coarse-graining with the scale *much smaller* than the scale of the ballistic behavior of the particles composing the large system.

The meaning and implications of this conjecture will be explained and clarified below.

2.2.3.1 Projection to a Single-Spin Subspace

Consider first a single classical spin vector of length $|S|$. We envision the evolution of the path of the spin vector tip on the surface of the Bloch sphere as representing the dynamical evolution of the spin. Considering that all spin evolution paths are represented for a given spin, we make the following three important assumptions: (i) on the scale of the mean-free time T_2 and the mean-free path (on the order of $|S|$), each spin trajectory loses memory of its initial position in phase-space, (ii) the set of all possible spin evolution paths shows topological mixing sufficient that an arbitrarily small volume of phase space becomes dispersed over the whole phase space (in a volume conserving way), and (iii) the evolution of this set of single-spin trajectories becomes representative of the evolution of all one-spin trajectories in the problem.

The above assumptions are similar to those of Brownian motion on an infinite plane. This suggests a treatment of the problem in terms of Brownian diffusion. However, one is thwarted before beginning upon the realization that there is no length scale in the problem that is larger or smaller than the mean-free path. Utilization of a conventional Brownian approach will then necessarily require an extension of conventional notions of diffusion to accurate formalisms for distances much smaller than the mean-free path. This is the intent behind the conjecture quoted above, which is further explained below. For now, we envision the evolution of a point corresponding to the tip of a classical spin vector on a sphere as representing the evolution of that spin vector. Extending the idea to all possible trajectories representing different spin evolutions, we envision that all such points form a collection of sample points moving together on the spherical surface, and we subdivde the sphere into tiny coarse-grained elements such that each subdivision looks locally flat. We then consider the case of two adjacent subdivisions, neglecting for the moment that the coarse-graining is much smaller than the mean-free path.

2.2.3.2 Markovian Description of Diffusion

Consider two adjacent volumes x_i and x_j of dimension Δx (much longer than the mean-free path of the particles) and occupied by populations f such that the population in the i^{th}

volume at time t is given by $f(x_i, t)$ [77]. At time $t+\tau$, the population then is $f(x_i, t+\tau)$. We can consider the change in the number of particles in the i^{th} volume during time τ to be

$$f(x_i, t+\tau) - f(x_i, t) = W[f(x_j, t) - f(x_i, t)], \tag{2.10}$$

where W is the transition probability for a particle to move from one volume to the adjacent volume. Noting that

$$f(x_j, t) = f(x_i + \Delta_x, t), \tag{2.11}$$

we can rewrite Eq. (2.10) as

$$f(x_i, t+\tau) - f(x_i, t) = W[f(x_i + \Delta_x, t) - f(x_i, t)]. \tag{2.12}$$

Taking the limit as $\tau \to 0$, and expanding the right hand side, we recover the familiar diffusion equation [77]

$$\frac{\delta f(x,t)}{\delta t} = D\frac{\delta^2 f(x,t)}{\delta x^2}, \tag{2.13}$$

where D is the appropriate combination of constants. More generally, we can add terms to the right hand side of Eq. (2.13) to reflect a bias in the diffusion. For example, when discussing conductivity as a diffusive process, Eq. (2.13) is known as Fick's second law, and is often modified to reflect a bias in the diffusion proportional to the applied field (Ohm's Law). In the following section, we will argue that it is appropriate to add a similar term to Eq. (2.13) to reflect correlation effects due to the existence of a nonzero polarization. This will provide a bias in the evolution of the spin state of an individual spin, and it is this term which will provide the rich physics of the model.

Now, we recall that we have coarse-grained our bound spherical surface into elements much smaller than the mean-free path. This will lead to correlations in time between the populations entering and leaving a coarse-grained region. In equilibrium, however, we see

that these non-Markovian correlations should be balanced by the system's dynamics. If the system is slightly out of equilibrium, it is the nonequilibrium inflow and outflow of points that governs the nonequilibrium evolution of the population inside a subvolume; the large majority of "equilibrium events" will continue to be balanced. In this light, the conjecture in Sec. 2.2.3 can be restated: in the long-time regime of the system's evolution, no important correlations remain between the nonequilibrium inflow and outflow events for any two moments of time, even if the times in question are separated by much less than the mean-free time. If this conjecture is true, it implies that the problem may now, with this assumption, be treated as Brownian diffusion with a mean-free path much smaller than the size of the subvolume.

2.2.3.3 Correlated Diffusion on Sphere

If the probability density of spin trajectories were in equilibrium at the infinite temperature limit, Eq. (2.13) would be sufficient to describe the evolution. At finite temperature, however, the local spin distribution on neighboring spin sites is slightly out of equilibrium due to the nonzero polarization. This implies that the transition probability from one subvolume to another becomes slightly larger than the probability of transition in the opposing direction. This will create an imbalance in the equilibrium probability distributions, implying the addition of a new term in Eq. (2.13) as alluded to above, which will account for the additional flux between the subvolumes. Following Ref. [33], we term this effect "correlated diffusion."

We can write down the equation of correlated diffusion of probability flux on the sphere defined by a single radial spin as

$$\frac{\delta f(t,x)}{\delta t} = \frac{\delta}{\delta x}\left[D(x)\frac{\delta f(t,x)}{\delta x} - \int_V K(x,x')f(t,x')dx'\right] \tag{2.14}$$

which is the usual diffusion equation (2.13) in the presence of a nonequilibrium bias given by the kernel $K(x,x')$. In this schematic notation, we represent the many-dimensional space as a one-dimensional problem; $D(x)$ therefore is the tensor diffusion coefficient corresponding to the equilibrium diffusion environment, and $K(x,x')$ is the kernel representing the response of the probability flux to the slight deviation from the equilibrium distribution on neighboring sites. Like any ordinary diffusion equation in a finite volume, Eq. (2.14) has a set of discrete solutions of the form

$$f(t,x) = \sum_i e^{-\lambda_i t} u_{\lambda_i}(x), \tag{2.15}$$

where λ_i is one of the eigenvalues of the linear operator acting on $f(t,x)$, and $u_{\lambda_i}(x)$ is the corresponding eigenfunction.

The importance of the introduction of the second term in Eq. (2.14) lies in the lack of Hermiticity of the kernel $K(x,x')$. This kernel describes the interactions between the spins on the lattice, and significantly, it describes not simply pair correlations such as nearest-neighbor interactions, but also indirect interactions, *i.e.*, spin a affects spin b by creating a preferred local field direction, and spin b then affects spin c. There are also terms wherein spin a affects spin b, which then acts back on spin a. These complicated dynamics are contained in the polarization kernel K, which is as a result non-Hermitian. One crucial consequence of this fact is that the eigenvalues of the diffusion modes will in general have both real and imaginary parts, *i.e.* $\lambda = \lambda_{Re} + i\lambda_{Im}$.

2.2.3.4 Pollicott-Ruelle Resonances and Hyperbolic Chaos

The operator which describes the time evolution of the probability densities in phase space is called the Frobenius-Perron operator; it plays a prominent role in the statistical evaluation of chaotic systems. The time evolution operator for the spin system is shown in Eq. (2.14). It can be shown [65, 78] that for certain classes of systems, and in particular when the spectral frequencies admit extension into the complex plane (as was the case when we allowed nonreal eigenvalues to the evolution operator), that the location of the singularities in the complex plane is an *intrinsic* property of the dynamics of the system, and is independent of any specific observable. This implies that physical manifestations of such singularities should be visible in any observable of the system, and, as it is a property of the system's dynamics, should be further independent of the initial conditions of the system's evolution.

This property was shown in a class of systems called Axiom-A,[6] or hyperbolic chaotic systems, by Pollicott [80] and Ruelle [81] in 1986, and the singularities were thereafter termed Pollicott-Ruelle resonances. In such systems, the dynamic singularities correspond to the eigenvalues of the Frobenius-Perron operator, the operator which governs the flow of

[6] A term coined by S. Smale, see Ref. [79].

probability density in the phase space. Therefore, we may think of the complex eigenmodes (2.15) obtained from Eq. (2.14) as analogous to Pollicott-Ruelle resonances in chaotic hyperbolic systems. Pollicott-Ruelle resonances are important to our problem for several reasons. As mentioned above, they are robust and stable properties of the dynamics of the system; therefore their manifestation should be independent of any particular evolution of the systems. Second, they are indicative of extreme randomness in the system's evolution which does not have a lower spatial bound, *i.e.*, the randomness may propagate to very small length scales [65].

Hyperbolic dynamics are manifest in smooth dynamical systems, which are characterized by the presence of expanding and contracting directions in phase space. As a visual example, consider the prototypical "Arnold's cat map," which shows the hyperbolic evolution of a specific mapping of the image of a cat attributed to Vladimir Arnold. In Fig 2.1 the evolution of an image under a hyperbolic mapping is shown. The image represents an particular initial probability distribution in phase space. After several iterations of the mapping, the original image is shown to have evolved in the way characteristic of hyperbolic systems: expanding along unstable directions and contracting along stable ones. If in lieu of the image of a cat we have an ordered probability density in phase space, the dynamics will proceed in much the same way, so that some time later a pattern similar to that shown in Fig. 2.1c is obtained. At the late stages of the evolution, where the extreme stretching dominates the phase space, small subregions of the phase space begin to look increasingly similar. Averaging over them would then produce nearly identical results. In contrast, at the beginning of the evolution (Fig. 2.1a), small randomly chosen subregions have distinctly unique character.

The classical system considered above allows generalization to the quantum case with one modification [33]. Instead of trajectories of the tip of the classical spin on a sphere, we consider trajectories in the space of parameters describing the density matrix of a quantum spin. This is not the way Markovian assumptions are normally introduced into quantum problems. Indeed, the recent bias is to relate the notion of chaos with the statistics of energy levels (Wigner-Dyson statistics). Note, however, that the numerical simulations of quantum spin systems that have been carried out to date do not exhibit Wigner-Dyson statistics. The extension of the classical analog discussed above to the quantum regime is fully treated in Ref. [33]. Here, it will suffice to point out that each 2×2 density matrix for a spin-1/2 particle can be described by three independent variables, and that the time evolution of such a spin can be mapped to the trajectory of the tip of a Bloch vector in

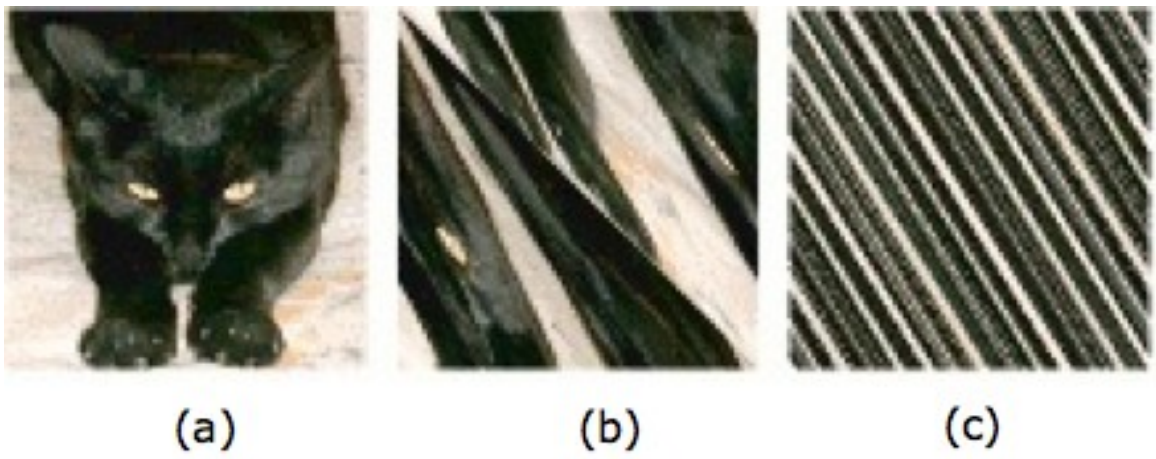

Figure 2.1: **Arnold's cat map.** (a) The original image. (b)-(c) several iterations of a hyperbolic mapping, analogous to the continuous evolution of the phase space probability density in a spin system. By (c), the system has already achieved extreme randomness. Image created by Claudio Rocchin and used by permission under the terms of the GNU Free Documentation License.

the three-dimensional space corresponding to those variables. The probability distribution which results from an average over all such trajectories for each spin will play the same role as the probability distribution of the classical spin vector trajectories treated in the classical analog above.

2.2.3.5 Consequences for NMR - Predictions of the Model

If the above treatment is valid for the spin system, then the eigenmode with the slowest real part will dominate in the long-time regime of a spin system's decay. Furthermore, if the slowest eigenvalue governing the decay for a given system has a nonzero imaginary component, this component will appear as an oscillation in the FID. The model therefore naturally predicts two of the common NMR decay behaviors: mono-exponential decay corresponding to the case of the slowest eigenmode (2.15) having zero imaginary part, and sinusoidally modulated exponential decay corresponding to the case of the slowest eigenmode (2.15) having a nonzero imaginary part

$$F(t) = \begin{cases} ae^{-\gamma t} & \text{if } \lambda_{Im} = 0, \\ ae^{-\gamma t}\cos(\omega t + \phi_a) & \text{if } \lambda_{Im} \neq 0. \end{cases} \tag{2.16}$$

Here, γ, ω, and ϕ_a are constants that are on order of the spin-spin relaxation rate T_2^{-1}, and a is the amplitude of the function. If these constants are indeed manifestations of the slowest decaying eigenmode present in the system, and if those eigenmodes can be thought of as analogous to Pollicott-Ruelle resonances, then according to Sec. 2.2.3.4, those constants should be intrinsic properties of the dynamics of the system, and *independent* of the method of preparation or evolution of the spin system. This suggests the first test of the chaos-based model: Prepare an isolated spin system in a controlled manner and observe the decay to equilibrium, characterizing the decay constants γ and ω. Next, prepare the spin system in a completely different way, and compare the decay to equilibrium. In the paradigm of the model, the long-time portion of the FID or echo signals should be characterized by Eq. (2.16) with the *same* values of γ and ω, irrespective of the initial state of the spin system. This is what is meant by "universal" behavior — every possible decay channel will, irrespective of the initial state of the spin system, eventually converge to the same shape. This then constitutes the first prediction of the model, which we call Prediction I:

Prediction I: In the long-time portion of the decay to equilibrium of an isolated spin system, a universal behavior of the form (2.16) will dominate the relaxation characterized by values of the decay coefficient γ and beat frequency ω that are independent of the manipulated values of the initial interaction coefficients in the Hamiltonian describing the spin-spin interactions.

Again, the "long-time" of the FID or echo is defined as a few times T_2, where T_2 is the characteristic timescale for the transverse decay determined by the interspin interactions, and represents the shortest ballistic timescale in the spin system. The fact that T_2 is the shortest intrinsic timescale of the system implies that (2.16) cannot be derived from conventional statistical mechanical formulations, all of which require a separation of timescales that do not exist in the system. Specifically, (2.16) cannot be viewed as an example of a damped harmonic oscillator, which requires that the slow oscillations be superimposed against a fast-equilibrating microscopic heat bath. The model appeals instead to the hyperbolic chaotic evolution of the spin system (shown visually in Fig. 2.1 and explained in Sec. 2.2.3.4) to demonstrate the appearance of a dynamically developing small parameter that plays the role of the fast timescale implied in the basic conjecture in Sec. 2.2.3. This fast timescale, which is also necessary to justify the use of Eq. (2.14), is the ratio of the characteristic scales of the expansion and contraction directions in the evolved phase space.

This said, it becomes clear why Prediction I should hold after a sufficiently long time. After such a time has elapsed, all coarse-grained regions in the phase space evolve from distinct subregions characteristic of the initial conditions imposed on the spin system to basically identical volumes characteristic of the long-time evolution. As far as ensemble averaging is concerned, each subregion of the phase space now has a generic, or universal, character. As the timescale for spin evolution is T_2, one might expect this behavior to set in after a time on the order of T_2. Reference [33] points out, however, that both the slowest exponent γ in Eq. (2.16) and the next slowest exponent will be on the order of T_2^{-1}. This means that it will take another time T_2 for the second slowest decay mode to die out. Therefore, the prediction is that the long-time regime will set in after a few times T_2.

The convergence of various initial spin states to a universal behavior can also be seen in a more physical way. Recall that the FID is a measure of first-order or single-spin quantum coherences in a sample; that is, the off-diagonal terms in the density matrix connecting eigenstates with $\Delta m = \pm 1$. Higher-order (multispin) coherences develop dynamically during the evolution of the FID, and then begin to decay away [82]. It takes some time for these higher-order coherences to develop, and some further time for their effects to propagate back and affect the observable first-order coherences measured by the FID. The higher coherence orders will also develop with decreasing amplitudes [82], which serves to attenuate their total observable effect on the system.

As discussed in Sec. 2.2.3.4 above, the eigenfunctions and eigenvalues of the time-evolution operator are expected to be the same for all coherences, single- and multi-spin. The FID or solid-echo can be thought of as being expanded in this set of common eigenfunctions with the caveat that the coefficients of each eigenfunction in the expansion will be different for the different order coherences. In fact, it is expected that the fastest decaying eigenmodes are more present in the higher-order coherences [33], which means that while these eigenmodes may decay faster, they initially have larger amplitudes in the higher-order coherences. (We will return to this argument in Sec. 2.3.1 when we explain the method of generating distinct initial spin conditions in our experiments.)

In principle, all coherences that can affect the signal may be expanded with the same set of eigenmodes and all but the slowest will eventually decay away. This is the fundamental concept that underlies the universal behavior expected in the model. If the long-time portion of a signal initiated in any arbitrary way is reached, it is expected that a universal behavior will be present corresponding to the physical fact that only the slowest decaying eigenmode

remains contributing to the signal. All the coherences that may affect the signal, even if they have not decayed away as such, will eventually each be dominated by decay parameters γ and ω, characteristic of the slowest decaying eigenmode (2.15), and the total signal will thus be of the form (2.16) with the corresponding γ and ω. This prediction was first tested under limited conditions by Morgan [26], and subsequently under a much broader array of conditions and for various systems by me [36, 37]. The original prediction can be found in Refs. [76, 35, 33].

The remaining predictions of the model are specific to a particular manipulation of the spin system known as solid echoes, and were originally elucidated in Ref. [37]. Solid echoes will be described more fully in Sec. 2.4.1.2; for now we simply recall that the solid echo pulse sequence is 90°_x – τ – 90°_y– Acquire. The many-spin density matrices of the system after the first 90°_x pulse can be represented as

$$\rho_{kl}(t) = \rho_{0,kl} e^{-(\gamma + i\omega)t} + \rho^\dagger_{0,kl} e^{-(\gamma - i\omega)t}. \tag{2.17}$$

The density matrix depends on the constants γ and ω of the slowest decaying eigenmode which is determined by the Hamiltonian of the system, and is written in the above form to guarantee Hermiticity. In (2.17), $\rho_{kl}(t)$ is the density matrix for any subsystem of the entire spin system: one-spin density matrix, two-spin density matrix, or n-spin density matrix, so long as n is much smaller than the total number of spins. The evolution of the two terms in Eq. (2.17) is predicted to be controlled by the time-independent matrices $\rho_{0,kl}$ which is also determined by the Hamiltonian of the system, and the evolution of $\rho_{kl}(t)$ reduces to rescaling and changing the relative phases of these terms. This fundamental assumption underlies the following predictions of the model that pertain to solid echoes.

If Eq. (2.17) holds, the FID resulting from the first 90°_x pulse should then be written as a sum of two terms, after the interpulse delay time τ has elapsed, as

$$\begin{aligned} F(\tau) &= f(\tau) + f^*(\tau) \\ &= \frac{a}{2} e^{-(\gamma + i\omega)\tau} + \frac{a^*}{2} e^{-(\gamma - i\omega)\tau} \end{aligned} \tag{2.18}$$

so that Eq. (2.18) is identical to Eq. (2.16). The response of the system to the first pulse is represented by $f(\tau)$. We explicitly choose τ long enough that the FID has already reached

its long-time behavior (Prediction 1). Then, after the second 90°_y pulse, the density matrix is converted into the form

$$\rho_{kl}(\tau_+) = e^{-(\gamma+i\omega)\tau} e^{-iI_y\frac{\pi}{2}} \rho_{0,kl} + e^{-(\gamma-i\omega)\tau} e^{-iI_y\frac{\pi}{2}} \rho^\dagger_{0,kl}. \tag{2.19}$$

As in Eq. (2.18), the solid echo signal will then be written as

$$\tilde{F}(\tau) = f(\tau)\tilde{f}(t-\tau) + f^*(\tau)\tilde{f}^*(t-\tau) \tag{2.20}$$

where we define the time-dependent signal resulting from the second 90°_y pulse as

$$\tilde{f}(t-\tau) = b_1 e^{-(\gamma+i\omega)(t-\tau)} + b_2 e^{-(\gamma-i\omega)(t-\tau)}. \tag{2.21}$$

Unlike those in Eq. (2.18), the amplitudes b_1 and b_2 are two complex constants that are not necessarily complex conjugates of one another, since the only physical requirement is that Eq. (2.20) is real, and this is guaranteed by the construction. A straightforward algebraic calculation reduces Eq. (2.20) to

$$\begin{aligned} \tilde{F}(\tau,t) &= |a| e^{-\gamma\tau} \left[\cos(\omega\tau - \phi_a) \Re\tilde{f}(t-\tau) + \sin(\omega\tau - \phi_a) \Im\tilde{f}(t-\tau) \right] & (2.22) \\ &= \frac{|a|}{2} e^{-\gamma t} |C(\tau)| \cos[\omega t + \phi_C(\tau)], & (2.23) \end{aligned}$$

where Eq. (2.23) follows if $|C(\tau)|$ and $\phi_C(\tau)$ are the amplitude and phase of a complex function

$$C(\tau) = b_1^* e^{-i\phi_a} + b_2 e^{i(\phi_a - 2\omega\tau)}. \tag{2.24}$$

Reference [37] then makes the following predictions relating to solid echoes initiated in the long-time portion of the FID:

Prediction II: The amplitudes $|C(\tau)|$ of various solid echoes, characterized by different values of the interpulse delay τ, will consist of a τ-independent constant and a τ-dependent

oscillating term with frequency 2ω and will be related to the long-time constants of the FID by the relationship

$$|C(\tau)|^2 = |b_1|^2 + |b_2|^2 + 2|b_1||b_2| \cos\left(2\omega\tau - 2\phi_a - \phi_{b_1} - \phi_{b_2}\right). \tag{2.25}$$

Prediction III: The phases $\phi_C(\tau)$ of various solid echoes, characterized by different values of the interpulse delay τ, will consist of a τ-independent constant and a τ-dependent oscillating term with frequency 2ω and will be related to the long-time constants of the FID by the relationship

$$|C(\tau)| \cos\left[\phi_C(\tau)\right] = |b_1| \cos\left(\phi_a + \phi_{b_1}\right) + |b_2| \cos\left(2\omega\tau - \phi_a - \phi_{b_2}\right). \tag{2.26}$$

Prediction IV: A solid echo generated in the long-time of the FID will be of the form

$$\tilde{F}(\tau, t) = |a| e^{-\gamma\tau} \left[\cos\left(\omega\tau - \phi_a\right) \Re\tilde{f}(t-\tau) + \sin\left(\omega\tau - \phi_a\right) \Im\tilde{f}(t-\tau)\right], \tag{Same as Eq. (2.22))}$$

where the functions $\Re\tilde{f}(t-\tau)$ and $\Im\tilde{f}(t-\tau)$ are experimentally measurable shapes determined by examining the shapes of two previous solid echo shapes.

2.3 Experimental Procedures

Morgan, Fine, and Saam [26] were the first to look for the evidence of Prediction I in Sec. 2.2.3.5 (the universal behavior) in the long-time decays of NMR manipulated spin systems using two solid polycrystalline xenon samples: one composed of 86% ^{129}Xe (isotopically enriched) and the other composed of 27% ^{129}Xe (naturally abundant). They found that the transverse magnetization decays in these samples did indeed approach the universal form given by Eq. (2.16) by measuring the FID and various solid echoes. These samples were both measured at the same field of 1.5 T at the same temperature under the same conditions.

Starting from this set of preliminary experiments, the first task was to extend the evidence of the long-time behavior by attempting to observe it in more than the two samples in which it had been previously observed. These experiments constitute an important check that the effect is indeed repeatable in many systems. I prepared and tested 10 samples

to search for the universal behavior in many different experiments (*i.e.*, different pulse sequences, sample preparation techniques, experiment types) under different conditions (*i.e.*, different temperatures, magnetic fields, frequencies) and on a variety of samples (*i.e.* different isotopic ratios, nuclei, phases). Six of the samples tested were made by mixing a controlled amount of various xenon isotopes to create different "lattices" where the dipolar fields experienced by the ^{129}Xe would be very different. The xenon samples I made and tested are listed in Sec. 2.4.1. It is important for claims of generic behavior to observe the behavior in an entirely different system under a different set of circumstances. I therefore undertook to study the predictions of the chaos-based model by observing the behavior of ^{19}F in a variety of CaF_2 single crystals, and in CaF_2 powders at various magnetic fields. I also observed convergence to the long-time behavior in various other fluorite crystals, including BaF_2 and SrF_2. The last test of the universal behaviors was to verify with a range of different pulse sequences and manipulation procedures that the long-time behavior would be robust enough to develop after any arbitrary manipulation of the spin system. I therefore employed the Jeener-Broekaert sequence and the magic echo – two sequences which produce known and different initial spin states – in addition to a wide range of solid echoes, to attempt to observe the long-time behavior dominate the long-time signals in each case. Performing these measurements at different temperatures, magnetic fields, and using different techniques provides conclusive evidence that the predicted long-time behavior is a robust and universal property of the spin systems measured, irrespective of the wide range of manipulations employed to vary the initial conditions.

2.3.1 Generation of Distinct Initial Conditions

An ensemble of thermally isolated interacting nuclear spins is described by the truncated magnetic dipole Hamiltonian in the rotating frame [23]

$$\mathcal{H} = \sum_{k<n} \left[J_{kn}^{\perp} (I_k^x I_n^x + I_k^y I_n^y) + J_{kn}^z I_k^z I_n^z \right], \tag{2.27}$$

where I_n^α is the quantum mechanical operator of the n^{th} nuclear spin. The coefficients for the interaction of the k^{th} and n^{th} spins are

$$J_{kn}^{\perp} = -\frac{1}{2} J_{kn}^z \simeq -\frac{(1 - 3\cos^2\theta)}{2|\mathbf{r}_k - \mathbf{r}_n|^3}, \tag{2.28}$$

where θ is the angle between the z-axis defined by the external static magnetic field and the internuclear vector $\mathbf{r}_k - \mathbf{r}_n$. It is here that we notice why perturbative approaches to solving the problem of the lineshape have so much difficulty. Were it not for the first two terms in Eq. (2.27), the Hamiltonian would be exactly solvable. However, these terms are present, and as Eq. (2.28) shows, they are not small compared to the the final term of Eq. (2.27). There is therefore no obvious expansion parameter that would justify a perturbative approach. The transverse NMR decays can be described by the function $F(t)$ which can be expressed as

$$F(t) = \mathrm{Tr}\left\{\sum_n S_n^x \rho(t)\right\} \tag{2.29}$$

where

$$\rho(t) = e^{i\mathcal{H}t}\rho_0 e^{-i\mathcal{H}t}, \tag{2.30}$$

and ρ_0 is the density matrix at time $t = 0$. Here we have chosen time origin ($t = 0$) to be at the time corresponding to the end of the final pulse in each applied rf sequence. Equation (2.16) is the long-time form of Eq. (2.29) predicted by Ref. [76].

Equation (2.30) is the form of the density matrix after a 90°_x rotation pulse. When $t = \tau$, a second pulse may be applied to the spin system as in the case of solid echoes described in Sec. 2.4.1.2. At differing values of τ, multispin quantum coherences in the sample will have evolved and decayed to different intensities, and the state of the system will then be unique for that value of τ. The application of the second pulse arrests this dynamical evolution and mixes the amplitudes of the coherences in a nontrivial way [82, 26]. As discussed above, each of these coherences can be expressed as an expansion in the eigenmodes of the time-evolution operator (2.15) with different amplitudes, the fastest of which will then decay away leaving each dominated by the slowest eigenmode. Mathematically, these higher-order spin coherences that develop dynamically correspond to higher-order commutators in the power-series expansion of the density matrix which become more and more important as the evolution proceeds (see supplemental material to Ref. [26]).

To generate distinct initial density matrices for our spin ensembles, we used a variety of pulse sequences with varying interpulse delay times τ. We analyzed the FID (90°_x), various solid echoes [83, 23] ($90^\circ_x - \tau - 90^\circ_y$), the Jeener-Broekaert (JB) echo [84, 85]($90^\circ_x - \tau_1 - 45^\circ_y - \tau_2 - 45^\circ_{\bar{y}}$), and the magic echo [86, 23] ($90^\circ_y - \tau - 90^\circ_{\bar{y}} - \tau'_{H1} - \tau'_{\bar{H}1} - 90^\circ_y$). Each generates a distinct initial spin density matrix ρ_0. Here the subscripts for the angles indicate the axis of the rf pulse-induced rotation in the Larmor reference frame. $\bar{y}$ indicates the negative direction along the y-axis. The meaning of H_1 will be explained at the end of Sec. 2.4.2.3. The solid echo, JB echo, and magic echo manipulate spin coherences generated by spin-spin interactions, and, in this sense, are not like Hahn echoes that simply compensate for an inhomogeneous external field. Each sequence will be briefly described in its respective section below; they are reviewed and analyzed in great detail elsewhere [23].

2.3.2 Convection Cell Hyperpolarization

Rapid and repetitive production of large amounts of polarized xenon is generally a challenging task. Due to its large spin-destruction cross section, a ^{129}Xe atom has a high affinity for destroying the spin polarization of the optically-pumped Rb vapor. This limits the volume-averaged Rb polarization, which decreases the achievable ^{129}Xe polarization (Eq.(1.11) from Ch. 1). This intrinsic limitation could theoretically be overcome by increasing the optical pumping rate, *i.e.*, by supplying more photons. In practice, however, the practical limits of available laser power to pump the Rb atoms restricts the number of ^{129}Xe atoms that can be effectively polarized by SEOP. Conventional methods for polarizing xenon rely on flow-through technology [87, 88], or batch-mode production — both of which can only polarize low vapor pressures of ^{129}Xe. Flow-through methods can ultimately produce large amounts of hyperpolarized ^{129}Xe with cryogenic accumulation of the flowing gas; total accumulation of hyperpolarized ^{129}Xe is then only limited by the flow-rate of low pressure gas and the relaxation time of the xenon in the solid ($\approx$ 2.5 hrs) [89]. However, a simpler and rapid technique for producing solid hyperpolarized ^{129}Xe in batch mode is desirable. The challenge is to simultaneously create conditions wherein only a low vapor pressure of xenon gas is present for SEOP, but the ultimate density of solid xenon is as large as possible to create large NMR signals.

In my experiments involving ^{129}Xe, I employed a third way to produce hyperpolarized ^{129}Xe in a rapid, economic, and reproducible way. The idea was initially proposed and tested by the Saam group in 2004 as part of a different set of experiments [90], but has

since proven most useful in experiments unrelated to its original purpose [91]. The method, which I will call phase-exchange SEOP, involves the construction of a cell similar to that shown in Fig. 2.2. The cell, made of Pyrex glass and coated with SurfaSil[7] to inhibit ^{129}Xe wall relaxation [92], is filled with gases to the desired pressures as well as a few milligrams of Rb metal using standard techniques [93, 91, 94]. Table 2.1 lists the contents of the cells I made for use in these experiments.[8] The cell is placed in the oven/refigerator shown in Fig. 2.3, and the entire apparatus is placed in a 2 T magnetic field.

The design works by keeping the left side of the cell in Fig. 2.2 below the boiling point of xenon (165 K), but above the melting point (161 K). This allows most of the xenon to exist in the cell in liquid phase and to collect in the liquid reservoir. The remaining gas phase xenon atoms are those involved in the SEOP process. The vapor pressure of xenon is a sensitive function of its temperature and the partial pressure of xenon atoms in the gas phase can therefore be tuned somewhat for optimal performance by controlling the temperature of the cold side of the cell within the narrow permissible range. We kept the cold side of the cell at 163 K for my experiments; the vapor pressure of the xenon was

[7]Pierce Biotechnology, Rockford, IL 61105

[8]Note the large pressures of xenon gas; these pressures far exceed the normally permissible number density of xenon atoms to allow for effective SEOP.

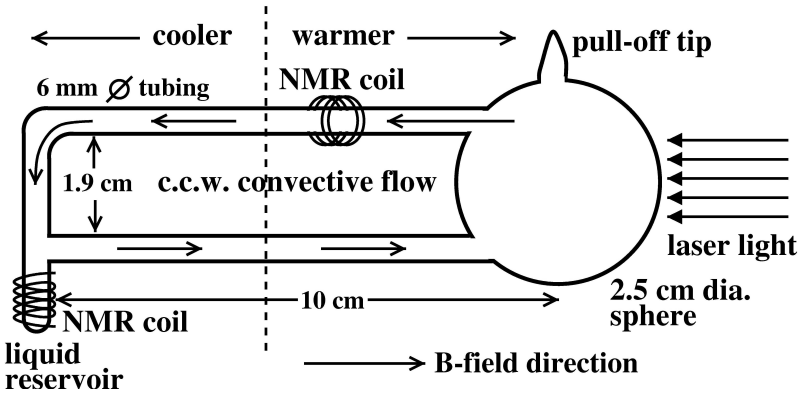

Figure 2.2: **Diagram of the phase-exchange SEOP cell.** Optical pumping occurs in the spherical side of the cell, which is kept at around 370 K to generate Rb vapor. The gases traverse the entire cell via convective currents in the direction shown by the arrows, and the xenon phase exchanges with a liquid xenon column on the cold side of the cell (163 K). The dotted line indicates a boundary in the oven/refrigerator between hot and cold regions.

Table 2.1: Description of the xenon lattices under consideration. Cells differ in the concentration of ^{129}Xe and ^{131}Xe. NMR is performed exclusively on the ^{129}Xe spins in the lattice. The partial pressures of xenon listed in mbar and are referenced to 20 °C.

Name	System	$\%^{129}$Xe	$\%^{131}$Xe	$\%^{even}$Xe	Xe partial pressure
43A	I	85.6	1.9	12.5	1620 mbar
145C	II	62.7	27.3	10.0	1700 mbar
146A	III	54.7	36.1	9.2	2500 mbar
146B/145A	IV	46.5	45.2	8.3	1700 mbar
145B	V	29.6	64.0	6.4	2500/1700 mbar
123A	VI	27.5	21.5	51.0	6500 mbar

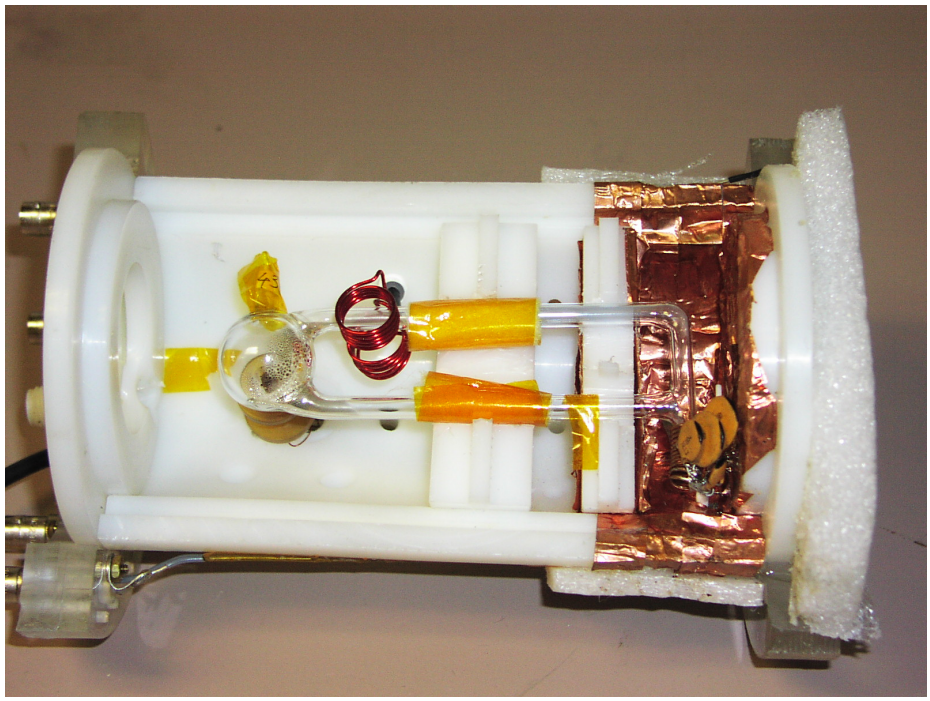

Figure 2.3: **Apparatus used for phase-exchange SEOP.** Oven/refrigerator used to maintain the temperatures necessary for phase-exchange SEOP (the lid has been removed and is not shown). The oven is made of high-density polyethylene. The front is heated to 370 K by air forced over a filament heater. The back is cooled to 163 K by nitrogen gas boiled from liquid and heated by a filament. Resonant laser light enters the oven via the glass window just visible on the left and illuminates the spherical region of cell. Physical barriers separate the hot and cold regions. Liquid xenon collects in the coil on the right side of the oven below the capacitors, and is frozen by immersion in liquid nitrogen after sufficient polarization has built up.

therefore about 900 mbar. The hot side of the cell is maintained at sufficient temperatures to generate the desired Rb vapor pressures (typically 370 K).

SEOP proceeds by introducing laser light to the spherical region on the hot side of the cell (see Figs. 2.2 and 2.3). Here, the Rb vapor is polarized by the incident photons as described in Ch. 1. Since the vapor pressure of the xenon is low, spin-exchange can proceed with maximum efficiency. The large temperature gradient across the cell drives a convective current around the cell in the direction indicated by the arrows in Fig. 2.2. The polarized xenon gas traversing the cell phase exchanges with the liquid column in the cold side of the cell, building up a column of polarized liquid xenon. The total polarization of the liquid xenon column is limited only by the ≈ 20 min wall relaxation time of the liquid xenon, which sets the timescale for the achievement of maximum polarization in the experiment. After maximum polarization levels have been reached (10 - 15% in our experiments), the cold side of the oven/refigerator is flooded with liquid nitrogen, rapidly freezing the liquid column and producing a cylindrical hyperpolarized solid xenon sample. After the desired measurements have been made, the refrigerator is simply warmed to revolatilize the xenon solid. Hundreds of freeze/thaw cycles were performed on some cells, and each time solid xenon with similar polarizations was prepared in under 30 minutes. The phase-exchange SEOP method is therefore an excellent way to reproducibly generate the solid hyperpolarized ^{129}Xe for these experiments.

2.3.3 Solid ^{129}Xe

Hyperpolarized ^{129}Xe is an ideal system for investigating the hypothesis of a universal long-time behavior. In this van der Waals solid at 77 K, the xenon lattice is thermally well-isolated from its environment. The NMR signals from a macroscopic sample are large (greater than 1mV before amplification); the long-time regime can thus be examined with good signal-to-noise-ratio (SNR). Additionally, T_2 is long (≈ 0.5 ms), allowing for relatively simple radio-frequency (rf) manipulation of the sample, as the corresponding bandwidths are small and the deadtimes short. These conditions make the use of short "hard" rf pulses practical. Finally the ^{129}Xe nuclei have spin = 1/2, which makes them maximally nonclassical in terms of spin angular momentum quantization, and eliminates the need to account for a nuclear quadrupole moment. Therefore, the ^{129}Xe nuclei are an ideal system for exploring quantum connections to conventionally classical phenomena such as chaos.

We used dynamic nuclear polarization in the form of SEOP [12] to generate nuclear

polarizations of $\approx 10\%$ in solid ^{129}Xe nuclei. We then measured the transverse relaxation of these nuclei over many orders of magnitude (see Fig. 2.4). These experiments generated extremely large signals that could be precisely measured over unconventionally long times, *i.e.*, many times T_2. The spin-exchange convection cells [90] described above allowed for rapid and repetitive generation of a few millimoles of highly polarized liquid xenon, which were then rapidly frozen by exposing the sample to a stream of liquid nitrogen. During rapid freezing, the majority of the polarization in a liquid xenon sample survives the phase transition to a solid.

The solid xenon samples were generated in an applied magnetic field of 2 T (^{129}Xe Larmor frequency 24.56 MHz), and maintained at a temperature of 77 K. Induction signals were acquired with an Apollo (Tecmag) NMR spectrometer using 10 μs square excitation pulses with a receiver dead time of 60 μs. At 77 K, ^{129}Xe $T_1 \approx 2.5$ hrs [95] while $T_2 \approx 0.5$ ms [96], justifying our assumption of thermal isolation during the transverse decay. The samples consisted of 1 to 2 mM xenon in various isotopic ratios (see Table 2.1). The transverse decay was acquired after one 90° pulse (in the case of the FID), or after the last of a series of pulses that create various echoes. The enormous signals thus acquired were too large to fit into the 16-bit digitizer native to the Apollo system. Acquisition was therefore carried out in two separate experiments with two different NMR-gain settings. There was sufficient overlap of the temporal signal in both experiments to ensure that the reconstruction of the entire decay was unambiguous.

2.3.4 CaF_2

CaF_2 is another ideal system for exploring phenomena where a large SNR is desired. Like xenon, the ^{19}F nuclei have spin=1/2, and therefore no quadrupole moment. ^{19}F nuclei are 100% abundant, and the gyromagnetic ratio of ^{19}F is the third largest of all the elements. This gives the ^{19}F nuclei a magnetic moment 95% that of the proton. Moreover, ^{19}F in CaF_2 are arranged in a simple cubic lattice, allowing for easy analytical calculations. Additionally, the calcium is inert chemically and magnetically; only one tenth of one percent is magnetically active.[9] Finally, the high Debye temperature of 474 K assures that phonon motion in the crystal will be negligible at room temperature and lower. In fact, it is necessary to dope our crystals with a small density of paramagnetic impurities in order to reduce T_1 to realistic timescales.

---

[9] ^{43}Ca is 0.14 % abundant with spin of 7/2 and a tiny $\gamma = 2.8$ MHz/T.

The CaF_2 crystals used in our experiments were obtained from Optovac, Inc[10] and are doped with 0.1% yttrium or gadolinium to reduce T_1 to $\approx$ 1 s. These are nominally cylindrical samples (1 cm x 0.3 cm), with the cylinder axis perpendicular to the [100], [110], or [111] crystal direction. These respective directions would thus be parallel to the applied magnetic field in a typical transverse solenoidal NMR coil. Because these samples were altered somewhat to fit into our NMR probe, the crystal directions are no longer exact (though care was taken to maintain them as much as possible). $T_2 \approx 25$ μs for all CaF_2 samples. The signals are acquired at 2 T (^{19}F Larmor frequency 83.55 MHz) with the same Apollo (Tecmag) NMR spectrometer using 2 μs square pulses with a receiver dead time of 15 μs at room temperature. The CaF_2 powder was obtained from J. T. Baker Chemical Co., and contains nominally 98% CaF_2 with traces of chlorides, sulfates, heavy metals, and iron. T_1 of the powder was measured by saturation-recovery to be $\approx$ 1 second.

2.4 Results: Testing the Chaos-based Model

We explored a wide parameter space in search of experimental evidence for the predicted universal long-time behavior in isolated quantum systems. First, we looked at six different isotopic compositions of solid hyperpolarized xenon using the solid echo sequence with varying values of τ. Then, using one of these compositions (System I), we applied three different pulse sequences (FID, solid echo, JB echo) to observe the long-time behavior associated with each composition. Next, we examined ^{19}F in CaF_2 single-crystals, with three different orientations of applied magnetic field, as well as in polycrystalline CaF_2 powder. We used three different pulse sequences to observe their long-time behavior (FID, solid echo, magic echo).

2.4.1 Solid Xenon Systems

Here we will present the experimental results obtained in solid ^{129}Xe which were motivated by the predictions for the chaos-based model stated in Sec. 2.2.3.5. We will first present the free induction decay for the ^{129}Xe systems in order to extract the long-time parameters of the transverse decay γ and ω. Next, we well show the data from the six xenon systems produced to test the universality of the generic behavior Prediction I. Many different solid echoes, distinguishable by their interpulse delay times, were applied to each system. Then I will describe and show the data obtained using a completely different pulse

[10]Now owned by Corning.

sequence, which produces an entirely different type of initial order in the system, in order to observe the long-time behavior of that manipulation. After establishing the robustness of the universal long-time behavior in these ^{129}Xe systems, I will investigate the remaining three predictions relating to the amplitude, phase, and lineshapes of the solid echoes.

2.4.1.1 Free Induction Decay

In Fig. 2.4 we show a typical ^{129}Xe FID at 2 T and 77 K. The magnitude of the quadrature signal vs. time is shown on a semilog plot to illustrate the decay over many orders of magnitude. The SNR here is about an order of magnitude better than in the initial study [26]. Since the plot shows the log of the absolute value of the FID signal, the cusps indicate the zero-crossings of the FID (see the inset graph of Fig. 2.4 for a linear-scale plot of the absorption signal explicitly showing the zero-crossings). The decay coefficient $\gamma = 1.25\pm$ 0.04 ms^{-1} and the oscillation frequency $\omega = 2.06 \pm 0.04$ rad/ms were extracted from a fit of the long-time portion of the FID to Eq. (2.16). These parameters are on the order of T_2^{-1} and agree well with the values obtained by Morgan *et al.* [26]. T_2 was estimated as $\sqrt{1/M_2}$ where M_2 is the second moment of the FID.

2.4.1.2 Solid Echo Universal Behavior

In the solid echo sequence $(90^\circ_x - \tau - 90^\circ_y)$, two 90° pulses are applied out of phase with an interpulse delay time τ that can be varied [83, 23]. The density matrix following the second pulse is given by

$$\rho_0 = e^{i\mathcal{H}_R\tau} \exp\left\{\frac{\sum_n I_n^x H}{k_B T}\right\} e^{-i\mathcal{H}_R\tau} \tag{2.31}$$

where the "rotated Hamiltonian" $\mathcal{H}_R$ is given by [26]

$$\mathcal{H}_R = \sum_{k<n} \left[J_{kn}^{\perp} I_k^x I_n^x + J_{kn}^z I_k^y I_n^y + J_{kn}^{\perp} I_k^z I_n^z \right]. \tag{2.32}$$

For pairs of interacting spins 1/2, the solid echo yields a perfect recovery of the initial magnetization at time τ after the second pulse, similar to the conventional Hahn echo. However, in many-spin systems complete refocusing does not occur, and the deviations from complete refocusing become more pronounced as τ is lengthened [82]. As follows from

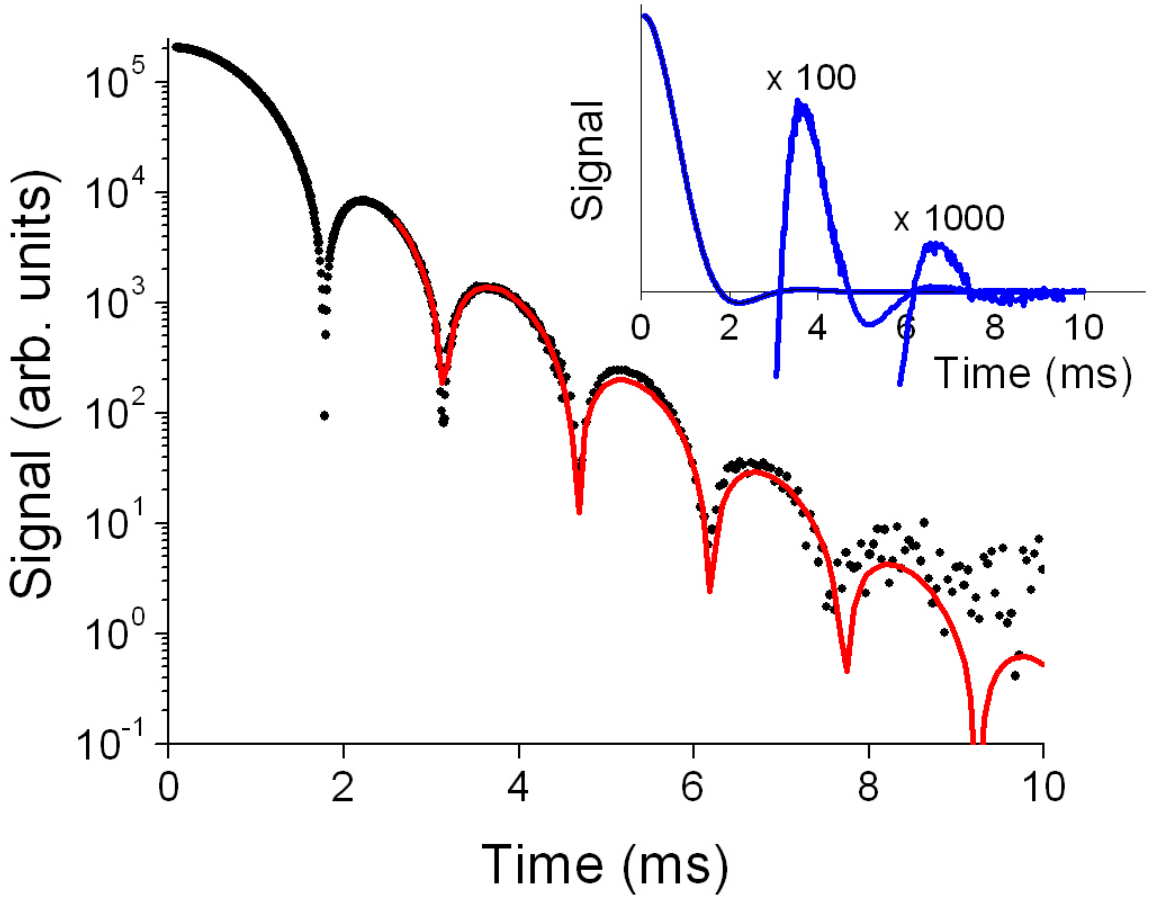

Figure 2.4: ^{129}**Xe FID corresponding to System I** (86% ^{129}Xe; see Table 2.1) shown on a semilog plot. The solid line is a fit of the absolute value of Eq. (2.16) to the long-time signal at $t > 2.5$ ms. The inset shows the FID absorption signal on a linear scale to illustrate the zero-crossings of the FID. The later sections of the signal have been enhanced as indicated.

Eq. (2.31), the solid echo pulse sequence creates new initial spin density matrices as τ is varied (see supplementary material to Ref. [26]).

In Fig. 2.5 we show signals associated with ten solid echoes obtained for different values of the interpulse delay time τ, together with the free induction decay. These data were collected for 86% ^{129}Xe (System I). The initial portion of the FID following the first pulse was acquired along with the solid echo following the second pulse in order to provide a relative amplitude normalization, and thus to correct for polarization levels that varied somewhat from experiment to experiment. Care was taken to eliminate residual longitudinal

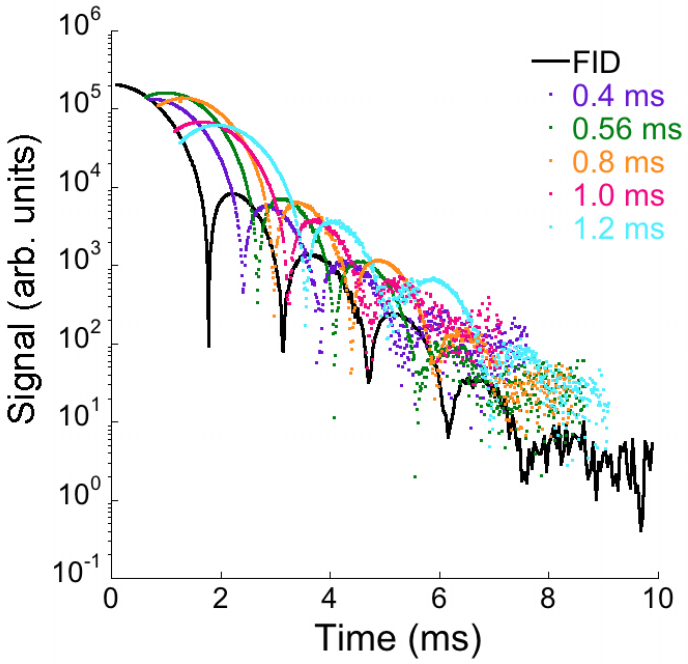

(a)

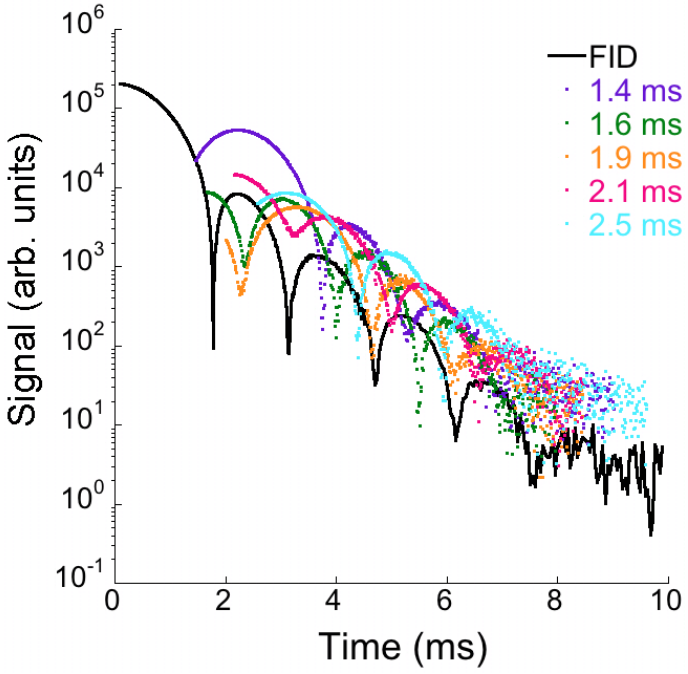

(b)

Figure 2.5: **^{129}Xe solid echoes in xenon enriched to** 86% **^{129}Xe (System I)**. In (a) and (b) we show ten solid echoes on a semilog plot together with the FID of Fig. 2.4. Signals are split between (a) and (b) for visual clarity only.

magnetization from the echo signal, and this was checked by using a $90^\circ_x - \tau - 90^\circ_x$ sequence prior to each echo experiment and verifying a null signal (*i.e.*, precise 90° pulses). We note that some of the data reported in Morgan *et al.* [26] from a similar experiment likely have some contaminating longitudinal magnetization in the early part of the echo. The observed phase-shift of the echoes with respect to the FID shown in that work was therefore likely coincidental. This does not affect their conclusions concerning the universal long-time behavior of the signals, but it is critical for exploring relations concerning the amplitudes and phases of solid echo signals relative to the FID in the long-time regime.

In Fig. 2.6, we make explicit time shifts to the data shown in Fig. 2.5a and Fig. 2.5b to compare the behavior of each signal in the long-time regime. Figure. 2.5a shows early echoes and Fig. 2.5b shows later echoes; the figures are split for visual clarity. The dashed line in Fig. 2.6 is a plot of Eq. (2.16) with the parameters obtained from the fit in Fig. 2.4. These values agree well with those obtained in the previous work using the same material [26]. Similar long-time fits to the individual solid echoes produced values for γ and ω consistent with those obtained for the FID. It is in this sense that the long-time behavior is universal, in contrast to the varied decay shapes exhibited in the initial portions of the decays. Table 2.2 lists the values of the decay constant γ and the beat frequency ω for six different xenon isotopic compositions. For each composition, the parameters were obtained from a fit to the FID. As a check, fits were also performed to each individual echo to verify that the extracted parameter values were in agreement with those obtained from the fit to the FID.

Figures 2.7, 2.8, 2.9, 2.10, and 2.11 show the data for Systems II - VI. Though the lower isotopic concentration of ^{129}Xe and relatively high abundance of ^{131}Xe reduces the SNRs in these systems relative to System I, we still observe convergence of different transverse decays to the respective universal values of γ and ω for each system. The echo amplitudes are normalized in the same way for each xenon composition as described above for System I. Part (a) of each figure shows the FID of the ^{129}Xe in the sample relaxing with the characteristic oscillatory fashion. As in Fig. 2.6, each signal shown is the magnitude of the acquired signal, and the cusps therefore correspond to zero-crossings of the FID or echo. Also shown in part (a) of each figure is the magnitude of one or more solid echoes acquired with the interpulse delay times indicated in the legends. In part (b) of the figures, the echoes are shifted in time to illustrate the convergence of the long-time behavior of each echo signal to that of the FID.

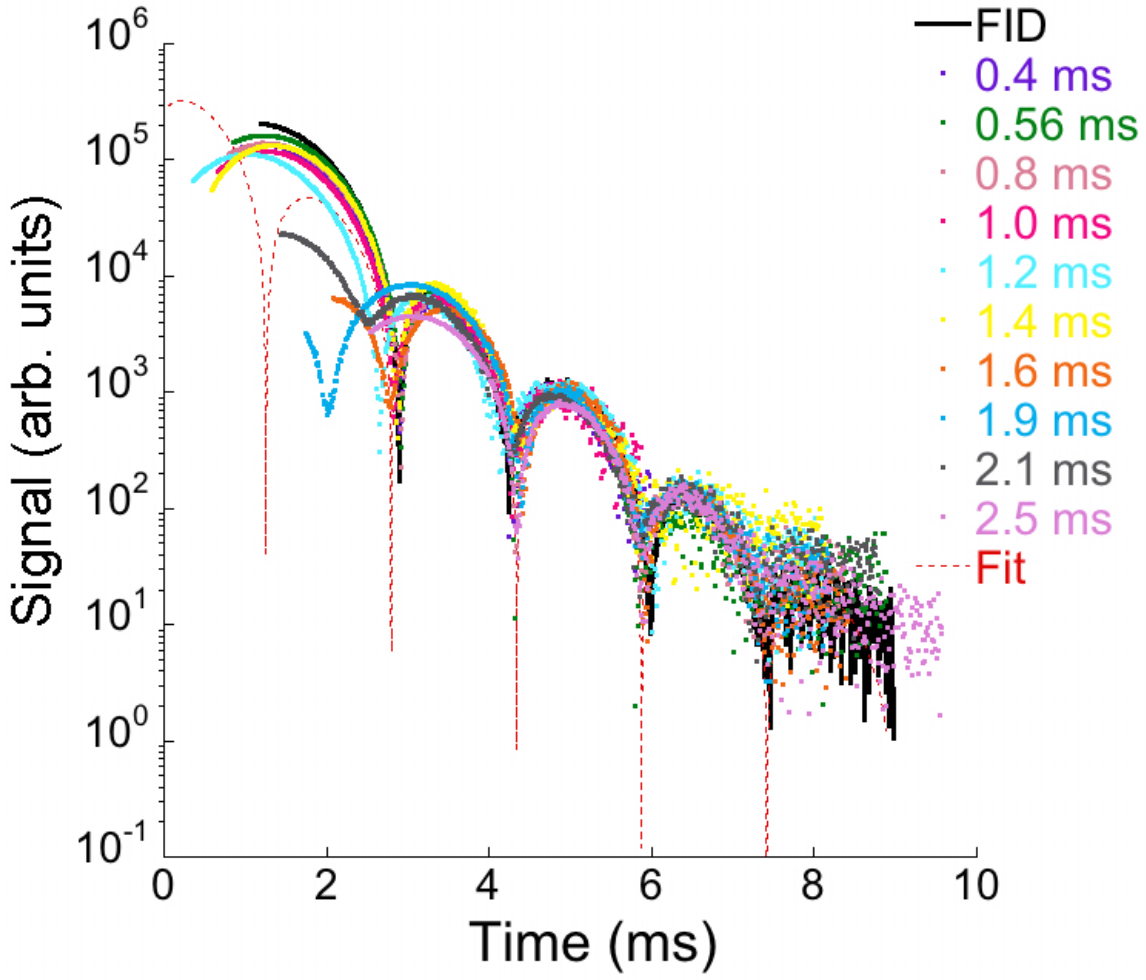

Figure 2.6: **^{129}Xe solid echoes in xenon enriched to** 86% **^{129}Xe (System I)**. Here we show the data from Fig. 2.5a and Fig. 2.5b together with the echoes time-shifted to illustrate the convergence of the long-time behavior. The broken line is the fit to the FID, also shown in Fig. 2.4, demonstrating that the solid echoes all exhibit the same long-time behavior as the FID with the same values of γ and ω (see Table 2.2).

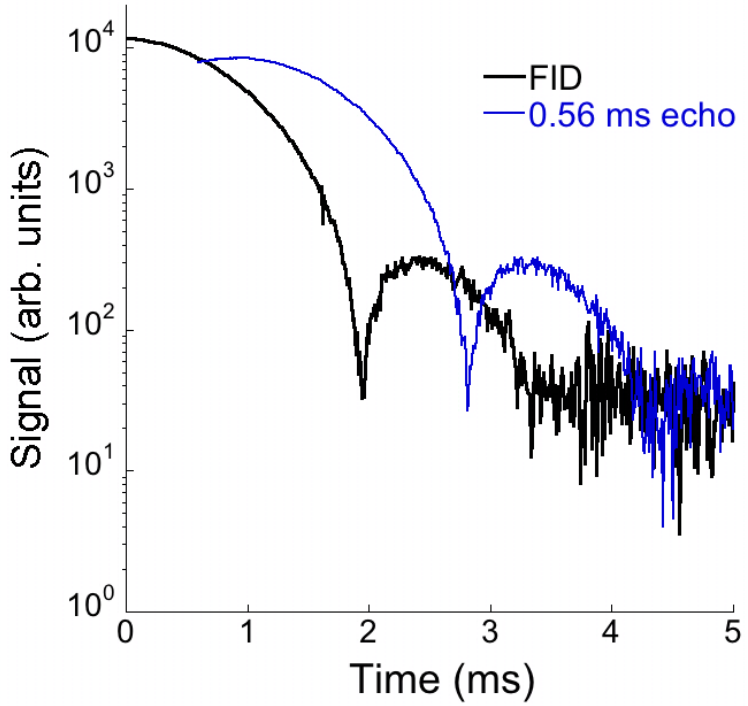

(a) Solid echo signal shown on a semilog plot with the FID.

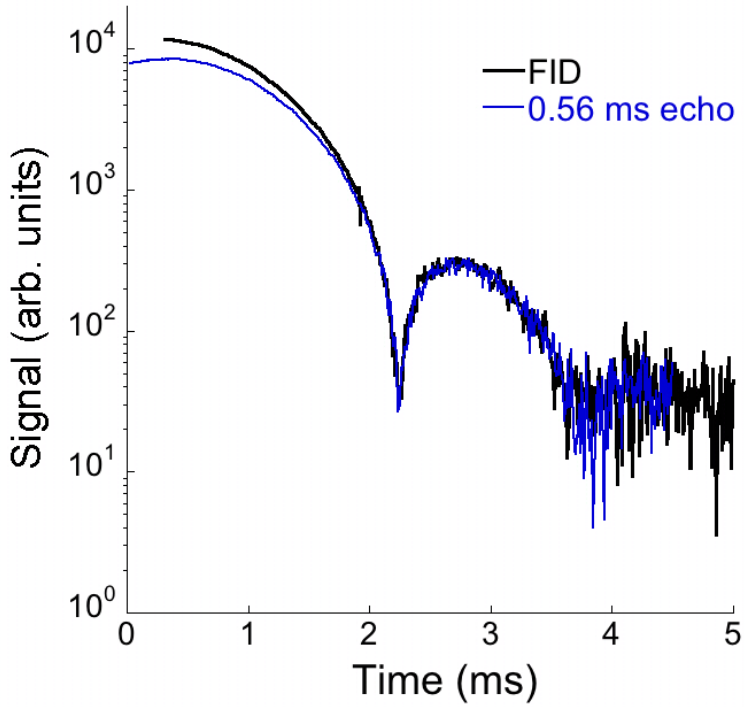

(b) The same data as in (a) are shown time-shifted to illustrate the convergence of the long-time behavior.

Figure 2.7: **^{129}Xe FID and solid echoes in** 62.7% **^{129}Xe (System II)**.

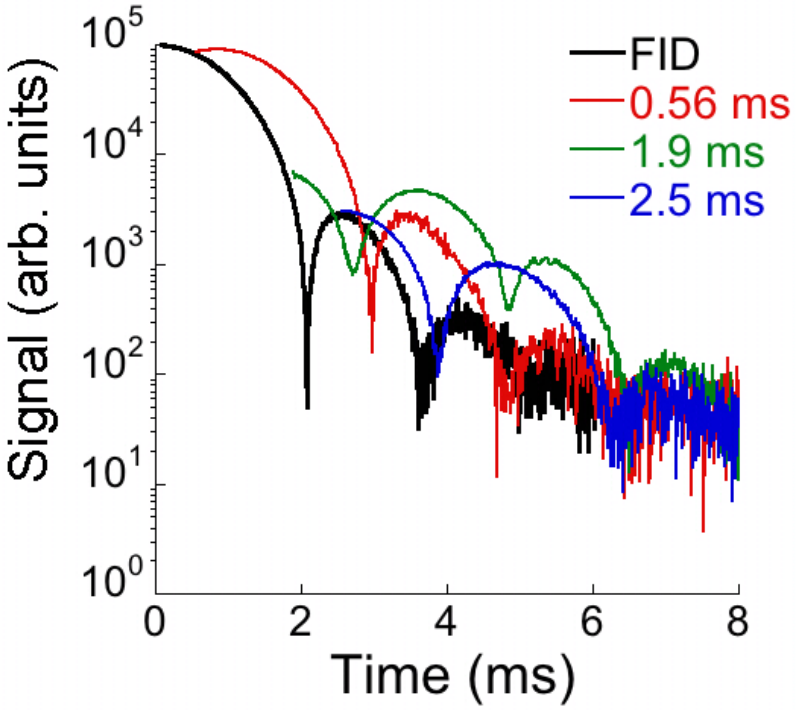

(a) Solid echo signals shown on a semilog plot with the FID.

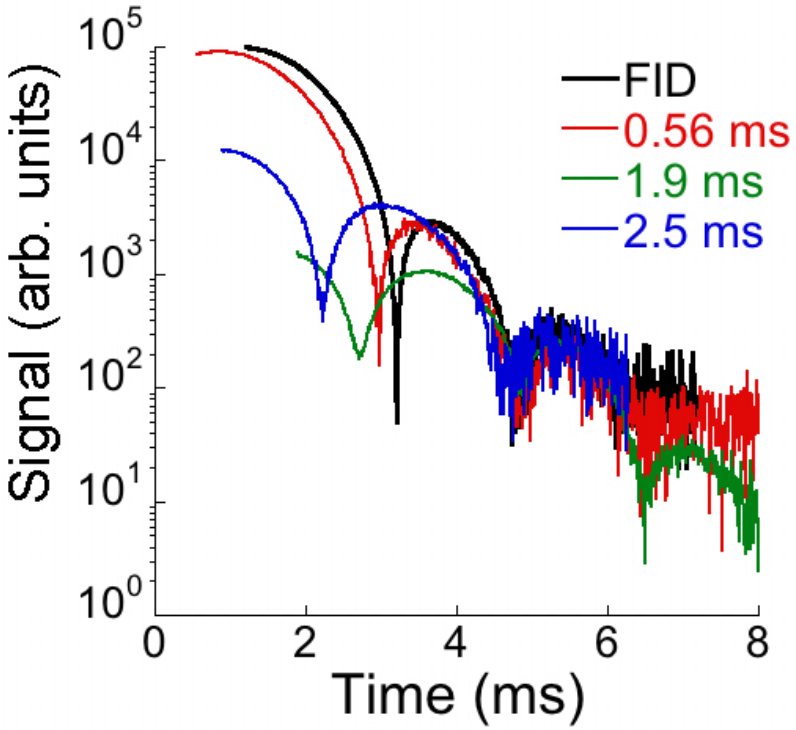

(b) The same data as in (a) are shown time-shifted to illustrate the convergence of the long-time behavior.

Figure 2.8: **^{129}Xe FID and solid echoes in** 54.7% **^{129}Xe (System III).**

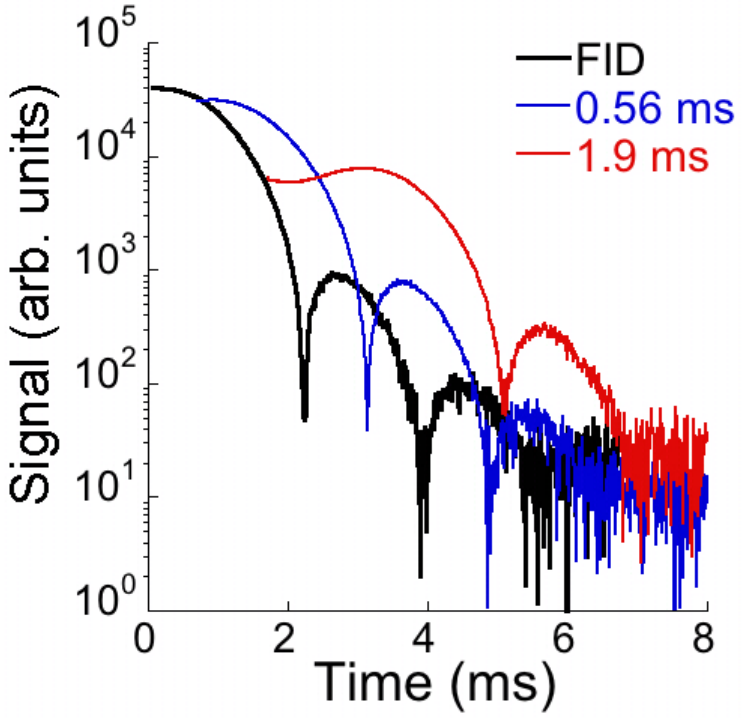

(a) Solid echo signals shown on a semilog plot with the FID.

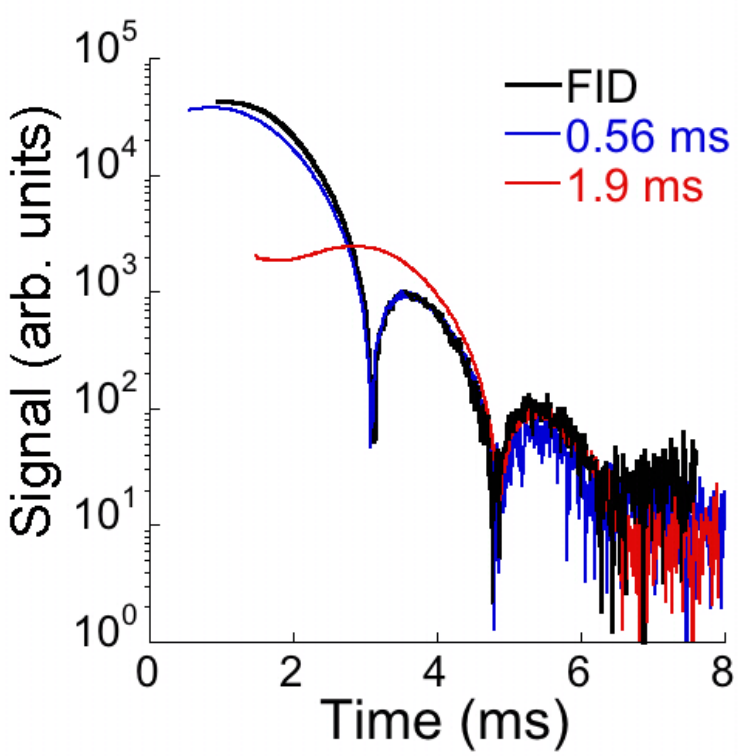

(b) The same data as in (a) are shown time-shifted to illustrate the convergence of the long-time behavior.

Figure 2.9: **^{129}Xe FID and solid echoes in** 46.5% **^{129}Xe (System IV).**

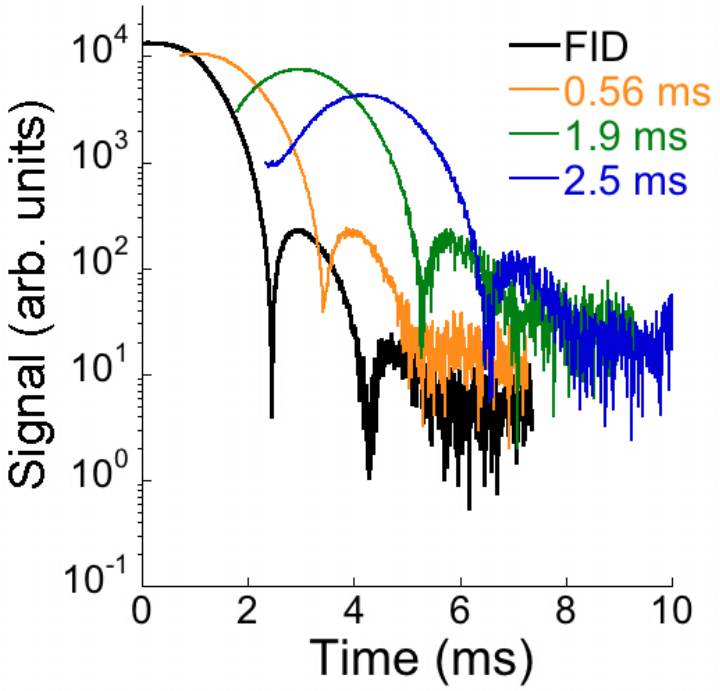

(a) Solid echo signals shown on a semilog plot with the FID.

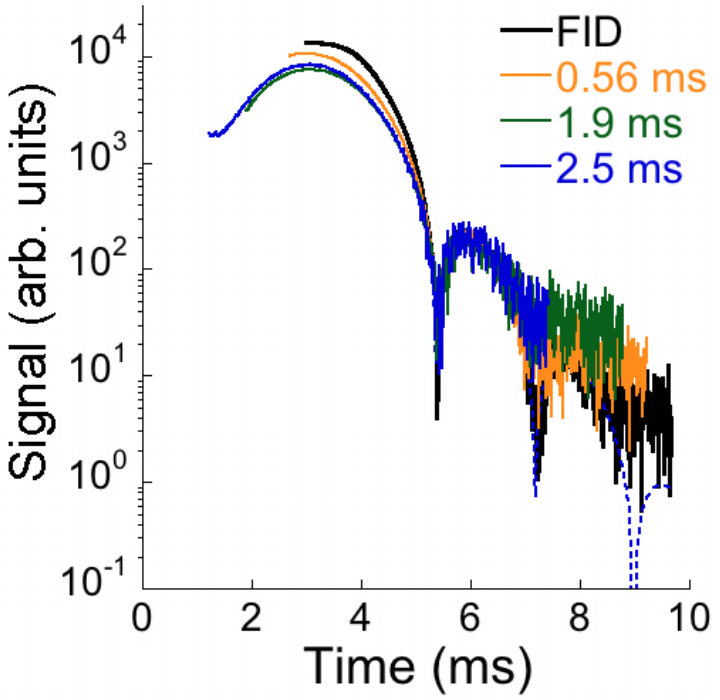

(b) The same data as in (a) are shown time-shifted to illustrate the convergence of the long-time behavior.

Figure 2.10: ^{129}**Xe FID and solid echoes in** 29.6% ^{129}**Xe (System V).**

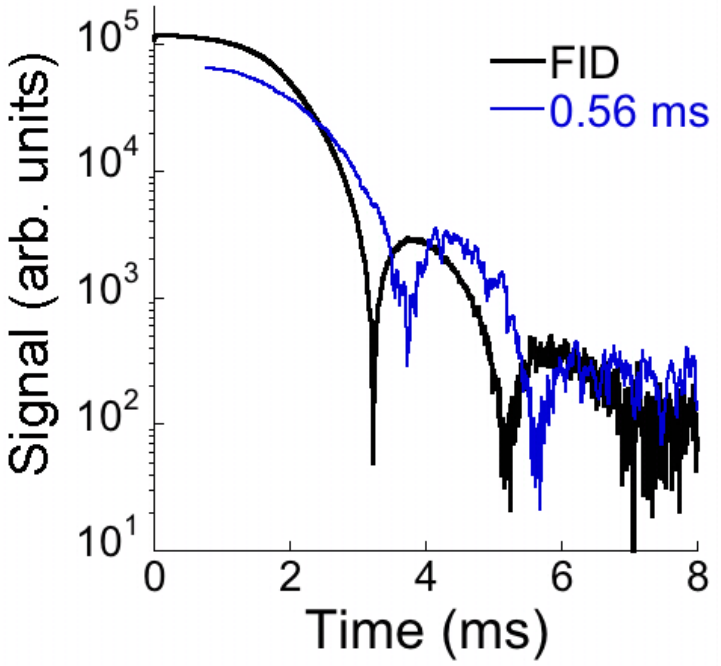

(a) Solid echo signal shown on a semilog plot with the FID.

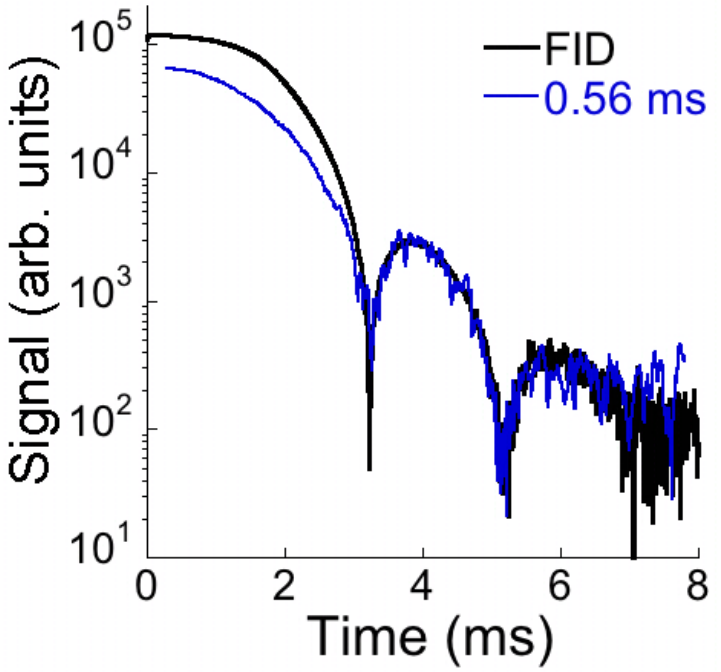

(b) The same data as in (a) are shown time-shifted to illustrate the convergence of the long-time behavior

Figure 2.11: **^{129}Xe FID and solid echoes in** 27.5% **^{129}Xe (System VI).**

Table 2.2: Values of the decay coefficient γ and beat frequency ω for each xenon isotopic composition tested in our experiments. The fourth column refers to the percentage of even (spin-zero) xenon isotopes.

System	$\%^{129}$Xe	$\%^{131}$Xe	$\%^{\text{even}}$Xe	γ (ms^{-1})	ω (rad/ms)
I	85.6	1.9	12.5	1.25 ± 0.04	2.06 ± 0.04
II	62.7	27.3	10.0	1.34 ± 0.34	1.95 ± 0.14
III	54.7	36.1	9.2	1.42 ± 0.19	1.96 ± 0.05
IV	46.5	45.2	8.3	1.24 ± 0.05	1.71 ± 0.10
V	29.6	64.0	6.4	1.50 ± 0.06	1.74 ± 0.05
VI	27.5	21.5	51.0	1.03 ± 0.10	1.53 ± 0.05

2.4.1.3 Jeener-Broekaert Echo

The Jeener-Broekaert (JB) echo ($90^\circ_x - \tau_1 - 45^\circ_y - \tau_2 - 45^\circ_{\bar{y}}$) partially transforms Zeeman order into dipolar order [84, 85]. The 45°_y pulse performs the partial transformation into dipolar order, which is a state similar to that produced by adiabatic demagnetization in the rotating frame. The $45^\circ_{\bar{y}}$ pulse partially transforms the dipolar order back into Zeeman order for signal observation.

Figure 2.12 shows the JB echo ($90^\circ_x - \tau_1 - 45^\circ_y - \tau_2 - 45^\circ_{\bar{y}}$) for System I, along with the corresponding FID from Fig. 2.4. The interpulse delays are $\tau_1 = 0.5$ ms and $\tau_2 = 3$ ms. Usually, τ_2 is much longer than T_2 in the JB echo sequence. In our experiments, $\tau_2 \approx 6 \times T_2$ – sufficiently long to generate a spin state distinct from that generated by the FID or solid echoes. While the initial portion of the JB echo is distinct from that of both the FID and the various solid echoes, its long-time behavior exhibits the form of Eq. (2.16) and with the same values of γ and ω (see Fig. 2.12).

2.4.1.4 Solid Echo Amplitudes

The xenon FID reaches the long-time regime after a time of $\approx$ 2.5 ms, as shown in Fig. 2.4. The echo with the longest value of τ and good SNR acquired was $\tau = 2.5$ ms. Echoes initiated with longer interpulse delay times did not have enough intensity to observe their long-time behavior with good SNR. Therefore Predictions II-IV, which are only asserted to apply to echoes generated *after* the FID has achieved its long-time behavior, cannot be strictly tested in this system. Nonetheless, I present the results of these predictions and include the data here as they show an interesting trend toward agreement with the predictions.

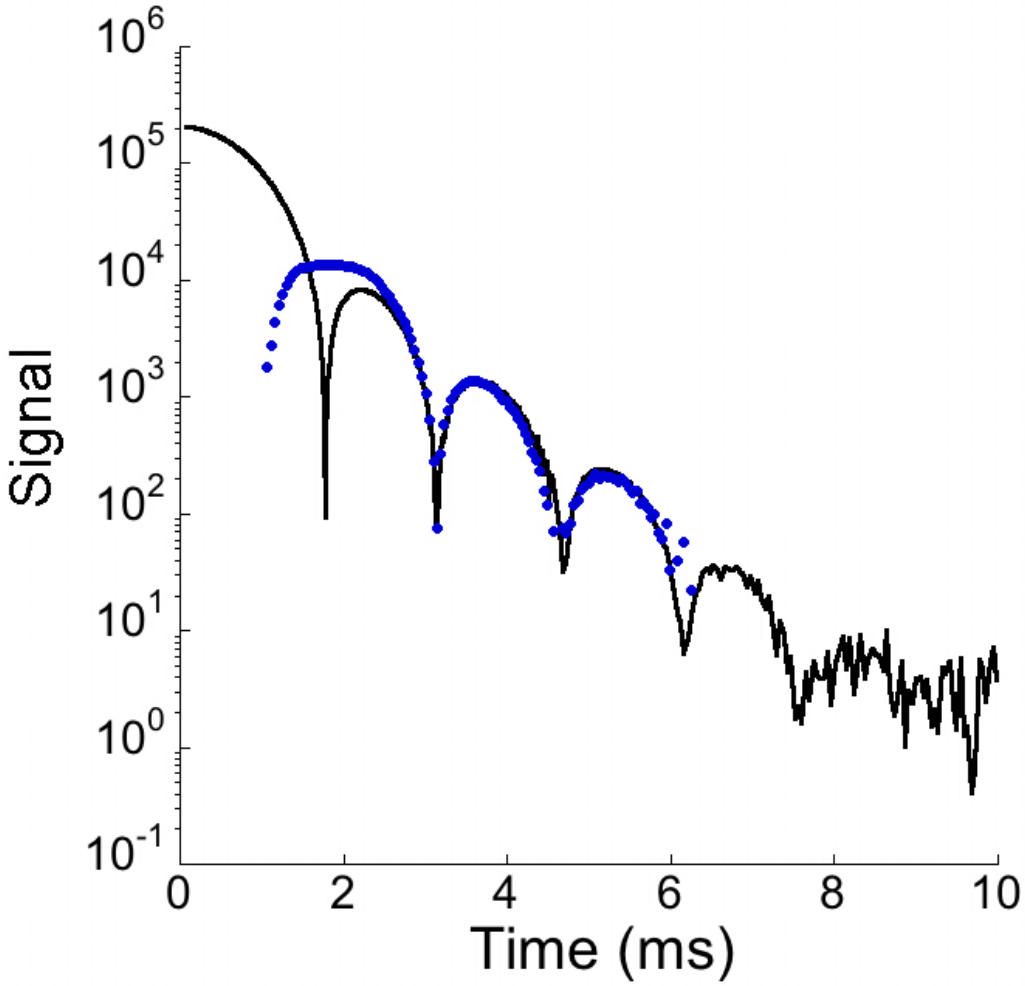

Figure 2.12: **^{129}Xe Jeener-Broekaert echo in solid xenon.** ^{129}Xe FID (solid black line) and Jeener-Broekaert echo (blue points) in solid xenon enriched to 85.6% ^{129}Xe (System I). The echo is scaled and time-shifted to show the similarity of its long-time behavior with that of the FID. The interpulse delays are $\tau_1 = 0.5$ ms and $\tau_2 = 3$ ms.

According to Prediction II, the square of the amplitudes of solid echoes generated in the long-time of the FID will have the form of Eq. (2.25). For the sake of the fitting procedure, Eq. (2.25) is reparameterized as

$$|C(\tau)|^2 = B_1 + D_1 \cos(2\omega\tau + \phi_1). \tag{2.33}$$

The values of the solid echo amplitudes (circles) are plotted along with the predicted dependence of Eq. (2.33) (solid line) as a function of the interpulse delay time τ in Fig. 2.13. Again, the latest echo ($\tau = 2.5$ ms) is barely in the long-time portion of the FID; yet, the final four echoes (shown as filled circles) are already beginning to converge to the predicted curve (shown in red). The predicted curve Eq. (2.33) is a fit to these final four data points, with the values of B_1, D_1, and ϕ_1 as free parameters. Note, however, that the frequency of the amplitude oscillation is fixed from the asymptotics of the FID and is not a free parameter in the fit. We admittedly have a three parameter fit to only four data points, but these data are presented for completeness in the light of the results we achieved in CaF_2 (to follow below). The values of the parameters extracted from the fit to Eq. (2.33) are presented in Table 2.3.

2.4.1.5 Solid Echo Phases

According to Prediction III, the amplitude $\times$ phase of the solid echoes generated in the long-time of the FID will have the form of Eq. (2.26). For the sake of the fitting procedure, Eq. (2.26) is reparameterized as

$$|C(\tau)| \cos[\phi_C(\tau)] = B_2 + D_2 \cos(2\omega\tau + \phi_2). \tag{2.34}$$

Table 2.3: Parameters of the solid echo fits for ^{129}Xefrom the theoretical curves (2.25) and (2.26) reparameterzied as (2.33) and (2.34), along with the values of the long-time constants obtained from the FID asymptotics.

Parameter	Value	Parameter	Value
B_1	78 ± 13	B_2	1.9 ± 0.1
D_1	77 ± 18	D_2	5.4 ± 0.2
ϕ_1	0.49 ± 0.09	ϕ_2	6.4 ± 0.1
$\lvert a \rvert$	152000 ± 1615	ϕ_a	$1.25 \pm .01$
γ (ms^{-1})	1.250 ± 0.004	ω (rad/ms)	2.10 ± 0.01

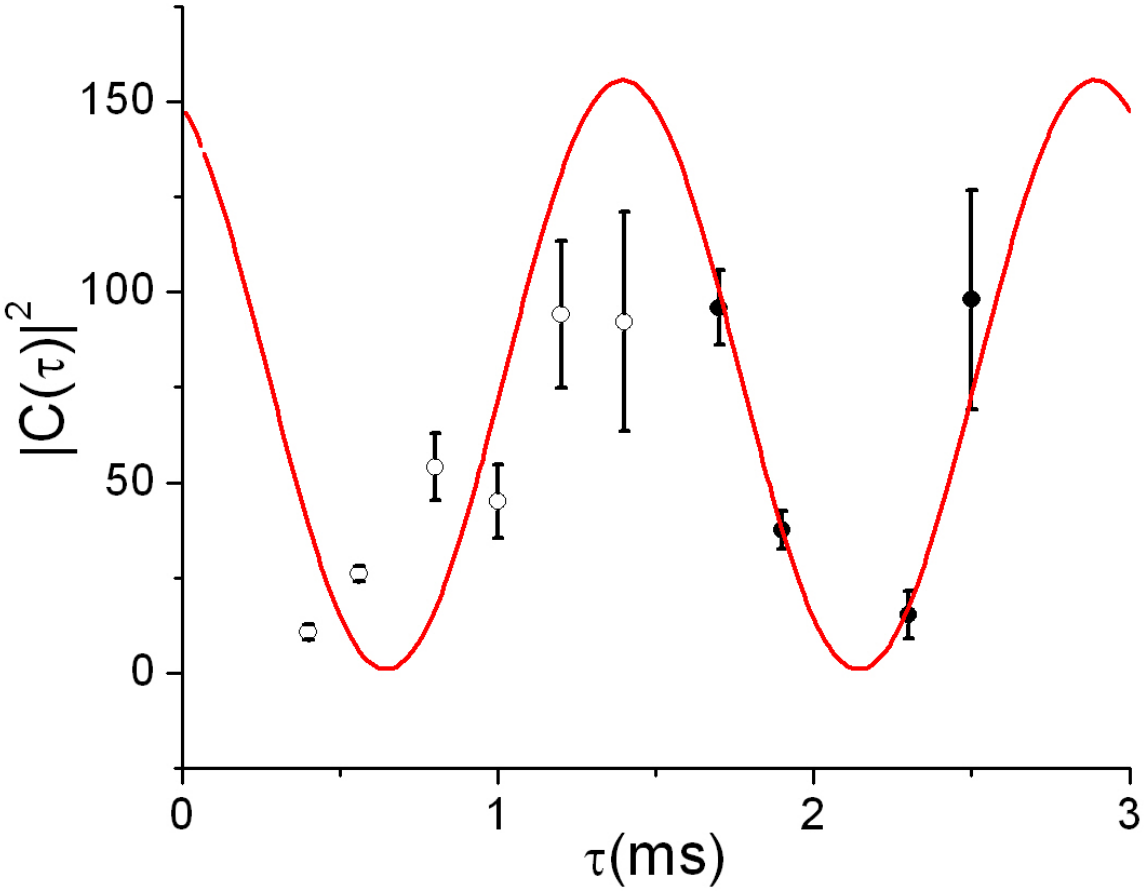

Figure 2.13: **Amplitudes of ^{129}Xe solid echo signals.** Data points represent the amplitudes of ^{129}Xe solid echoes in solid xenon as a function interpulse delay time τ. None of the echoes acquired were initiated in the long-time regime of the FID; for xenon, such regions are inaccessible with current polarization techniques. The data are nonetheless consistent with the theory for the latest echoes (shown as filled circles).

The values of the solid echo phases (circles) are then plotted along with the predicted dependence of Eq. (2.34) (solid line) as function of the interpulse delay time τ in Fig. 2.14. Again, only the latest echo is in the long-time portion of the FID; however, the final four echoes – shown as filled circles – follow the predicted curve shown in red. As with the echo amplitudes, the predicted curve (2.34) is a fit to these final four data points, with the values of B_2, D_2, and ϕ_2 as free parameters. The values of the free parameters extracted from the fit to Eq. (2.34) are also presented in Table 2.3.

Observation of the echo behavior in Figs. 2.13 and 2.14, *i.e.*, oscillations of a τ-dependent term around a τ-independent value with the frequency of 2ω, is already a nontrivial test

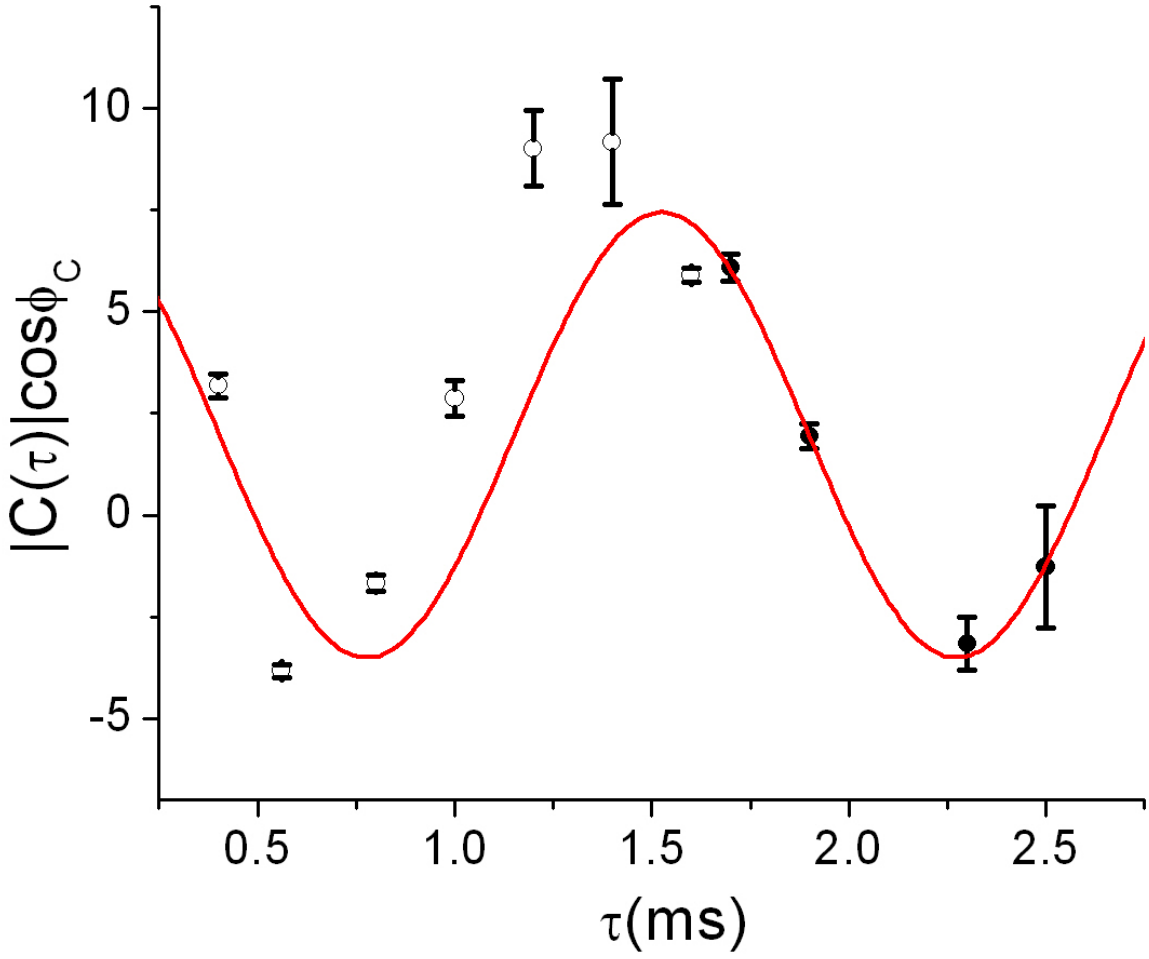

Figure 2.14: **Phases of ^{129}Xe solid echo signals.** Data points represent the phase $\times$ amplitude of ^{129}Xe solid echoes in solid xenon as a function interpulse delay time τ. None of the echoes acquired were initiated in the long-time regime of the FID; for xenon, such regions are inaccessible with current polarization techniques. The data are nonetheless consistent with the theory for the latest echoes (shown as filled circles).

of the chaos-based model. It remains, however, to map the reparameterized versions of Eqs. (2.25) and (2.26) back into their original forms to see if Prediction II and Prediction III hold for this system. The procedure, as laid out in [37], is as follows:

1) Obtain the parameters $|a|$, ϕ_a, γ, and ω from the asymptotics of the FID. This is done by fitting Eq. (2.16) to the long-time portion of the FID ($t > 2.5$ ms). The values of the constants are given in Table 2.3.

2) The values of $|C(\tau)|$ and $\phi_C(\tau)$ are obtained for each τ by fitting the tails of the echo responses with Eq. (2.23). These values are plotted in Figs. 2.13 and 2.14.

3) Obtain the parameters listed in Table 2.3 with the fitting procedures as described above. 4) Map the parameters of Eq. (2.33) and (2.34) back onto the physical quantities in Eqs. (2.25) and (2.26), and check whether the predicted values match the experiment.

For the final step, we find that $b_2 = D_2$, so $|b_1| = \sqrt{B_1 - |b_2|^2}$. Then Prediction II is that $D_1 = 2|b_1||b_2|$. Additionally, we obtain $\phi_{b_2} = -\phi_2 - \phi_a$, and then $\phi_{b_1} = -\phi_1 - 2\phi_a - \phi_{b_2}$. It then follows that Prediction III is $B_2 = |b_1| \cos(\phi_a + \phi_{b_1})$. We find for Prediction II that

$$\begin{aligned} D_1(calc) &= 75.9 \pm 13 \\ D_1(fit) &= 77 \pm 18, \end{aligned} \tag{2.35}$$

and for Prediction III that

$$\begin{aligned} B_2(calc) &= 5.6 \pm 3 \\ B_2(fit) &= 1.9 \pm 0.5, \end{aligned} \tag{2.36}$$

where the values marked ($calc$) are the calculated values using the formulae above, and the values marked (fit) are the comparing values obtained from the fits to Figs. 2.13 and 2.14. Though the errors are large for reasons discussed above, we nonetheless conclude based on (2.35) and (2.36) that the longest-time echoes in the solid ^{129}Xe System I are fairly consistent with the Predictions II and III of the chaos-based model.

2.4.1.6 Solid Echo Lineshapes

Prediction IV states any solid echo initiated in the long-time regime of the FID should have a shape which conforms to Eq. (2.22). As mentioned previously, echoes in the long-time regime of the FID with enough SNR to observe their long-time behavior were not accessible. Therefore, we were not able to attempt to verify Prediction IV in the ^{129}Xe systems.

2.4.2 CaF_2 Systems

Now we move to a different system where the predictions made by the chaos-based model can be tested. As explained in Sec. 2.3.4, ^{19}F in CaF_2 provides an even better test case for the evaluation of the model's predictions given its large magnetic moment, consequent good

thermal polarizations, and short T_1 relaxation times allowing for averaging. In single-crystal CaF_2, different orientations of the applied magnetic field H_0 with respect to the crystal planes imply different interaction coefficients in the interaction Hamiltonian $\mathcal{H}$ [Eq. (2.27)]. Hence, experiments performed with each orientation of H_0 amount to independent checks of the validity of the long-time equation Eq. (2.16).

2.4.2.1 Free Induction Decay

In Fig. 2.15 we show a typical ^{19}F FID at 2 T and 290 K. As with xenon, a semilog plot is used and the cusps indicate zero-crossings. The beat frequencies in each crystal orientation were first measured by Lowe and Norberg [31], and then more accurately by Engelsberg and Lowe [1]. The beat frequency ω measured by us for each orientation of H_0 is compared to that obtained by Engelsberg and Lowe [1] in Table 2.4. The small discrepancies between these values and those obtained by Engelsberg and Lowe are due to slight misalignments of the samples in our experiment — we did not need as exact a precision in our alignments as did Engelsberg *et al.* We plot our FIDs along with the time-domain signals obtained by Engelsberg and Lowe obtained from Ref. [1] in the following section.

2.4.2.2 Solid Echo Universal Behavior

Solid echo data for single-crystal CaF_2 are shown in Figs. 2.16 - 2.25. As with the xenon data, the explicit time shifts to the data show that the long-time behavior is universal according to Eq. (2.16) for ^{19}F in a single-crystal sample of CaF_2. We therefore find Prediction I is also consistent with the experimental data obtained on these three single crystals.

Table 2.4: Values of the decay coefficient γ and beat frequency ω for each CaF_2 system tested. Columns 4 and 5 are experimental data for the decays obtained in this work. The last column lists the values of ω calculated from the data obtained by Engelsberg and Lowe (taken from Ref. [1]) for purposes of comparison. The impurities for the powder sample (System X) are as follows: 0.9% Cl, 0.5% SO_4, 0.3% heavy metals (such as Pb), 0.3% Fe.

System	Direction	Impurtiy	γ (ms^{-1})	ω (rad/ms)	ω_{EL} (rad/ms)
VII	[100]	0.01 % Gd	51.0 ± 0.1	144.4 ± 0.1	153.32 ± 0.09
VIII	[110]	0.01 % Y	43.3 ± 0.1	106.2 ± 0.1	101.9 ± 0.7
IX	[111]	0.01 % Gd	31.9 ± 0.1	66.2 ± 0.1	65.6 ± 0.3
X	powder	2%	n/a	n/a	n/a

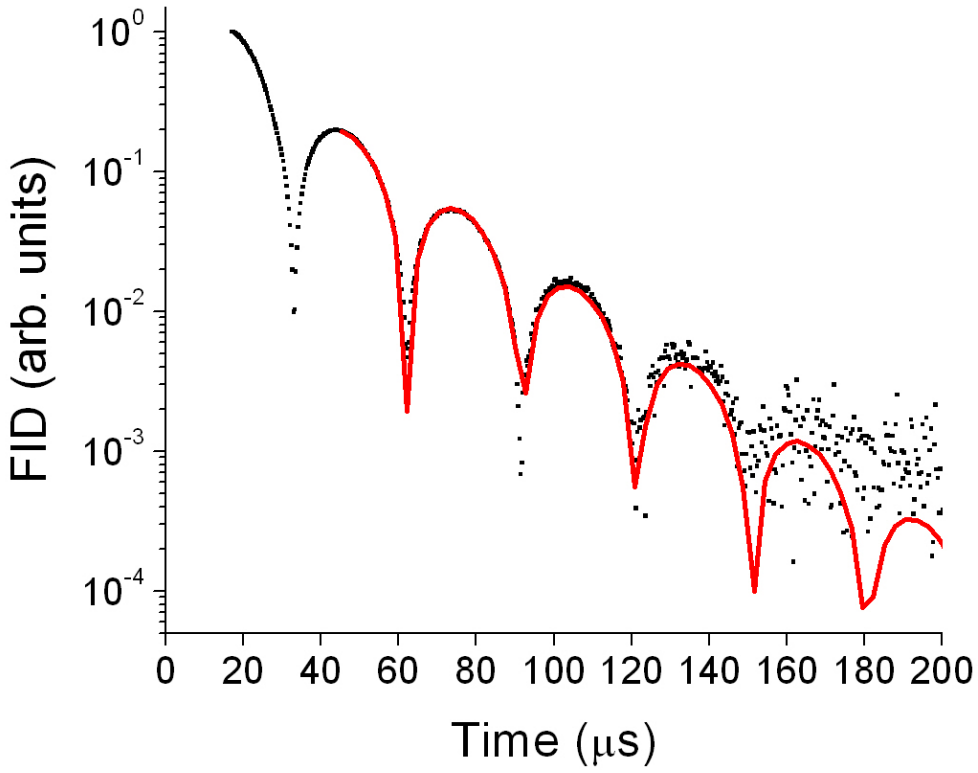

Figure 2.15: **^{19}F FID in [100] single crystal CaF_2.** Normalized ^{19}F FID in CaF_2 corresponding to the applied field $\mathbf{H}_0$ along the [110] direction (System VIII; see Table 2.4). The solid line is a fit of the absolute value of Eq. (2.16) to the long-time signal at $t > 45$ μs. T_2 is approx 25 μs in this system.

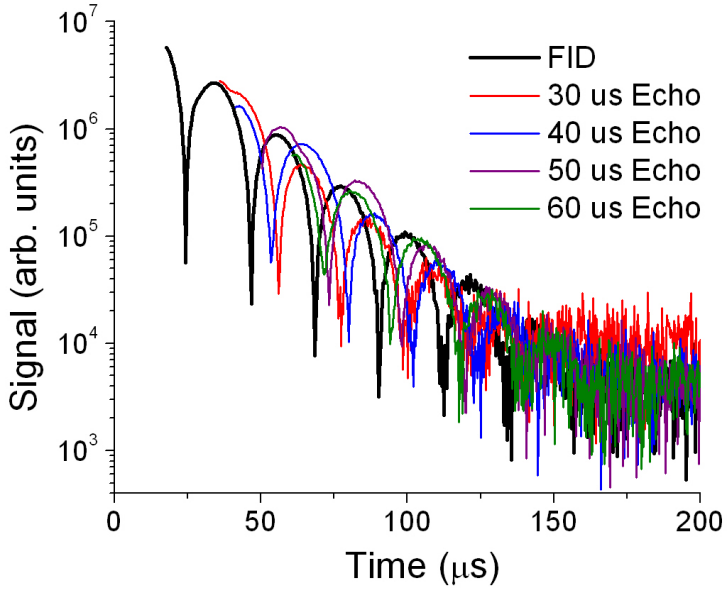

Figure 2.16: **^{19}F FID and solid echoes in [100] single-crystal CaF_2 (System VII)**; see Table 2.4. Solid echo signals shown on a semilog plot with the FID.

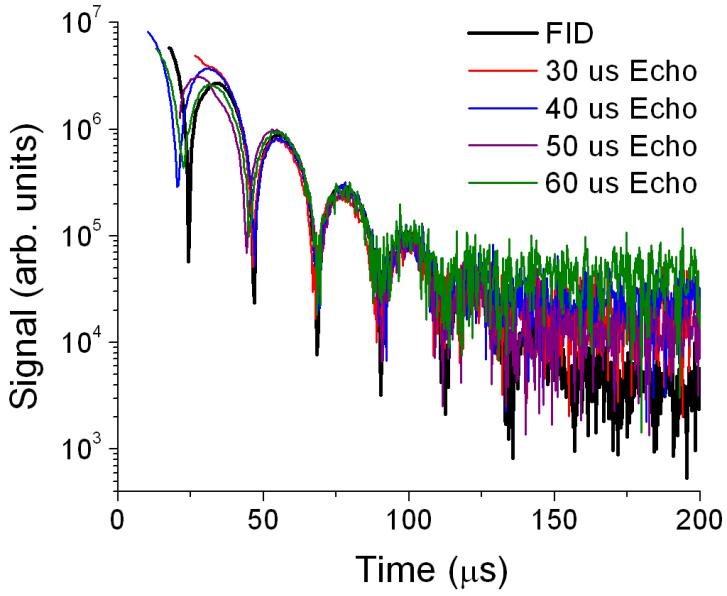

Figure 2.17: **^{19}F FID and solid echoes in [100] single-crystal CaF_2 (System VII)**; see Table 2.4. The same data as Fig. 2.16 are shown again with the echoes time-shifted to illustrate the convergence of the long-time behavior.

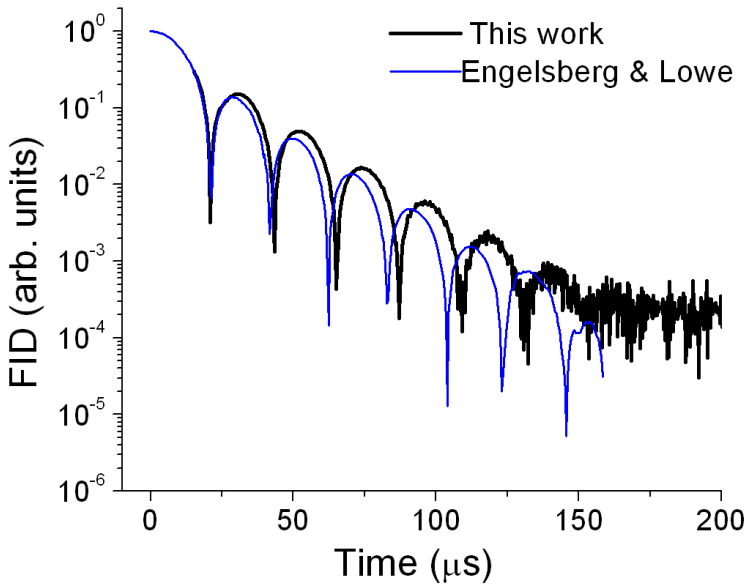

Figure 2.18: **^{19}F FID in [100] CaF_2 comparison with data of Ref. [1].** ^{19}F FID obtained in this work, plotted with that obtained in Ref. [1]. Discrepancies in the beat frequency can be attributed to slight differences in crystal alignment.

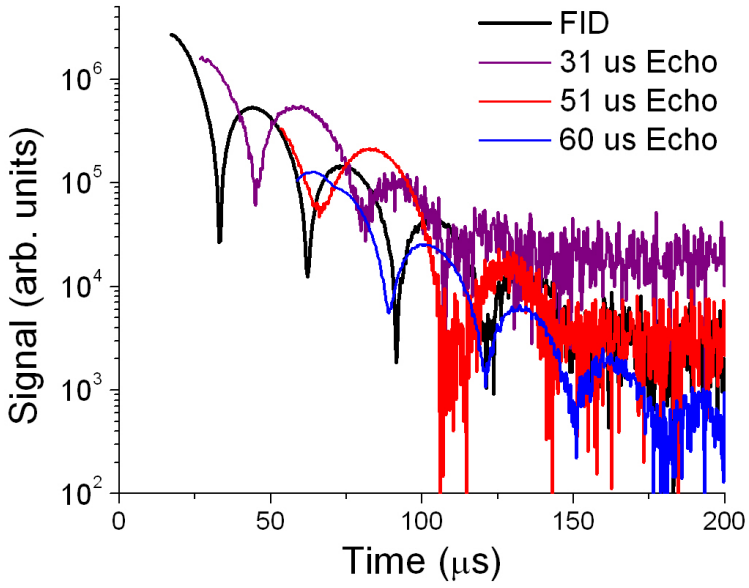

Figure 2.19: **^{19}F FID and solid echoes in [110] single-crystal CaF_2 (System VIII)**; see Table 2.4. Solid echo signals shown on a semilog plot with the FID.

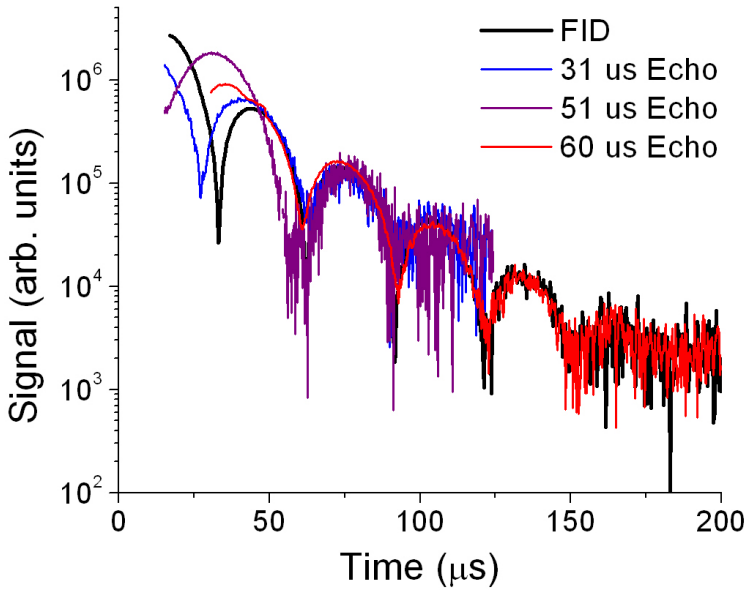

Figure 2.20: **^{19}F FID and solid echoes in [110] single-crystal CaF_2 (System VIII)**; see Table 2.4. The same data as in Fig. 2.19 are shown again with the echoes time-shifted to illustrate the convergence of the long-time behavior.

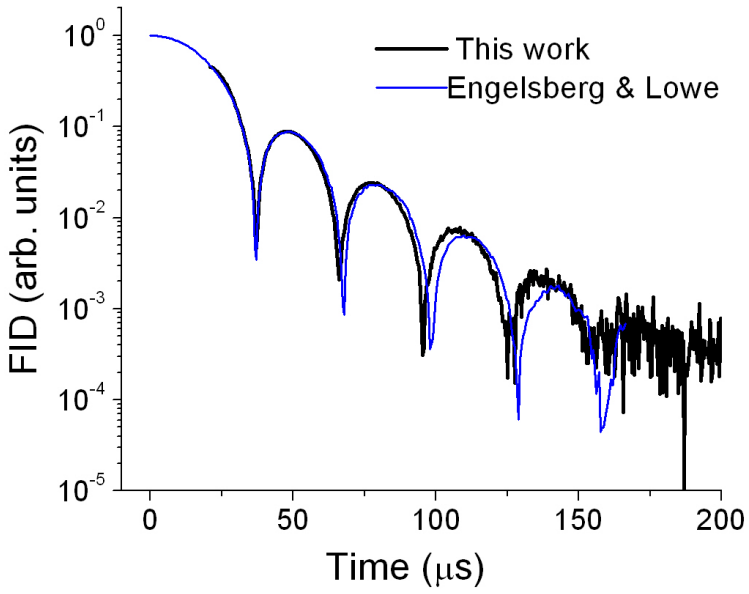

Figure 2.21: **^{19}F FID in [110] CaF_2 comparison with data of Ref. [1].** ^{19}F FID obtained in this work, plotted with that obtained in Ref. [1]. Discrepancies in the beat frequency can be attributed to slight differences in crystal alignment.

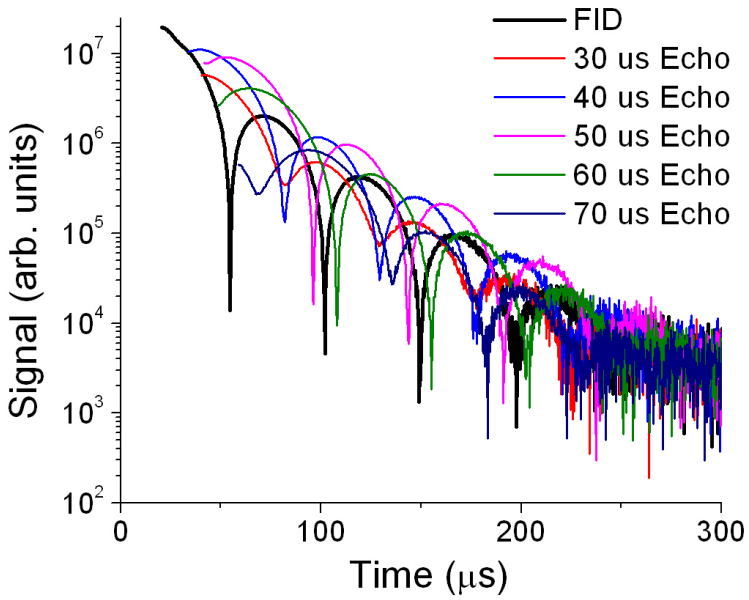

Figure 2.22: **Early ^{19}F solid echoes and FID in [111] single-crystal CaF_2 (System IX)**. External field along [111]; see Table 2.4. Solid echo signals shown on a semilog plot with the FID.

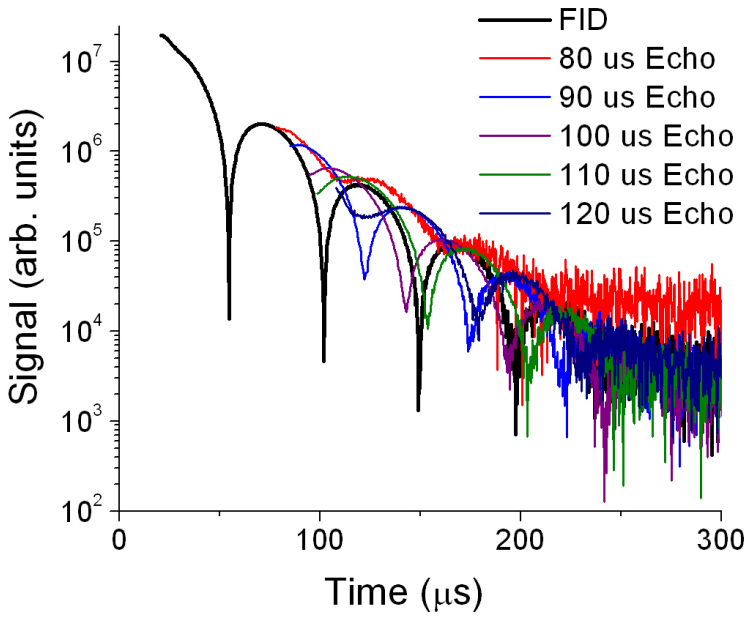

Figure 2.23: **Late ^{19}F solid echoes and FID in [111] single-crystal CaF_2 (System IX)**. External field along [111]; see Table 2.4. Solid echo signals shown on a semilog plot with the FID.

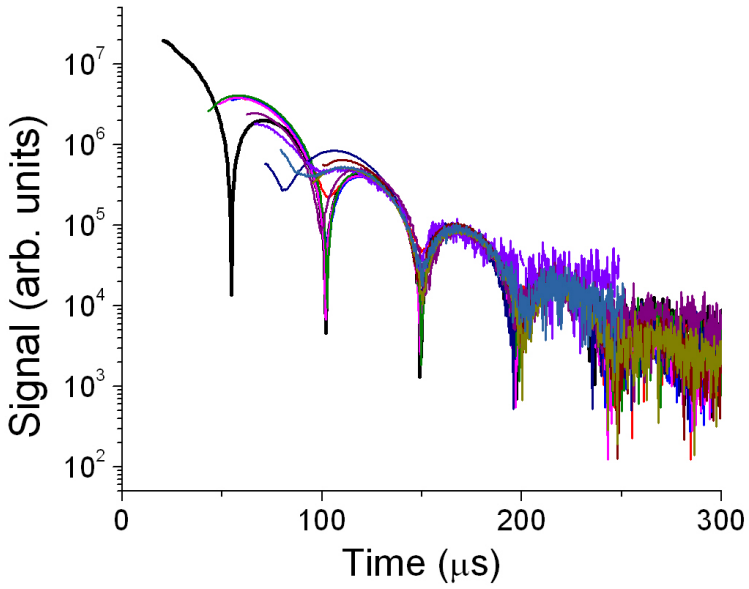

Figure 2.24: ^{19}**F solid echoes and FID in [111] single-crystal CaF$_2$ (System IX)**; see Table 2.4. The same data as in Figs. 2.22 and 2.23 are shown again time-shifted to illustrate the convergence of the long-time behavior.

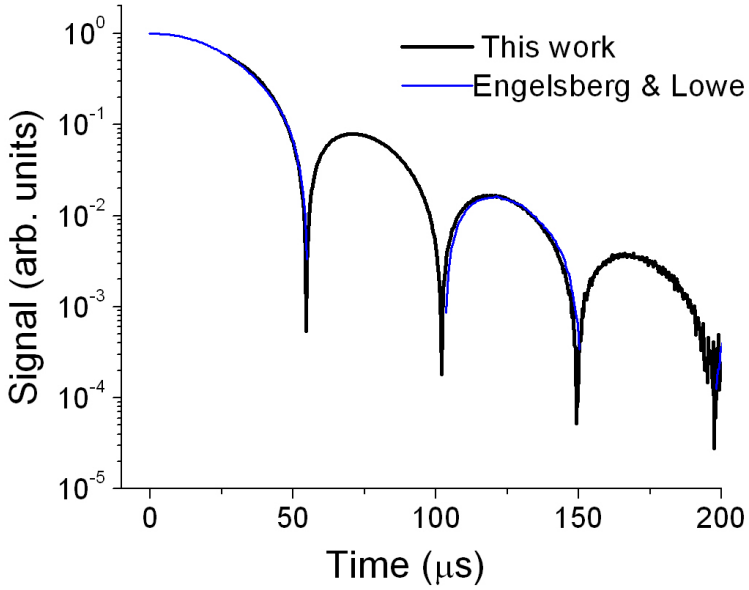

Figure 2.25: ^{19}**F FID in [111] CaF$_2$ comparison with data of Ref. [1]**. Discrepancies in the beat frequency can be attributed to slight differences in crystal alignment.

2.4.2.3 Magic Echoes

To contrast our use of the solid echo and JB echo to generate distinct initial transverse spin configurations that then evolve to a universal long-time behavior, we used the magic echo [86] ($90^\circ_y - \tau - 90^\circ_{\bar{y}} - \tau'_{H1} - \tau'_{\bar{H}1} - 90^\circ_y$) in [111] single-crystal CaF_2 as a form of control experiment to show that it is possible in these systems to reverse the sign of the Hamiltonian and reproduce the *entire* FID. The resulting signal from the magic echo sequence shown in Fig. 2.26 is indeed found to have nearly the same shape as the FID generated from a single 90° pulse, notably even in the early portion of the FID decay. For our experiment, $\tau = 11$ μs and $\tau'_{H_1} = \tau'_{\bar{H}_1} = 180$ μs. The left-hand side of the magic echo near the time origin is not perfectly symmetric with the signal at $t > 200\mu$s due to residual effects of the strong rf excitation pulse. It is important to note that the FID and magic echo intensities have been scaled to illustrate the similarity in the shape; the actual intensity of the magic echo is a factor of 5 lower than that of the FID. However, as expected [23], the full dipolar refocusing (and therefore the maximum of the magic echo signal) occurs at a time $t = \tau'_{H_1} - \tau$.

The suppression of the magic echo intensity is qualitatively similar to the polarization echo experiments done by Pastawski *et al.* [97, 98]. We are currently in the process of investigating this suppression in more detail. As an example, we show in Fig. 2.27 the larger and larger suppression of the magic echoes that occurs as τ' is lengthened, indicating poorer and poorer ability to refocus the transverse decays. One should notice that, although the FID looks to have a smaller intensity than the echoes in Fig. 2.27, this is simply an illusion caused by the ≈ 15 μs receiver dead-time. During this time, we cannot acquire signal. Indeed, this was the original intent for the development of the magic echo — the desire to acquire signals prior to the inevitably finite receiver recovery time. A more accurate comparison of the relative intensities is to compare the height of the first beat in the FID and the individual echoes.

2.4.2.4 Solid Echo Amplitudes

T_2 in the CaF_2 crystals is $\approx$ 25 μs. The long-time behavior is therefore expected to dominate after about $60-70$ μs (several times T_2). In contrast to the ^{129}Xe systems studied above, the solid echoes ^{19}F in CaF_2 are much less complicated to acquire, and many echoes were measured that were initiated well into the long-time of the FID decay. This is largely due to the ability to measure the signals at room temperature, and to the short T_1 values that allowed for signal averaging for long periods of time to improve the SNR. The CaF_2

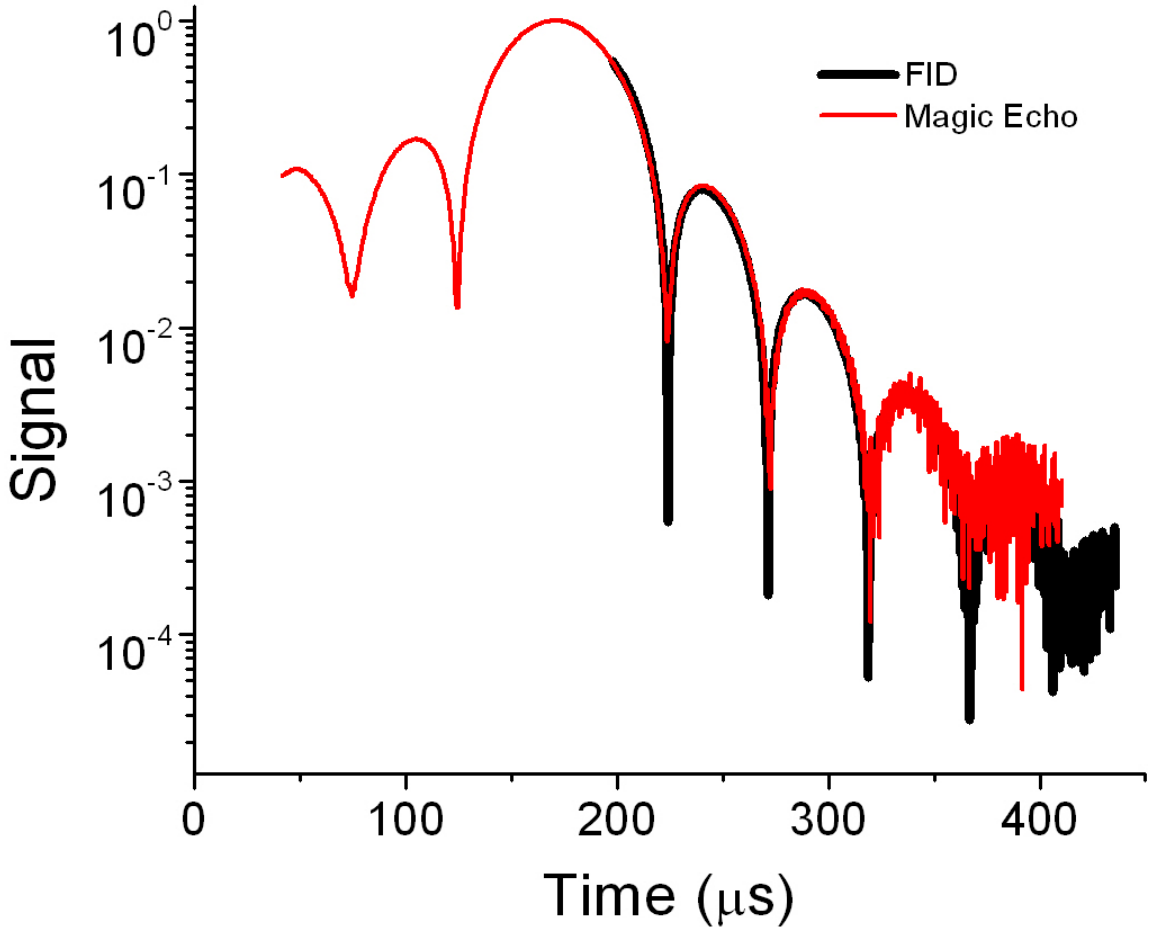

Figure 2.26: **^{19}F FID and magic echo in [111] single-crystal CaF_2** (System IX; see Table 2.4). Black line shows the FID, while the red line maps out the signal obtained following the magic echo pulse sequence. The time origin corresponds to the end of the final pulse in the magic echo sequence. The magic echo signal begins after a 50μs receiver recovery time. The FID has been time-shifted to lie over the portion of the magic echo that reproduces the FID. Note that the decays are indistinguishable even in the early (nonuniversal) portion of the FID signal.

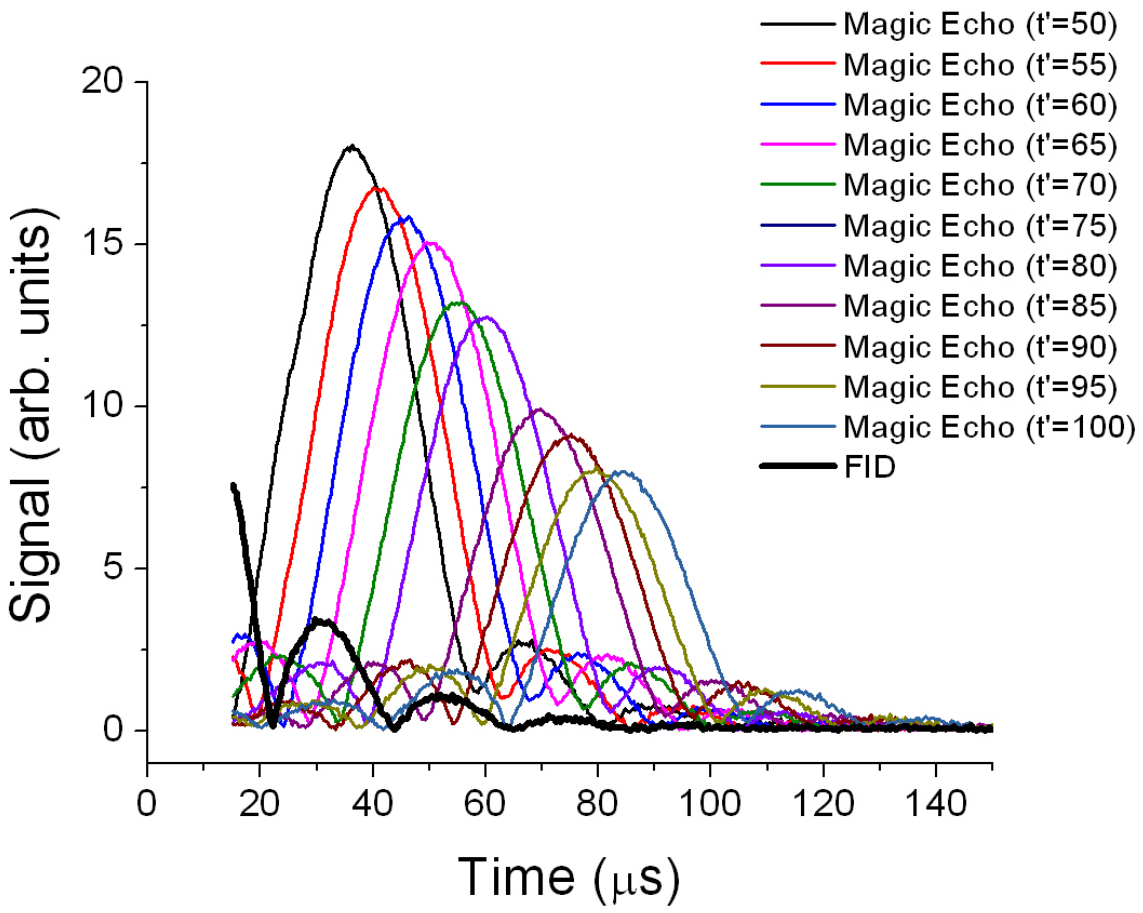

Figure 2.27: **Multiple ^{19}F magic echoes in [111] single-crystal CaF_2.** Heavy black line shows the FID, and various echoes are shown in color. Note that while the FID looks to have a smaller intensity than the echoes, this is an illusion based on the inability to acquire the first 15μs of the FID decay, wherein the FID would been seen to have a much larger intensity.

crystals therefore provide a much better test system for Predictions II-IV than do the ^{129}Xe.

According to Prediction II, the square of the amplitudes of solid echoes generated in the long-time portion of the FID will have the form of Eq. (2.25). For the sake of the fitting procedure, Eq. (2.25) is reparameterized as

$$|C(\tau)|^2 = B_1 + D_1 \cos(2\omega\tau + \phi_1). \qquad \text{(Same as Eq. (2.33))}$$

The values for the amplitudes and phases of the solid echoes were obtained as shown in Fig. 2.28. The experimentally obtained echo is plotted (hollow and solid points), and a fit

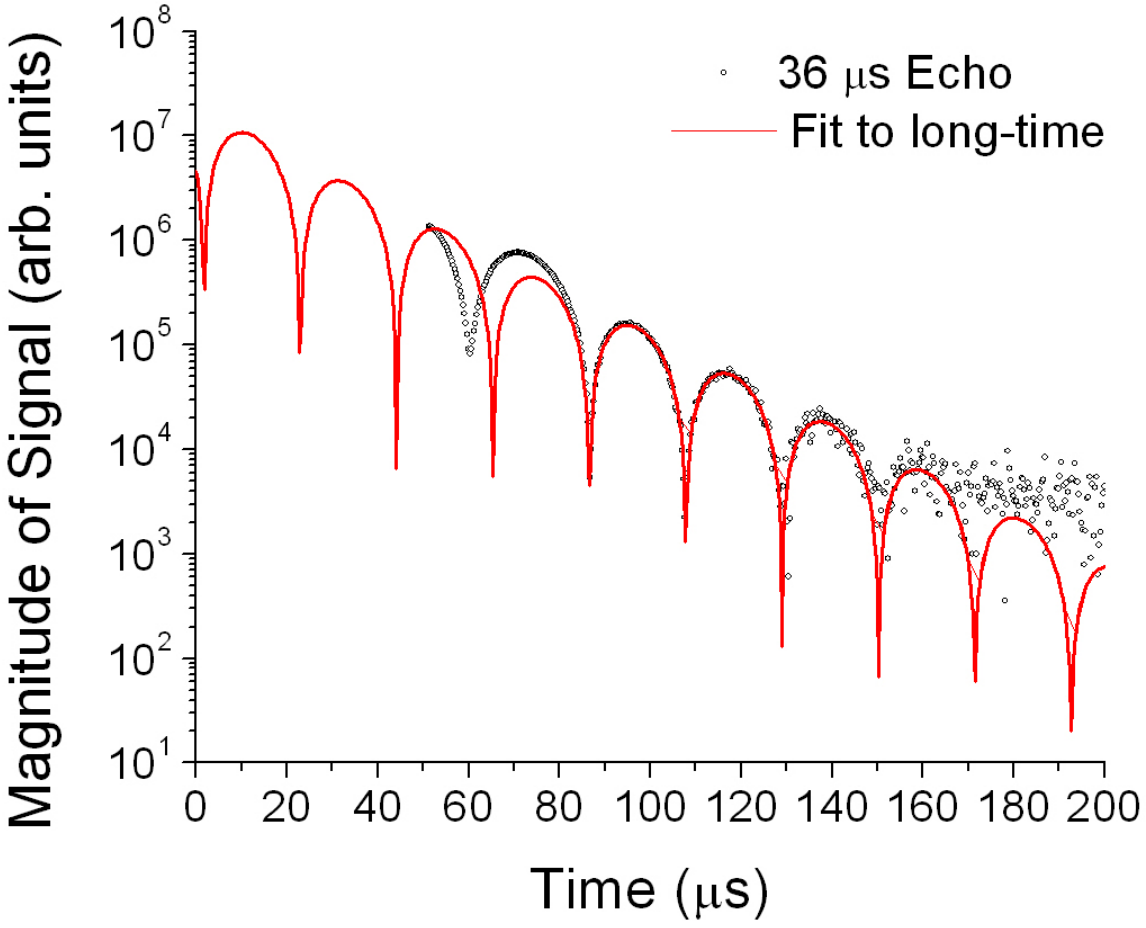

Figure 2.28: **Solid echo with $\tau = 36\mu$s on ^{19}F in [100] CaF_2**, along with fit to Eq. (2.16) made to the long-time portion of the echo. The amplitudes $|C(\tau)|$ and phases $\phi_C(\tau)$ for each echo are extracted from these fits for use in Figs. 2.29 and 2.30.

to Eq. (2.16) is made to the long-time portion of the echo that has reached the universal behavior. The amplitudes $|C(\tau)|$ and phases $\phi_C(\tau)$ are extracted from this and the similar plots for the other solid echoes.

In Fig. 2.29 we plot the values of the solid echo amplitudes (circles) along with the predicted dependence of Eq. (2.33) (solid line) as a function of the interpulse delay time τ. The hollow points show echoes that have not yet reached the predicted behavior, while the solid points show the long-time echoes. The predicted curve (2.33) is a fit to these solid data points, with the values of B_1, D_1, and ϕ_1 as free parameters. As these fits include many more data points than the ^{129}Xe, they provide a much more conclusive demonstration of the predicted amplitude behavior. The values of the free parameters extracted from the

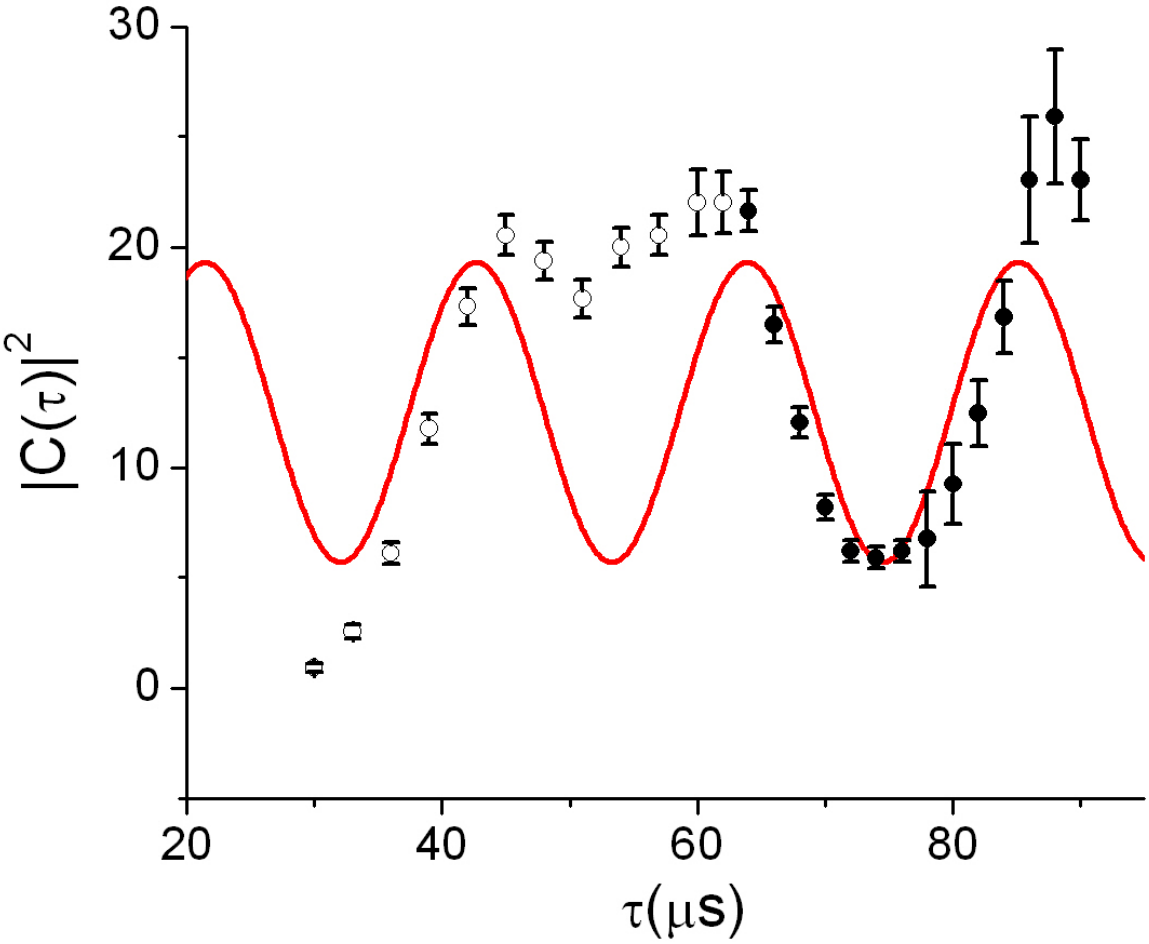

Figure 2.29: **Amplitudes of ^{19}F solid echo signals.** Data points represent the amplitudes of the ^{19}F solid echoes in CaF_2 as a function of the interpulse delay time τ. Open circles represent echoes in the early-time of the evolution of the FID, while solid circles represent echoes in the long-time portion of the FID evolution. The solid line (red) is the best fit of the long-time data to Eq. (2.33).

fit to Eq. (2.33) are presented in Table 2.5.

2.4.2.5 Solid Echo Phases

According to Prediction III, the amplitude × phase of the solid echoes generated in the long-time of the FID will have the form of Eq. (2.26). As for the xenon, Eq. (2.26) is reparameterized as

$$|C(\tau)|\cos\left[\phi_C(\tau)\right] = B_2 + D_2\cos\left(2\omega\tau + \phi_2\right). \qquad \text{(Same as Eq. 2.34)}$$

The values of the solid echo phases (circles) are then plotted along with the predicted dependence of Eq. (2.34) (solid line) as function of the interpulse delay time τ in Fig. 2.30. The hollow circles show the early-time echoes, while the solid circles show the echoes in the long-time regime. As with the echo amplitudes, the predicted curve (2.34) is a fit to the solid data points, with the values of B_2, D_2, and ϕ_2 as free parameters. The values of the free parameters extracted from the fit to Eq. (2.34) are also presented in Table 2.5.

Observation of the echo behavior in Figs. 2.29 and 2.30, *i.e.*, oscillations of a τ-dependent term around a τ-independent value with the frequency of 2ω, is yet again a nontrivial test of the chaos-based model. It remains once again to map the reparameterized versions of Eqs. (2.25) and (2.26) back into their original forms to see if Prediction II and Prediction III hold for this system. Following the same procedure as in Sec. 2.4.1.5, we find the following comparison

Table 2.5: Parameters of the CaF_2 fits to the theoretical curves (2.25) and (2.26) reparameterized as (2.33) and (2.34) along with the values of the long-time constants obtained from the FID asymptotics.

Parameter	Value	Parameter	Value
B_1	12.5 ± 0.8	B_2	0.73 ± 0.3
D_1	6.75 ± 0.9	D_2	3.4 ± 0.4
ϕ_1	0.07 ± 0.2	ϕ_2	5.97 ± 0.14
$\lvert a\rvert$	15,214,800	ϕ_a	1.39 ± 0.01
γ (μs^{-1})	0.050 ± 0.0002	ω (rad/μs)	0.148 ± 0.0001

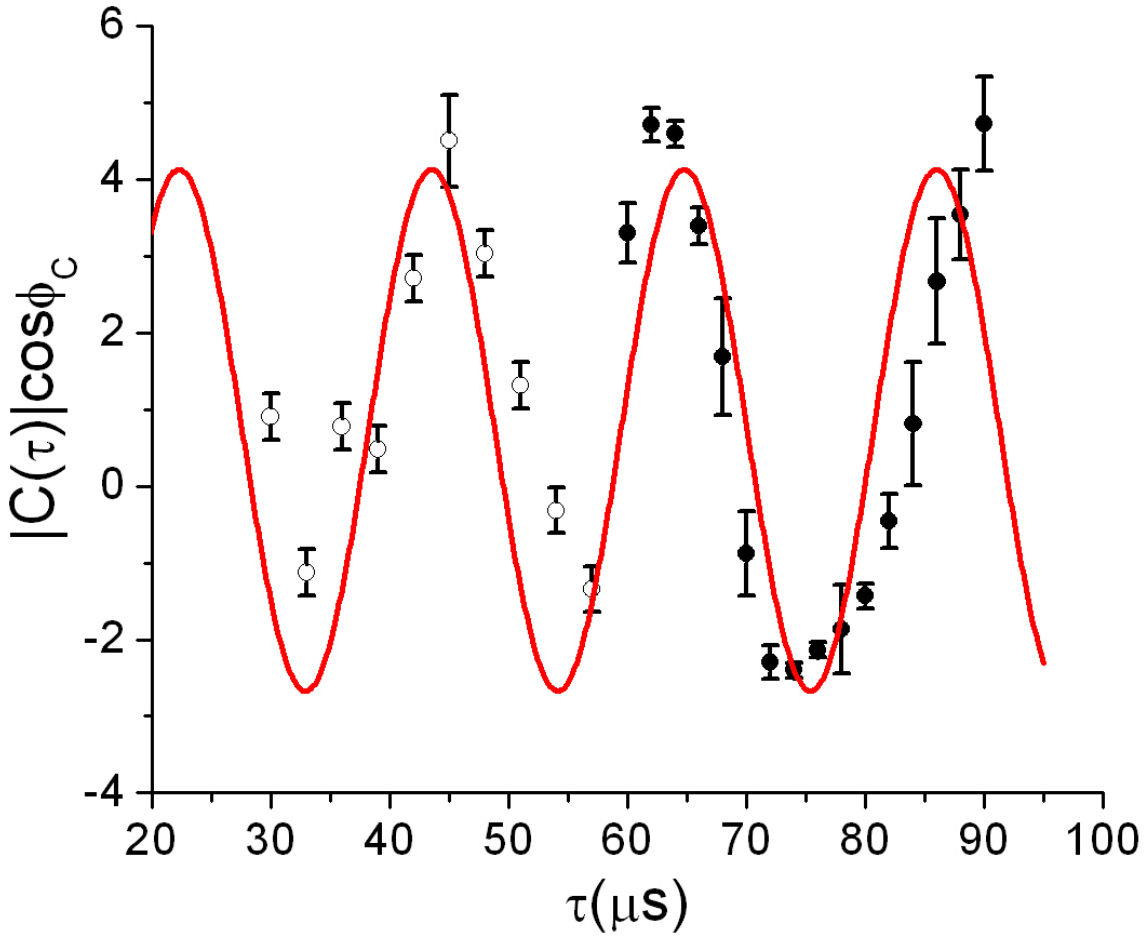

Figure 2.30: **Phases of ^{19}F solid echo signals.** Data points represent the amplitude $\times$ phase of ^{19}F solid echoes in CaF_2 as a function of the interpulse delay time τ. Open circles represent early-time echoes, and solid circles represent long-time echoes. The solid line (red) is the best fit of the long-time echoes to Eq. (2.33).

$$\begin{aligned} D_1(calc) &= 6.6 \pm 1 \\ D_1(fit) &= 6.75 \pm 0.09 \end{aligned} \tag{2.37}$$

and for Prediction III that

$$\begin{aligned} B_2(calc) &= 0.9 \pm 1 \\ B_2(fit) &= 0.73 \pm .01 \end{aligned} \tag{2.38}$$

where the values marked $(calc)$ are the calculated values, and the values marked (fit) are the comparing values obtained from the fits to Figs. 2.29 and 2.30. We conclude based on (2.37) and (2.38) that the long-time echoes in the CaF_2 System are also consistent with the Predictions II and III of the chaos-based model.

2.4.2.6 Solid Echo Lineshapes

Prediction IV states that any solid echo initiated in the long-time regime of the FID should have a shape which conforms to Eq. (2.22), which is reproduced here for convenience

$$\tilde{F}(\tau,t) = |a|e^{-\gamma\tau}\left[\cos(\omega\tau-\phi_a)\Re\tilde{f}(t-\tau) + \sin(\omega\tau-\phi_a)\Im\tilde{f}(t-\tau)\right]. \tag{Same as Eq. (2.22))}$$

All parameters in Eq. (2.22) are determined from the asymptotics of the FID with the exception of the functions $\Re\tilde{f}(t-\tau)$ and $\Im\tilde{f}(t-\tau)$. We can experimentally measure $\Im\tilde{f}(t-\tau)$ by choosing τ such that it occurs at a node of the FID where $\cos(\omega\tau-\phi_a) = 0$ and measure $\Re\tilde{f}(t-\tau)$ by choosing τ to occur during a maximum of the FID beating where $\sin(\omega\tau-\phi_a) = 0$. Once we have obtained these two functions, Prediction IV states that Eq. (2.22) will then be the shape of a solid echo of any chosen value of τ.

CaF_2 is an ideal system to test Prediction IV. In this system, 28 solid echoes shapes are acquired in [100] single-crystal CaF_2, 16 of which are in the long-time portion of the FID. Fig. 2.31 shows the echoes acquired, with the initial point of each echo emphasized by a circle for visual clarity.

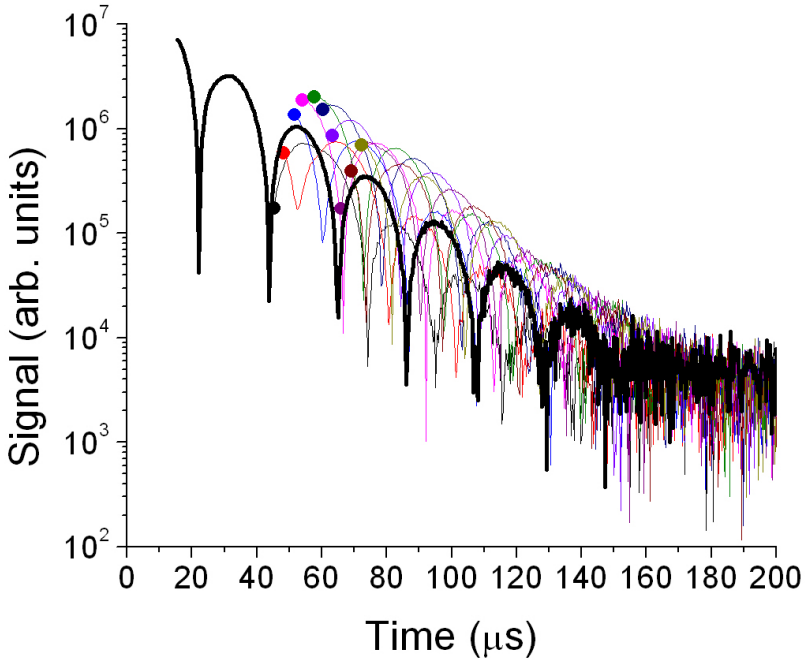

(a)

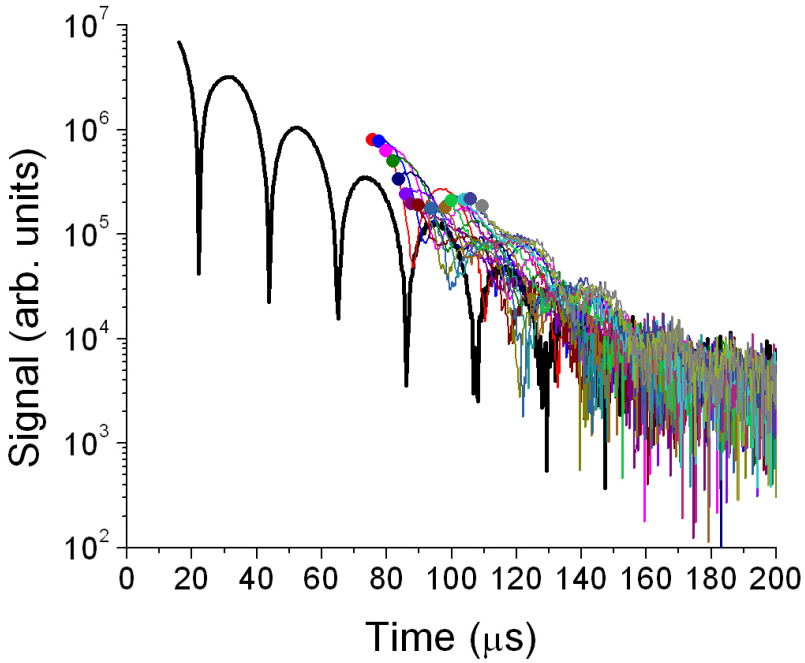

(b)

Figure 2.31: **^{19}F solid echoes in [100] single-crystal CaF_2.** (a) Early-time echoes: one echo every 3 μs from 30 μs $\leq \tau \leq$ 57 μs, and the FID (solid black line). (b) Long-time echoes: one echo every 2 μs from 60 μs $\leq \tau \leq$ 94 μs, and the FID (solid black line).

To solve Eq. (2.22), we choose echoes $\tilde{F}(\tau_1 = 76\ \mu s, t)$ and $\tilde{F}(\tau_2 = 86\ \mu s, t)$, corresponding roughly to a node and a maximum of the FID. In each echo, the zero of time is redefined as the origin of the echo pulse, *i.e.* the time argument of $\tilde{F}(\tau_1, t)$ is shifted by $\tau_1 = 76\ \mu$s ($t' = t - \tau_1$), while the time argument of $\tilde{F}(\tau_2, t)$ is shifted by $\tau_2 = 86\ \mu$s ($t' = t - \tau_2$). Eq. (2.22) is then solved as a system of linear equations

$$\begin{aligned}\tilde{F}(\tau_1, t' + \tau_1) &= A_1 \Re\tilde{f}(t') + B_1 \Im\tilde{f}(t') \\ \tilde{F}(\tau_2, t' + \tau_2) &= A_2 \Re\tilde{f}(t') + B_2 \Im\tilde{f}(t')\end{aligned} \tag{2.39}$$

where the A_i and B_i are real constants determined by the asymptotic behavior of the FID for each echo from Eq. (2.22). From this system of equations, the shapes of the functions $\Re\tilde{f}(t')$ and $\Im\tilde{f}(t')$ are found and plotted in Fig. 2.32.

We can now use the two functions in Fig. 2.32 to generate the predicted shapes for the other solid echoes that were generated in the long-time of the FID. The predicted shapes are shown, along with the experimentally obtained echoes in Figs. 2.33, 2.34, 2.35, and 2.36, for the four echoes falling between the 76 μs and 86 μs. We find remarkable consistency between the data and the predicted lineshapes, and conclude that Prediction IV is also shown to be consistent with the experimental behavior.

Throughout this discussion, we have focused on the long-time portion of the FID. We defined that region as the time after which only the slowest eigenmode of the time-evolution operator remains in the decay profile of the signal. At the end of Sec. 2.2.3.5, we noted that echoes generated *before* the onset of the long-time regime of the FID would have unique character corresponding to the particular realization of the other eigenmodes in the system that were still present when the decay was interrupted with additional pulses; such echoes would not be expected to behave according the relationships described by Eqs. (2.25) or (2.26), and would not have shapes describable by (2.22). One way to observe this evolution to the long-time behavior is to examine solid echo signals that originate at a self-similar place in the FID decay. For example, one could acquire solid echoes that are initiated at each node of the FID. If all the fast-decaying eigenmodes are absent (that is, have decayed away), such echoes would be expected to have the same shape (zero-crossing, decay constants, beat frequency) as every other echo initiated at a node of the FID. However, if there are still other eigenmodes present with sufficient intensity in the early signals, we would not expect to see shapes described by Eq. (2.22).

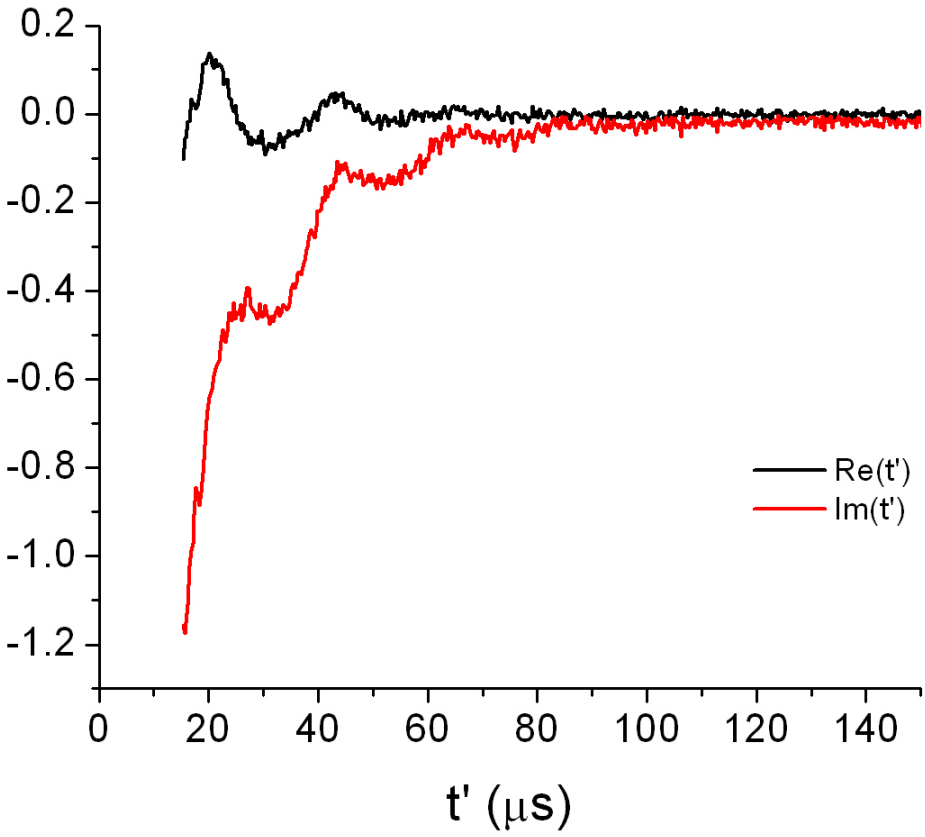

Figure 2.32: **The shape functions** $\Re\tilde{f}(t')$ **and** $\Im\tilde{f}(t')$ obtained from the linear system (2.39) for ^{19}F in CaF_2. These functions are sufficient to calculate the shapes of all solid echoes initiated in the long-time regime of the FID by use of Eq. (2.22).

Figure 2.37 shows the [100] CaF_2 FID with the times of the nodes and maxima of the FID explicitly marked. Solid echoes were initiated at each node of the FID ($\tau = 23.2, 44.8, 66.0$ and 87.7 μs) in order to compare their shapes and observed the evolution of the shapes of the echoes initiated later and later in the FID decay to the shape predicted by Eq. (2.22).

Figure 2.38 shows the echoes initiated at each of the first four nodes of the FID (Fig. 2.37). These echoes have been shifted in time so that their origins coincide, but their amplitudes have not been manipulated. As expected, the earlier echoes have a larger signal intensity which decreases as τ is lengthened. More interesting, however, is the evolution of the echo shapes themselves. We notice that the earliest echo corresponding to the first node of the FID at $\tau = 23.2$ μs (shown in black) bears little relation to the other echoes in terms of its frequency and location of zero-crossings. The echo $\tau = 44.8$ μs has the first zero-crossing coinciding with that of the later two echoes, but shows some divergence after that. The

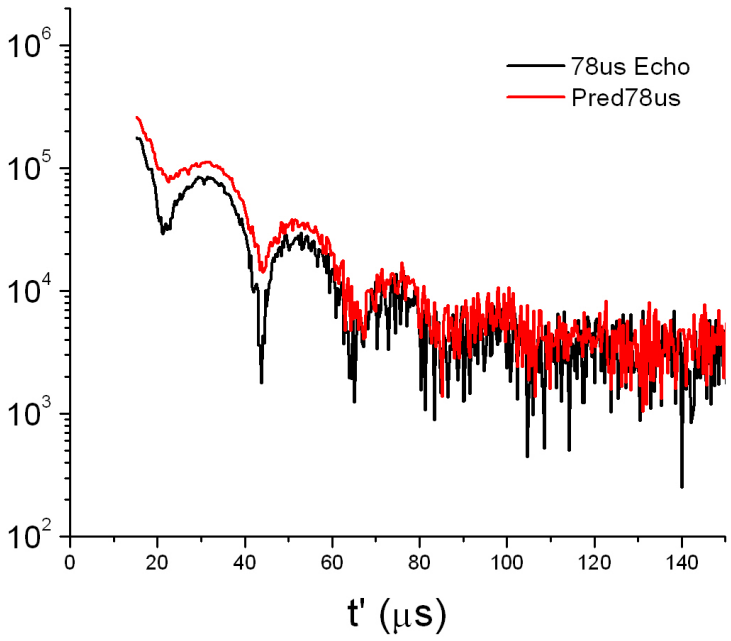

Figure 2.33: **Predicted and experimental solid echo shapes for ^{19}F in [100] CaF_2-78 μs.** ^{19}F long-time $\tau = 78\mu$s solid echo (black), and predicted shape (red) from Eq. (2.22).

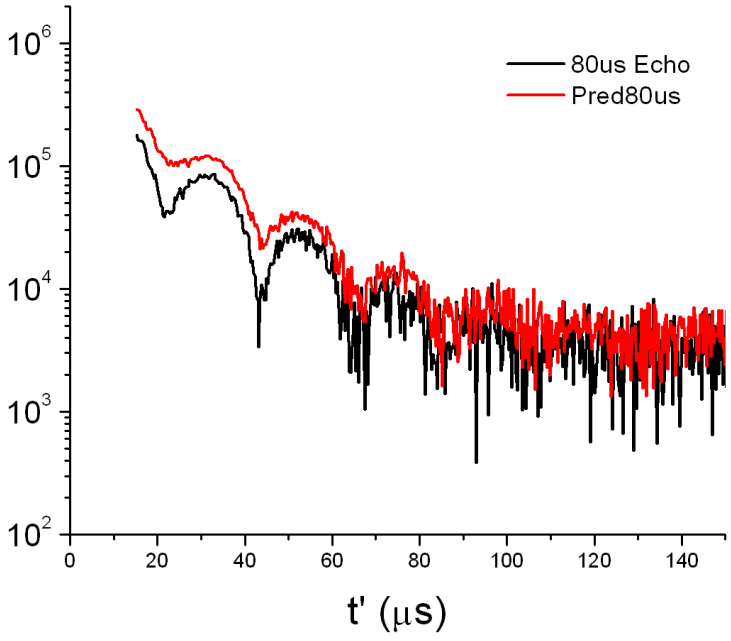

Figure 2.34: **Predicted and experimental solid echo shapes for ^{19}F in [100] CaF_2-80 μs.** ^{19}F long-time $\tau = 80\mu$s solid echo (black), and predicted shape (red) from Eq. (2.22).

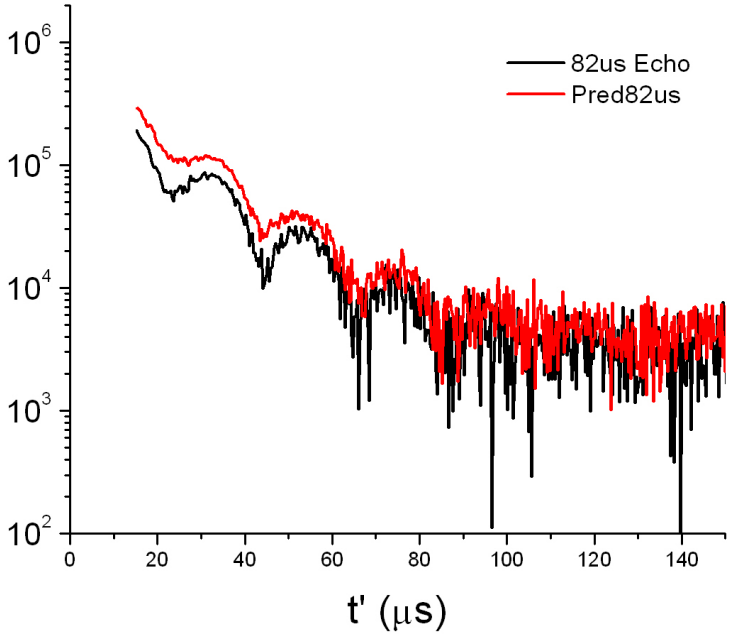

Figure 2.35: **Predicted and experimental solid echo shapes for ^{19}F in [100] CaF_2-82 μs.** ^{19}F long-time $\tau = 82\mu$s solid echo (black), and predicted shape (red) from Eq. (2.22).

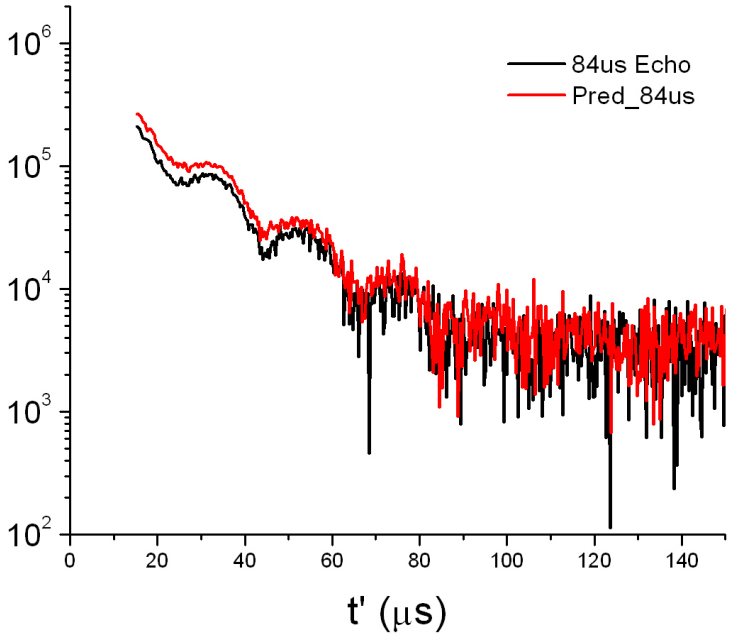

Figure 2.36: **Predicted and experimental solid echo shapes for ^{19}F in [100] CaF_2-84 μs.** ^{19}F long-time $\tau = 84\mu$s solid echo (black), and predicted shape (red) from Eq. (2.22).

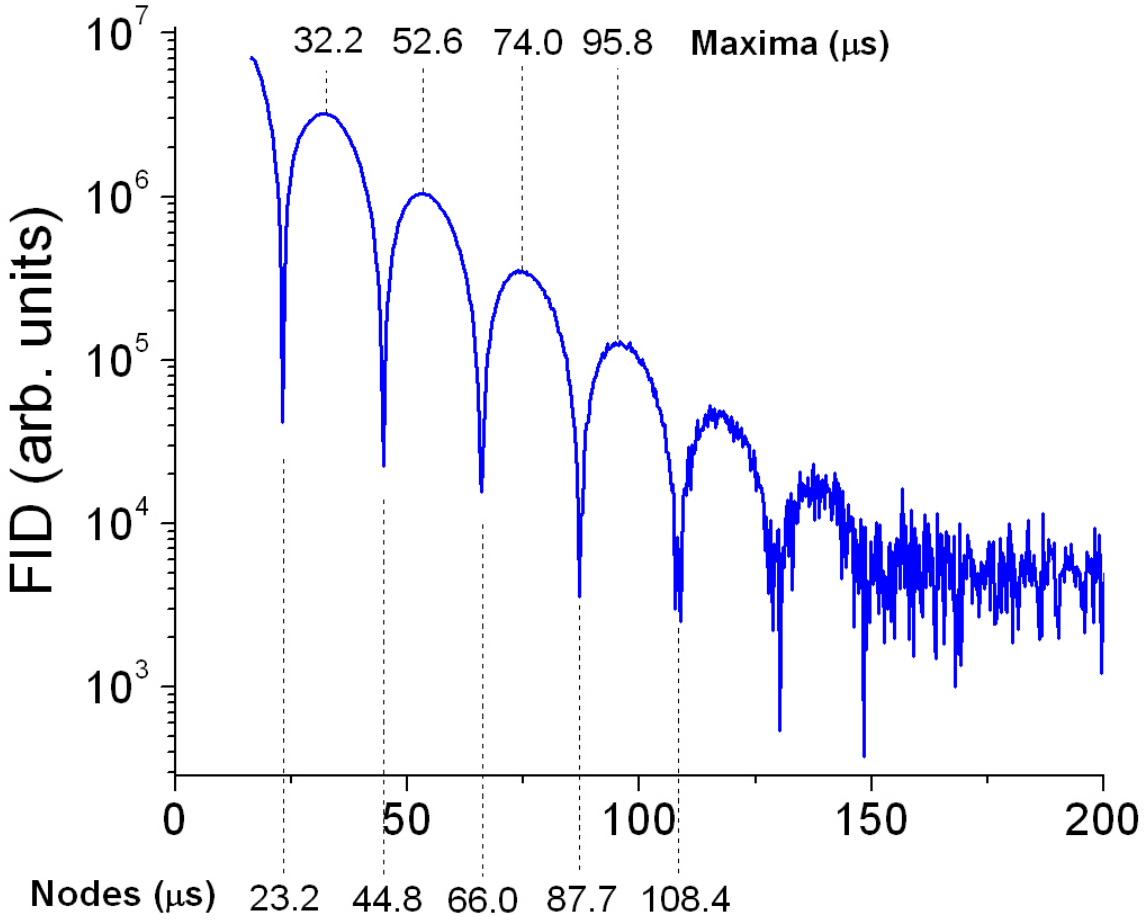

Figure 2.37: **Nodes and maxima of [100] CaF_2 FID.** The ^{19}F FID for [100] CaF_2 is shown with the locations of the maxima and minima of the oscillating decay marked explicitly.

echo $\tau = 66.0$ μs is almost identical to the the final echo, $\tau = 87.8\mu$s. Again, this is the evolution of shapes one would expect to see in the paradigm of the chaos-based model: the evolution of the echo shapes is a measure of the time necessary for the slowest eigenmode of Eq. (2.15) to dominate the decay and for the faster-decaying eigenmodes to disappear. We note that the echo at $\tau = 66$ μs is already showing a shape that is consistent with the echoes measured after 66 μs, indicating that around this time the long-time condition has been met. This timescale corresponds with the onset of the predicted amplitude and phase behavior at approximately 60 μs seen in Figs. 2.29 and 2.30.

Finally, in Fig. 2.39, we show the analog to Fig. 2.38 for echoes acquired at the *maxima* of each beat of the FID. Again, we see a smooth evolution of shapes from a distinctly unique character for the early echoes to a convergence (after the approximately 60 μs) of the later echo shapes. Figures 2.38 and 2.39 are striking visual examples of the decay of the fast eigenmodes of the time-evolution operator of the nuclear spin system.

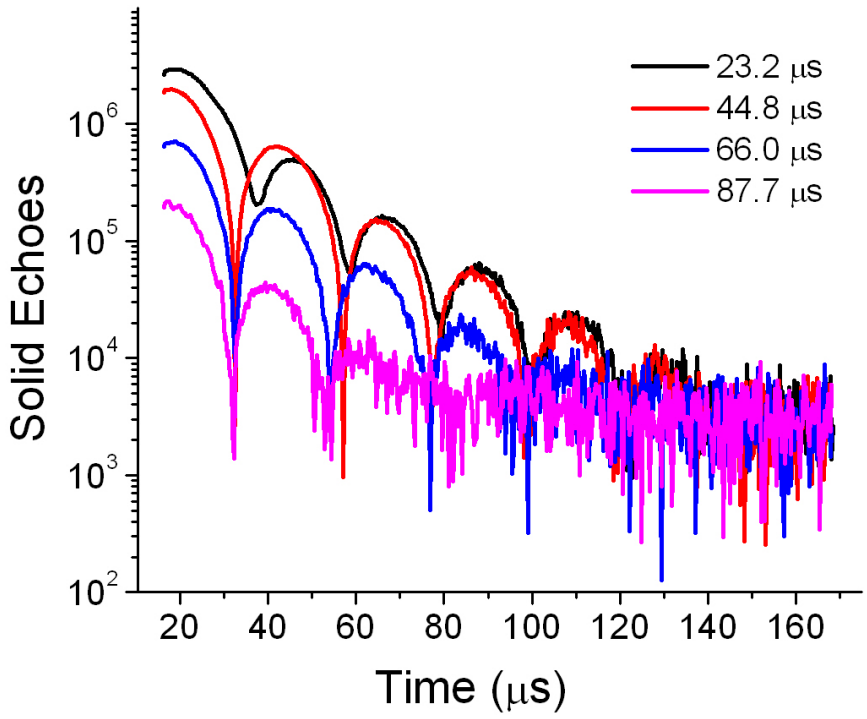

Figure 2.38: **Solid echoes in [100] CaF_2 initiated at FID nodes.** Echoes are time-shifted to a common origin. The fast-decaying eigenmodes of the time-evolution operator that persist in the early echoes give rise to unique behavior, while echoes initiated at times $t > 60$ μs can be seen to converge to the same beat frequency ω and decay constant γ characteristic of the slowest decaying eigenmode.

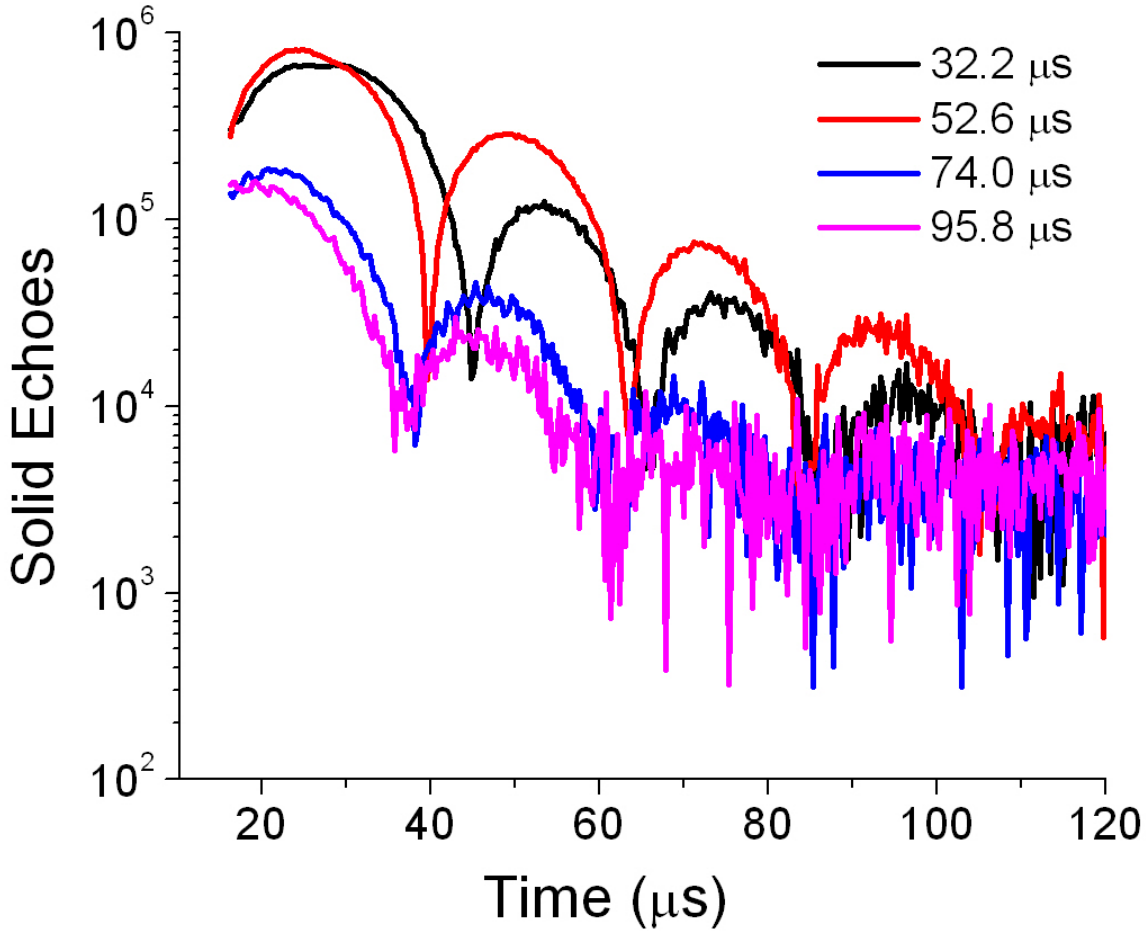

Figure 2.39: **Solid echoes in [100] CaF_2 initiated at FID maxima.** Echoes are time-shifted to a common origin. The fast-decaying eigenmodes of the time-evolution operator that persist in the early echoes give rise to unique behavior, while echoes initiated at times $t > 60$ μs can be seen to converge to the same beat frequency ω and decay constant γ characteristic of the slowest decaying eigenmode.

2.5 ^{129}Xe and CaF_2 Powders

Fig. 2.40 shows the FID and four solid echo signals associated with the CaF_2 powder (System X; see Table 2.4) acquired at room temperature in a 2 T field. The CaF_2 powder samples, as with all of the xenon samples, have many crystallites with random orientations; the transverse decays are therefore independent of sample orientation. However, unlike in xenon, the initial beating seen in the signal washes out such that a single decay parameter and beat frequency are not present. Accordingly, the long-time regime cannot be characterized by a universal behavior within our experimental resolution. Furthermore, the time-shifts and amplitude manipulation of the solid echo signals shown in Fig. 2.40b do not give conclusive evidence of a convergence of these signals to the behavior of the FID after several times T_2. Numerical simulations of the lineshapes expected by averaging over the distribution of angles expected in a powder with randomly oriented simple cubic crystals shows that the long-time behavior is expected to take much longer to become established in this system than in the single crystals [99]. We are pursuing work on the subject of powders at present, but preliminary calculations indicate that the CaF_2 powder should show a short beat, followed by a longer beat, and then a series of beats approaching the long-time behavior beginning around $t = 300\mu$s – well outside the SNR range of our 2 T signals [99].

It is interesting to note that solid xenon samples frozen from the liquid phase should also be in a polycrystalline state with randomly oriented crystalline regions, similar to a polycrystalline powder. Previous work has shown [1], and it has been verified here, that distinct orientations of single-crystal CaF_2 with respect to the external magnetic field produce different beat frequencies in the transverse decay. The frequency differences are large enough that mixing them (as is the case in a polycrystalline powder) may cause the Lowe beating to wash out after a few times T_2 (see Fig. 2.40). A similar wash out effect could be anticipated in polycrystalline xenon. Instead, the solid xenon signals exhibit a very precise beat pattern that lasts over 5 orders of magnitude (see Fig. 2.4). This phenomenon could be explained if the beat frequencies of a xenon single-crystal in different orientations with respect to the external magnetic field were similar, or if the xenon were frozen in a glassy state with less order than a rigid polycrystalline structure. Despite some claims in the early literature that it should be possible [100], however, all recent attempts to vitrify monatomic liquids (noble-gases, metals, or otherwise) have been unsuccessful to date, despite achieving freezing rates on the order of 10^{10} K/s and pressures on the order of

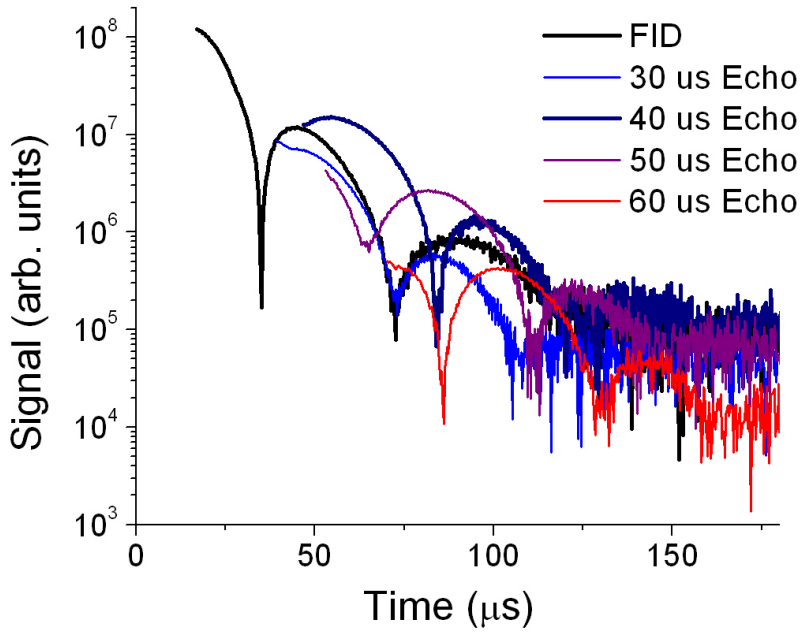

(a)

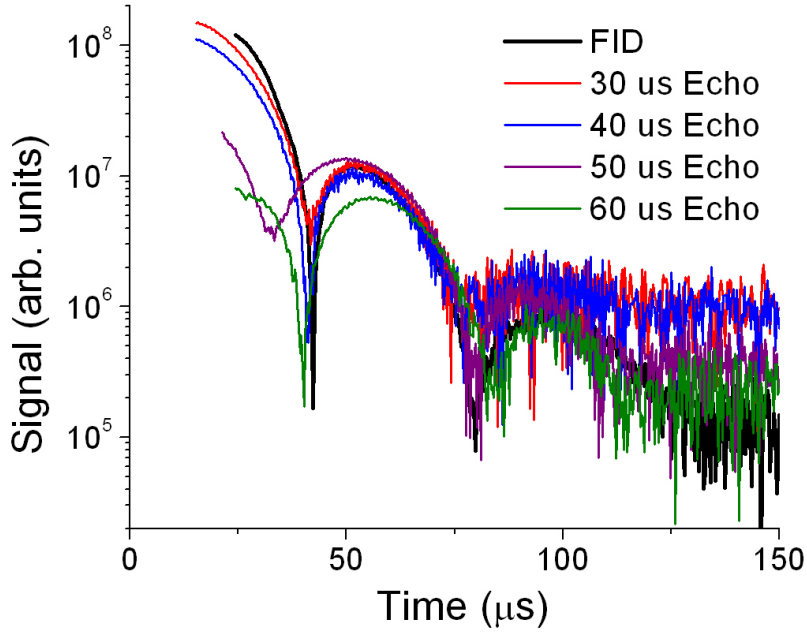

(b)

Figure 2.40: **^{19}F signals in CaF_2 powder** (System X; see Table 2.4). In (a), solid echoes for four different values of τ are shown with the FID (black). In (b), the solid echo signals are time- and amplitude-shifted to attempt to match the long-time portions of the signals. The Lowe beats wash out after several times T_2, and they are neither similar to each other nor can they be characterized by a single beat frequency and decay coefficient within experimental resolution.

10 GPa. The only reported exception is a study which achieved vitrification of monatomic germanium by exploiting a particular property of tetrahedral liquids that does not exist in noble-gases [101]. No other monatomic liquid has yet been vitrified. Our own X-ray diffraction data confirm that the frozen xenon is polycrystalline with no glassy component (see Fig. 2.41).

Why the xenon samples exhibit such well-defined beats and universal long-time behavior is an outstanding question which our group is pursuing (with some recent success). It is likely related to the difference between the f.c.c. lattice of solid xenon and the simple cubic lattice formed by ^{19}F in CaF_2. We plan to address this question theoretically and experimentally elsewhere [99]. Unfortunately, noble-gas single-crystals can be generated only with considerable difficulty and in very small sizes [102]. To further generate single-crystals with hyperpolarized ^{129}Xe spins appears close to impossible, making direct experimental NMR measurements of single-crystal solid xenon prohibitively difficult.

To investigate the atomic arrangement of the xenon in our samples, we undertook X-ray diffraction studies on a natural xenon sample with the isotopic makeup of System VI. A room-temperature sample was exposed to nitrogen gas at 100 K (well below the 160 K freezing point of xenon), freezing it suddenly in a manner similar to our NMR experimental procedure. X-ray diffraction was performed with a 4.1 kW Bruker Copper K-Alpha X-ray source operating at a wavelength of $\lambda = 1.5814$ Å. The sample was maintained at 100 K by a built-in cryostat. Typical results from one of ten runs are shown in Fig. 2.41. The sharp well-defined rings are characteristic of a polycrystalline solid, *i.e.*, randomly oriented crystals of definite atomic spacing. Analysis of the rings due to xenon (after background subtraction) yields the known nearest-neighbor spacing of ~ 4.4 Å [89] for xenon in an f.c.c. lattice.

2.6 Conclusions

We have observed sinusoidally modulated exponential decay of ^{129}Xe in solid xenon for six different isotopic compositions. All exhibited generic behavior in the long-time regime, irrespective of distinct initial conditions imposed by various spin manipulations. We have further observed evidence of similar universal decay of ^{19}F in CaF_2 single-crystals. Unlike the other samples, the Lowe beat pattern of ^{19}F in the CaF_2 powder washes out within our experimental resolution and therefore cannot be characterized by Eq. (2.16). In principle, the washing out of Lowe beats is expected in a powder where the frequencies

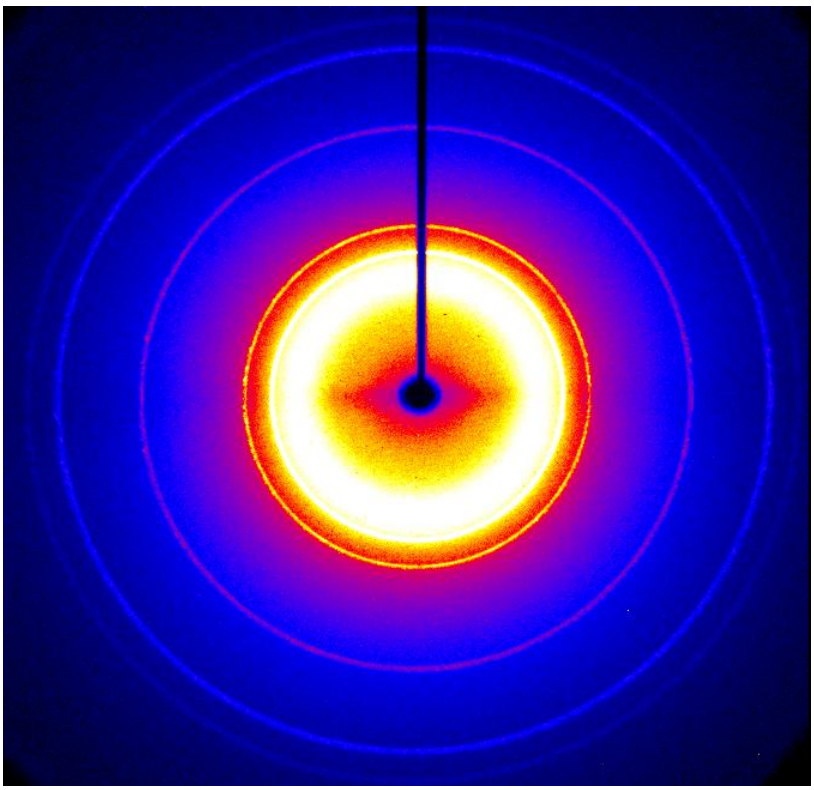

Figure 2.41: **X-ray diffraction experiment for rapidly frozen xenon**. Sharp rings indicate a polycrystalline sample with well-defined lattice spacing, determined to be 4.4 Å (nearest-neighbor spacing) in agreement with the known value [89].

of the various crystallites are distinct, such as in CaF_2 powder. It is intriguing that the universal behavior survives in the polycrystalline xenon systems, given the expectation that the Lowe beats may wash out in a similar fashion as in CaF_2. The bulk of this work provides evidence in support of the conjecture that a universal behavior will dominate the long-time transverse relaxation of manipulated spin coherences. This conjecture is based on the notion of microscopic chaotic mixing induced by the interaction between nuclear spins. We note that as our system for hyperpolarizing xenon nuclei continues to improve, the resulting highly spin-polarized lattice will represent yet another unique transverse spin configuration that can be used for further verification of the universal long-time behavior. *We find that Prediction I is consistent with the experimental data.*

We have further observed the amplitudes and phases of solid echoes of ^{19}F in CaF_2 at room temperature, and in ^{129}Xe in solid phase at 77 K. The echoes generated in the early-time of the decay of the FID in each case do not show any particular relationship,

and none is anticipated. In this regime, the dynamically developing and decaying quantum coherences are still interacting in a nontrivial way; the eigenmode of the evolution operator with the slowest decay has not yet had time to dominate the FID in this regime. In echoes generated in the long-time regime of the FID, however, we see in both CaF_2 and ^{129}Xe systems the convergence of the echo amplitudes and phases to the functional forms predicted by the chaos-based theory. The agreement is most striking in the case of the ^{19}F in CaF_2as in this system many echoes were acquired in the long-time regime of the FID. *We find that Predictions II and III are consistent with the experimental data.*

Finally, we have compared the predicted solid echo shapes with the measured echo shapes in the [100] crystal of CaF_2. This crystal orientation has the highest frequency and therefore shows the most oscillations with good SNR of all the CaF_2 crystals. We find that the predicted echo lineshapes match well with the experimentally obtained shapes in this crystal. *We find that Prediction IV is consistent with the experimental data.*

We conclude that the current predictions derived from the chaos-based model agree with all experimental data thus far. We consider this agreement a significant achievement of the theory since none of the rather extensive array of theoretical tools brought to bear on the problem of calculation of NMR lineshapes has yet been successful in predicting the behavior (particularly that of the long-time regime), while the current model has begun to show great promise in this regard. We hope the extensive experiments reported here, and published in the literature, will stimulate further development and refinement of the theory, which should have applications even beyond the important problem of NMR lineshapes.

2.7 Final Thoughts and Discussion

It has been argued in Refs. [103, 33] that the occurrence of the well-defined long-time behavior (2.16) for FIDs in the absence of the separation of timescales is already a strong indication of the role of microscopic chaos. However, such a behavior also appears in approximate theories of spin dynamics as a consequence of rather crude approximations. It was the prediction of the identical frequency and decay constants for the FID and all sorts of echoes [76] that set apart the theory based on the notion of microscopic chaos from other theoretical descriptions, [31, 44, 104, 55, 58, 105, 64, 106]. To the best of our knowledge, these theories are not in position to make such a prediction. Below we elaborate on these issues.

Although the long-time behavior (2.16) is reminiscent of the behavior of a damped

harmonic oscillator, this similarity is superficial. The damping in the latter case originates from friction or a similar mechanism, which is usually caused by microscopic motion, which, in turn, is much faster than the period and the decay time of the damped oscillator. In the context of NMR, well-defined exponential damping similar to the case of the damped harmonic oscillator appears in the problems of exchange narrowing and motional narrowing [22, 23]. However, in the general case described in subsection 2.3.1, no separation of timescales is present, and, therefore, no conventional justification for the friction-like mechanism can be given.

It should be further noted that the occurrence of well-defined frequency beats in the tail of FIDs and echoes is a somewhat counterintuitive effect, which is determined primarily by the negative relative sign of the J^z and $J^\perp$ in Eq. (2.28). Note, in particular, that these beats have little connection to the oscillations associated with a Pake doublet [107, 22], which originates from a highly discrete quantum structure of the FID problem for two isolated spins 1/2. In solid xenon and in CaF_2, each spin 1/2 is coupled to the whole lattice through many interacting neighbors. If the coupling constants J^z and $J^\perp$ were of the same sign, the FIDs in CaF_2 and solid xenon would likely exhibit no beats, while the beats associated with a Pake doublet would remain with a modified frequency value. The above emphasis on correlation effects is corroborated by simulations for a lattice of classical spins [103] where similar beats have been observed — clearly without any role for quantum discreteness. These and other factors determining the occurrence of beats are discussed in detail in Ref. [103]. Another difference between the Pake-doublet signal and the FIDs in CaF_2 or solid xenon is that the corresponding power spectrum in the former case has a well pronounced peak at the oscillation frequency, while in the latter case it exhibits no detectable signature of the long-time beats [40]. Historically, the absence of the separation of timescales was the reason why no universal shape for the FID tails was expected *a priori*. Noteworthy in this respect was the proposal of Abragam to approximate FIDs in CaF_2 by function $e^{\frac{-a^2t^2}{2}}\sin(bt)/bt$, where the parameters a and b were to be determined from fitting the exact values of the second and the fourth moments [22].

In general, the theoretical problem of calculating the FID in solids is nonperturbative. Many attempts to deal with it resulted in various uncontrollable approximation schemes. These schemes aimed at reproducing the entire behavior of the FID, of which the long-time tail was a rather insignificant part. At the same time, relatively crude approximations [44, 104, 55, 58, 105, 64] made to predict the initial FID behavior sometimes resulted in the

long-time behavior having form (2.16).

A particularly strong claim of predicting the long-time behavior (2.16) was made by Borkmans and Walgraef [104]. However, this claim was criticized as inconclusive by Cowan Ref. [50, Ch. 8], and in the appendix of Ref. [103]. Borkmans and Walgraef described the long-time behavior of FIDs by a memory-function-like integro-differential equation with memory function (integration kernel) having known initial behavior but unknown long-time behavior. Looking at the initial behavior, they assumed that the entire memory function had a Gaussian shape, and thereby obtained the long-time behavior of form (2.16). In fact, the long-time behavior of the FID was entirely controlled by the unknown long-time behavior of the memory function; for the long-time FID behavior (2.16) to follow from the memory function equation, the asymptotic decay of the memory function should be no slower than exponential. If it were slower than exponential, *e.g.*, a power-law, then the asymptotic FID behavior would also exhibit a power-law decay rather than (2.16).

To the best of our knowledge, the theory of Borkmans and Walgraef has never been applied to solid echoes and other pulse sequences investigated in this work, and, in fact, we are not sure whether, if applied, it would be manageable at all. If it were manageable, it is further difficult to see how that theory would reproduce the main result of this work, namely, the same long-time constants for different pulse sequences. Different pulse sequences would result in different initial conditions, and hence different parameters for the memory functions. It then appears rather unlikely that different memory functions would lead to the same long-time decay constants. A similar critique is applicable to all other approximations attempting to predict the long-time behavior of NMR signals from the knowledge of a few initial time derivatives.

The prediction of quantitatively identical long-time behavior for different pulse sequences was not made until the long-time behavior of NMR signals was considered on the basis of the notion of microscopic chaos [76, 33]. The analysis of Ref. [103] has focused exclusively on the fundamental reasons behind the fact that the long-time functional form (2.16) is not a crude approximation, but rather a robust accurate property. This analysis predicted that nonintegrable lattices of interacting classical or quantum spins universally exhibit the long-time behavior (2.16), while the integrable cases amenable to the analytical calculations of FIDs exhibit nonuniversal behavior different from (2.16). Nonintegrability in the interacting spin systems is the rule, while integrability is an exception. In classical spin systems, nonintegrability is generally associated with microscopic chaos caused by

nonlinear interaction between spins. Mathematically, chaos is defined as an exponential instability of the phase space trajectories with respect to small differences of the initial conditions. Calculation of classical FIDs requires averaging over all possible chaotic phase space trajectories. In the quantum case, the notion of chaos cannot be defined at the level of exponential instabilities in the phase space, because the Heisenberg uncertainty principle precludes one from defining a phase space trajectory. However, the connection between classical and quantum manifestations of chaos can be conjectured for spin lattices at the level of spin correlation functions [108, 33].

According to the analysis of Ref. [103], almost any initial probability distribution in a chaotic classical spin system would evolve to exhibit universal patterns associated with stable and unstable directions in the phase space. These patterns are complicated and intrinsic to a given Hamiltonian. They exhibit a dynamically developing small parameter, representing the ratio of characteristic scales along stable and unstable phase space directions. This small parameter, in effect, substitutes for the separation of timescales, and leads to Markovian long-time behavior of ensemble-averaged quantities on non-Markovian timescales [*e.g.*, Eq. (2.16)]. As time progresses, the above patterns become increasingly singular and are expected to underlie chaotic eigenmodes of the time-evolution operator. These eigenmodes are known as Pollicott-Ruelle resonances [81, 65]. Their singular character is masked by ensemble averaging, but what remains after averaging are the exponential decays, with or without oscillations. In terms of spin correlation functions, the formation of the above patterns implies the transfer of weight from lower-order to higher-order correlations (spin coherences in NMR language). It was conjectured in Refs. [76, 108, 103] that the same transfer of spin correlations also occurs in quantum spins systems and underlies the observed exponential decays. The slowest of these decays then controls the long-time behavior in a given symmetry class of initial conditions. (NMR signals studied in this work correspond to the initial conditions having zero wave vector symmetry, *i.e.*, all spins are equivalent from the viewpoint of initial conditions). It was estimated in Ref. [103] that the onset of this single exponential behavior occurs in the NMR context on the scale of a few times T_2. The prediction of the identical long-time behavior for different pulse sequences was based on the fact that the above Pollicott-Ruelle resonances and the associated exponential decays are intrinsic for a given Hamiltonian, but not to the initial conditions, and therefore the exponential decay associated with the slowest resonance would dominate the behavior of many-spin density matrices. Hence, the same decay would

manifest itself in the behavior of all observable quantities in the same symmetry class, independent of the initial condition [76].

An alternative perspective on the role of chaos was explored by Pastawski in the context of the intensity loss of NMR polarization echoes [97, 109, 98] intended to induce a complete reversal of spin dynamics in heteronuclear spin systems. The authors of Ref. [97] have interpreted the echo intensity loss as the result of the amplification of rf pulse imperfections caused by the chaotic instabilities intrinsic to the spin dynamics. While we share the intuition of Ref. [97] that chaotic instabilities lead to intrinsic constraints on the experimental ability to refocus the polarization echoes, we believe that the role of chaos in this context needs to be further clarified. Namely, it is necessary to discriminate between chaotic and integrable systems as far as the suppression of the echo intensity is concerned. This subject is beyond the scope of this dissertation, apart from the fact that the magic echo experiments reported below in Sec. 2.4.2.3 also reveal incomplete reversal of the spin dynamics, which may also be caused by the experimental imperfections of the rf pulse sequence.

At present, the theory of chaos in both classical and quantum many-body systems is still at an early development stage; the use of conjectures in the theoretical analysis is therefore unavoidable. However, since the conjectures are not rigorously proven, it is essential to substantiate theoretical claims by extensive experimental tests, and this is what the present work does. We also hope that the robustness of the long-time behavior (2.16) will stimulate the search for controllable theoretical methods of calculations of the parameters γ and ω in Eq. (2.16).

CHAPTER 3

MEASUREMENT OF FREQUENCY-SHIFT ENHANCEMENT FACTORS IN RB—NOBLE-GAS MIXTURES

3.1 Introduction

In 1978, Grover [110] observed that the noble-gases ^{83}Kr and ^{129}Xe produced resonances that were shifted from their predicted values when in the presence of spin-polarized alkali-metal vapors.[1] To describe this effect, he defined a dimensionless enhancement factor κ_{XA} which can be understood as ratio of the shift that is actually experienced by a noble-gas nucleus (X) due to an alkali-metal electron (A) to the shift it would experience due to a continuos spherical distribution of alkali-metal vapor of the same density and polarization. That is, one can consider a macroscopic addition to any externally imposed magnetic field from a continuous spherical distribution of magnetization, which can be shown [111] to be $8\pi\mathbf{M}/3$. The incremental field that is actually experienced by the noble-gas nucleus in a spherical environment of alkali-metal spins δB_{a} is larger than the expected $8\pi\mathbf{M}/3$, and κ_{XA} is then defined as the ratio of the actual field enhancement to that expected as

$$\kappa_{\mathrm{XA}} = \frac{\delta B_{\mathrm{a}}}{\frac{8\pi}{3}|M|}, \tag{3.1}$$

where the magnetization $\mathbf{M}$ resulting from the polarized alkali-metal vapor is

$$\mathbf{M} = \mu_B g_S [A] \langle S_z \rangle \hat{e}. \tag{3.2}$$

In Eq. (3.2), μ_B is the Bohr magneton, g_S is the Landé factor, [A] is the alkali-metal

[1] Some of the data presented in this section have already been published [28]; such material is copyright 2011 by the American Physical Society and is reproduced here by permission of the American Physical Society.

number density, and $\langle S_z \rangle$ is the volume-averaged expectation value of the z-component of the alkali-metal electron spin (in units of $\hbar$). Using (3.1) and (3.2) we may express the incremental energy ΔE associated with the incremental field as

$$\Delta E = h\Delta\nu_X = \mu \cdot \delta B_a = \frac{|\mu_K|}{K}\frac{8\pi}{3}\mu_B g_S \kappa_{\mathrm{XA}}[A]\langle, S_z\rangle \tag{3.3}$$

or, solving for the shift in frequency, we obtain

$$\Delta\nu_X = \frac{1}{h}\frac{|\mu_K|}{K}\frac{8\pi}{3}\mu_B g_S \kappa_{\mathrm{XA}}[A]\langle S_z\rangle, \tag{3.4}$$

which is the actual shift experienced by a noble-gas nuclei in the presence of a polarized alkali-metal vapor.

The relevant spin-dependent interaction term of the Hamiltonian that gives rise to perturbations in resonance frequency in this context is

$$H = \alpha(r)\mathbf{K} \cdot \mathbf{S}, \tag{3.5}$$

which is the collisional Fermi-contact hyperfine coupling between the electron spin $\mathbf{S}$ and the nuclear spin $\mathbf{K}$ of the noble-gas. The interaction described by Eq. (3.5) is directly analogous to the pressure-shift of alkali-metal-vapor frequency standards [112] and the Knight shift caused by polarized conduction electrons in metals [113], and is responsible for spin-exchange hyperpolarization of noble-gases [18]. Though we have focused exclusively on the frequency shift of the noble-gas resonance in the above discussion, the interaction (3.5) simultaneously gives rise to a complementary EPR frequency shift of the alkali-metal electron resonance proportional to the nuclear magnetization [27] characterized by an analogous parameter κ_{AX}. We note that in the preceding discussion a spherical geometry was chosen to avoid unnecessary digressions as to the shift experienced from the *through-space* portion of the dipolar fields; such fields vanish everywhere inside a spherical distribution. The nonzero shifts from the through-space dipolar fields present in nonspherical geometries was exploited by Barton *et al.* [29] in the original frequency shift measurement of the ^{3}He nuclear resonance $(\kappa_0)_{\mathrm{HeRb}}$.

3.2 Motivation and Result

The study of hyperpolarized noble-gases generated by spin-exchange optical pumping (SEOP) [12] continues to be vital and integral to recent work in many other fields, including condensed matter physics [36, 26], materials science [114], medical imaging [115, 116], searches for permanent electric dipole moments in atoms [117], surface studies [118, 119], and polarized nuclear targets [120]. In many of these applications, precise frequency measurements are required; a thorough understanding of the mechanisms which may result in frequency shifts is therefore necessary. Additionally, these shifts provide insight into the nature of the interatomic potentials, which ultimately determine spin-exchange rates for a given alkali-metal—noble-gas pair. If properly calibrated, the EPR shift also offers a simple and robust means to do noble-gas polarimetry in a typical low-field (few gauss) SEOP apparatus. The enhancement factor κ_{XA} that characterizes the frequency-shift calibration has been successfully measured for Rb-^{3}He to about 2% [121, 29], but until now was known to only about 50% for Rb-^{129}Xe and for Rb-^{83}Kr [27]. The Rb-^{129}Xe measurement we performed presents several method dependent challenges, among them the fact that, unlike helium, high densities of xenon are difficult to polarize by SEOP. Indeed, the current lean-xenon flow-through method for generating large quantities of highly polarized ^{129}Xe [122, 87] would benefit greatly from a more precise measurement of $(\kappa_0)_{\mathrm{XeRb}}$ for Rb-^{129}Xe. To evaluate $(\kappa_0)_{\mathrm{XeRb}}$, we made consecutive measurements of the NMR shifts of both ^{3}He and ^{129}Xe at 2 T in the same glass cell under steady-state SEOP conditions. In cells having relatively low Xe density ([Xe] $\leq$ 10 Torr at 20 °C), we use the ratio of these shifts to deduce a much more precise temperature-independent value

$$(\kappa_0)_{\mathrm{XeRb}} = 493 \pm 31 \tag{3.6}$$

from the known value of $(\kappa_0)_{\mathrm{HeRb}}$. With this measurement, we can further employ the previously measured ratio [27]

$$\frac{\kappa_{\mathrm{XeRb}}}{\kappa_{\mathrm{KrRb}}} = 2.38 \pm 0.13 \tag{3.7}$$

to deduce a value

$$(\kappa_0)_{\mathrm{KrRb}} = 207 \pm 17 \tag{3.8}$$

for the frequency shift enhancement of ^{83}K in the presence of polarized Rb. In cells having [Xe] approximately ten times greater, we observed an anomalous depression ($\approx 20\%$) of the shift ratio at the highest temperatures.

3.3 Theory

The enhancement factor κ_{XeRb} can be written in the form

$$\kappa_{\mathrm{XeRb}} = (\kappa_0 - \kappa_1) + \epsilon_{\mathrm{XeRb}}\kappa_1. \tag{3.9}$$

Here, $\kappa_0 - \kappa_1$ is the contribution to κ_{XeRb} from pairs of atoms with short lifetimes (binary collisions and short-lived molecules), and $\epsilon_{\mathrm{XeRb}}\kappa_1$ describes contributions from pairs of atoms with long lifetimes (long-lived molecules). As is discussed in the literature (*e.g.*, [27, 29]), the enhancement factor κ_{XeRb} in general contains contributions from both types of atomic pairs. To quantify the lifetime and differentiate between the two cases, we introduce the phase angle

$$\phi = \frac{\gamma N \tau}{\hbar}, \tag{3.10}$$

which is a product of the mean lifetime τ of the pair of atoms and the spin-rotation coupling frequency $\gamma N/\hbar$. The quantity ϕ then represents the mean angle through which the nuclear spin $\mathbf{K}$ will precess about the intermolecular field during a collision event of duration τ. Such a collision may be a binary two-body collision, generally of picosecond duration; such a collision represents a ^{129}Xe–Rb pair who interact for a time τ such that $\phi << 1$. In this regime, the pair interact for times so short that neither $\langle K_z \rangle$ nor $\langle S_z \rangle$ have time to be perturbed very much. In much rarer events, a ^{129}Xe and Rb atom may collide with each other and a third atom simultaneously, and in doing so, may form a van der Waals molecule with a lifetime that may vary from picoseconds to a few nanoseconds [18]. In the latter case — the case of long molecular lifetime — the electron and nuclear spins of the alkali-metal begin to precess about the noble-gas nuclear spin $\mathbf{K}$, and about the rotational

angular momentum **N**, for times such that $\phi >> 1$. If the molecule lives long enough to meet this condition, the effective magnitudes of $\langle K_z \rangle$ and $\langle S_z \rangle$ in that molecule will be reduced as the spins begin to scramble.

It is instructive to consider the effect that van der Waals molecules have on the spin-destruction rate and on the frequency shift enhancement factor separately. These two quantities are both affected by the presence of molecules in the vapor, but the effect is very different in the two cases. Spin-destruction, which involves a simple randomization of the alkali-metal electron polarization, is efficiently achieved in a van der Waals molecule at low fields because the total intramolecular field experienced by the electron spin (dominated by **N**) causes the electron to precess around it, and randomizes the electron spin ($\phi > 1$). That is, there are significant portions of the time-varying transverse fields experienced by a spin while bound in a molecule that have components at the Larmor frequency, and cause the spin to be torqued away from the quantization axis. Application of large magnetic fields will suppress the spin-destruction rate; at such fields the time dependent transverse components of magnetic field that a molecule experiences during its molecular lifetime no longer have frequency components at the Larmor frequency of the precessing spin, and the spin is therefore not perturbed. Molecules that are efficient at destroying the spin polarization of the electrons may have short or long lifetimes.

The nuclear resonance frequency shift, on the other hand, is the average additional *coherent phase* the nuclear spin acquires when precessing around the component of the total intramolecular field due to $\langle S_z \rangle$. In Eq. (3.4) the change in resonance frequency of the nuclear spin was written as proportional to $\langle S_z \rangle$, which is the ensemble average Rb polarization, multiplied by the enhancement factor κ_{XeRb}. So long as all the pairs of atoms in the vapor have short lifetimes such that $\phi << 1$, $\epsilon_{\mathrm{XeRb}} = 1$ and, by Eq. (3.9), κ_{XeRb} $=(\kappa_0)_{\mathrm{XeRb}}$. The presence of short-lived molecules in a vapor may effectively relax the Rb polarization and reduce $\langle S_z \rangle$; the frequency shift will then decrease proportionally according to Eq. (3.4), but κ_{XeRb} is still equal to $(\kappa_0)_{\mathrm{XeRb}}$. However, at low third-body pressures, there will be a fraction of atoms bound in van der Waals molecules with long lifetimes such that $\phi > 1$. When the fraction of these atoms becomes significant, $\epsilon_{\mathrm{XeRb}} < 1$ and $\kappa_{XeRb} \neq$ $(\kappa_0)_{\mathrm{XeRb}}$. The characteristic third-body pressure below which a significant fraction of such long-lived molecules may exist is around 100 Torr for N_2 and somewhat higher for He [123]. In cells with low third-body partial presssures, the full value of Eq. (3.9) must be used. This will lead to a decrease in the average coherent phase accumulation by the nuclear spin and

thus to a smaller frequency shift, characterized by a smaller frequency shift enhancement factor. However, as the vast majority of xenon atoms involved in pairs are experiencing binary collisions, the molecular suppression effect is small even at the lowest pressures ($< 10\%$ for ^{129}Xe-Rb) [27].

The mean lifetime τ of atomic pairs is inversely proportional to the total gas pressure in the cell. In the cells used for all our measurements, we were careful to ensure N_2 partial pressures of several hundred Torr and He gas pressures in excess of 10^3 Torr (see Table 3.1). Such pressures guarantee that $\phi << 1$, *i.e.*, atomic pairs in our cells are either in binary collisions or short-lived molecules [27, 28]. The xenon nuclear spins that are involved in binary collisions or short-lived molecules during the measurement will all experience a frequency shift due purely to the overlap of the electron wave function at the nuclear site. This shift is therefore independent of field, is proportional to the average electron polarization of the Rb vapor, and is characterized by the parameter $(\kappa_0)_{\mathrm{XeRb}}$ which can be defined (and in principle calculated) by the radial integral

$$\kappa_0 = \eta^2 \int_0^\infty |\Psi_0(r)|^2 e^{-V(r)/kT} 4\pi r^2 dr, \tag{3.11}$$

where $\Psi_0(r)$ is the unperturbed wave function of the alkali-metal valence electron, $V(r)$ is the interatomic van der Walls potential which describes the force between the alkali atom and the noble-gas atom, and η is a wave function enhancement factor.

Table 3.1: Summary of $(\kappa_0)_{\mathrm{XeRb}}$ cell contents. All cells are sealed 7 mm i.d. uncoated Pyrex spheres. Quoted pressures are referenced to 20 °C and the Xe pressure is subject to $\approx 50\%$ uncertainty due to the filling procedure. $(\kappa_0)_{\mathrm{XeRb}}$ is computed for each of the low-[Xe] cells from the weighted average of that cell's data; we have excluded the high-[Xe] cells because of their anomalous behavior at high T.

Cell	Xe:N_2:He (Torr)	$((\kappa_0)_{\mathrm{XeRb}})_{\mathrm{RbXe}}$
155A	5:160:2200	495 ± 6
155B	10:250:2300	490 ± 5
155C	10:170:2300	530 ± 9
150A	50:175:1000	
150B	110:350:2040	
155D	50:170:1200	

Equation (3.11) contains two quite poorly known quantities: $V(r)$ and η. In making theoretical calculations of $(\kappa_0)_{\mathrm{XeRb}}$, Schaefer *et al.* [27] used values of $V(r)$ determined by Pascale and Vandeplanque [124] from atomic scattering experiments that are heavily model dependent. In the interpretation of their data, Pascale and Vandeplanque assumed that the effective potential $V(r)$ could be separated into three parts: an electrostatic interaction to model the behavior at large r, and two Gombàs type pseudopotentials based on the statistical atomic models of Thomas and Fermi that have a repulsive character and dominate at small internuclear distances [125]. Using potentials calculated by other authors (*e.g.*, Buck [126]) who used different assumptions and interpretations of scattering data lead to the calculations of potentials with different structures which can cause the calculation of $(\kappa_0)_{\mathrm{XeRb}}$ in Eq. (3.11) to vary by as much as 30%. Herman [127] first pointed out that the alkali-metal electron wave function $\Psi(r)$ is substantially larger at the site of the noble-gas nucleus than its unperturbed value Ψ_0. He introduced the wave function enhancement factor η as $\Psi(r) = \eta\Psi_0(r)$ to parameterize this effect. Walker *et al.* [128] report partial wave results for η using Coulomb wave functions proposed by Bates and Damgaard [129] and it was these results that were used to make the theoretical estimate of $(\kappa_0)_{\mathrm{XeRb}}$. The calculation of η also contains many simplifying assumptions and is poorly known.

Using the above parameters for $V(r)$ and η, Schaefer *et al.* [27] solved Eq. (3.11) numerically, and made the first theoretical predictions of $(\kappa_0)_{\mathrm{XeRb}}$. They calculated

$$\begin{aligned} (\kappa_0)_{\mathrm{XeRb}} &= 726 \\ (\kappa_0)_{\mathrm{KrRb}} &= 276. \end{aligned} \tag{3.12}$$

An estimate of the predicted temperature dependence of $(\kappa_0)_{\mathrm{XeRb}}$ can be made by differentiating Eq. (3.11) with respect to temperature

$$\frac{d\kappa_0}{dT} = \frac{\eta^2}{kT^2}\int_0^\infty |\Psi_0(r)|^2 V(r) e^{-V(r)/kT} 4\pi r^2 dr, \tag{3.13}$$

and numerically evaluating the integral. Using the same parameters as used in evaluating Eq. (3.11), the predicted temperature dependence of $(\kappa_0)_{\mathrm{XeRb}}$ is

$$(\kappa_0)_{\mathrm{XeRb}}(T) = 705 + 0.21\ T, \tag{3.14}$$

where the temperature T is in °C. The error (not represented here) depends on the poorly known interatomic interaction potential and wave function enhancement factor, and may therefore be quite large. Nonetheless, if we consider that Eq. (3.14) is at least qualitatively accurate over the temperature range of our experiment, we see that the expected temperature dependence for $(\kappa_0)_{\mathrm{XeRb}}$ is very weak to independent of temperature. Indeed, over the temperature range of our experiments ($\approx$ 140 °C to 220 °C), $(\kappa_0)_{\mathrm{XeRb}}$ is expected to vary with temperature by less than the 6% error of our measurement; we expect therefore that our measurements will be independent of temperature within error.

A direct measurement of $(\kappa_0)_{\mathrm{XeRb}}$ using Eq. (3.4) requires a measurement of the Rb magnetization (proportional to $[\mathrm{Rb}]\langle S_z\rangle$). The inability to perform a Faraday rotation experiment or other direct measure of either [Rb] or Rb magnetization in our experiment would make it necessary to rely on published vapor pressure curves to estimate [Rb]. This is problematic, as actual Rb vapor pressures in SEOP cells are known to vary from such curves by up to a factor of two. Variations is [Rb] from cell to cell under similar conditions are thought to be a result of ill-defined reactions of Rb with uncontrolled impurities in the cell's walls [130]. Further approximations would have to be made to estimate the alkali-metal polarization $\langle S_z\rangle$, potentially destroying accuracy and precision in the final answer. To avoid this and substantially simplify the experiment, we instead formed the ratio

$$(\kappa_0)_{\mathrm{XeRb}} = (\kappa_0)_{\mathrm{HeRb}} \left(\frac{\gamma_{\mathrm{He}}}{\gamma_{\mathrm{Xe}}}\right) \left(\frac{2\Delta\nu_{\mathrm{Xe}}}{2\Delta\nu_{\mathrm{He}}}\right), \tag{3.15}$$

where γ_{X} are the noble-gas gyromagnetic ratios and $2\Delta\nu_{\mathrm{X}}$ are the shifts of the respective noble-gas NMR frequencies when the Rb vapor is exactly flipped from the low- to the high-energy Zeeman polarization state (LES and HES, respectively); $|[\mathrm{Rb}]\langle S_z\rangle|$ is presumed to remain constant under steady-state SEOP conditions. We note that "LES" and "HES" will be used strictly in reference to the Rb polarization state, and never to that of the ^{3}He or ^{129}Xe. In this work, we measured directly the frequency-shift ratio in Eq. (3.15), averaging many measurements to reduce the statistical uncertainty. We then multiplied by the previously measured $(\kappa_0)_{\mathrm{HeRb}} = 4.52 + 0.00934\ T$ [121] (presumed valid over our

temperature range), where T is the temperature in °C, to deduce $(\kappa_0)_{\mathrm{XeRb}}$. Finally, we use the previously measured ratio (3.7) to infer $(\kappa_0)_{\mathrm{KrRb}}$.

3.4 Experimental Setup

Measurements were made on six $d = 7$ mm i.d. sealed uncoated Pyrex-glass spheres containing a few milligrams of naturally abundant Rb metal, along with ^{3}He, Xe (enriched to 86% ^{129}Xe), and N_2 in the various ratios shown in Table 3.1. The cells are broadly divided into two categories containing high (50-100 Torr) and low (5-10 Torr) partial pressures of Xe. Spheres were used because Eq. (3.15) is strictly valid only for the case of a uniform spherical distribution of Rb magnetization for which the net average through-space dipole field is everywhere zero. Effects due to imperfect geometry will alter the ^{3}He shift only, because $(\kappa_0)_{\mathrm{HeRb}}$ is on the order of unity, whereas $(\kappa_0)_{\mathrm{XeRb}}$ is two orders of magnitude larger. The small "pull-off" volume that results from cell fabrication (1-3% of the total cell volume in our case), and an inhomogeneous laser intensity through the cell, can both give rise to imperfect geometry. We note that geometrical shifts due to the nonspherical nuclear magnetization distributions are less significant: rapid diffusion (compared to spin-exchange) more readily guarantees a near-spherical distribution, and the ^{3}He magnetization is not inverted when the Rb magnetization is reversed. In the case of ^{129}Xe, the magnetization is quickly attenuated/inverted because of rapid spin exchange; however, low [Xe] and low γ_{Xe} make any residual shift negligible. We have determined through a combination of numerical modeling and experimentation that geometrical shifts amounted to no more than a 1-2% effect in even the most extreme cases.

NMR free-induction decays (FIDs) were acquired at 67.6 MHz (^{3}He) and 24.5 MHz (^{129}Xe) in a horizontal-bore 2 T superconducting magnet (Oxford). The Apollo (Tecmag) console is equipped with room-temperature shims and a gradient coil set for imaging. The probe is a 35 mm diameter Helmholtz coil immersed, along with the cell, in an oil bath contained in an Al-block reservoir with a plate-glass window to admit laser light. For the lower temperature data, the cell was immersed in mineral oil; for the higher temperature points, safflower oil (with a higher boiling point) was used. The probe could be tuned *in situ* from one nucleus to the other by manually switching in/out additional capacitance without otherwise disturbing the apparatus. The Al block was heated with air that flows past an external filament heater. The IR-transparent oil bath reduced the temperature inhomogeneity across the cell to < 1 °C. (The temperature inhomogeneity was observed

with the laser on to be as large as 30 °C in a flowing-air oven). A 30 W diode-laser array model A317B (QPC Lasers), externally tuned to the 795 nm Rb D_1 resonance and narrowed to ≈ 0.3 nm FWHM with a Littrow cavity [131], was mounted on an optical table with the optical axis aligned with the magnet bore (and the cell) for SEOP; the maximum narrowed output was ≈ 20 W. The quarter-wave plate in the optical train was mounted in such a way as to allow precise and reproducible manual rotation about the vertical axis by 180° in order to rapidly reverse the Rb magnetization. The magnetization reversal is accomplished in a time on the order of the characteristic optical pumping rate (a few tens of microseconds) after the waveplate has been rotated into place; in practice the reversal takes ≈ 0.5 s.

3.5 Experimental Challenges

Here I will give a brief history of the iterations of the experiment and some of the problems we faced and solved. The hope is that some of the ideas we tried might shed light on some common experimental challenges associated with high-field SEOP, give some idea of the experimental constraints that contributed to the error in our results, and provide a brief historical record of the experiment for the benefit of future iterations and extensions of the experiment.

The original working setup of the experiment consisted of an air-heated oven with a glass window to allow the passage of laser light (see Fig. 3.1). The cell was mounted on a Teflon stand and surrounded by a set of Helmholtz transmit/receive coils. Resistive thermal devices (RTDs - F3105 Omega) were mounted on either side of the cell behind white Teflon shields, and a third RTD was mounted ≈ 2 cm from the cell in the back of the oven and also shielded so that it was not directly exposed to the laser light.

3.5.1 Temperature

The RTDs were mounted on either side of, and in physical contact with, the cell so that an estimate of the temperature gradient across the cell could be made. Our suspicions were raised that the cell temperature was not the same as the temperature reading on the RTD near the back wall of the oven when an inspection of a cell after running an experiment showed that the glass had deformed along the back wall of the cell opposite to the incident laser light. Since the softening point of Pyrex glass is near 800 °C, we became concerned that the laser was causing excessive heating of the cell that was not represented by the distant RTD.

Subsequent carefully controlled experiments confirmed that our 30 W laser was causing excessive heating of the cell in an inhomogeneous way; thermal gradients across the cell were measured to be as great as 30 °C with the heating air flowing. When the air was turned off, the gradients grew to over 60 °C across the 0.7 cm cell with the absolute temperatures on one side reaching well over 300 °C before the laser was blocked and the experiment aborted to preserve the integrity of the cell.

Attempts to homogenize the temperature across the cell included: coating the cell in GC electronic thermal paste with a high thermal conductivity, directing independent air streams at either side of the cell, and attempting to spatially broaden the laser at the cost of losing some power to more uniformly illuminate the cell. Such attempts improved the situation incrementally, but did not solve the problem. Finally, we abandoned the probe design shown in Fig. 3.1 in favor of a design which would allow the cell to be immersed in an IR-transparent oil of high thermal conductivity to facilitate thermal homogenization across the cell. The physical probe is shown in Fig. 3.2a with a schematic representation in Fig. 3.2b to illustrate the idea.

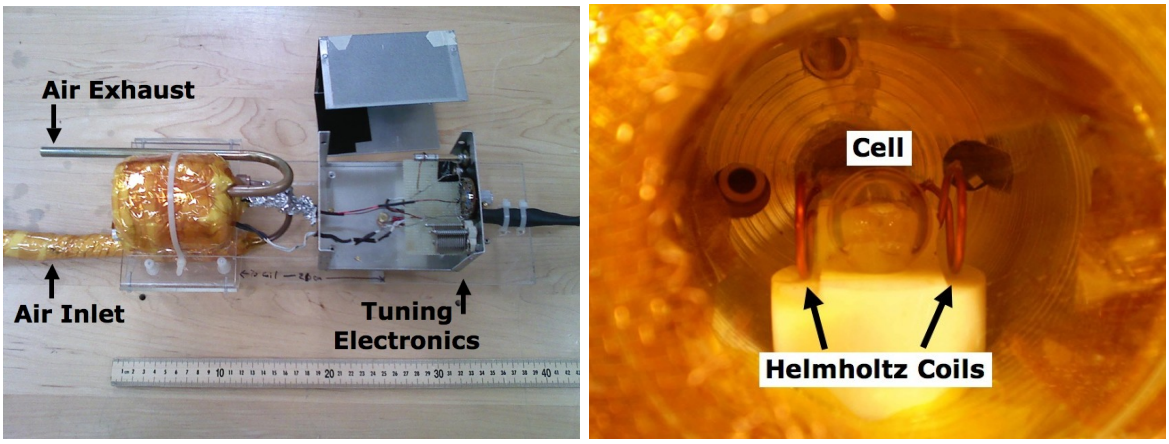

(a) (b)

Figure 3.1: **Forced-air heated probe**. Original working design of the forced-air heated probe. (a) External view of probe showing main components. (b) Looking along the air inlet into the oven. The Helmholtz transmit/receive coils are shown surrounding the cell. The air inlet and exhaust holes are seen in the back of the oven.

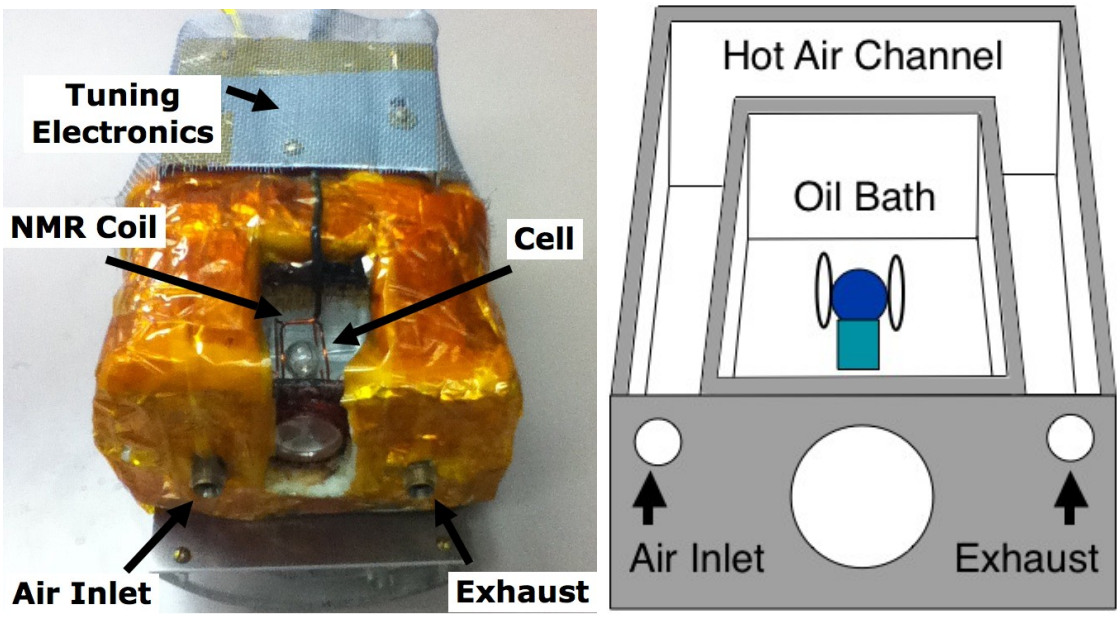

(a) (b)

Figure 3.2: **Final oil-bath probe design.** (a) Physical probe. The cell is seen between the Helmholtz coils inside the oil bath. (b) Schematic drawing of the probe with the top removed to reveal the hot air channel. Oil was introduced into the bath, and the aluminum block was then heated with hot air flowing through the air channel. Laser light is incident through the window on the front of the probe.

3.5.2 Magnet Stability

As discussed above, the frequency shift enhancement factor for Rb-^{3}He is on the order of unity [29]. Therefore, the absolute shifts in the ^{3}He resonance are correspondingly small – approximatley one Hertz (about 20 parts per billion) at 2 T. ^{3}He resonance lineshapes shift about 3 Hz/mG; the experiment therefore required stability in the applied external magnetic field to around 100 μG in order to resolve ^{3}He shifts. The main field from the 2 T superconducting magnet which provided our external field easily met this standard. However, natural gradients in the magnet (both intrinsic and those resulting from finite cell size and inexact cell placement in the magnet) broadened the ^{3}He resonance line too much to resolve shifts on the order of one Hertz. We were thus obliged to use external shims to narrow the ^{3}He lineshape. While properly shimming our samples lead to very narrow lineshapes of about 5 Hz FWHM, the shims introduced a fair amount of field jitter at about the 0.5 Hz level (see Fig. 3.3) during the timescales of our experiments. Such fluctuations of the same magnitude as the expected shifts in the ^{3}He resonance were large enough to

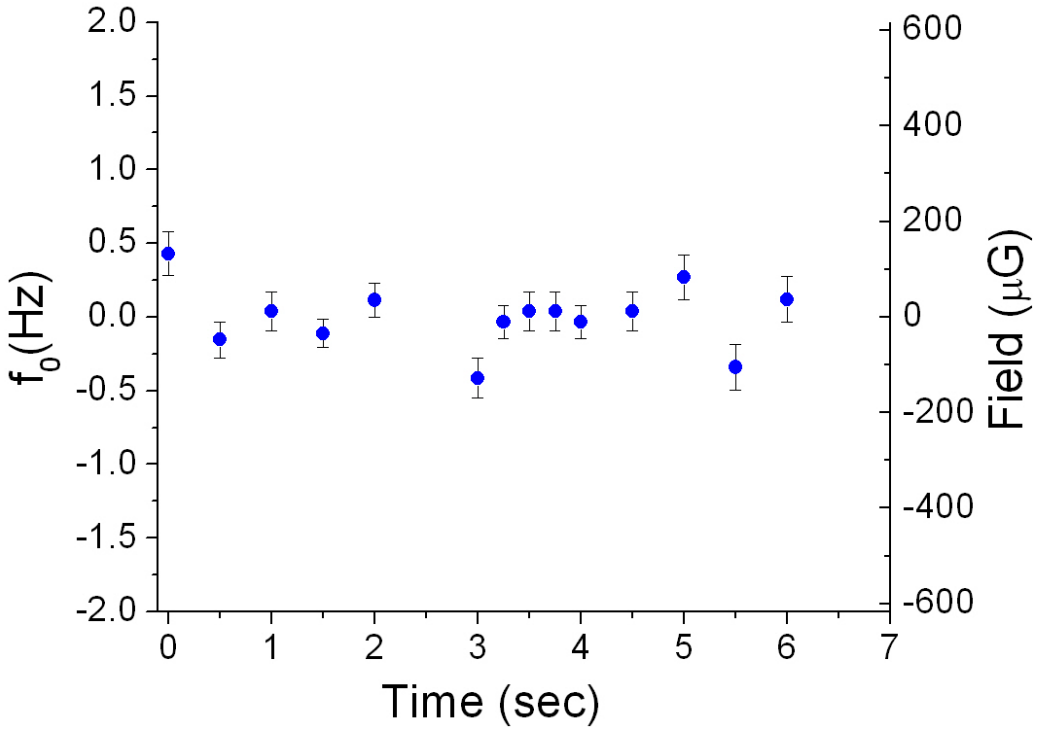

Figure 3.3: **Center frequency of the shimmed ^{3}He resonance curve as a function of time** during steady-state SEOP conditions. Points show the random fluctuations in the external field in the shimmed 2 T superconducting magnet.

endanger the experimental method. Given the random nature of the field fluctuations, however, we were able to average together many measurements and thereby reduce the effective fluctuation to acceptable levels.

3.5.3 Cells

We used the Carr-Purcell Meiboom-Gill (CPMG) pulse sequence (a standard pulsed-gradient technique [132]) to measure the diffusion of ^{129}Xe across our cells in typical steady state conditions for our experiments. Using cell 150A (see Table 3.1) at 170 °C, we measured the diffusion coefficient D_{Xe}. Representative data are shown in Fig. 3.4. The amplitude of the refocused transverse magnetization as the ^{129}Xe diffuses across the applied gradient is

$$M_{\mathrm{grad}}(t) = M_{\mathrm{max}} e^{-t/T_2} \exp\left[\left(-\gamma_{Xe}\frac{\delta H}{\delta z}\right)^2 D_{Xe}\frac{\tau^2}{3}t\right], \tag{3.16}$$

where M_{max} is the maximum echo amplitude, $\delta H/\delta z$ is the applied gradient, and 2τ is

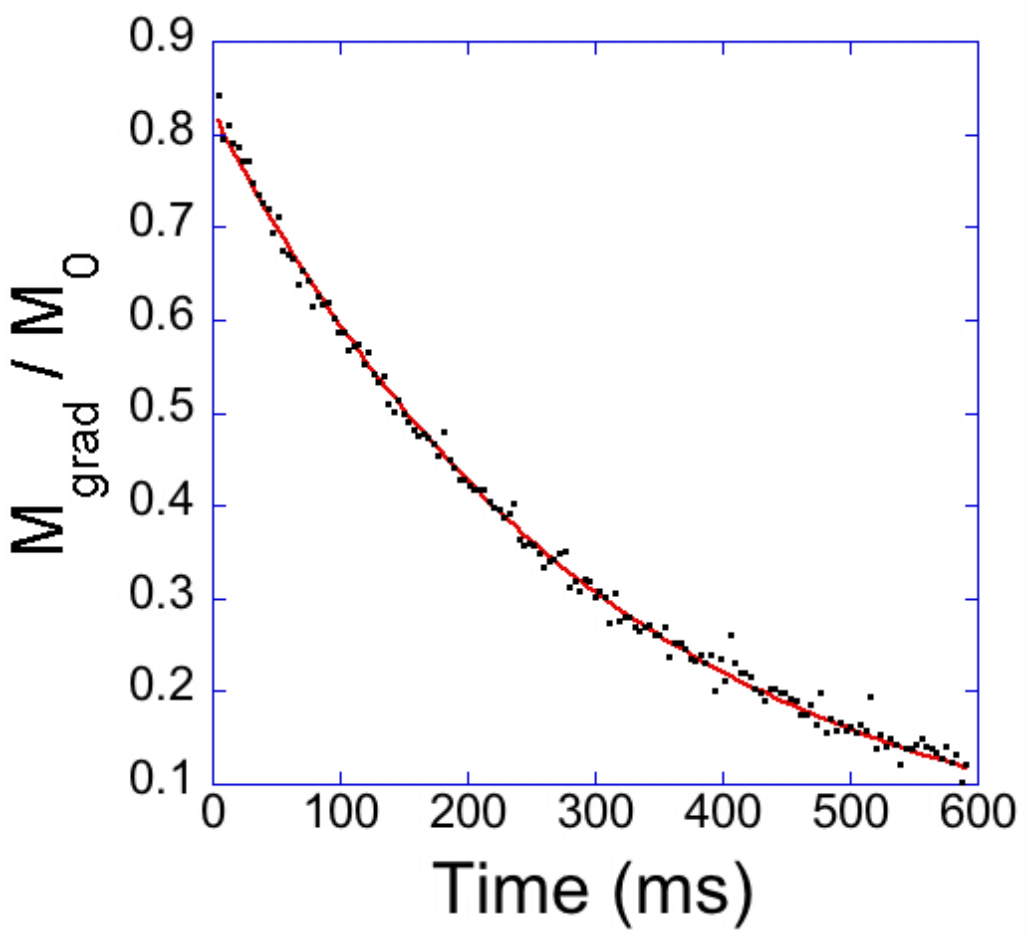

Figure 3.4: **CPMG diffusion measurement.** Ratio of the echo amplitudes for ^{129}Xe acquired with an applied gradient to echo amplitudes acquired without an applied gradient. $\tau = 985\mu$s in this sequence. Data were acquired at 170 °C in cell 150A with a gradient strength of 620 mG/cm.

the time between successive echo maxima. In the absence of gradients, the magnetization dephases due only to the interspin interactions. We define this relaxation as M_0 such that

$$M_0(t) = M_{\max} e^{-t/T_2}. \tag{3.17}$$

The quantity plotted in Fig. 3.4 is the ratio of Eq. (3.16) to Eq. (3.17). A fit to a simple exponential allows us to then extract $D_{Xe} = 0.53 \pm 0.05$ cm^2/s. In acquiring these data we applied a gradient of $\delta H/\delta z = 620$ mG/cm across our sample, which dominates our 2 mG/cm intrinsic gradients estimated from the shimmed linewidths.

To further characterize our cells, we acquired 1-dimensional magnetic resonance images of the ^{129}Xe magnetization. A typical image is shown in Fig. 3.5. The image is a 1-D phase encode along the z-direction, which means that the transverse directions are averaged for each slice selection in the z-direction. The data shown in Fig. 3.5 are the most asymmetric we acquired; most of the other data sets are even more symmetric than those data shown. As each frequency bin represents the average ^{129}Xe magnetization as one moves along the z-direction, the symmetry corresponds to an homogeneous ^{129}Xe magnetization across the cell. The magnetic resonance images corroborated the diffusion measurements shown in Fig. 3.4, which suggest that the average cell transit time τ_d for a ^{129}Xe atom is approximately $\tau_d = d^2/6D_{\mathrm{Xe}} \approx 150$ ms. It follows that τ_d is much faster than the fastest measured spin-exchange times (on the order of several seconds), and we conclude that the ^{129}Xe magnetization is reasonably uniformly distributed in the measurement cells at all times.

Both the diffusion measurements and the ^{129}Xe imaging were at least partially motivated by the actual shapes of the acquired noble-gas spectra. The lineshapes, examples of which are shown below, show some initially surprising features that complicated the data analysis. The details of the analysis are explained in Sec. 3.7. First, we comment briefly on the character of the lineshapes in Fig. 3.6 and postulate a model to facilitate their interpretation.

3.6 Data Acquisition

Prior to data acquisition, SEOP was performed on the cell for a time ≥ 1 h, sufficient to build up polarization in both nuclear species. An auto-shimming procedure was performed with the laser blocked using the ^{3}He frequency spectrum to narrow the resonance line to ≈ 5 Hz FWHM. Blocking the laser during the shimming procedure was necessary to avoid shim compensation for Rb magnetization inhomogeneities (explained below). After unblocking the laser and allowing a SEOP steady state to be established, the probe electronics were switched to acquire one of the nuclear resonances (either ^{129}Xe or ^{3}He). As quickly as possible an FID was acquired, the Rb magnetization was reversed by a rapid rotation of the quarter-wave plate in the optical path, and a second FID was acquired. This basic procedure took < 1 second to perform, minimizing the effect of static field drift (see Fig. 3.3); it was then repeated ≈ 15 times before switching to the other nucleus. Provided $|[\mathrm{Rb}]\langle S_z\rangle|$ remains constant throughout the measurement, the resulting frequency spectra yield ^{3}He and ^{129}Xe shifts suitable for use in Eq. (3.15), although the analysis necessitates some care.

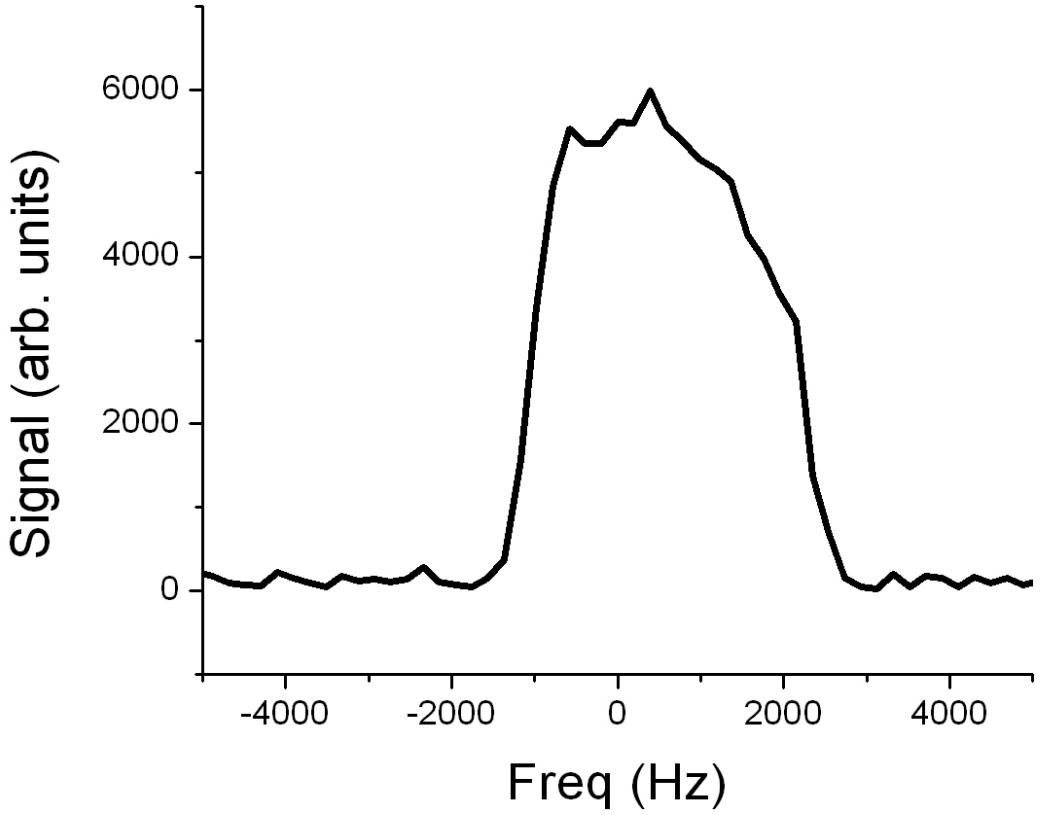

Figure 3.5: **Image of ^{129}Xe magnetization.** 1-D phase encode image of the ^{129}Xe magnetization in cell 150A. These data show the extreme of nonsymmetry in all the acquired images; the majority were even more symmetrical. These images corroborate our assumptions of uniform nuclear magnetization in the cells during steady-state SEOP conditions.

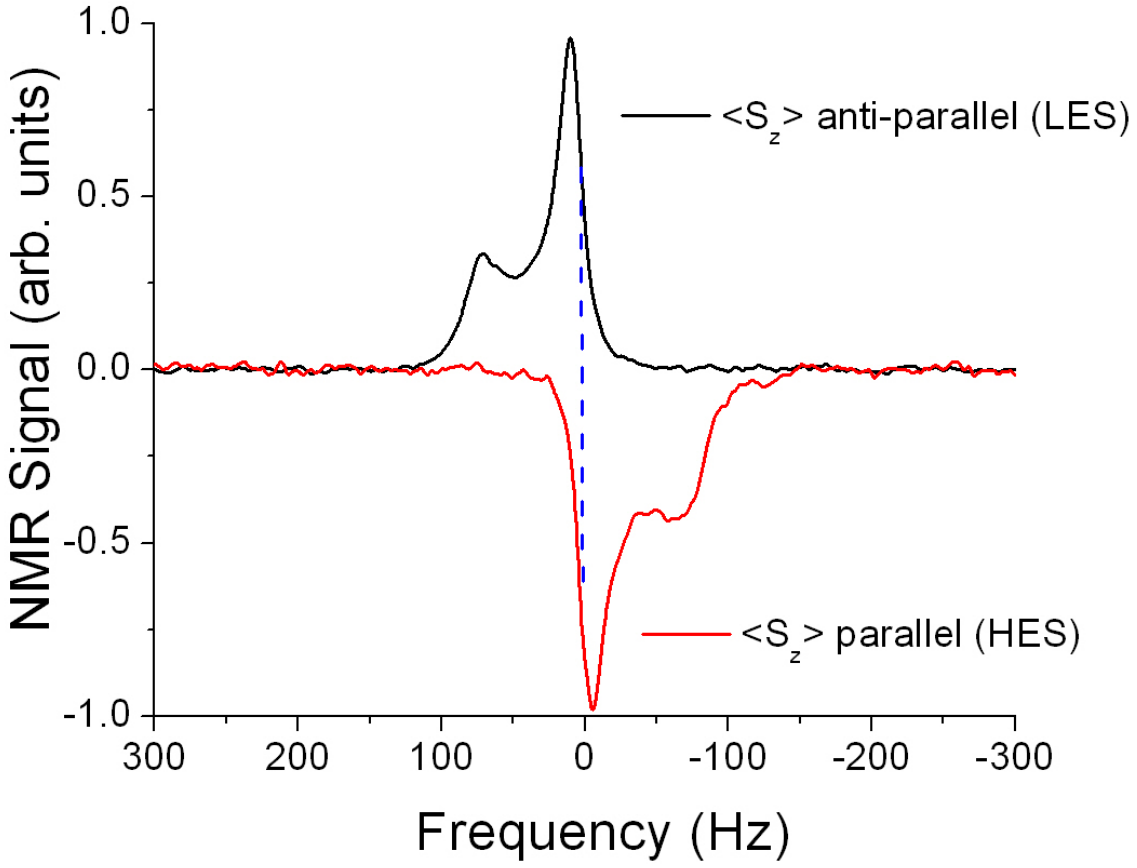

Figure 3.6: ^{129}**Xe spectra in the presence of polarized Rb** in the high-energy state (HES) and the low-energy state (LES). The blue dotted line shows the location of the center of the narrow single-peak spectrum acquired in the presence of unpolarized Rb (not shown). The broadening, shifts, and features are due to inhomogeneous Rb magnetization.

3.6.1 ^{129}Xe Spectra

Consider Fig. 3.6. The xenon spectrum above the x-axis is acquired with the Rb in the low-energy state (LES = $\langle S_z \rangle$ antiparallel to the static magnetic field). The spectrum below the x-axis is acquired after the quarter-wave plate has been switched, *i.e.*, with the Rb in the high-energy state (HES = $\langle S_z \rangle$ parallel to the static magnetic field). Given the results of the diffusion measurements and the xenon images (see Sec. 3.5.3), the xenon magnetization is considered to be uniform across the cell. The xenon spectra therefore can be considered as a one-dimensional map of NMR frequency shift associated with the inhomogeneous distribution of Rb magnetization. However, the shape is also affected by xenon diffusion. Diffusion of xenon is fast enough on the time scale of the FID that a given spin sees at least a partial average of frequency shifts. We hypothesize that the two-peak structure for ^{129}Xe resonance emerges as [Rb] increases due to the abrupt transition in the cell between fully polarized and nearly unpolarized Rb [12].

The small shifted and large unshifted peaks evident in each lineshape in Fig. 3.6 can then be regarded as a measure of the xenon atoms in contact with polarized and unpolarized Rb atoms, respectively. For this reason we term the unshifted peak near 0 frequency as the "dark" peak and the shifted feature the "light" peak. At 200 °C where these spectra were acquired, the Rb number density [Rb] is very high — there are no longer enough photons incident on the cell to keep the Rb vapor fully polarized. Additional dark areas of unpolarized Rb may be present due to lensing effects at the cell wall. As the laser intensity is increased, or the temperature (and therefore [Rb]) is decreased, we see the dark peak begin to decrease in size in favor of the light peak, indicating that more and more xenon is in contact with polarized Rb. We thus observed that there were substantial fractions of the cell volume at the highest temperatures where the Rb polarization was quite low. The situation is not unlike exchange between two chemically inequivalent sites, where the spectrum changes from two distinct peaks in the limit $\tau_{ex}\Delta\omega >> 1$ to a single motionally narrowed peak in the opposite limit. Here, τ_{ex} is the exchange time between sites, and is analogous to the diffusion time τ_d across the cell. $\Delta\omega$ is the difference in frequency for the two sites, analogous to the frequency difference between ^{129}Xe in contact with polarized and unpolarized Rb. In our ^{129}Xe data is it often the case that $\tau_d\Delta\omega \geq 1$.

3.6.2 ^{3}He Spectra

Figure 3.7 shows the ^{3}He spectra corresponding to the ^{129}Xe spectra shown in Fig. 3.6. Once again, the spectrum above the x-axis is acquired with the Rb in the low-energy state while the spectrum below the x-axis is acquired with Rb in the high-energy state. In contrast to the ^{129}Xe spectra, the ^{3}He lineshapes show only symmetric single peaks. In our model of exchange between two chemically inequivalent sites, the ^{3}He, with faster diffusion and a much smaller frequency-shift dispersion, is in the limit $\tau_d \Delta\omega << 1$, corresponding to a single-peak spectrum.

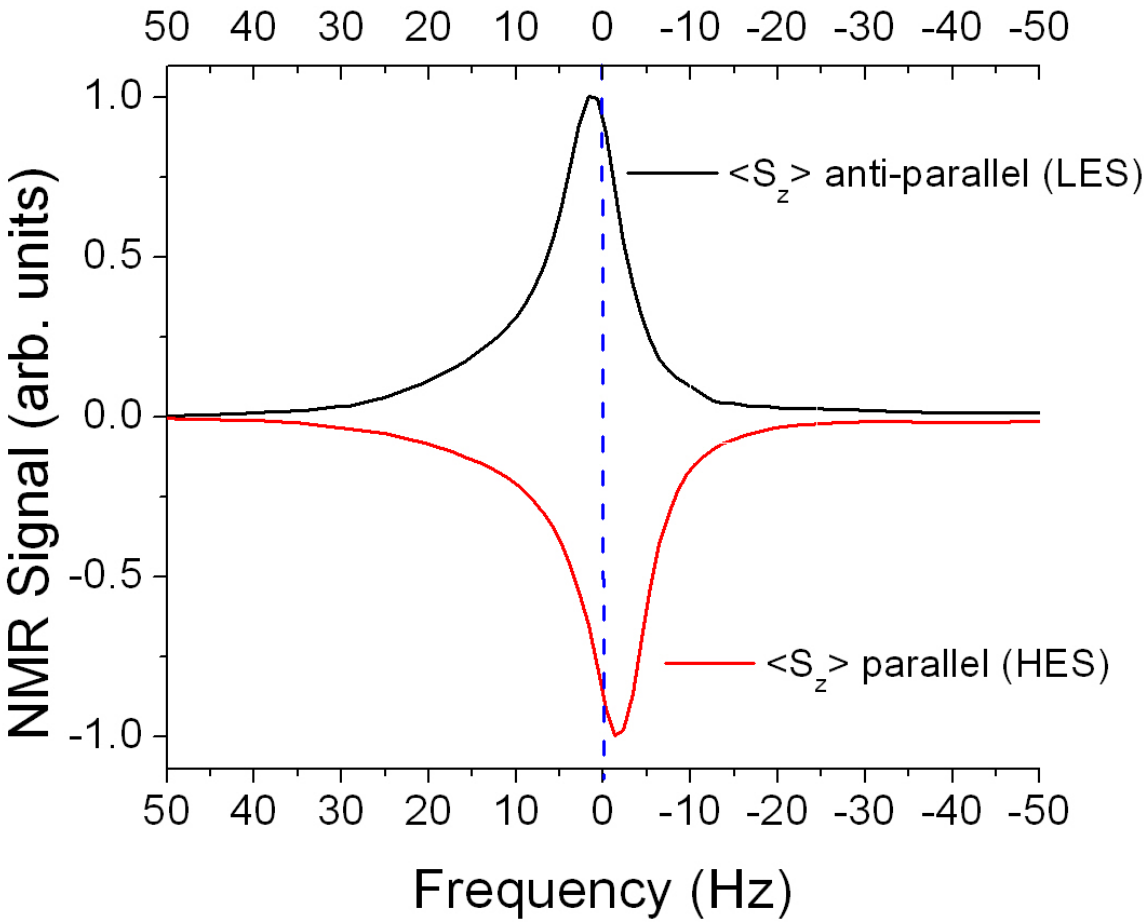

Figure 3.7: **^{3}He spectra in the presence of polarized Rb** in the high-energy state (HES) and the low-energy state (LES). The blue dotted line shows the location of the center of the narrow single-peak spectrum acquired in the presence of unpolarized Rb.

3.7 Data Analysis

We note that the shapes of the HES and LES ^{129}Xe spectra in Fig. 3.6 are symmetric about the narrow spectrum acquired with unpolarized Rb. This unpolarzied spectrum is not shown in Fig. 3.6, but the location of its maxima is marked with the dotted line. Symmetry about this unpolarized peak was not always observed, although it is true of all the data used in determining the enhancement factor. Significant asymmetry in the ^{129}Xe spectra in the LES vs HES can be understood by considering the transitions that are induced by the $\sigma+$ or $\sigma-$ photons generated when the quarter-wave plate is rotated. Fig. 3.8 shows schematically that at 2 T the absorption profile for the $\sigma+$ and $\sigma-$ photons changes from the common low-field picture shown in Fig. 3.8a to the less symmetric high-field case shown in Fig. 3.8b. Our laser spectrum was narrow enough ($\approx$ 150 GHz) that the optical pumping was affected by the $\approx$ 75 GHz Zeeman shift of the D_1 resonance in a 2 T field for $\sigma+$ compared to $\sigma-$ light, as seen in Figs. 3.8c and 3.8d. For some data, a small reproducible laser-tuning adjustment was made after flipping the quarter-wave plate, in order to re-center the absorption line with the laser spectrum. In this case, the symmetry of the HES and LES spectra was used as an indicator that this adjustment had been made properly. For other data, we broadened the laser to $\approx$ 950 GHz to guarantee symmetric absorption.

The condition of a uniform nuclear polarization (verified by imaging for ^{129}Xe ,and clearly true for ^{3}He from the shape of the resonance lines) assures that all Rb spins in the cell are weighted equally in the NMR spectra. This means that the shift in the spectral "center of mass" (COM) that occurs when the Rb magnetization is flipped corresponds to the volume-averaged frequency shift for both species, regardless of which regime of diffusion-driven exchange (discussed above) holds for either species. To determine volume-averaged frequency shift for the ^{129}Xe spectra, the FIDs are multiplied by an apodizing exponential with a characteristic decay time about four times smaller than that of the FID. The subsequent fast Fourier transform produces a single broad symmetric spectral line that peaks at the spectral COM, the value of which is unchanged by the apodization procedure. As the raw ^{3}He spectra already consist of a single symmetric peak, they need no manipulation prior to measuring the shift. The shifts $\Delta\nu_{\mathrm{He}}$ and $\Delta\nu_{\mathrm{Xe}}$ are then determined by comparing the respective HES and LES spectra and measuring the shift in a single peak. We note that for the equal-weighting assumption to be satisfied, the radio-frequency excitation field has to be homogeneous over the cell; if not, the shift ratio can depend weakly on the flip angle used. This was observed in our early data when using a Helmholtz coil

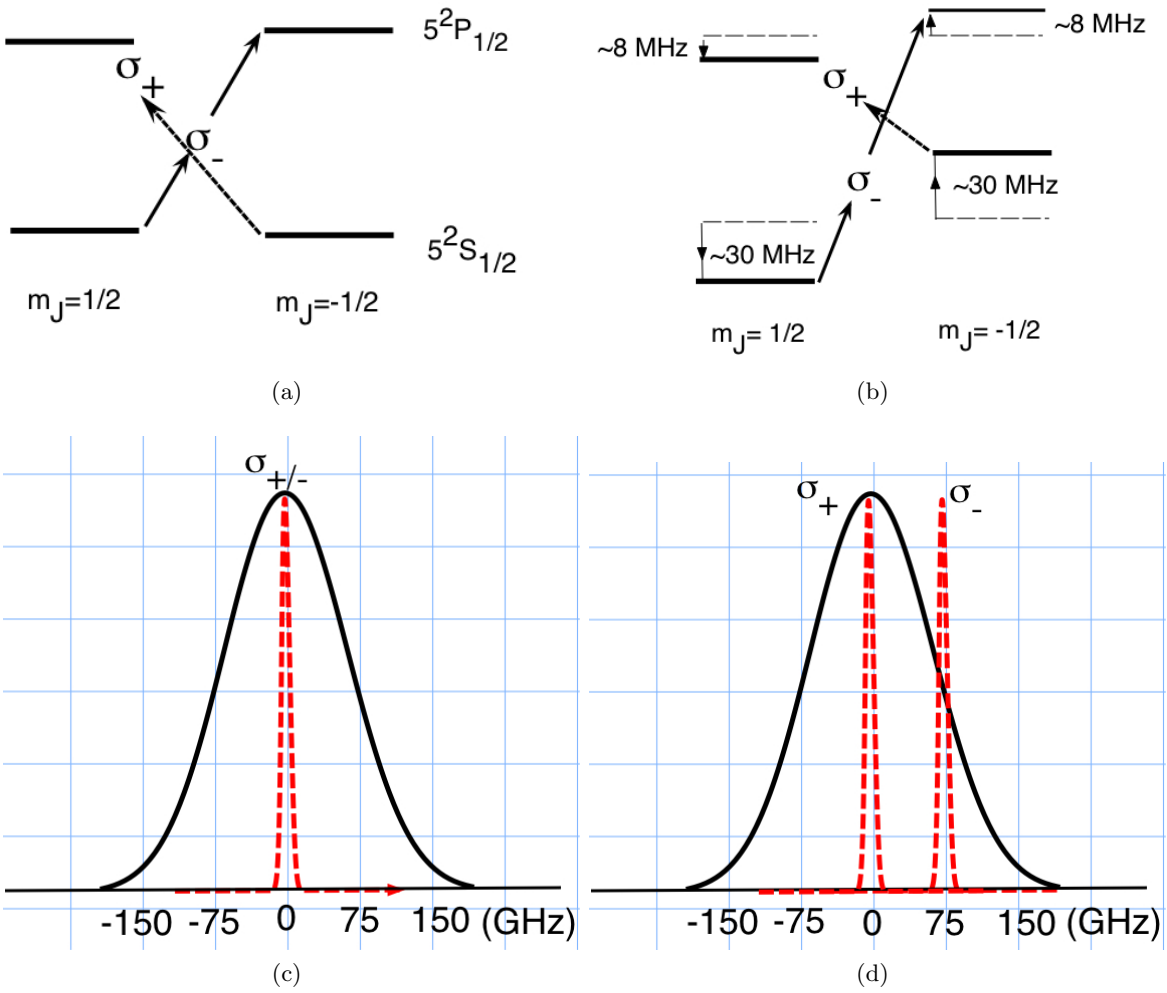

Figure 3.8: **Rb 87 D_1 hyperfine structure in an external magnetic field.** (a) D_1 splitting in the low-field regime with levels labeled by the uncoupled projection of the total electron angular momentum m_J. Equivalence of the σ_+ and σ_- induced transitions is indicated by the energy level diagram. (b) D_1 splitting in the high field regime. Dashed lines indicate the low-field energy levels, with solid lines indicating the shifted levels at 2 T. (c) 150 GHz FWHM laser emission line (solid) centered at the D_1=3.77 × 10^{14} GHz (shown as 0 on the graph). The dotted line shows the Rb absorption profile indicated by the arrows in (a). Pumping into the LES with $\sigma-$ light occurs at roughly the same energy as pumping into the HES with $\sigma+$ light. (d) 150 GHz FWHM laser emission line (solid) centered at the shifted $\sigma+$ D_1 frequency (shown as 0 on the graph). The dotted lines show the Rb absorption profile indicated by the arrows in (b). Resonance with the LES with $\sigma-$ transition now occurs roughly 75 GHz from the HES transition induced by $\sigma+$ light.

similar to the one shown in Fig. 3.1. We later employed a larger Helmholtz probe coil as shown in Fig. 3.2 (sacrificing some sensitivity) to mitigate this problem.

3.7.1 Low [Xe] Cells

The calculated values for $(\kappa_0)_{\mathrm{XeRb}}$ are plotted vs. temperature T for the three low-[Xe] cells in Fig. 3.9. The error bars shown reflect only the statistical uncertainty in the measured frequency-shift ratio, and do not include the uncertainty in $(\kappa_0)_{\mathrm{HeRb}}$; they are dominated by the large relative uncertainty in the small ^{3}He frequency shifts. The low-[Xe] cells (both individually and collectively) show no significant temperature dependence between 140-220 °C; the weighted average of all of these points yields an uncertainty of $< 1\%$. If the same weighted average is taken on a cell-by-cell basis, there is a larger spread (see Table 3.1), suggesting some unknown systematic errors at the few-percent level. These could include, for example, small cell-dependent geometrical effects. We accordingly increased the uncertainty in the shift ratio, which is represented by the hatched range in Fig. 3.9. Finally, we add the 1.8% uncertainty in the value of $(\kappa_0)_{\mathrm{HeRb}}$ [121] in quadrature to arrive at our final result in Eq. (3.6).

3.7.2 High [Xe] Cells

The calculated values for $(\kappa_0)_{\mathrm{XeRb}}$ are plotted vs. temperature T for the three high-[Xe] cells in Fig. 3.10. Below $T \approx 175$ °C, the data for the high-[Xe] cells are generally consistent with the hatched range (reproduced in Fig. 3.10 for comparison) which characterizes the low-[Xe] data. However, at the highest temperatures the measured shift ratio drops by about 20%. These ten or so data points out of 60 acquired from all 6 cells are at the extremes of high temperature, high [Rb], and rapid Rb spin destruction (due to higher [Xe]); yet, we are unable to connect these physical conditions in a plausible way to the observed systematic depression of the shift ratio. We considered whether fast Rb-^{129}Xe spin exchange might lead to a violation of our fundamental assumption of uniform nuclear magnetization, but this would *increase* the shift ratio by preferentially weighting the regions of higher Rb magnetization in the ^{129}Xe spectrum. We also tested for extreme geometrical effects by remeasuring the shift ratio for both high- and low-[Xe] cells at a given temperature after significantly decreasing the laser power. The ^{129}Xe spectrum changed dramatically under these conditions, but the shift ratio was unchanged within error. We note that this test also served as a check on the robustness of the COM data-analysis method.

Schaefer *et al.* [27] calculated $(\kappa_0)_{\mathrm{XeRb}} = 726$ and measured $(\kappa_0)_{\mathrm{XeRb}} = 644 \pm 260$ by

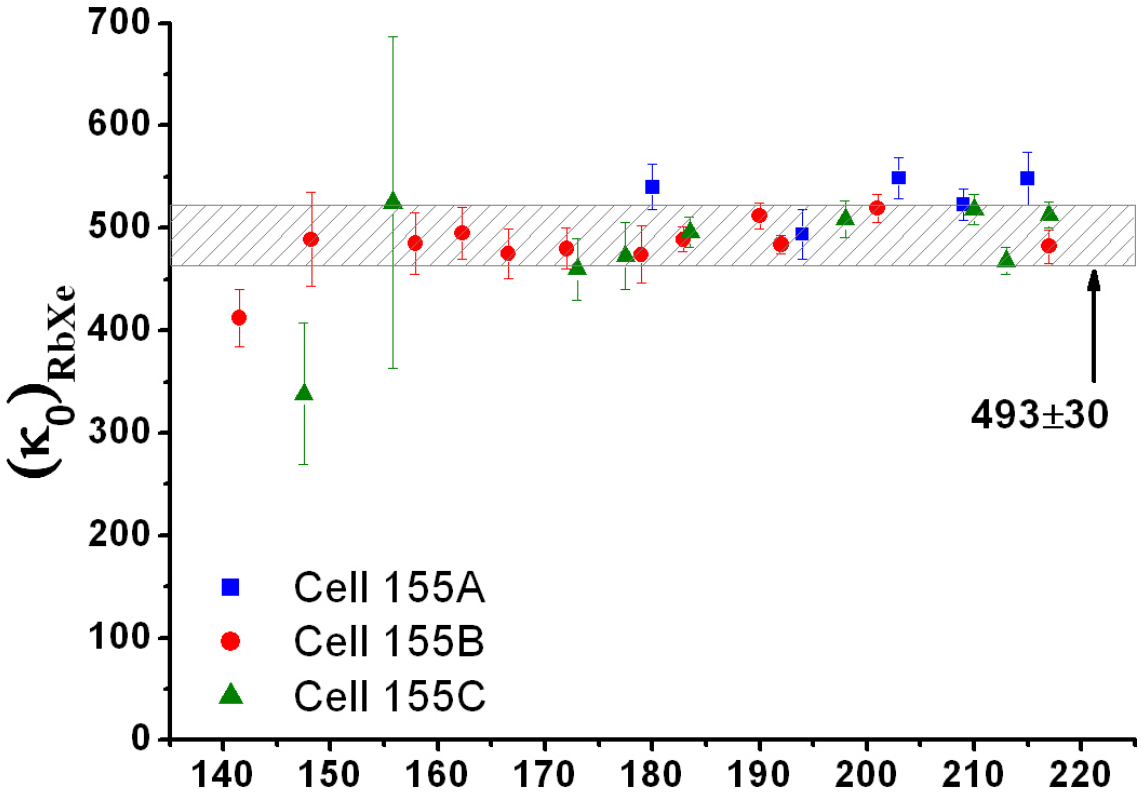

Figure 3.9: **Enhancement factor $(\kappa_0)_{\mathbf{XeRb}}$ plotted vs. temperature for three low-[Xe] cells**. The weighted average of all the low-[Xe] data points shown is 493, with the estimated uncertainty shown by the hatched region. We take these temperature independent data to represent the best estimate of $(\kappa_0)_{\mathrm{XeRb}}$.

mapping the ^{129}Xe and ^{83}Kr NMR spectra with the Rb EPR shift at low field. The dominant source of error in their measurement came from modeling the Rb polarization. The theory that Schaefer *et al.* present favors a zero to weakly-positive temperature dependence. The anomalous behavior of our high-[Xe] cells at high temperatures is neither consistent from cell to cell nor consistent with a plausible theoretical temperature dependence. We thus take the global average of the low-[Xe] data as expressed in Eq. (3.6) as our best estimate of $(\kappa_0)_{\mathrm{XeRb}}$, independent of temperature.

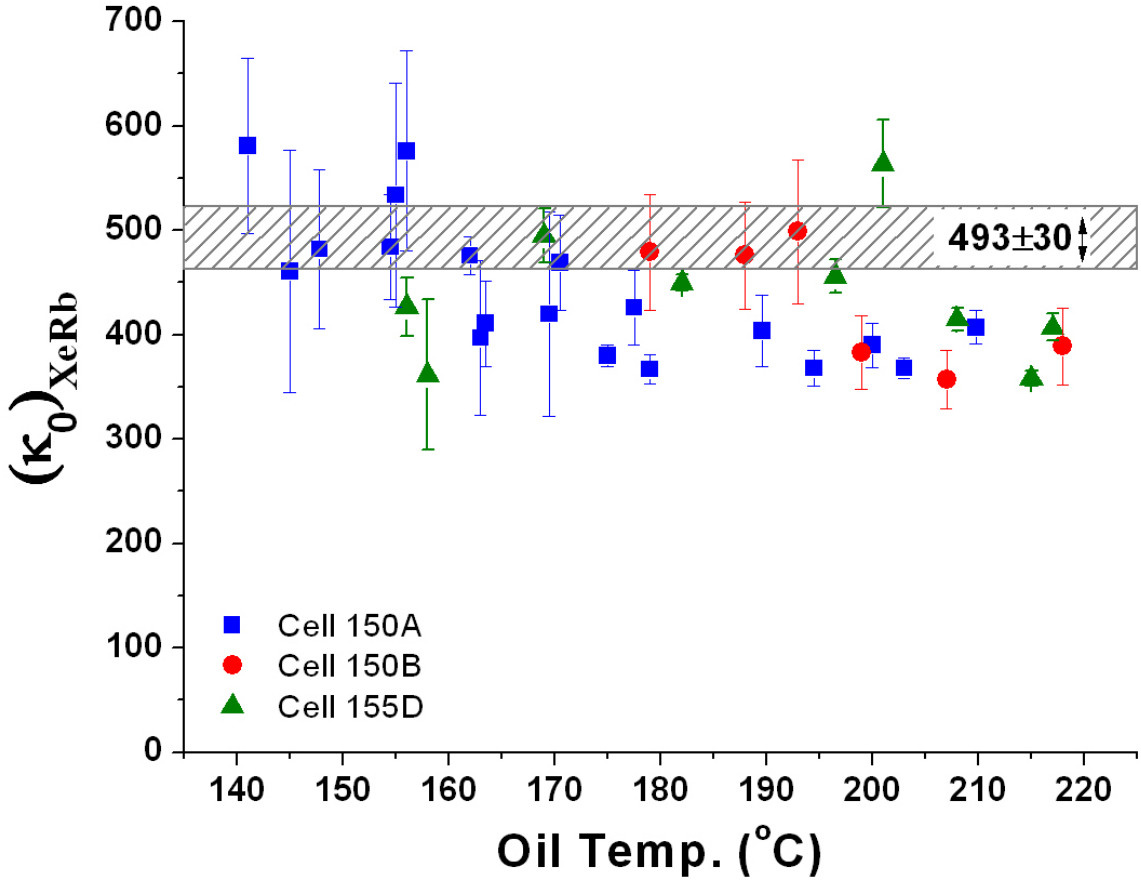

Figure 3.10: **Enhancement factor $(\kappa_0)_{\mathbf{XeRb}}$ plotted vs. temperature for three high-[Xe] cells**. The weighted average of all the low-[Xe] data points is 493, represented by the hatched region with the width showing the estimated uncertainty. The high-[Xe] data are consistent with the low-[Xe] data up to about 175 °C; the ≈ 20% drop-off at the highest temperatures is not yet understood.

3.8 Conclusions

We have measured the frequency-shift enhancement factors $(\kappa_0)_{\mathrm{XeRb}}$ and $(\kappa_0)_{\mathrm{KrRb}}$ to be

$$(\kappa_0)_{\mathrm{XeRb}} = 493 \pm 31$$
$$(\kappa_0)_{\mathrm{KrRb}} = 207 \pm 17.$$

Many of the diverse fields in which the use of hyperpolarized noble-gases generated by spin-exchange optical pumping (SEOP) has become essential require a precise understanding of the mechanisms that affect the frequency-shifts of the noble-gases. Consistent and accurate measurements of such shifts allow us to quantify and demonstrate understanding of these mechanisms. Moreover, accurate measurements of changes in the resonance frequencies can provide constraints on poorly known quantities such as the wave function enhancement factor η and the noble-gas—alkali-metal interaction potentials $V(r)$ that affect much of the fundamental physics of spin-exchange optical pumping. In a practical sense, these measurements will allow the first accurate polarimetery measurements of noble-gases in flow-through polarizer systems.

CHAPTER 4

OPTICAL PUMPING OF SI:P

In early 2008, D. R. McCamey and C. Boehme demonstrated an innovative new technique for achieving high nuclear polarizations in phosphorus-doped silicon (Si:P) without resonant manipulations of either the electronic or nuclear spin. The effect was demonstrated at the National High Magnetic Field Laboratory using electron spin resonance (ESR) and electrically detected magnetic resonance (EDMR), and the work was subsequently published in a 2009 Physical Review Letter [133]. With hope to observe the nuclear polarization enhancement directly with NMR, Boehme approached our group in 2008 to instigate a collaboration. I was assigned to work on the project. Though we were ultimately unsuccessful in achieving our aims for publishable data for reasons speculated on below, the year's worth of work yielded some interesting and useful physics that bear documentation.

4.1 Introduction

When a silicon atom is replaced by a member of the VB group of the periodic table such as phosphorus, antimony, or arsenic, the replacement atom is termed a "donor." Such an atom has five valence electrons; four will form paired bonds with the surrounding silicon atoms leaving one in a loosely bound Coulomb-like potential of the donor nucleus. The ionization energy of a phosphorus donor in a silicon matrix is ≈ 0.045 eV, corresponding to a temperature of around 500 K. At room temperature, therefore, many of the donors are ionized and the electrons are free to move about the crystal; at low temperatures they may become loosely bound to the donor nuclei.

Fletcher *et al.* [134, 135] were the first to observe spin resonance from bound electrons at low temperatures in antimony-, aresenic- and phosphorus-doped silicon. They observed multiple resonance lines with spacing proportional to the hyperfine splitting in the samples. They observed 4 resonance lines in spin-3/2 arsenic, 6 resonance lines in spin-5/2 antimony, and 2 in spin 1/2-phosphorus. That is, they observed $2I + 1$ lines, where I is the nuclear spin. The following year, Kohn and Luttinger used approximations to effective mass theory

to calculate the donor state wave function $|\Psi(0)|$. Their calculations (which, in light of necessary approximations, they deemed accurate only within a factor of five) yielded a result within a factor of two of the experimentally measured value [136]. With that agreement, they felt confident ascribing the hyperfine splitting of the nuclear resonance lines as being due to electrons bound to the donors.

4.2 Motivation

Impurity centers such as phosphorus in silicon have been widely studied as model systems due, among other reasons, to the very long relaxation times achieved for the electrons in pure samples, and the impurity dependent relaxation times that scale with the impurity concentration [137]. This long (and tunable) relaxation time is the feature that makes these spins attractive as qubits. In Si:P, the longitudinal relaxation time ranges from a few microseconds at 20 K to thousands of seconds at 2 K [138, 139], and the more relevant transverse decoherence time varies from one microsecond at 20 K to around 500 μs at 2 K [140]. These relaxation times are long enough that serious consideration has been given to these systems as the basis of nuclear spin quantum computers [141]. Such considerations have been the motivation behind many studies seeking to improve control and understanding of the Si:P system and the physical processes that underlie its magnetic properties.

4.3 The Model

Four years after demonstrating the "thermodynamically unlikely"[1] Overhauser effect [20] experimentally, Pines, Bardeen, and Slichter [21] showed an analog of that effect operating in doped silicon that was useful in explaining the enhanced nuclear polarization measured in their experiments. Building on these ideas, McCamey and Boehme showed in 2009 [133] that an above-band-gap optical excitation of charge carriers in Si:P could create large nuclear polarizations in a quick and efficient manner, and the effect could be explained using an extension of the ideas of the Overhauser effect [20] (explained in Ch. 1) with some important modifications.

Figure 4.1, which is adapted from Ref. [133], shows the energy level diagram as well as the spin relaxation processes relevant to the system. The relaxation mechanisms are

[1]Reference to famous criticisms made by Bloch and Ramsey among others about the likelihood of the the effect postulated by Albert Overhauser during his postdoctorate years at the University of Illinois.

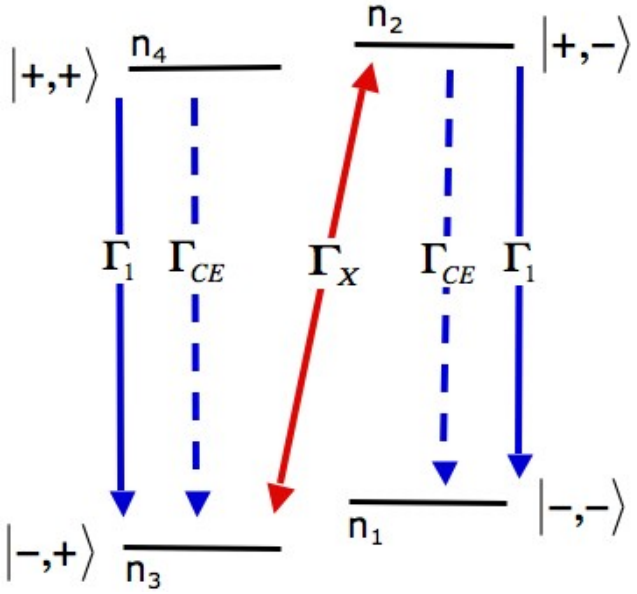

Figure 4.1: **Energy states of a Si:P donor impurity.** Vertical transitions (shown in blue) correspond to electronic T_1 processes, while the diagonal transition (red) is an Overhauser process. Under illumination, solid lines of both colors indicate transitions that attempt to establish equilibrium at the phonon bath temperature T_p, while the dashed lines indicate relaxation processes that occur at the (lower) thermalized electron temperature T_e. When no illumination is present, $T_p = T_e$.

indicated by their rates Γ_i, and the energy levels are labeled as $n_1 - n_4$ for purposes of discussion.

The Overhauser rate Γ_x and the spin-lattice relaxation rate Γ_1 are dominated by phonon-mediated interactions. Importantly, there are two distinct sources of phonons in the system. First, as the sample is immersed in a liquid helium bath, the lattice quickly equilibrates to an equilibrium phonon distribution at the temperature of the helium bath. However, when above-band-gap light (Si:P band-gap is about 1.1 eV) is shone on the sample, it excites photocarriers high into the conduction band. These hot photoexcited carriers quickly thermalize, emitting nonequilibrium temperature phonons in the process. These phonons are in addition to the equilibrium phonons; the combination of the two give the final phonon spectrum characterized by quasitemperature T_p. This temperature characterizes the spin populations generated by the phonons in the system via the relaxation rates Γ_X and Γ_1, both of which are phonon modulated [138].

Figure 4.1 shows an additional relaxation channel labeled Γ_{CE}. This relaxation mech-

anism exists only with the sample illuminated, and is driven by photoexcited carriers promoted into the conduction band by the energetic photons incident on the sample. These carriers can be captured and re-emmitted by a phosphorus donor, leading to the relaxation of the charge carriers; this mechanism may actually be the fastest relaxation mechanism of the thermal electrons [142, 143]. As McCamey *et al.* point out in Ref. [133], the electrons contributing to this process are exclusively thermalized electrons, as the timescale for thermalization is very short compared with the lifetime of the charge carrier.

The important point here is that the thermalized electron spin temperature T_e is not necessarily the same as the quasiequilibrium temperature T_p of the phonon bath because of the constant injection of the photoexcited carriers by the incident light. Differences between T_p and T_e have been seen by others [138, 144], and are known to perturb the populations of spins from equilibrium. The consequence of this temperature imbalance is that the Γ_X processes, which attempt to establish thermal equilibrium between the diagonal states n_2 and n_3, are phonon dominated and will occur at the established phonon temperature T_p. The dominant electron longitudinal spin relaxation processes Γ_{CE} which tend to establish thermal equilibrium between the vertical states n_1 and n_2 and between n_3 and n_4 will attempt to approach an equilibrium dictated by the temperature T_e, the temperature of the thermalized electrons involved in the capture-emission process of the donors. For $T_p > T_e$, this leads to the over-population of level n_1 in the following way. The lower temperature T_e will create a Boltzmann distribution of population with levels n_4 and n_2 at lower occupation levels relative to the more highly populated n_3 and n_1. The higher T_p, however, will push n_3 and n_2 closer to equal populations, in effect forcing some of the overpopulation from n_3 into n_2. The Γ_{CE} process operating at temperature T_e is all the time moving spin population down from n_2 to n_1, and this leads to the overpopulation of n_1 and thus to a polarized nuclear state. This is the analog to the Overhauser effect proposed in Ref. [133], with the temperature imbalance $T_p > T_e$ generated by photoexcitation of charge carriers substituting for the saturation of the electron spin resonance.

4.4 ESR and EDMR Data - Motivation for NMR Experiments

The experiments performed by McCamey *et al.*, as detailed in Ref. [133], show striking nuclear polarizations detected by two indirect methods: electron spin resonance (ESR) and electrically detected magnetic resonance (EDMR). Operating at high magnetic fields

around 8.5 T and temperatures of 3 K, they showed an enhancement of the hyperfine-split ESR spectrum corresponding to a nuclear polarization. An enhancement of the electron resonance associated with the $n_1 \rightarrow n_2$ transition corresponds to the nucleus in the high energy (spin anti-parallel to the field) state, while the $n_4 \rightarrow n_3$ transition corresponds to the nucleus in the low energy (spin parallel to the field) state. The enhancement was shown to disappear when the illuminating light was removed, and to reappear with a time constant on the order of 150 seconds when the light was reintroduced. At the same magnetic fields but lower temperatures of around 1.3 K, they then observed the change in current in an EDMR experiment which indicated a nuclear polarization of around 68% as shown in Fig. 4.2 (reproduced from Ref. [133]). The effect was shown with several different light sources, all of which have spectral components above the Si:P bandgap.

These results inspired the desire to perform a direct measurement of the nuclear polar-

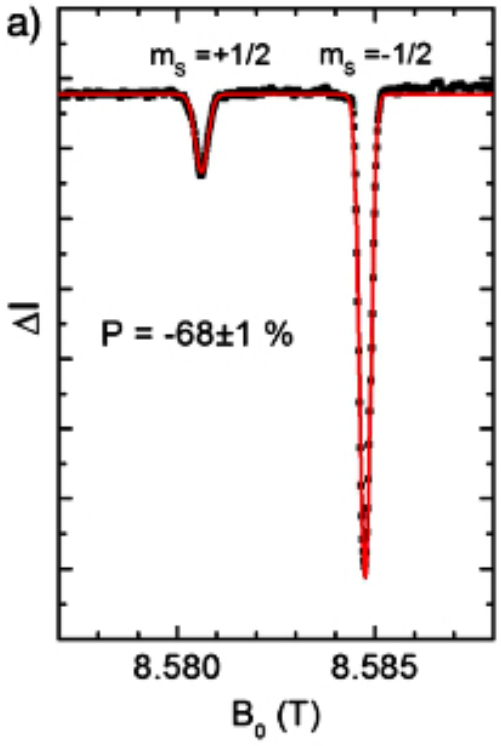

Figure 4.2: **Electrically detected magnetic resonance spectrum of Si:P** from Ref. [133] showing enhanced nuclear polarization. The hyperfine split spectrum shows the two electron transitions corresponding to $n_1 \rightarrow n_2$ transition, (the peak labeled $m_S = -1/2$) and the $n_4 \rightarrow n_3$ transition (the peak labeled $m_S = +1/2$).

ization enhancement by detection of an NMR signal due to the hyperpolarized phosphorus nuclei. If a significant enhancement of the NMR signal could be measured in the presence of light illuminating the sample, it would provide direct evidence of nuclear spin hyperpolarization by excited photocarriers.

4.5 NMR Experiments on Si:P

Nuclear magnetic resonance signals are inherently weak compared to ESR signals due to the small size of the nuclear magnetic moment relative to the electronic moment. Conventional bulk NMR experiments rely on sheer numbers of nuclei to provide detectable signals. A typical solid sample of protons contains 10^{23} nuclear spins which at room temperature have a polarization of about 3×10^{-6} in a magnetic field of 1 T; therefore only 3 atoms in a million contribute to the observed signal. Thus we have 3×10^{17} atoms contributing to the free induction decay signal, which can yield a typical SNR of perhaps 1000:1. Gas phase NMR is more difficult, as a typical sample will start with only 2×10^{19} atoms[2], meaning that after the polarization is computed there are only around 10^{14} atoms contributing to the observable signal; our SNR will be at best around 1:1 with this number of atoms. This represents the lower end of the capability of nuclear magnetic resonance. Densities of atoms in this range require much averaging, often for long periods of time, to tease a usable signal out of the noise.

The Si:P samples we set out to measure were necessarily very lightly doped, as the electrically detected effects were observed to disappear at high dopant concentrations. The typical total number of phosphorus impurities in our samples were on the order of 10^{14} atoms. Under the conditions of the experiment (8 T and 2 K), the polarization of the phosphorus nuclei would be around 3×10^{-3}; with no hyperpolarization only 10^{11} atoms would contribute to the signal and there would be no chance of detection by NMR. Only with near 100% polarization of the phosphorus nuclei would there be a chance of detecting an NMR signal.

4.5.1 Experimental Setup

The physical setup is shown in Fig. 4.3. A 1.6 m aluminum rod spanned the length of the dewar down to the magnet center and secured the sample in the magnet, while

[2]Loschmidt's number is 2.69×10^{19}, which is the number density of atoms of an ideal gas per cc at STP (0 °C and 1 atmosphere).

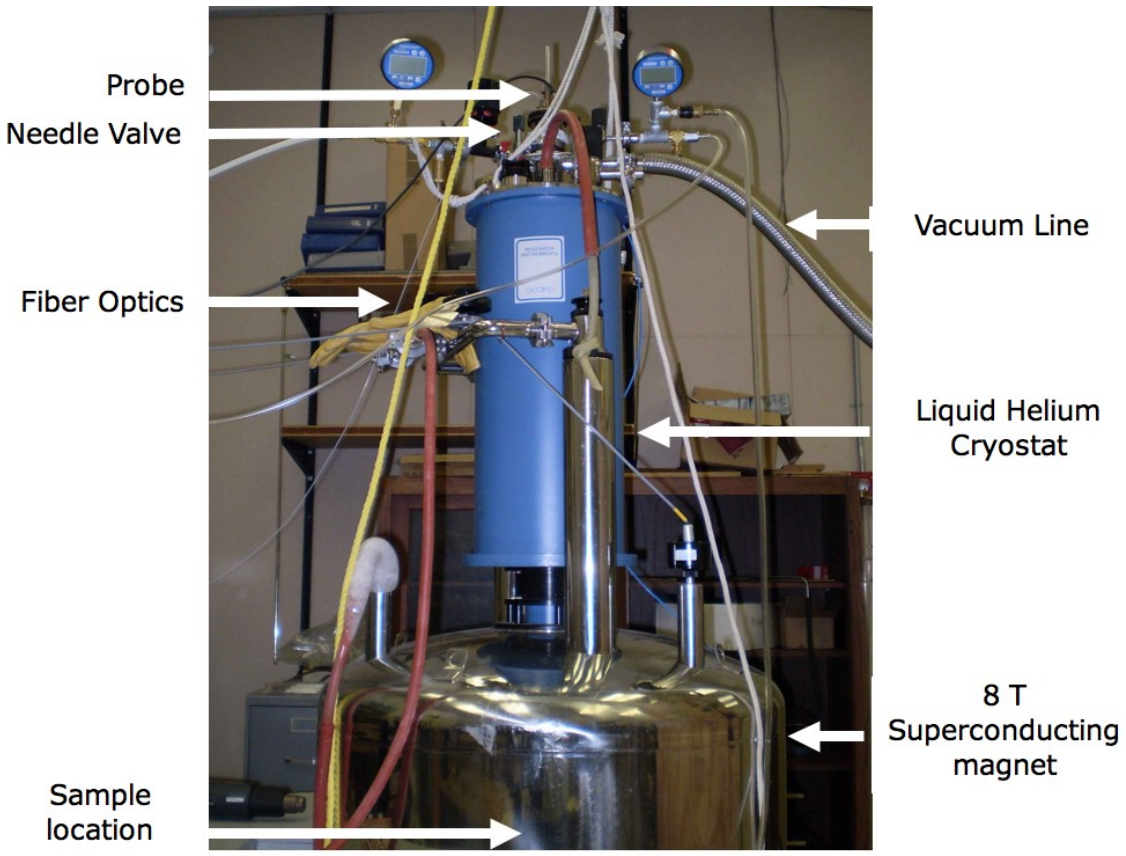

Figure 4.3: **Si:P NMR experimental setup - 8 T superconducting magnet**. The Oxford 8 T vertical-bore superconducting magnet is shown with liquid helium dewar. The vacuum line pulls on the sample space to provide sub liquid helium temperatures. The sample is mounted at the end of the 1.6 m probe that traverses the vertical length of the cryostat. Fiber optics conduct light to the sample.

providing access to the electronic connections outside of the cryostat. Light was conducted into the sample via a low OH 400 μm core multimode optical fiber with a 0.48 numerical aperture to allow for as uniform an illumination at the sample as possible. The fibers ran for approximately 4 meters from the light source to the sample. A 15 W 769 nm infrared laser and a 600 W Oriel xenon discharge lamp were used for illumination of the sample, both of which have the majority of their spectral components above the 1.1 eV bandgap of the Si:P sample. Spectra of both light sources are shown in Fig. 4.4.

The temperature was monitored with a Rox ruthenium oxide resistive thermal device (RX-202A) from Lakeshore Cryogenics and by monitoring the helium vapor pressure above

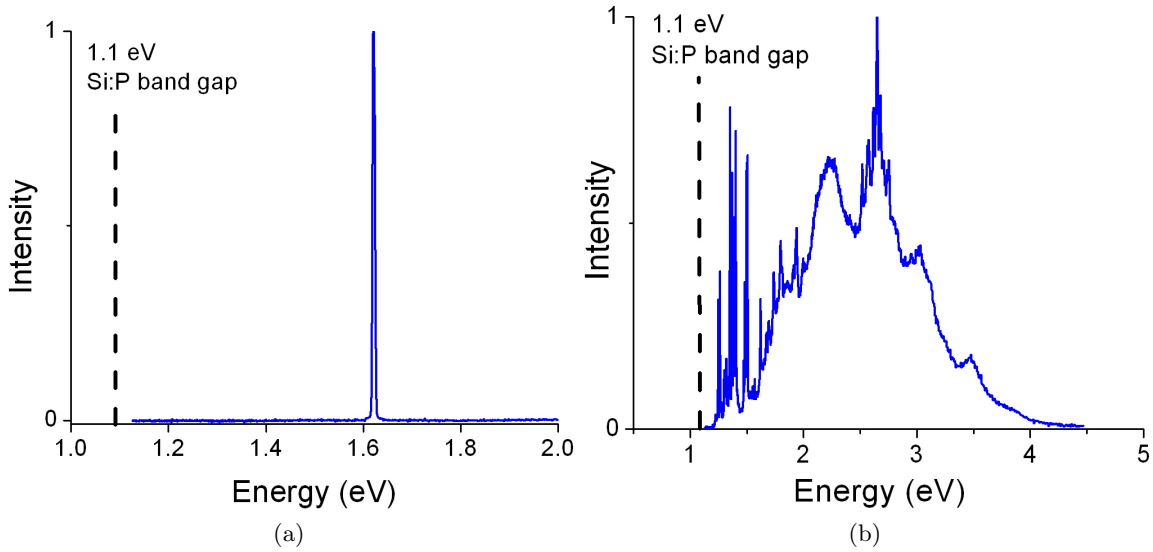

Figure 4.4: **Spectra of two light sources used to illuminate the Si:P samples.** Dotted lines show the location of the Si:P band gap energy. (a) 769 nm infrared laser spectrum. (b) Xenon discharge lamp spectrum.

the helium liquid column in the cryostat (see Appendix B for a table of helium vapor pressures as a function of liquid temperature). Temperatures agreed between the two monitoring methods to within 0.1 K during all experiments. The temperature was maintained by immersing the sample in liquid helium and pumping on the liquid column with a Stokes pump (4000 L/min capacity). This was sufficient to maintain temperatures as low as 1.5 K during our experiments, provided the illumination from the optical fibers did not exceed 2-5 mW. Higher intensities had a heating effect that caused undesirable temperature increases.

NMR measurements were performed on an Aires (Tecmag) spectrometer at frequency $f = 196.69$ MHz. The nuclear precession frequency ω_n was determined as the Larmor frequency plus the hyperfine frequency [23] as

$$\omega_n = \gamma_P H_0 + \frac{A m_S}{\hbar}, \tag{4.1}$$

where γ_P is the phosphorus nuclear gyromagnetic ratio, $A = \Delta B \hbar \gamma_e$ is the hyperfine coupling in the presence of an electron with gyromagnetic ratio $\gamma_e = 1.76 \times 10^{11} \frac{rad}{sT}$, and ΔB is measured from the ESR spectra as 4.2 mT.

4.5.2 NMR Results

Initial calibration experiments were carried out on thallium bromide (TlBr), a rather toxic substance that utilizes the potassium uptake channels in the skin to infiltrate the body with deleterious effects. However, thallium has a spin-1/2 nucleus with gryomagnetic ratio such that we could operate at a similar frequency, $f = 196$ MHz at 8 T, as would be necessary with the Si:P after taking into account the hyperfine shift (4.1). It was necessary to prepare a callibration sample simply because the actual Si:P samples had such a low number density of phosphorus atoms that observation of a signal would only be achieved if the nuclei had already become hyperpolarized, as discussed above.

After the calibration experiments verified that everything was operating optimally, and that temperatures of 1.5 K could be maintained under operating conditions for sufficient periods of time, the samples were switched from TlBr to Si:P and light was shown on the sample. We made educated guesses of the nuclear $T_1 = 150$ s from the ESR data in Ref. [133], which lead to typical NMR acquisition times of 8-10 hours to obtain just 50 averages. Several months of measurements resulted in no discernible signals.

There are several reasons why we may not have obtained a signal even if we were indeed achieving hyperpolarization of the phosphorus nuclei. First, there was some uncertainty in the exact value of the resonance frequency we calculated in (4.1); the inability to measure a bulk signal in the actual sample prevented us from ever knowing if we were looking in the correct place on the frequency spectrum. Second, the incident power of illuminating light used in the experiments in Ref. [133] was a uniform $20 - 100$ mW/cm^2, while within the physical constraints of the NMR magnet shown in Fig. 4.3 we could at best achieve a rather nonuniform $2 - 5$ mW on either side of the sample. It is possible that we simply were not able to provide enough light to achieve the disparity in the temperatures T_p and T_e necessary to achieve hyperpolarization. Third, if all of the above conditions were satisfied appropriately, it is likely that we simply could not accumulate signal averages long enough to observe a signal above the noise; as mentioned above the densities of phosphorus atoms in the samples are on the extreme lower limit of the weak sensitivity of NMR spectroscopy, and even with 100% nuclear polarization would be somewhat difficult to observe. Other concerns included the stability of the electronic receiver circuits over time periods of many hours while immersed in a liquid helium bath, the difficulty of the illuminating light diffusing in the liquid medium before illuminating the sample, variable heating of the sample from inconstant light sources, the absolute guess of appropriate flip angle extrapolated from the

TlBr calibration sample, etc. The detriment of not having an observable signal from an actual sample to optimize prior to the experiment is a difficult obstacle to overcome.

4.5.2.1 Optimum Flip Angle for Long T_1 Experiments

It is interesting to note that in cases such as this experiment where many averages are needed and at the same time T_1 is very long, the "rule of thumb" often followed in NMR signal acquisition of waiting $5 \times T_1$ between acquisitions for full signal recovery is not optimal. The following simple calculation illustrates the point.

Assume a steady-state magnetization M_1. After flipping M_1 by an angle θ, the remaining magnetization along the $z-$direction M_2 is

$$M_2 = M_1 \cos\theta. \tag{4.2}$$

The subsequent recovery of the magnetization after a time t is given by the recovery equation

$$M(t) = M_0 \left(1 - \frac{M_0 - M_2}{M_0} e^{\frac{-t}{T_1}}\right). \tag{4.3}$$

So for a given repetition time between pulses $t = T_{rep}$, the magnetization will have recovered by an amount

$$M(T_{rep}) = M_1 = M_0 \left(1 - \frac{M_0 - M_2}{M_0} e^{\frac{-T_{rep}}{T_1}}\right). \tag{4.4}$$

Plugging in (4.4), (4.2) becomes

$$M_2 = M_0 \cos\theta \frac{1 - e^{-T_{rep}/T_1}}{1 - \cos\theta e^{-T_R/T_1}}. \tag{4.5}$$

Now the observable signal is

$$\begin{aligned} S &= M_2 \sin\theta \\ &= \frac{M_0}{2} \sin 2\theta \frac{1 - e^{-T_R/T_1}}{1 - \cos\theta e^{-T_R/T_1}}. \end{aligned} \tag{4.6}$$

For a given acquisition time T_{acq}, the total number of acquisitions is

$$n = \frac{T_{acq}}{T_R}, \tag{4.7}$$

and the signal increases with n while the noise increases with $\sqrt{n}$. Therefore, the signal to noise (SNR) after n acquisitions will go as

$$\frac{S}{N} \propto \sqrt{n} \sin 2\theta \frac{1 - e^{-T_R/T_1}}{1 - \cos\theta e^{-T_R/T_1}}. \tag{4.8}$$

Figure 4.5 shows a color map of Eq. (4.8) with T_R/T_1 plotted against flip angle θ. The colors show the SNR for given values of these two parameters. The angle that maximizes the SNR for a given T_R is known as the Ernst angle. We can obtain a better SNR *per hour*

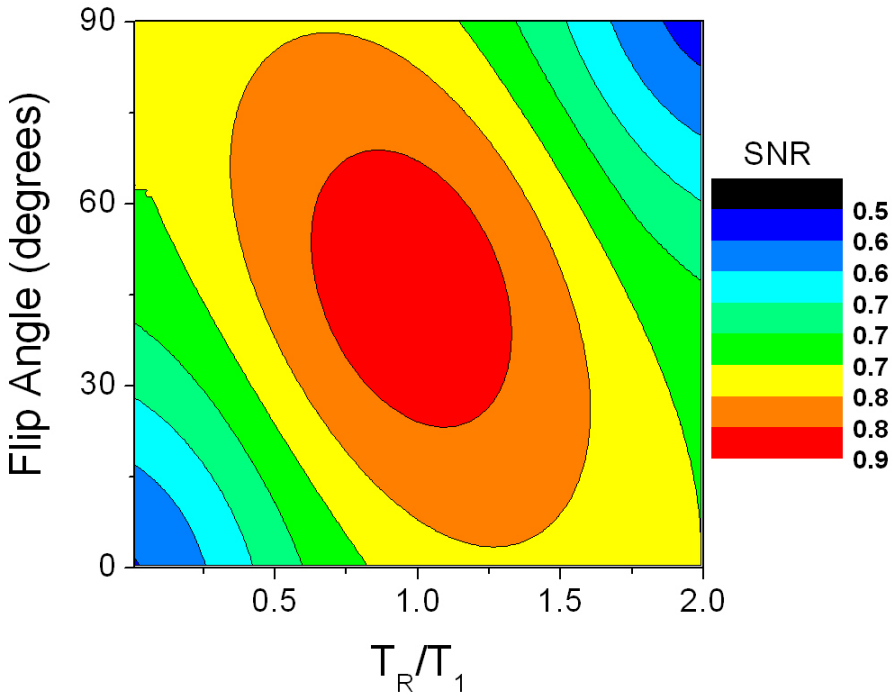

Figure 4.5: **Ernst angle calculation for optimal SNR per unit time** for multiple transient acquisition in samples with long longitudinal relaxation times. The red region shows that improved SNR can be obtained in shorter times by choosing more averages at lower values of T_R than fewer averages at longer T_R.

of acquisition time by choosing something like $T_R/T_1 = 0.75$ and $\theta = 50°$ than we could by choosing $\theta = 90°$ and the conventional $T_R/T_1 = 5$.

4.5.3 ESR Results

An attempt was made to understand the unknown parameters mentioned at the end of Sec. 4.5.2 by observing the signal in a different way. The concept was to perform the hyperpolarization at 8 T and 2 K, and then attempt to measure the enhanced *ESR* signal similar to the measurement made in Ref. [133] (see Fig. 4.4 for the EDMR data; the ESR data look similar). Observation of an enhancement of the ESR spectra, corresponding to a nuclear polarization, would indicate that hyperpolarization was indeed taking place and put constraints on many of the variables mentioned in Sec. 4.5.2.

Unfortunately, the ESR facilities to which we had access have a maximum magnetic field of 2 T and corresponding microwave range up to ≈ 50 GHz; performing electron resonance measurements at the $f = 240$ GHz resonance in 8 T was therefore impossible. Such high fields are, however, vital for the hyperpolarization effect to become operative, so it became necessary to develop a hybrid experiment.

The experimental procedure was as follows. The sample was mounted on a specially designed detachable probe, and was once again subjected to temperatures of 2 K at 8 T while being illuminated with either the infrared laser or the xenon discharge lamp. The sample was allowed to equilibrate with the helium bath and then was allowed to "spin-up" for 15 minutes, approximately 5× the measured polarization time in Ref. [133]. After the wait time, the sample was removed from the magnet and its liquid helium bath and immediately placed into an inert atmosphere of nitrogen to prevent water condensation. The removable portion of the probe was detached, transported, and introduced into the ESR magnet which was already calibrated and ready for measurement. The entire transfer took approximately 1-2 minutes to achieve. The sample was once again cooled to 2 K and ESR spectra were taken every several minutes for approximately 20 minutes to attempt to measure depolarization as a function of time.

Figure 4.6 shows a typical ESR spectra as obtained after one such experiment. Visible in the figure are the two electron transitions corresponding to the $n_1 \rightarrow n_2$ transition and the $n_4 \rightarrow n_3$ transition (see Fig. 4.1). The data were acquired by lock-in amplifier; the resulting signals therefore trace out the derivatives of the Gaussian resonance curves. Also visible in the spectrum between the two electron resonance peaks is a feature unrelated to our experiments. Features such as these have been seen to arise from a variety of imperfections

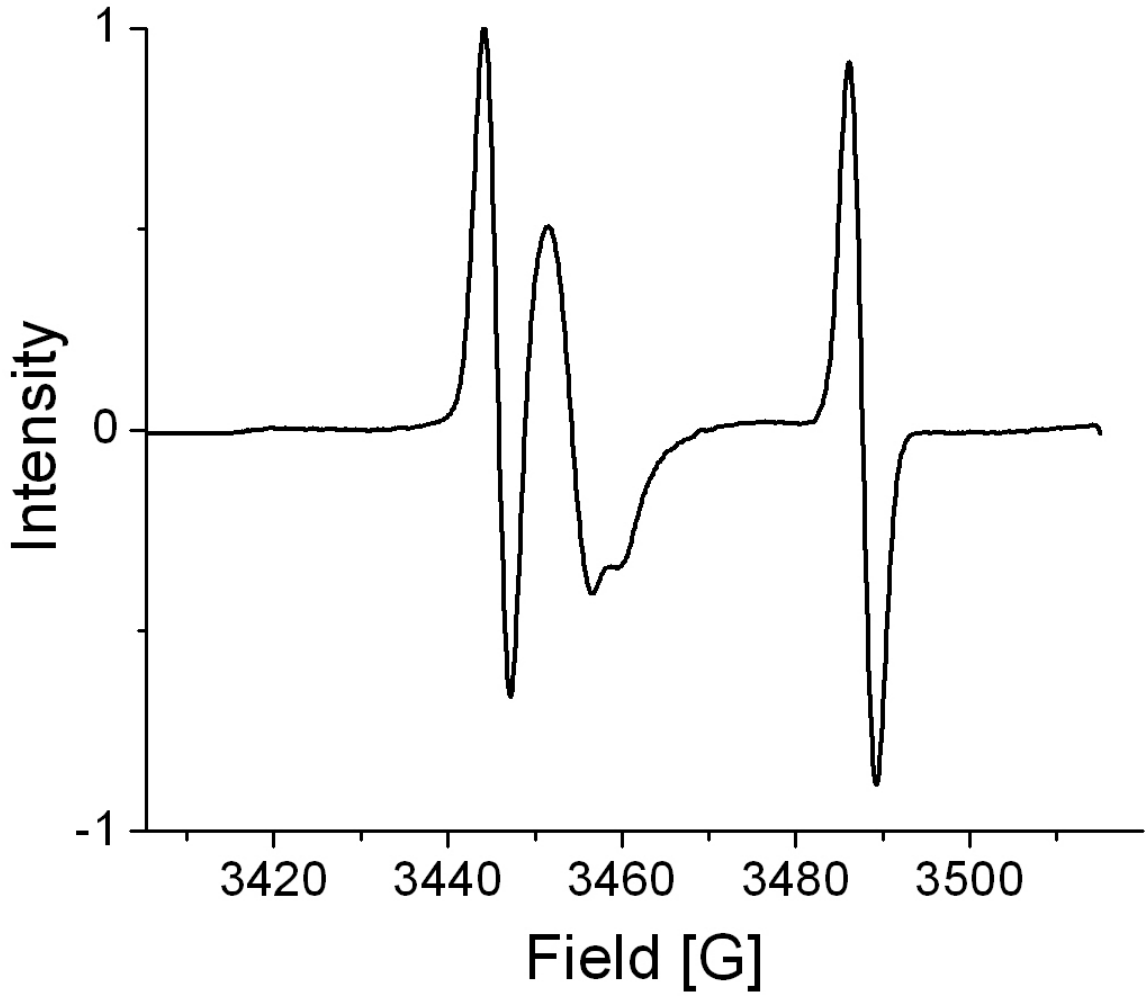

Figure 4.6: **ESR spectrum in Si:P for a typical run.** The hyperfine split spectrum shows the two electron transitions corresponding to $n_1 \rightarrow n_2$ transition and the $n_4 \rightarrow n_3$ transition. The feature to the right of the low-field peak is a P_b center, not relevant to our experiment.

in Si:P cyrstals such as oxidation states, Si dangling bonds, contaminating surface effects, etc; such imperfections are termed "centers" and have been studied in detail (for example, see Ref. [138]). For our purposes, such imperfections are undesirable, and simply lead to errors in our analysis when present.

The data were analyzed by isolating the high-field peak (HFP) and the low-field peak (LFP) individually. The HFP was then fit to a Gaussian derivative (a 3 parameter fit), and the amplitude, center, and variance were extracted from the fit. The LFP was fit

to the sum of two Gaussian derivatives – one for the LFP and the other to absorb the effects of the contaminating imperfection center evident in the spectrum. The center of the relevant LFP Gaussian derivative was fixed at the known hyperfine frequency relative to the center of the HFP. In this way the fitting routine extracts a corrected amplitude for the LFP that ignores the influence of the contaminating feature. A positive confirmation of hyperpolarization would then correspond to a ratio of LFP/HFP < 1 for polarization in the high-energy state, or LFP/HFP > 1 for polarization in the low-energy state. Based on the data measured by McCamey *et al.* [133] shown in Fig. 4.4, we expected to see a ratio of LFP/HFP < 1.

Figure 4.7 shows the resulting data from 14 experiments run with illumination by the xenon discharge lamp along with 7 experiments run as controls where the sample was not illuminated during the initial spin-up time. We were able to discern no obvious distinction in the ratio of the amplitudes of the LFP and HFP between the control experiments and those where hyperpolarization was expected. Similar results were obtained by illuminating the sample with the IR laser.

Apart from the afore mentioned possible problems that would prevent nuclear hyperpolarization from being generated or being detected by NMR, the ESR experiments introduced still further uncertainties which could readily explain the null result presented in Fig. 4.7. The necessity of extracting the sample from the 8 T magnet and transporting it nearly 50 m to the ESR spectrometer was an unfortunate complication in these experiments. Unavoidable exposure of the sample to strong magnetic field gradients and several dramatic thermal cycles could no doubt influence any nuclear polarization. The large contaminating imperfection centers also introduced systematic errors into the analysis algorithm, even after attempts to minimize them were made by annealing the sample.

4.6 Conclusions

The ESR experiments were meant to confirm the existence of the nuclear hyperpolarization, and to fix the values of several of the uncertain parameters such as the resonance frequency and uniform light illumination. Had that signal been obtained, the hyperpolarization would have been confirmed, and optimization of the NMR measurement could have then been carried out. Having failed in that endeavor, we discontinued the experiments, and to date no direct confirmation of the hyperpolarization technique presented in Ref. [133] by nuclear magnetic resonance has been achieved by any group to the best of our knowledge.

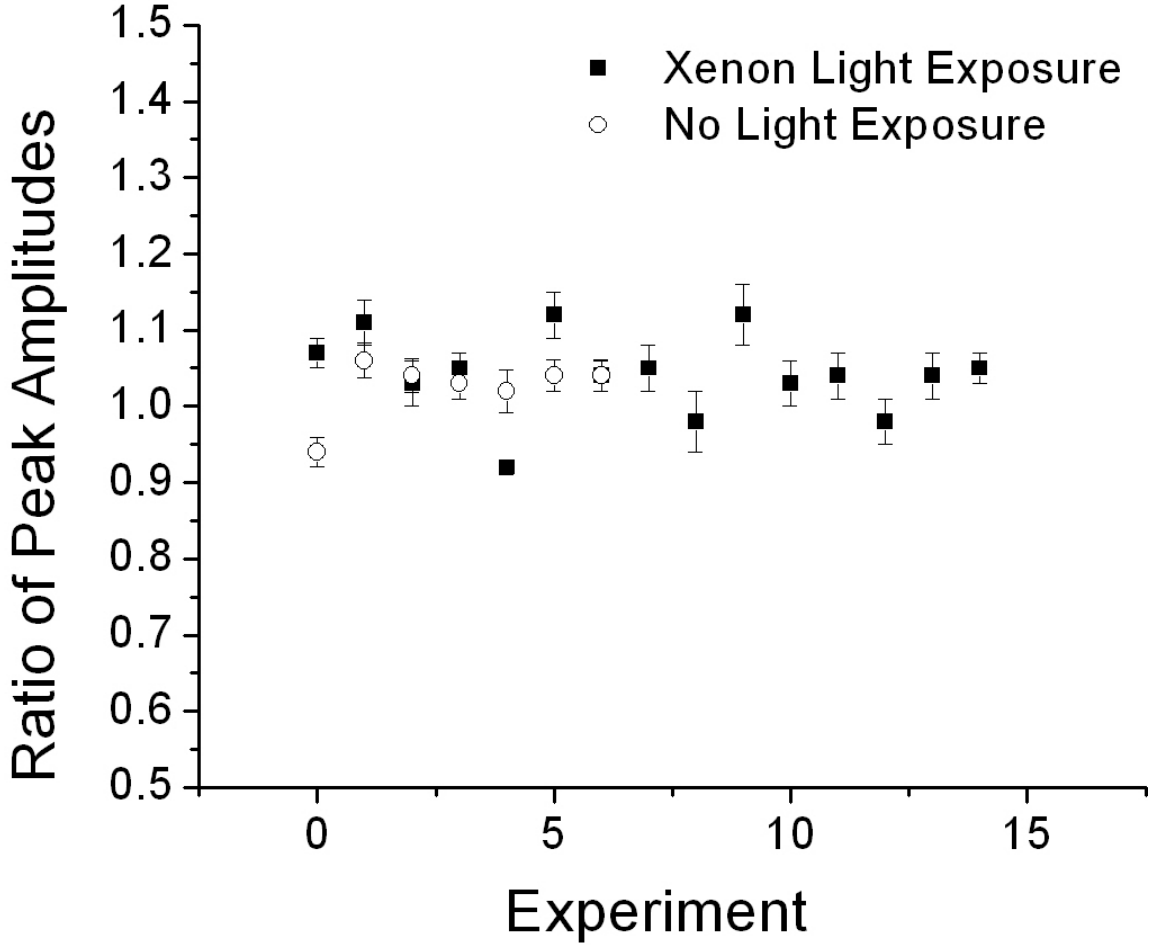

Figure 4.7: **ESR results in Si:P.** Results of several hyperpolarization attempts (solid squares), along with control experiments where no light was introduced to the sample (hollow circles). The quantity plotted is the ratio of the low-field peak amplitude to the high-field peak amplitude, expected to be less than 1 for cases of hyperpolarization.

CHAPTER 5

SUMMARY OF RESULTS

We have discussed a range of experiments in this dissertation; some have had surprising, and hopefully, impactful results. Here I will make a quick summary of the most important conclusions from each of the experiments presented here.

In Chapter 2, a comprehensive study of multiple ^{129}Xe and ^{19}F systems in different lattices was explained. The intent of these experiments was to attempt observation of previously unpredicted behavior in the long-time transverse decays of the nuclei in these solids. The unique forms of the nuclear spin decays tested here were predicted based on a new model of spin interaction, which includes the insight that microscopic chaos may play a role in the decays of these isolated spin systems. These predictions are made in a regime where first principle calculations are not possible, and perturbative methods have been shown to fail. A few of the mathematical and physical consequences of this model are: 1) The nuclear spin's transverse decay should approach a universal behavior in the long-time portion of a decay that begins from any arbitrary set of initial spin conditions, meaning that both the FID and any type of spin echo should all have identical shapes in the time domain after sufficient time has elapsed; 2) A solid echo initiated in the long-time regime of the FID will have a shape that is predictable over its entire decay regime; 3) A solid echo will have a phase that is determined by the long-time oscillation phase of the FID; and 4) A solid echo will have an amplitude that will also depend directly on the long-time parameters of the FID. In 9 of the 10 unique lattices tested in this work, we have found that each of these predictions correctly reflect the experimental behavior of the nuclear spin decays. In one of the systems, CaF_2 powder, we were unable to achieve sufficient resolution to observe the long-time regime of the transverse decays. The experiments relating to this work were published in Refs. [36] and [37].

In Chapter 3 we measured the frequency shift enhancement factor $(\kappa_0)_{\mathrm{XeRb}}$ to 6% precision, improving the semi-empirical number that was measured to within 50% over 20 years ago. From this measurement we were also able to infer $(\kappa_0)_{\mathrm{KrRb}}$ based on precise

measurements of the ratios of these two numbers by Schafer *et al.*[27]. These experiments were published in Physical Review Letters in 2011 [28].

In Chapter 4, we made attempts to directly measure the nuclear hyperpolarization observed in Si:P by McCamey *et al.* in 2009. Extensive NMR and ESR experiments on the low density phosphorus nuclei in these samples failed to reveal a non-thermal spin temperature distribution; however, we attribute this null result to the extreme difficulty of the measurement of very low-density nuclear number densities under extreme conditions, rather than to a contradiction of the effects measured by McCamey. Accordingly, we did not publish the results of these experiments in peer-reviewed journals, and the experiments and results are included here as the sole record.

The first appendix gives a brief account of a project that I headed as a new graduate student to characterize internal topography of oil shales under a research grant from Chevron Corporation. The second gives a spreadsheet of liquid helium vapor pressures for determining the temperature of a pumped helium bath.

APPENDIX A

APPLICATIONS OF HIGH PRESSURE GAS NMR TO OIL SHALE CHARACTERIZATION

A.1 Introduction

NMR techniques have been used extensively as noninvasive methods for study of a wide variety of porous materials. Using different techniques, information such as surface-area-to-volume ratios, average pore size, pore connectivity and continuity, and models of fluid transport can be obtained. Often, water-saturation of the sample is achieved, and diffusion of the water spins is measured in a pulsed gradient spin echo experiment. This method is widely used to study pore spaces from 50 μm and smaller since spin relaxation normally attenuates the NMR signal to within the noise for larger pores before the water molecule can diffuse across even one pore.

The Walsworth group at Harvard has shown that diffusion NMR techniques can be applied in porous media imbibed with polarized gas rather than liquid [145]. Such a procedure has important advantages over liquid-imbibed experiments. First, gases have diffusion coefficients orders of magnitude larger than those of liquids, allowing researchers to probe larger pore spaces and volumes. In the case of ^{129}Xe the diffusion coefficient is about 3 orders of magnitude larger than that of water (5.7×10^{-2} cm^2 s^{-1} at one atmosphere), allowing for diffusion measurements to probe length scales of millimeters. Also, the spin-1/2 noble-gases are chemically inert, reducing the probability of contaminating reactions with the sample and reducing surface T_1 relaxation. Finally, the opportunity exists to chose or tune the desired diffusion coefficient within a restricted range by simply altering the gas pressure in the sample.

Oil shale is a blanket term for any fine sedimentary rock that contains kerogens.[1] It is estimated that over 2 trillion barrels of oil lie locked in this solid form below Wyoming,

[1]Kerogens are the long chain organic polymer inclusions in sedimentary rocks.

Utah, and Colorado, which would translate into over 100 years of domestic supply at the current consumption rate of around 20 million barrels per year. These large and mostly untapped resources have stimulated many people to attempt liberation and utilization of the hydrocarbons trapped in these shales.

The natural process for the conversion of kerogens to oil deposits happens in the earth's crust, where temperatures in the neighborhood of 200 °C slowly convert portions of the kerogens into the hydrocarbons that we use as fossil fuels: crude oil and natural gas. Rarely content to let nature take its course, people have long sought ways to stimulate or replicate the process in the hope of developing further oil reserves. There are several methods currently being used or experimented with to extract oil from shales, most of which involve pressurized pyrolysis and/or solvent processes of reactive chemicals. Basically, the idea is to break up the long chain organic kerogen polymers, induce the necessary reactions to convert them to usable hydrocarbons, and then to extract the hydrocarbons from the earth. A useful piece of knowledge in devising realistic extraction processes is to understand the structure of the shales on all length scales as well as their characteristic internal topology as a function of pressure and temperature.

The Saam research group was approached in 2007 by the Chevron Corporation to explore whether the expertise of our group could be employed to help determine the internal structure of some oil shale samples from a shale bed the corporation was interested in developing. The basic question was whether the samples we were provided with were porous at any length scale. This project provided the opportunity for me to start working in the Saam labs during my second year of gradate school and become familiar with the basics of NMR.

A.2 High Pressure Fluorinated Gas

One way to probe porous media with NMR is to imbibe them with fluorinated gases, and observe the relaxation properties of the gas in contact with the sample. Commonly used fluorinated gases include sulfur hexafluoride (SF_6), hexaflouroethane (C_2F_6), tetrafluoromethane (CF_4), and perfluorocyclobutane (C_4F_8). These gases are chemically inert, non-toxic, and insoluable, allowing for ease of use and reasonably non-invasive measurements on the majority of materials. Additionally, they have very high signal intensities given the large number of ^{19}F atoms per molecule, all of which resonate at the same frequencies due to the molecular symmetry. The rapid longitudinal relaxation times of these gases (on the

order of 10 ms) make rapid signal averaging possible, and each gas is easy to obtain with 100% abundance of the fluorinated molecule. Finally, the high gyromagnetic ratio of ^{19}F makes these gases very straightforward to observe with large SNR. For our work, we chose to work with C_2F_6.

The initial experiments were intended to measure the longitudinal relaxation times of high pressures of C_2F_6 in the presence of oil shale samples. At high pressures, a significant fraction of C_2F_6 atoms could inhabit any pores in the samples. Fluorinated atoms confined in pores are known to relax with different time constants [114]; therefore, observation of more than one decay constant in a basic T_1 experiment could reveal the presence of pores in the rocks as well as give an indication of average pore size. Figure A.1 shows the experimental setup with the major components. I constructed the gas handling system to deliver the high-pressure gas in precise volumes into the freeze spoons. Here, the gas was cryopumped with liquid nitrogen so that more gas could be accumulated and result in higher pressures. Once the desired amount of gas had been frozen into the spoons, the spoons were allowed to warm and pressurize the high pressure cell. The high pressure cell was made to withstand up to 3000 psi and contained the sample and NMR circuitry.

Some of the samples used in the high pressure cell are shown in Fig. A.2a. The samples

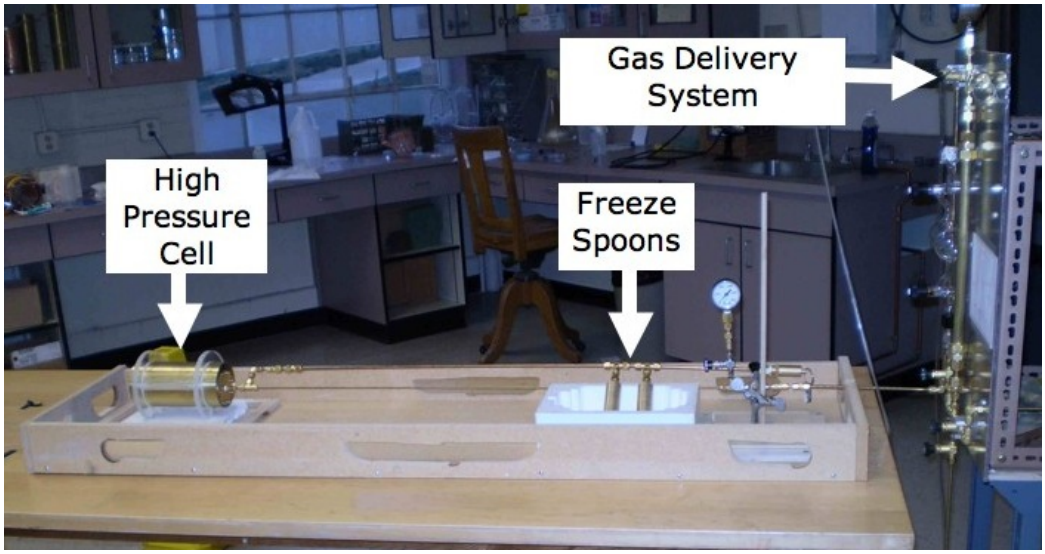

Figure A.1: **High pressure fluorinated gas experimental setup.** The gas delivery system shown delivers calibrated volumes of gas to the freeze spoons, which are kept under liquid nitrogen to accumulate the gas. Once the desired amount of gas has been frozen, the cell/spoon region is isolated and the solid revolatilized to provide high pressure.

(a) (b)

Figure A.2: **Typical oil shale samples for high pressure work.** (a) Upper - glass cells were used to contain the samples in the presence of a few atmospheres of gas. Lower - a typical sample of bare shale for use in the high pressure cell shown in Fig. A.1. (b) Samples for use in the 8 T xenon gas measurements.

in glass ampules were used in an initial version of the experiment where the gas was frozen into ampules and sealed; the experimental apparatus could then be much simplified since only the sample would be under high pressure, obviating the need for the setup in Fig. A.1. We soon found, however, that it was not possible to construct such samples at sufficiently high pressures, and so the setup evolved to that shown in Fig. A.1 where a sample like the one near the bottom of the photograph could be subjected to pressures around 1000 psi.

Initial control measurements were carried out on porous limestone rock that was obtained from the geophysics labs on campus. With these samples, we were indeed able to measure bi-exponential relaxation times in the ^{19}F due to gas confinement inside the rock. After we achieved this success, we proceeded with measurements on the oil shale samples.

Representative data from one of many runs are shown in Fig. A.3. These data were taken at an ambient fluorinated gas pressure of 100 psi, and are typical of the data taken over a range of pressures from 30 - 1000 psi. The figure shows a fit of the data to a single exponential with a time constant of $T_1 = 68$ ms. No bi-exponential relaxation was observed in any of the data we acquired at any pressure.

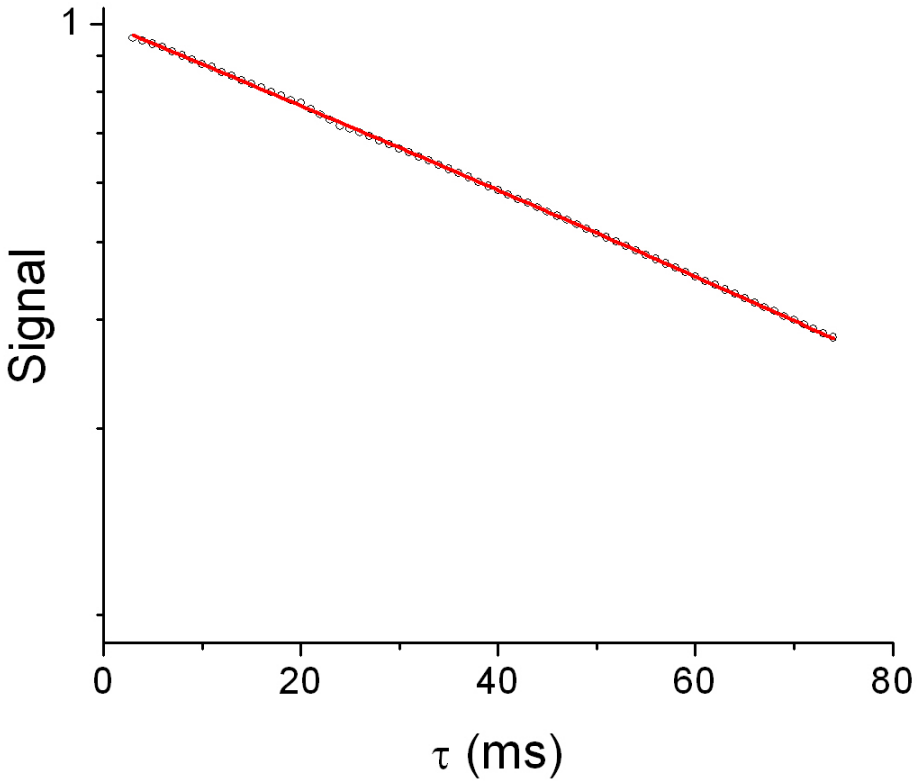

Figure A.3: **^{19}F T_1 in C_2F_6 showing no bi-exponential relaxation.** ^{19}F T_1 in C_2F_6 in the presence of oil shale at 100 psi gas pressure showing mono-exponential relaxation. Evidence of pore structure would show up as a departure from mono-exponential decay.

A.3 High Pressure ^{129}Xe

We next attempted measurements of the oil shales in the presence of high pressures of xenon gas. These measurements were carried out at 8 T and room temperature using the Aires (Tecmag) spectrometer at Larmor frequency $f = 94.6$ MHz. Using samples such as that shown in Fig. A.2b (the sample is contained in the nylon cap perpendicular to the brass gas line) we made measurements on several mesh sizes[2] of powders made from the oil shales in the presence of $^{129}Xe/O_2$ mixtures. In Fig. A.4 we show a typical spectral lineshape obtained from ^{129}Xe in the presence of a 400 mesh sample of oil shale compared with the spectrum obtained in a sample containing no shale. The intensities of the signals have been normalized to the same height for comparison purposes. Noteworthy in the

[2]Mesh is a method of characterizing particle sizes in a sample. A mesh of 400 corresponds to particles around 38 microns in size.

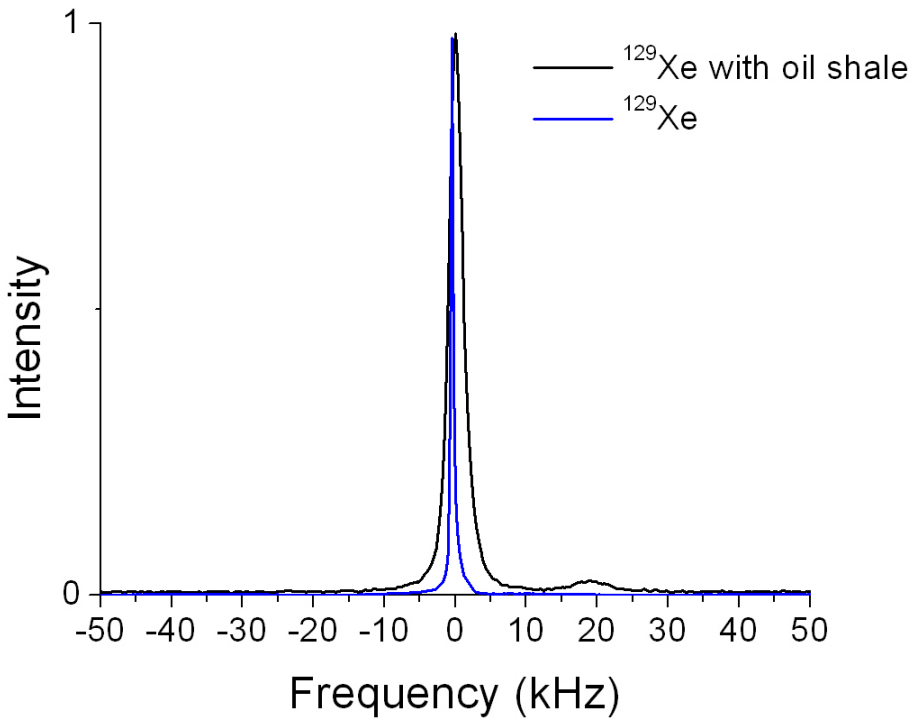

Figure A.4: **^{129}Xe spectra comparison showing 200 ppm shifted feature.** The black line shows a 200 ppm shifted peak in the presence of the oil shale in addition to the broadened free gas peak, compared to a xenon gas only sample (blue).

spectrum of the sample that contains the oil shale powder is the peak at around +18.5 kHz from the reference frequency, corresponding to a 200 ppm shift of the xenon resonance at 8 T. This feature, absent in the gas-only spectrum, was reproducible and indicative of some interaction of the ^{129}Xe with the oil shale.

Once we could identify a feature that was definitely due to interactions of the gas with the shale, we proceeded with our original experimental concept that the relaxation dynamics should be distinct in a confined pore relative to that of the free gas. If the small peak at 200 ppm could be attributed to gas trapped in pores inside the shale powder, the recovery time of that peak should differ from the recovery time of the large bulk gas peak. However, the lineshapes such as that shown in Fig. A.4 are significantly broadened by the susceptibility of the sample to over 6 kHz FWHM from several hundreds of Hertz in the gas only samples. Reasoning that removing such broadening would be beneficial in the measurements of the relaxation times, we moved our experiment to the the David M. Grant NMR facility where we could take advantage of the ability to measure the samples under

conditions of magic angle spinning to remove the majority of the dipolar broadening.

A.4 Magic Angle Spinning Work

Briefly, magic angle spinning is a solid-state NMR technique to remove certain tensorial components of the main line-broadening mechanisms that can obscure spectral features in NMR spectroscopy [146]. By spinning at the magic angle[3] the nuclear dipole interaction vanishes, and parts of the chemical shift anisotropy will also vanish. This can lead to a dramatic decrease in the second moment of the spectrum and allow the resolution of features otherwise hidden by the broadening mechanisms mentioned.

The relaxation experiments were carried out at 9.4 T (Larmor frequency $f = 110.59$ MHz) in 0.1 cc MAS rotors filled with enriched ^{129}Xe and O_2 to pressures of $1000 - 2000$ psi in the presence of different mesh sizes of oil shale powders. The samples were spun at 20 kHz. Both the 200 ppm feature and the large bulk gas peak were seen in these experiments, similar to the shapes shown in Fig. A.4. However, the FWHM of the lineshapes spinning at 20 kHz was reduced from tens of kilohertz to $5 - 10$ Hz, making the two features very well resolved.

T_1 measurements were made by saturation recovery. Initial findings on one sample (that containing coarse shale powder) showed that the two spectral features indeed showed different relaxation dynamics; the bulk peak had a measured $T_1 = 1.03$ seconds while the 200 ppm shifted smaller peak had $T_1 = 300$ ms. Similar measurements on the other samples of mesh size 200 and 400 did not show this behavior; the two spectral features in each of those samples all measured T_1 recovery times within error of one another.

We were left unclear as to the proper interpretation of the coarse shale data. It is possible to speculate that porous features exist in the coarsely ground shale that are destroyed when the shale is reduced to 400 mesh size, or that the relaxation dynamics were due to some other physics than pore confinement. Due to mounting evidence from other coincident experiments being carried out by other groups corroborated by the bulk of our results, we concluded that the oil shale samples we measured did not have porous structure in the range the NMR measurements were sensitive to. The decision was made not to pursue this project further.

---

[3]The magic angle is the angle such that the angle dependent dipole coefficient (2.28) vanishes, *i.e.*, where $\cos^2\theta = 1/3$. The angle is $\theta = 54.76^\circ$.

A.5 Atomic Force Microscopy Images

As a final step, I was assisted by the lab of Dr. Jordan Gerton to acquire atomic force microscopy images of a coarse oil shale sample. One such image, shown in Fig. A.5, shows an amplitude image of a small sample of a particle of the coarse oil shale powder in a 1μm $\times$1μm image. Interpretation of all the features of these data is not trivial; we will only comment that any pores in the shale are indiscernible here on the hundreds of nanometers scale.

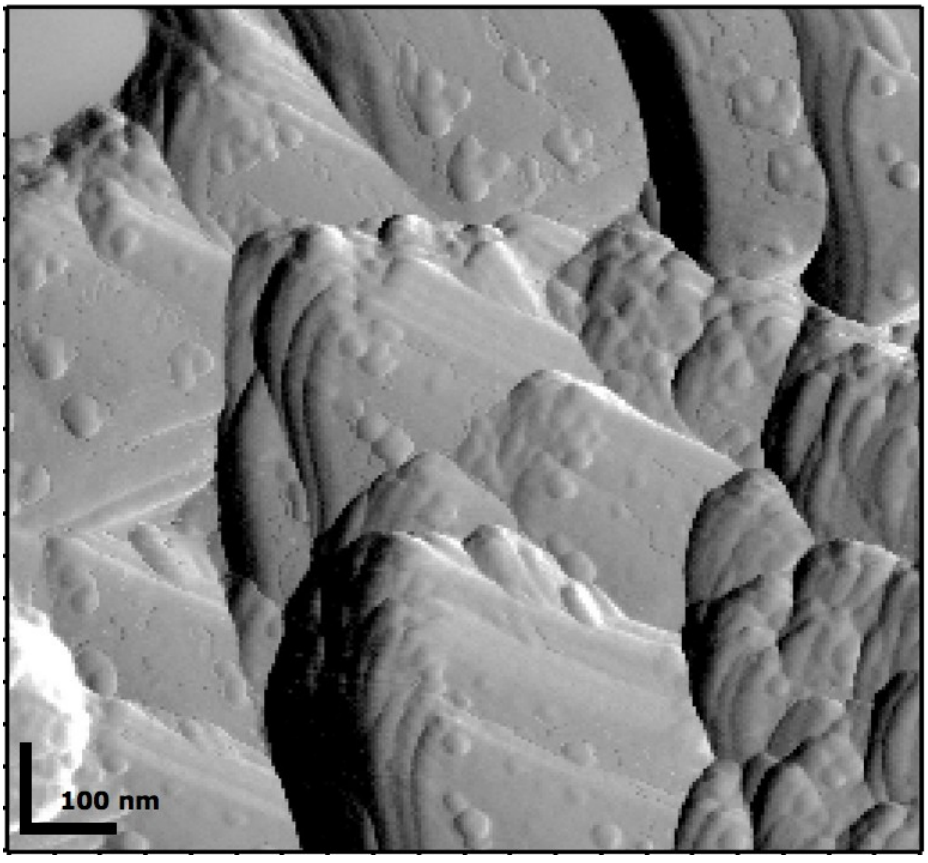

Figure A.5: **Atomic force microscopy image of coarse oil shale sample.** No pores are evident in the image at this scale.

APPENDIX B

MATRIX OF HELIUM VAPOR PRESSURE AS A FUNCTION OF TEMPERATURE

The vapor pressure of helium is a sensitive function of the temperature of the liquid. By pumping on the liquid helium column in which a sample is submerged, a sample can be controllably maintained below the 4.2 K boiling point of the liquid helium. Essentially, the effect works by removing the highest energy helium atoms (those which have escaped to the vapor) from the system. Removing these energetic atoms reduces the mean ensemble kinetic energy of all the atoms, effectively lowering the temperature of the liquid. The equation that relates the temperature T in Kelvin to the vapor pressure P in Torr is [147]

$$\ln P = I - \frac{A}{T} + B \ln T + \frac{C}{2} T^2 - D \left(\frac{\alpha\beta}{\beta^2 + 1} - \frac{1}{T} \right) \tan^{-1} (\alpha T - \beta) - \frac{\alpha D}{2(\beta^2 + 1)} \ln \frac{T^2}{1 + (\alpha T - \beta)^2)}$$

where the constants A, B, C, D, I, α, and β were determined by copious inspection of the available data up to that point. The values given by the authors in Ref. [147] for these constants are

$$\begin{aligned} A &= 6.399 \\ B &= 2.541 \\ C &= 0.00612 \\ D &= 0.5197 \\ I &= 4.6202 \\ \alpha &= 7.00 \\ \beta &= 14.14 \end{aligned}$$

To avoid constant calculation of this somewhat cumbersome equation, I prepared Table B.1 which I include here in the hopes that it may save someone else the trouble.

Table B.1: Chart of helium vapor pressure (Torr) vs T (K). The pressure is read off the table and the corresponding temperature is the sum of the column and row temperatures. For example, 2.66 Torr corresponds to 1.44 K.

T(K)	0.00	0.01	0.02	0.03	0.04	0.05	0.06	0.07	0.08	0.09
1.00	0.12	0.13	0.14	0.16	0.17	0.19	0.21	0.23	0.25	0.27
1.10	0.29	0.32	0.34	0.37	0.40	0.43	0.47	0.50	0.54	0.58
1.20	0.62	0.67	0.72	0.77	0.82	0.88	0.94	1.00	1.07	1.14
1.30	1.21	1.28	1.36	1.45	1.54	1.63	1.72	1.82	1.93	2.04
1.40	2.16	2.27	2.40	2.53	2.66	2.80	2.95	3.10	3.26	3.43
1.50	3.60	3.78	3.96	4.15	4.35	4.55	4.76	4.98	5.21	5.45
1.60	5.69	5.94	6.20	6.47	6.74	7.03	7.32	7.62	7.94	8.26
1.70	8.59	8.93	9.28	9.64	10.01	10.40	10.79	11.19	11.60	12.03
1.80	12.47	12.91	13.37	13.84	14.33	14.82	15.33	15.85	16.38	16.92
1.90	17.48	18.05	18.63	19.22	19.83	20.45	21.09	21.74	22.40	23.08
2.00	23.77	24.47	25.19	25.92	26.66	27.42	28.20	28.98	29.78	30.60
2.10	31.43	32.27	33.13	34.00	34.88	35.78	38.69	37.61	38.55	39.50
2.20	40.46	41.45	42.44	43.46	44.48	45.53	46.59	47.67	48.77	49.88
2.30	51.01	52.16	53.32	54.51	55.71	56.93	58.17	59.42	60.70	61.99
2.40	63.30	64.64	65.98	67.35	68.74	70.15	71.58	73.03	74.50	75.98
2.50	77.49	79.02	80.57	82.14	83.73	85.35	86.98	88.64	90.31	92.01
2.60	93.73	95.48	97.24	99.03	100.84	102.67	104.52	106.40	108.30	110.23
2.70	112.18	114.14	116.14	118.16	120.20	122.26	124.35	126.46	128.60	130.76
2.80	132.95	135.16	137.40	139.66	141.95	144.26	146.60	148.96	151.35	153.76
2.90	156.20	158.67	161.16	163.68	166.23	168.80	171.40	174.03	176.68	179.36
3.00	182.07	184.81	187.57	190.37	193.19	196.04	198.91	201.82	204.76	207.72
3.10	210.70	213.73	216.78	219.86	222.98	226.12	229.28	232.48	235.71	238.97
3.20	242.27	245.59	248.94	252.32	255.74	259.18	262.66	266.17	269.71	273.28
3.30	276.88	280.52	284.18	287.88	291.62	295.38	299.18	303.01	306.87	310.77
3.40	314.70	318.66	322.65	326.68	330.75	334.84	338.98	343.14	374.34	351.58
3.50	355.84	360.15	364.48	368.86	373.27	377.71	382.19	386.71	391.26	395.85
3.60	400.47	405.13	409.82	414.56	419.32	424.13	428.97	433.85	438.76	443.71
3.70	448.70	453.73	458.79	763.90	469.04	474.22	479.44	484.69	489.98	495.32
3.80	500.96	506.10	511.55	517.04	522.56	528.13	533.74	539.39	545.08	550.08
3.90	556.57	562.38	568.23	574.13	580.06	586.03	592.05	598.11	604.21	610.35
4.00	616.54	622.76	629.03	635.34	641.70	648.10	654.54	661.03	667.55	674.12
4.10	680.74	687.40	694.10	700.85	707.64	714.48	721.36	728.28	735.25	742.27
4.20	749.33	756.43	763.58	770.77	778.01	785.29	792.62	800.00	807.42	814.89
4.30	822.41	829.98	837.59	845.26	852.97	860.72	868.53	876.39	884.30	892.25
4.40	900.26	908.31	916.42	924.57	932.78	941.03	949.34	957.69	966.10	974.56

REFERENCES

[1] M. Engelsberg and I. Lowe, "Free-inducation-decay measurements and determination of moments in CaF2," *Physical Review B*, vol. 10, p. 822, Aug 1974.

[2] A. Dementyev, D. Cory, and C. Ramanathan, "Dynamic nuclear polarization in silicon microparticles," *Physical Review Letters*, vol. 100, p. 127601, March 2008.

[3] A. Abragam and M. Goldman, "Principles of dynamic nuclear polarisation," *Reports on Progress in Physics*, vol. 41, Jan 1978.

[4] G. Feher and E. Gere, "Polarization of phosphorus nuclei in silicon," *Physical Review*, vol. 103, pp. 501–503, May 1956.

[5] G. W. Morley, J. van Tol, A. Ardavan, K. Porfyrakis, J. Zhang, and G. A. D. Briggs, "Efficient dynamic nuclear polarization at high magnetic fields," *Physical Review Letters*, vol. 98, p. 220501, June 2007.

[6] W. G. Clark and G. Feher, "Nuclear polarization in InSb by a DC current," *Physical Review Letters*, vol. 10, p. 134, Feb 1963.

[7] A. Verhulst, I. Rau, Y. Yamamoto, and K. Itoh, "Optical pumping of 29Si nuclear spins in bulk silicon at high magnetic field and liquid helium temperature," *Physical Review B*, vol. 71, p. 235206, June 2005.

[8] S. Hayes, S. Mui, and K. Ramaswamy, "Optically pumped nuclear magnetic resonance of semiconductors," *The Journal of Chemical Physics*, vol. 128, p. 052203, Jan 2008.

[9] National Technical Information Service, *Proc. 2nd Int. Conf. on Polarized Targets*, (LB 500, UC-34 Physics, Springfield VA), 1972.

[10] C. D. Jeffries, *Dynamic Nuclear Orientation*. New York: Interscience, 1963.

[11] W. T. Wencheback, "Thermodynamics of spin systems in paramagnetic crystals," *Physical Reports*, vol. 14, no. 5, 1974.

[12] T. Walker and W. Happer, "Spin-exchange optical pumping of noble-gas nuclei," *Reviews of Modern Physics*, vol. 69, p. 629, Apr 1997.

[13] S. Appelt, A. Baranga, C. J. Erickson, M. V. Romalis, A. R. Young, and W. Happer, "Theory of spin-exchange optical pumping of 3He and 129Xe," *Physical Review A*, vol. 58, pp. 1412–1439, Aug 1998.

[14] E. Babcock, I. Nelson, S. Kadlecek, B. Driehuys, L. W. Anderson, F. W. Hersman, and T. G. Walker, "Hybrid spin-exchange optical pumping of 3He," *Physical Review Letters*, vol. 91, p. 123003, Sep 2003.

[15] E. Babcock, B. Chann, I. Nelson, and T. G. Walker, "Frequency-narrowed diode array bar," *Applied Optics*, vol. 44, p. 3098, May 2005.

[16] W. Happer, "Optical pumping," *Reviews of Modern Physics*, vol. 44, pp. 169–249, April 1972.

[17] Y. Jau, N. N. Kuzma, and W. Happer, "High-field measurement of the 129Xe-Rb spin-exchange rate due to binary collisions," *Physical Review A*, vol. 66, p. 052710, Nov 2002.

[18] W. Happer, E. Miron, S. Schaefer, D. Schreiber, W. V. Wijngaarden, and X. Zeng, "Polarization of the nuclear spins of noble-gas atoms by spin exchange with optically pumped alkali-metal atoms," *Physical Review A*, vol. 29, pp. 3092–3110, June 1984.

[19] W. Happer and W. V. Wijngaarden, "An optical pumping primer," *Hyperfine Interactions*, vol. 38, pp. 435–470, Jan 1987.

[20] A. Overhauser, "Polarization of nuclei in metals," *Physical Review*, vol. 92, pp. 411–415, Oct 1953.

[21] D. Pines, J. Bardeen, and C. Slichter, "Nuclear polarization and impurity-state spin relaxation processes in silicon," *Physical Review*, vol. 106, p. 489, May 1957.

[22] A. Abragam, *The Principles of Nuclear Magnetism*. Oxford University Press, 1961.

[23] C. Slicther, *Principles of Magnetic Resonance*. Springer, 1996.

[24] M. Levitt, *Spin Dynamics*. John Wiley and Sons, 2001.

[25] F. Bloch, "Nuclear induction," *Physical Review*, vol. 70, pp. 460–474, Oct 1946.

[26] S. W. Morgan, B. V. Fine, and B. Saam, "Universal long-time behavior of nuclear spin decays in a solid," *Physical Review Letters*, vol. 101, p. 067601, Aug 2008.

[27] S. R. Schaefer, G. D. Cates, T. Chien, D. Gonatas, W. Happer, and T. G. Walker, "Frequency shifts of the magnetic-resonance spectrum of mixtures of nuclear spin-polarized noble gases and vapors of spin-polarized alkali-metal atoms," *Physical Review A*, vol. 39, p. 5613, Jun 1989.

[28] Z. Ma, E. G. Sorte, and B. Saam, "Collisional 3He and 129Xe frequency shifts in Rb–noble-gas mixtures," *Phys. Rev. Lett.*, vol. 106, p. 193005, May 2011.

[29] A. Barton, N. Newbury, G. Cates, B. Driehuys, H. Middleton, and B. Saam, "Self-calibrating measurement of polarization-dependent frequency shifts from Rb-3He collisions," *Physical Review A*, vol. 49, p. 2766, Apr 1994.

[30] J. H. VanVleck, "The dipolar broadening of magnetic resonance lines in crystals," *Physical Review*, vol. 74, pp. 1168–1183, Nov 1948.

[31] I. Lowe and R. Norberg, "Free-induction decays in solids," *Physical Review*, vol. 107, p. 46, Jul 1957.

[32] W. S. Warren, W. Richter, A. H. Andreotti, and B. T. Farmer, "Generation of impossible cross-peaks between bulk water and biomolecules in solution NMR," *Science*, vol. 262, pp. 2005–2009, Dec 1993.

[33] B. V. Fine, "Long-time relaxation on spin lattice as manifestation of chaotic dynamics," *International Journal of Modern Physics B*, vol. 18, pp. 1119–1159, Feb 2004. "(cond-mat/9911230)".

[34] T. Prosen, "Ruelle resonances in kicked quantum spin chain," *Physica D*, vol. 187, pp. 244–252, 2004.

[35] B. V. Fine, *Theory of High Temperature Spin Dynamics*. PhD thesis, University of Illinois at Urbana-Champaign, 2000, Jul 2000.

[36] E. G. Sorte, B. V. Fine, and B. Saam, "Long-time behavior of nuclear spin decays in various lattices," *Phys. Rev. B*, vol. 83, p. 064302, Feb 2011.

[37] E. G. Sorte, B. V. Fine, and B. Saam, "Phase relationship between the long-time beats of free induction decays and spin echoes in solids," *arXiv:1102.0527v1*, 2011.

[38] E. M. Purcell, N. Bloembergen, and R. V. Pound, "Resonance absorption by nuclear magnetic moments in a single crystal of CaF2," *Physical Review*, vol. 70, p. 988, Dec 1946.

[39] G. E. Pake and E. M. Purcell, "Line shapes in nuclear paramagnetism," *Physical Review*, vol. 74, pp. 1184–1188, Nov 1948.

[40] C. R. Bruce, "19F nuclear magnetic resonance line shapes in CaF2," *Physical Review*, vol. 107, p. 43, July 1957.

[41] N. Bloembergen, E. M. Purcell, and R. V. Pound, "Relaxation effects in nuclear magnetic resonance absorption," *Physical Review A*, vol. 73, p. 679, April 1948.

[42] P. W. Anderson and P. R. Weiss, "Exchange narrowing in paramagnetic resonance," *Reviews of Modern Physics*, vol. 25, p. 269, Jan 1953.

[43] G. Glebashev *Zh Eksperim. i Teor. Fiz.*, vol. 32, no. 82, 1957. [CAS][Soviet Phys. JETP 5, 38 (1957)].

[44] J. Tjon, "Quantum theory of magnetic-resonance line shape in a rigid lattice," *Physical Review*, vol. 143, p. 259, March 1965.

[45] D. E. Barnaal and I. J. Lowe, "Measured nuclear magnetic resonance free-induction-decay shapes and moments for 19F in CaF2," *Physical Review*, vol. 148, pp. 328–331, Aug 1966.

[46] K. Tomita and M. Tanaka, "Greens function theory of magnetic resonance," *Progress of Theoretical Physics*, vol. 29, no. 4, pp. 528–549, 1963.

[47] P. Mansfield, "Nuclear-magnetic-resonance line shape in solids," *Physical Review*, vol. 151, pp. 199–207, Nov 1966.

[48] W. Evans and J. Powles, "The line shape problem in nuclear magnetic resonance," *Physics Letters A*, vol. 24, no. 4, pp. 218–219, 1967.

[49] P. Borckmans and D. Walgraef, "Long-time behavior of the free-induction decay in paramagnetic spin systems," *Physical Review Letters*, vol. 21, p. 1516, Oct 1968.

[50] B. P. Cowan, *Nuclear Magnetic Resonance and Relaxation.* Cambridge University Press, 1997.

[51] G. W. Parker, "Expansion theorems for magnetic-resonance line shapes," *Physical Review B*, vol. 2, pp. 2453–2459, Oct 1970.

[52] J. G. Powles and B. Carazza, "A non-classical information theory of spectral line shape," *Journal of Physics A Mathematical and General*, vol. 3, p. 335, March 1970.

[53] G. W. Canters and C. S. Johnson, "Numerical evaluation of moments and shapes of magnetic resonance lines for crystals and powders," *Journal of Magnetic Resonance (1969)*, vol. 6, no. 1, pp. 1 – 14, 1972.

[54] S. Jensen and E. Hansen, "Sixth and eighth moments of the magnetic-resonance lines of a dipolar-coupled rigid lattice," *Physical Review B*, vol. 7, p. 2910, April 1973.

[55] G. W. Parker and F. Lado, "Calculation of NMR line shapes in calcium fluoride from modified moment expansions," *Physical Review B*, vol. 9, p. 22, Jan 1973.

[56] *Proceedings of the First Specialized Colloque Ampere*, (Krakow, North Holland, Amsterdam), 1973.

[57] K. Vollmers, I. Lowe, and M. Punkkinen, "A method of measuring the initial behavior of the free induction decay," *Journal of Magnetic Resonance*, vol. 30, pp. 33–50, April 1978.

[58] M. Engelsberg and N. Chao, "Continued-fraction approximants to spin correlation functions. application to NMR line shapes," *Physical Review B*, vol. 12, p. 5043, Dec 1975.

[59] K. W. Becker, T. Plefka, and G. Sauermann, "Spin correlation function for free-induction decay in dipolar systems," *Journal of Physics C: Solid State Physics*, vol. 9, p. 4041, May 1976.

[60] A. Lundin and B. Provotorov, "Contribution to the statistical theory of the nuclear magnetic resonance line shape," *Zh Eksperim. i Teor. Fiz.*, vol. 70, no. 2201, 1976.

[61] A. Lundin and A. Makarenko, "Shape of NMR spectra in solids," *Zh. Eksp. Teor. Fiz*, vol. 87, no. 3, pp. 999–1009, 1984.

[62] R. Shakhmuratov, "Nuclear magnetic dephasing in solids," *Journal of Physics: Condensed Matter*, vol. 3, pp. 8683–8694, April 1991.

[63] P. A. Fedders and A. E. Carlsson, "Information-theoretic approach to high-temperature spin dynamics," *Physical Review B*, vol. 32, pp. 229–232, July 1985.

[64] J. Jensen, "Dipolar broadening of I=1/2 NMR spectra of solids," *Physical Review B*, vol. 52, p. 9611, Oct 1995.

[65] P. Gaspard, *Chaos, Scattering and Statistical Mechanics.* Cambridge University Press, 1998.

[66] V. A. Yurovsky and M. Olshanii, "Memory of the initial conditions in an incompletely chaotic quantum system: Universal predictions with application to cold atoms," *Physical Review Letters*, vol. 106, p. 025303, Jan 2011.

[67] F. L. Moore, J. C. Robinson, C. F. Bharucha, B. Sundaram, and M. G. Raizen, "Atom optics realization of the quantum-kicked rotor," *Physical Review Letters*, vol. 75, p. 4598, Dec 1995.

[68] M. F. Andersen, A. Kaplan, T. Grünzweig, and N. Davidson, "Decay of quantum correlations in atom optics billiards with chaotic and mixed dynamics," *Physical Review Letters*, vol. 97, p. 104102, Sept 2006.

[69] S. Wu, A. Tonyushkin, and M. G. Prentiss, "Observation of saturation of fidelity decay with an atom interferometer," *Physical Review Letters*, vol. 103, p. 034101, July 2009.

[70] V. A. Yurovsky and M. Olshanii, "Restricted thermalization for two interacting atoms in a multimode harmoic waveguid," *Physical Review A*, vol. 81, no. 043641, 2010.

[71] A. Peres, "Stability of quantum motion in chaotic and regular systems," *Physical Review A*, vol. 30, p. 1610, Oct 1984.

[72] H. Lee, "Theory and application of the quantum phase-space distribution functions," *Physics Reports*, vol. 259, pp. 147–211, July 1995.

[73] S. Chaudhury, A. Smith, B. E. Anderson, S. Ghose, and P. S. Jessen, "Quantum signatures of chaos in a kicked top," *Nature*, vol. 461, p. 768, Oct 2009.

[74] H. A. Weidenmüller and G. E. Mitchell, "Random matrices and chaos in nuclear physics: Nuclear structure," *Reviews of Modern Physics*, vol. 81, p. 540, May 2009.

[75] Y. Alhassid, "The statistical theory of quantum dots," *Reviews of Modern Physics*, vol. 72, p. 895, Oct 2000.

[76] B. V. Fine, "Long-time behavior of spin echo," *Physical Review Letters*, vol. 94, p. 247601, June 2005.

[77] A. Einstein, "On the movement of small particles suspended in stationary liquids required by the molecular-kinetic theory of heat," *Annalen der Physik*, vol. 17, pp. 549–560, Jan 1905.

[78] R. Florido, J. M. Martin-Gonzalez, and J. M. G. Llorente, "Locating Pollicott-Ruelle resonances in chaotic dynamical systems: A class of numerical schemes," *Physical Review E*, vol. 66, p. 046208, Jan 2002.

[79] S. Smale, "Differentiable dynamical systems," *Bulletin of the American Mathematical Society*, vol. 73, pp. 747–817, Jan 1967.

[80] M. Pollicott, "Meromorphic extensions of generalized zeta functions," *Inventiones Mathematicae*, vol. 81, no. 413, p. 147, 1986.

[81] D. Ruelle, "Resonances of chaotic dynamical systems," *Physical Review Letters*, vol. 56, p. 405, Feb 1986.

[82] H. Cho, T. Ladd, J. Baugh, D. Cory, and C. Ramanathan, "Multispin dynamics of the solid-state NMR free induction decay," *Physical Review B*, vol. 72, p. 054427, Aug 2005.

[83] P. Mansfield and J. G. Powles, "Double-pulse nuclear-resonance transients in solids," *Physics Letters*, vol. 2, pp. 58–59, Aug 1962.

[84] J. Jeener, "Dynamical effects of the dipolar field inhomogeneities in high-resolution NMR: spectral clustering and instabilities," *Physical Review Letters*, vol. 82, p. 1772, Feb 1999.

[85] P. Wang and C. Slichter, "A pictorial operator formalism for NMR coherence phenomena," *Bulletin of Magnetic Resonance*, vol. 8, p. 3, Jan 1986.

[86] W. K. Rhim, A. Pines, and J. S. Waugh, "Time-reversal experiments in dipolar-coupled spin systems," *Physical Review B*, vol. 3, p. 684, Feb 1971.

[87] B. Driehuys, G. D. Cates, E. Miron, K. Sauer, D. Walter, and W. Happer, "High-volume production of laser-polarized 129Xe," *Applied Physics Letters*, vol. 69, p. 1668, July 1996.

[88] G. Schrank, Z. Ma, A. Schoeck, and B. Saam, "Characterization of a low-pressure high-capacity 129Xe flow-through polarizer," *Physical Review A*, vol. 80, p. 063424, Jan 2009.

[89] R. J. Fitzgerald, M. Gatzke, D. C. Fox, G. D. Cates, and W. Happer, "Xe-129 spin relaxation in frozen xenon," *Physical Review B*, vol. 59, pp. 8795–8811, April 1999.

[90] T. Su, G. L. Samuelson, S. W. Morgan, G. Laicher, and B. Saam, "Liquid hyperpolarized Xe produced by phase exchange in a convection cell," *Applied Physics Letters*, vol. 85, no. 12, p. 2429, 2004.

[91] S. W. Morgan, *Relaxation of Solid Hyperpolarized 129Xe.* PhD thesis, University of Utah, Jan 2009.

[92] B. Driehuys, G. D. Cates, and W. Happer, "Surface relaxation mechanisms of laser-polarized 129Xe," *Physical Review Letters*, vol. 74, p. 4943, Jun 1995.

[93] B. Anger, *Polarization and Relaxation in Hyperpolarized 3He and 129Xe.* PhD thesis, University of Utah, Aug 2008.

[94] B. Saam, *Pulse-NMR Studies of Spin Relaxation Relevant to Laser-Polarized Noble Gases.* PhD thesis, Princeton University, Jul 1995.

[95] M. Gatzke, G. D. Cates, B. Driehuys, D. Fox, W. Happer, and B. Saam, "Extraordinarily slow nuclear spin relaxation in frozen laser-polarized 129Xe," *Physical Review Letters*, vol. 70, p. 690, Feb 1993.

[96] W. Yen and R. Norberg, "Nuclear magnetic resonance of 129Xe in solid and liquid xenon," *Physical Review*, vol. 131, p. 269, July 1963.

[97] H. M. Pastawski, P. R. Levstein, G. Usaj, J. Raya, and J. Hirschinger, "A nuclear magnetic resonance answer to the Boltzmann-Loschmidt controversy?," *Physica A*, vol. 283, pp. 166–170, Jan 2000.

[98] P. R. Levstein, G. Usaj, and H. M. Pastawski, "Attenuation of polarization echoes in nuclear magnetic resonance: A study of the emergence of dynamical irreversibility in many-body quantum systems," *The Journal of Chemical Physics*, vol. 108, p. 2718, Feb 1998.

[99] B. V. Fine, T. Elsayed, E. G. Sorte, and B. Saam, "Long-time properties of nuclear free induction decays in polycrystalline solids and powders," *in preparation*, 2011.

[100] M. Cohen and D. Turnbull, "Composition requirements for glass formation in metallic and ionic systems," *Nature*, vol. 189, p. 131, Jan 1961.

[101] M. Bhat, V. Molinero, E. Soignard, V. Solomon, S. Sastry, J. L. Yarger, and C. A. Angell, "Vitrification of a monatomic metallic liquid," *Nature Letters*, vol. 448, p. 787, Aug 2007.

[102] W. Allers, A. Schwarz, and U. D. S. R. Wiesendanger, "Dynamic scanning force microscopy at low temperatures on a noble-gas crystal: Atomic resolution on the xenon (111) surface," *Europhys. Letters*, vol. 48, pp. 276–279, Sept 1999.

[103] B. V. Fine, "Universal long-time relaxation on the lattices of classical spins: Markovian behavior on non-Markovian timescales," *Journal of Statistical Physics*, vol. 112, pp. 319–327, Jan 2003. [cond-mat/9911229].

[104] P. Borckmans and D. Walgraef, "Irreversibility in paramagnetic spin systems: Free induction decay and spin diffusion," *Physical Review*, vol. 167, p. 1516, Sep 1968.

[105] A. Lundin, "Shape of NMR spectra in solids: The pair interaction model," *Soviet Physics, JETP*, vol. 75, no. 1, pp. 187–188, 1992.

[106] B. V. Fine, "NMR spin-spin relaxation as kinetics in spin phase space," *Physical Review Letters*, vol. 79, p. 4673, Dec 1997.

[107] G. E. Pake, "Nuclear resonance absorption in hydrated crystals: Fine structure of the proton line," *The Journal of Chemical Physics*, vol. 16, p. 327, Dec 1948.

[108] S. W. Morgan, B. V. Fine, and B. Saam, "Universal long-time behavior of nuclear spin decays in a solid: Epaps supplement," *Physical Review Letters*, vol. 101, Aug 2008.

[109] S. Zhang, B. H. Meir, and R. R. Ernst, "Polarization echoes in NMR," *Physical Review Letters*, vol. 69, p. 2149, Oct 1992.

[110] B. C. Grover, "Noble-gas NMR detection through noble-gas-rubidium hyperfine contact interaction," *Physical Review Letters*, vol. 40, p. 391, Feb 1978.

[111] J. D. Jackson, *Classical Electrodynamics*. John Wiley and Sons, 1962.

[112] M. Arditi and T. R. Carver, "Frequency shift of the zero-field hyperfine splitting of 133Cs produced by various buffer gases," *Physical Review*, vol. 112, p. 449, Oct 1958.

[113] C. H. Townes, C. Herring, and W. D. Knight, "The effect of electronic paramagnetism on nuclear mangetic resonance frequencies in metals," *Physical Review*, vol. 77, p. 852, Jan 1950.

[114] L. Q. Wang, D. Wang, J. Liu, G. J. Exarhos, S. Pawsey, and I. Moudrakovski, "Probing porosity and pore interconnectivity in crystalline mesoporous TiO2 using hyperpolarized 129Xe NMR," *The Journal of Physical Chemistry*, vol. 113, pp. 6577–6583, Feb 2009.

[115] D. Yablonskiy, A. Sukstanskii, J. C. Woods, D. S. Gierada, J. D. Quirk, J. C. Hogg, J. D. Cooper, and M. S. Conradi, "Quantification of lung microstructure with hyperpolarized 3He diffusion MRI," *Journal of Applied Physics*, vol. 107, p. 1258, Aug 2009.

[116] B. Driehuys, H. E. Möller, Z. I. Cleveland, J. Pollaro, and L. W. Hedlund, "Pulmonary perfusion and xenon gas exchange in rats: MR imaging with intravenous injection of hyperpolarized 129Xe," *Radiology*, vol. 252, p. 386, 2009.

[117] T. G. Vold, F. J. Raab, B. Heckel, and E. N. Fortson, "Search for a permanent electric dipole moment on the 129Xe atom," *Physical Review Letters*, vol. 52, p. 2229, June 1984.

[118] Z. Wu, S. Schaefer, G. D. Cates, and W. Happer, "Coherent interactions of the polarized nuclear spins of gaseous atoms with the container walls," *Physical Review A*, vol. 37, p. 1161, Feb 1988.

[119] Z. Wu, W. Happer, and J. M. Daniels, "Coherent nuclear-spin interactions of adsorbed 131Xe gas with surfaces," *Physical Review Letters*, vol. 59, p. 1480, Sept 1987.

[120] T. E. Chupp, M. E. Wagshul, K. P. Coulter, A. B. McDonald, and W. Happer, "Polarized, high-density, gaseous 3He targets," *Physical Review C*, vol. 36, p. 2244, Jan 1987.

[121] M. V. Romalis and G. D. Cates, "Accurate 3He polarimetry using the Rb Zeeman frequency shift due to the Rb-3He spin-exchange collisions," *Physical Review A*, vol. 58, pp. 3004–3011, Oct 1998.

[122] I. C. Ruset, S. Ketel, and F. W. Hersman, "Optical pumping system design for large production of hyperpolarized 129Xe," *Physical Review Letters*, vol. 96, p. 053002, Feb 2006.

[123] X. Zeng, Z. Wu, T. Call, E. Miron, D. Schreiber, and W. Happer, "Experimental determination of the rate constants for spin exchange between optically pumped K, Rb, and Cs atoms and 129Xe nuclei in alkali-metal–noble-gas van der Waals molecules," *Physical Review A*, vol. 31, p. 260, Jan 1985.

[124] J. Pascale and J. Vandeplanque, "Excited molecular states of Cs-rare gas atom pairs," *Journal of Chemical Physics*, vol. 60, no. 6, p. 2278, 1974.

[125] W. E. Baylis, "Semiempirical, pseudopotential calculation of alkali–noble-gas interatomic potentials," *The Journal of Chemical Physics*, vol. 51, p. 2665, Sept 1969.

[126] U. Buck and H. Pauly, "Determination of intermolecular potentials by inversion of molecular beam scattering data," *Journal of Chemical Physics*, vol. 51, pp. 1662–1664, 1969.

[127] R. M. Herman, "Theory of spin exchange between optically pumped rubidium and foreign gas nuclei," *Physical Review*, vol. 137, p. 1062, Feb 1965.

[128] T. G. Walker, K. Bonin, and W. Happer, "Electron–noble-gas spin-flip scattering at low energy," *Physical Review A*, vol. 35, p. 3749, May 1987.

[129] D. R. Bates and A. Damgaard, "The calculation of the absolute strengths of spectral lines," *Philosophical Transactions of the Royal Society of London*, vol. 242, p. 101, 1949.

[130] T. Walker Private communication.

[131] B. Chann, I. Nelson, and T. G. Walker, "Frequency-narrowed external-cavity diode-laser-array bar," *Optics Letters*, vol. 25, p. 1352, Sept 2000.

[132] E. O. Stejskal and J. E. Tanner, "Spin diffusion measurements: spin echoes in the presence of a time-dependent field gradient," *The Journal of Chemical Physics*, vol. 42, p. 288, Jan 1965.

[133] D. R. McCamey, J. van Tol, G. W. Morley, and C. Boehme, "Fast nuclear spin hyperpolarization of phosphorus in silicon," *Physical Review Letters*, vol. 102, p. 027601, Jun 2009. 4 pages, 3 figures.

[134] R. C. Fletcher, W. A. Yager, G. L. Pearson, and F. R. Merritt, "Hyperfine splitting in spin resonance of group V donors in silicon," *Physical Review*, vol. 94, p. 844, June 1954.

[135] R. C. Fletcher, W. A. Yager, G. L. Pearson, A. N. Holden, W. T. Read, and F. R. Merritt, "Spin resonance of donors in silicon," *Physical Review*, vol. 95, p. 844, April 1954.

[136] W. Kohn and J. M. Luttinger, "Hyperfine splitting of donor states in silicon," *Physical Review*, vol. 97, p. 883, Feb 1955.

[137] G. Feher, R. C. Fletcher, and E. A. Gere, "Exchange effects in spin resonance of impurity atoms in silicon," *Physical Review*, vol. 100, p. 1784, Oct 1955.

[138] G. Feher and E. A. Gere, "Electron spin resonance experiments on donors in silicon. ii. electron spin relaxation effects," *Physical Review*, vol. 114, p. 1219, Jun 1959.

[139] T. Castner, "Direct measurement of the valley-orbit splitting of shallow donors in silicon," *Physical Review Letters*, vol. 8, p. 13, Jan 1962.

[140] A. M. Tyryshkin, S. A. Lyon, A. V. Astashkin, and A. M. Raitsimring, "Electron spin relaxation times of phosphorus donors in silicon," *Physical Review B*, vol. 68, p. 193207, Nov 2003.

[141] B. E. Kane, "A silicon-based nuclear spin quantum computer," *Nature*, vol. 393, pp. 133–137, May 1998.

[142] A. Honig and M. Moroz, "Precision absolute measurements of strong and highly inhomogeneous magnetic fields," *Review of Scientific Instruments*, vol. 49, no. 2, pp. 183–187, 1978.

[143] G. W. Morley, D. R. McCamey, H. A. Seipel, L. C. Brunel, J. van Tol, and C. Boehme, "Long-lived spin coherence in silicon with an electrical spin trap readout," *Physical Review Letters*, vol. 101, p. 207602, Nov 2008.

[144] S. A. Lyon, "Spectroscopy of hot carriers in semiconductors," *Journal of Luminesence*, vol. 35, no. 3, pp. 121–154, 1986.

[145] R. W. Mair, G. P. Wong, D. Hoffmann, M. D. Hürlimann, S. Patz, L. M. Schwartz, and R. L. Walsworth, "Probing porous media with gas diffusion NMR," *Physical Review Letters*, vol. 83, p. 3324, Oct 1999.

[146] E. R. Andrew, A. Bradbury, and R. G. Eades, "Nuclear magnetic resonance spectra from a crystal rotated at high speed," *Nature*, vol. 182, no. 4650, p. 1659, 1958.

[147] J. R. Clement, J. K. Logan, and J. Gaffney, "Liquid helium vapor pressure equation," *Physical Review*, vol. 100, p. 743, Oct 1955.